2021

The behaviour of advanced quenched and tempered steels during arc welding and thermal cutting

Muhammad Rizwan
University of Wollongong

THE BEHAVIOUR OF ADVANCED QUENCHED AND TEMPERED STEELS DURING ARC WELDING AND THERMAL CUTTING

By

MUHAMMAD RIZWAN

Supervisors

Professor Huijun Li (UOW)

Dr Andrew Kostryzhev (UOW)

Mr Chris C. Killmore (BlueScope)

Mr Chris A. Jones (BlueScope)

Dr Dake Yu (Bisalloy)

A thesis is submitted to fulfill the requirement for the award of the degree of

DOCTOR OF PHILOSOPHY

University of Wollongong, Australia

School of Mechanical, Materials, Mechatronic and Biomedical Engineering

MAR 2021

Thesis Certification

I, Muhammad Rizwan, declare that this thesis, submitted in fulfillment of the requirements for the award of Doctor of Philosophy, from the School of Mechanical, Materials, and Mechatronic and Biomedical Engineering, University of Wollongong, is wholly my work unless otherwise referenced or acknowledged. The document has not been submitted for qualifications at any other academic institution.

Muhammad Rizwan

March 2021

Table of Contents

Abstract

Quenched & tempered (Q&T) wear-resistant plate steels with martensitic microstructures have been in use for many years in the mining, defence, and construction industry due to their excellent mechanical properties (up to 1700 MPa of tensile strength and >10% elongation to failure). These mechanical properties are achieved by utilisation of up to 0.4 wt.% Carbon (C), <1.5 wt.% Manganese (Mn), microalloying with Molybdenum (Mo), Chromium (Cr), Nickle (Ni), Titanium (Ti), and sometimes Boron (B), and a combination of carefully designed thermomechanical processing schedule and post rolling heat treatment. In the last 10 years addition of <1.5 % Ti was shown to provide superior wear resistance at a moderate C content. Improvement in the wear resistance was achieved via the formation of TiC hard particles embedded in the tempered martensite matrix. Moderation of the C content in Ti-alloyed steels allowed to obtain steels with relatively low hardness, high toughness, and enhanced weldability (due to the low carbon equivalent of the steel composition). A combination of moderate hardness and high toughness positively influenced the wear resistance.

Fabrication of tools and equipment from the Q&T steels is carried out using conventional fusion arc welding and thermal cutting with oxy-fuel or plasma jet. The main problem, in this case, is the formation of an edge microstructure highly susceptible to cold cracking or hydrogen-induced cracking (HIC), which results in deterioration of mechanical properties, making steel unsuitable for the required application. In the case of Ti-alloyed steels, the heat input associated with thermal cutting and welding alters the TiC particle size distribution, in addition to the tempering of the martensitic microstructure, occurring in conventional Q&T steels. However, fabrication parameters may be controlled to avoid catastrophic microstructure deterioration and product failure. Generally, a type of welding process, environment, alloy composition, joint geometry, and size are the main causes of cracking after cutting and welding. Cracking susceptibility increases as the weld metal hydrogen content, material strength, and thickness increase. Cold cracking will occur if three conditions are satisfied: susceptible microstructure; type and magnitude of residual stresses; and importantly, the level of diffusible hydrogen that enters the weld pool. Cold cracking can be avoided through the selection of controlled heat input (depends upon current, voltage, and travel speed of welding) and preheating temperature.

This research work was dedicated to the investigation of the processing-microstructure-properties relationship in advanced Ti-alloyed Q&T steels during arc welding and thermal cutting. The post-weld cold cracking, hardness distribution in the heat-affected zone (HAZ) and weld metal, weld tensile properties, and toughness were related to steel composition (namely, C and Ti contents), cutting method (oxyfuel, plasma, and water jet), pre-heat temperature and heat input during cold thermal severity testing (CTS testing), bead on plate testing (BOP Testing) and K-type groove weld testing. Based on the obtained results, the optimum fabrication parameters were suggested.

In this project two commercially produced steel grades with varying C and Ti, contents were studied: Steel L (0.28C-0.4Ti, wt.%) and Steel H (0.38C-0.6Ti, wt.%). The investigation was conducted for the thickness of 12 mm and 32 mm for Steel L and 12 mm and 30 mm for Steel H. Oxy-fuel, plasma and, water jet cutting methods were used to cut these steels, almost similar cutting speed was applied for each method. Welding was carried out using flux core arc welding (FCAW) and gas tungsten arc welding (GTAW) methods. The heat input was set in the range of 1.2 – 3.5 kJ/mm and preheat temperatures in the range of 20 - 150 °C. Microstructural analysis and mechanical properties testing were carried out for the base plate, HAZ (during cutting and welding), and the weld metal. The mechanical properties (such as hardness, strength, and toughness variation with test temperature) were discussed in relation to the steel composition, plate thickness, cutting method, and welding parameters (heat input and pre-heat temperature).

Prior to processing, the **chemical composition** of as-received plate steels was measured using optical emission spark spectroscopy. After that, the **base metal mechanical properties** were evaluated through hardness testing, tensile testing and, Charpy V-notch impact testing. A more highly alloyed Steel H showed a higher strength but less toughness compared to less alloyed Steel L. The testing was conducted along and across the rolling direction. Evaluation of mechanical properties and microstructural parameters was also carried out for various cutting, welding, and testing conditions. All the samples for this research work were estimated for their sizes as per experiment design requirement or applicable code/ standard; on the basis of these sizes, the actual size of steel plates was calculated using AutoCAD software and the material was ordered accordingly.

The **microstructure characterisation** was carried out on un-etched and etched samples. They were subjected to optical and scanning electron microscopy (SEM) to reveal and evaluate the phase balance, grain sizes, and distribution of coarse and fine carbide particles of microalloying elements. Chemical analysis of particles was carried out using energy-dispersive X-ray spectroscopy analysis (SEM/EDS). These techniques were used for the characterisation of microstructure in the base metal, thermally cut edges, HAZ and, welded regions.

Cut edge microstructures were subjected to the metallographic analysis to reveal the effect of different cutting methods (oxy-fuel, plasma, and water-jet) for two chemistries and two thicknesses. The effect was studied on the basis of the change in hardness from the cut edge of test coupons. Cutting with oxy-fuel produced a wider heat-affected zone (HAZ) compared to the plasma cutting method while no variation was observed for the water-jet cutting method. In both steels of thickness 12 mm, the maximum decrease in hardness due to thermal cutting with oxy-fuel or plasma could reach 25% of the respective original hardness: 100 HV down from the original 400 HV in the lower alloyed steel with 0.28C-0.40Ti (wt.%) and 130 HV down from the original 500 HV in the more highly alloyed steel with 0.38C-0.6Ti (wt.%). Cutting with oxy-fuel produced a wider heat-affected zone (HAZ) (5 and 9 mm for the lower and higher alloyed steels, respectively), compared to plasma cutting (about 3 mm for both steels). No HAZ, microstructure, or hardness variation was observed for the water-jet cutting method. Maximum tempering of microstructure (minimum absolute hardness values or maximum relative decrease in hardness associated with the tempering) was observed in the lower alloyed steel (due to weaker solid solution and precipitation strengthening) cut with oxy-fuel (characterised by higher heat input). Minimum tempering occurred in the more highly alloyed steel (due to stronger solid solution and precipitation strengthening) cut with plasma (characterised by lower heat input). In the lower alloyed steel, coarse TiMoVCN, fine Ti-rich, and Fe_3C dissolved during thermal cutting. In the more highly alloyed steel, both coarse TiMoVCN and fine Ti-rich particles precipitated and grew, while Fe_3C dissolved. For both steels of thickness 32 mm and 30 mm, the maximum decrease in hardness due to thermal cutting with oxy-fuel or plasma could reach up to 34% of the respective original hardness: 131 HV down from the original 381 HV in the oxy cut lower alloyed steel with 0.28C-0.40Ti (wt. %) and 132 HV down from the original 483 HV in the oxy cut more highly alloyed steel with 0.38C-0.6Ti (wt. %).

Cutting with oxy-fuel produced a wider heat-affected zone (HAZ) (5 and 9 mm for the lower and higher alloyed steels, respectively), compared to plasma cutting (about 3 mm for both steels). No HAZ, microstructure, or hardness variation was observed for the water-jet cutting method. With respect to microstructure-properties variation with steel composition and cutting method, the following fundamental outcomes can be highlighted. Maximum tempering of microstructure (minimum absolute hardness values) was observed in the lower alloyed steel (due to weaker solid solution and precipitation strengthening) cut with oxy-fuel (characterised by higher heat input). Minimum tempering occurred in the more highly alloyed steel (due to stronger solid solution and precipitation strengthening) cut with plasma (characterised by lower heat input). In the lower alloyed steel, coarse TiMoVCN particles dissolved, and fine Ti-rich particles precipitated and grew during thermal cutting. In the more highly alloyed steel, both coarse TiMoVCN and fine Ti-rich particles precipitated and grew.

Welding tests included the following:

- Cold Thermal Severity (CTS) testing was conducted to study the effect of preheating required to avoid cold cracking phenomena as given in international standard ISO 17642-2-2005. The test coupons were prepared as per the requirement of the applicable standard. Steel L test coupons welded with a heat input of 1.2-1.6kJ/mm showed no cracking when preheated at 80˚C and above. The average hardness measured for test coupons was noted in the range of 470-504 HV for the HAZ region, 404-450 HV for parent metal, and 356-382 for weld metal. Steel H test coupons welded with a heat input of 1.2-1.6 kJ/mm showed no cracking when preheated at 90˚C and above temperatures. The average hardness measured for test coupons was noted in the range of 527-562 HV for the HAZ region, 519-555 HV for parent metal, and 456-473 HV for weld metal.

- Bead On Plate (BOP) testing was performed to study the effect of heat input on the through-thickness hardness of welded steels of higher thickness as per conditions of BS 7363:1990 international standard. The test coupons were prepared as per the requirement of the applicable standard. Higher preheat temperatures as specified by the steel manufacturer were used before welding. Both steels showed crack-free microstructures along with a drop in hardness for higher welding heat input values.

- K-type groove weld testing was carried out to assess the HAZ and weld toughness properties for both steels with higher thicknesses via Charpy V-notch testing as per the requirement of AS 2205.7.1-2003 standard. Toughness properties were studied on the basis of changes in hardness from the fusion boundary of the weld zone. Transition curves obtained for both steels at the fusion line, 2 mm and 5 mm from the fusion line, showed shifting of positions with microstructural parameters. Higher toughness was observed at 2 mm from the fusion line for Steel L and the fusion line for Steel H. Microstructural analysis via optical microscopy and SEM/EDS was carried out to investigate the effect of change of toughness properties with respect to grain size and precipitation/ dissolution of TiC particles at weld and HAZ regions. No sharp transition from ductile to brittle temperatures was observed for curves obtained for samples tested at various temperatures. However, the weld centre line and HAZ analysis showed a dependence of microstructural parameters on the thermal cycle associated with the welding process. All samples from both steels showed a decrease in toughness at respective testing temperatures, i.e. from room temperature to the lowest temperature of -70˚C.

Mechanical testing methods included:

- Hardness Testing: For the base metal, Australian standard AS 1817-1 (Vickers Hardness Test for Metallic Materials, Method-1: Test Method ISO 6507-1:1997, MOD) was followed while for the welded samples AS 2205.6.1-2003 R218 (Methods for destructive testing of welds in metal, method 6.1: weld joint hardness test) was used.

- Charpy V-notch Testing: For the base metal, Australian standard AS 1544.2-2003 was used while for the weld and HAZ AS 2205.7.1-2003 (Methods for destructive testing of welds in metal, Method 7.1: Charpy V-notch impact fracture toughness test) was used for evaluation.
- Tensile Testing: For base metal testing, Australian standard AS 1391-2007 was followed.

This thesis consists of 8 chapters.

Chapter 1 presents the literature review starting from the application of Ti-microalloyed steels, the requirement of wear-resistant properties, the effect of steel thickness, preheat and heat input in conventional welding and cutting methods on weld quality, quality control methods, and finally a case study to compare the available information with respect to conventional Q&T steel grades to explore the knowledge gap and formulate aims and objectives for the current project.

Chapter 2 describes the types/ thicknesses of materials used and methods of testing/examination exercised to highlight effects on these materials due to cutting and welding technology used in this research work.

Chapter 3 presents the evaluation of mechanical properties, such as strength, hardness, and toughness, of as-received Ti-alloyed plate steels through mechanical testing.

Chapter 4 includes a study of the thermal cutting effect on hardness and microstructural parameters of these Ti-microalloyed steel grades for different thicknesses.

Chapter 5 addresses the influence of preheating temperature on the weld cracking propensity of these steels of higher thicknesses.

Chapter 6 elucidates the influence of a different set of heat inputs on hardness variation in these steels.

In Chapter 7, the K-type groove weld joint was considered to study toughness properties. Flux-cored arc welding (FCAW) process was selected to weld plates of thicknesses 32 mm for Steel L and 30 mm for Steel H.

In Chapter 8, general conclusions and recommendations for practical application of welding technologies were discussed on the basis of obtained results. It also covers possible directions of future work that can be conducted to further improve the quality of thermally cut and welded high-strength Q&T steels.

Acknowledgements

I would like to express my deepest gratitude to my academic supervisors, Prof. Huijun Li and Dr Andrew Kostryzhev. The successful completion of this thesis is due to their continuous support and well-directed guidance. The discussions with Huijun and Andrew always broadened my knowledge and boosted my creativity. Being my co-supervisor, Andrew also helped me obtain a good start point at the University of Wollongong. He always encouraged me to work hard and live a positive life, which helped me overcome academic difficulties. He was always ready to give corrections and comments on my drafts whenever I needed his input.

I am also very grateful to Dr Paul Zulli (Director, ARC Research Hub for Australian Steel Manufacturing), Dr Dake yu (Technical Manager R&D, Bisalloy), Chris C. Killmore (Specialist Product Innovation, BlueScope), and Chris A. Jones (Manager Welding & Materials Evaluation, BlueScope) working as industrial supervisors with me. They helped me a lot through their valuable feedback for this research work to understand the technical concepts from the academic and industrial application points of view.

I am also thankful to UOW Central Workshop staff including Mr Ron Marshal, Mr. Stuart Rodd, Mr. Alex Gonzalez, and Mr. Leighton Hill for their support to prepare samples for this research project. Many thanks to Mr Matthew Franklin (Senior Technical Officer Materialographic Labs at UOW) for training and guidance. I am very grateful to Dr Kristin Carpenter (Research Fellow at UOW) for his support to conduct testing of toughness assessment of steels under research. I am also thankful to Azdiar Gazder (Incharge SEM, AIIM, UOW Innovation campus) for training and support to use JEOL JSM-7001F FEGSEM (supported by grant LE0882613) at the Electron Microscopy Centre at the University of Wollongong.

This project was financially funded by ARC Research Hub for Australian Steel Manufacturing under the Industrial Transformation Research Hubs scheme (Project ID: IH130100017), together with M/S BlueScope Steel and M/S Bisalloy Steels. Without such support, it was not possible to execute and accomplish this project, for which I am very grateful.

I would like to thank all my friends for the happy times we had in the university and outdoors. Finally, I would like to acknowledge my Parents & Family for their unconditional love & support.

List of Figures

List of Tables

Chapter 1

1. Literature Review

1.1 Background

Quenched & tempered (Q&T) steels, usually, have high strength and toughness in comparison to conventional carbon steels, hence improved their structural efficiency due to the high strength to weight ratio. They have 850 –1700 MPa tensile strength and a maximum 80% of yield ratio as well as high hardness that offer exceptional resistance to indentation and shock. They have been developed and produced for many strategic applications that require a combination of toughness, tensile strength, and hardness [1-5]. For this research project, titanium microalloyed advanced quenched & tempered martensitic high strength wear-resistant steels were selected to study the behaviour of such steels during arc welding and thermal cutting.

The fabrication of these steel structures, presently, utilises conventional fusion arc welding processes. The main problem, in this case, is the formation of a microstructure highly susceptible to cold cracking [6-13].

According to Easterling [14], "good weldability" is a function of several factors. It is a complex property of the steel that covers both sensitivity to weld cracking and the toughness required by service conditions and test temperature. The factors involved are:

a) type of welding process,
b) environment,
c) alloy composition and
d) joint geometry and size.

The incongruity of any of the above factors may cause the problem of cracking. Weldability may be simply defined as the vulnerability of steel to various types of cracking associated with the weld. It can vary with the welding process type and the selected welding variables when the factors (b), (c) and (d) are constant.

Though there are recommendations and welding standards to prevent hydrogen assisted cold cracking (HACC) in the heat-affected zone (HAZ), such as AS/NZS 1554.1-2000, AS/NZS 1554.4-1995, AWS D l.1-2000, and EN 1011.2-2001, a universal and dependable model for HACC prevention in the weld metal is likely to be more

multifarious and difficult than for hydrogen cracking in the parent metal [15]. Hence, independent management rules to avoid HACC in the weld metal are yet to be established.

Commonly, the weld metal cold cracking susceptibility increases with the weld metal hydrogen content, strength and section thickness increases [16, 17]. It is more complex than cracking in HAZ [16].

The cold cracking test was developed in the 1940s [18] when HAZ cracking was found because of martensite in the microstructure. Advanced methods were developed later on to evaluate hydrogen assisted cracking of weldments. These tests became gradually more sophisticated, with some designed specifically for the investigation of the mechanism of HACC, and for the proper selection of welding materials and conditions for its avoidance during weld fabrication. Historically, most methods were designed to simulate some particular application in which cracking was experienced. The main objective of weldability tests is to examine the effects of various factors on cracking susceptibility, including parent metal composition, type of welding consumable, preheat temperature and other welding conditions [19].

While studying the continuous cooling behaviour of quenched and tempered armour steel, Kuzmikova [20] highlights that when steel is subjected to welding, the area surrounding the weld pool, known as the heat-affected zone (HAZ), undergoes complex thermal cycles which cause microstructural changes in the material. The extent and character of these changes depend on thermal cycles experienced and may lead to undesirable effects such as HAZ softening (or hardening) and hydrogen-induced cold cracking (HICC).

The degree to which the HAZ softens depends on chemical composition, thermal cycle, and kinetics of phase transformation [9]. Whether HICC will occur relies on three aspects occurring together, these being a susceptible microstructure; type and magnitude of residual stresses; and importantly, the level of diffusible hydrogen that enters the weld pool [21]. Cracks typically form in the coarse-grained (CG) sub-zone of the HAZ (CGHAZ), which has been exposed to a temperature between 1100°C to 1450°C [22]. It has been shown that the risk of CGHAZ cracking is linearly related to austenite to ferrite transformation temperature, as well as to Martensite finish (Mf) temperature during transformation, both of which may be predicted from experimental cooling curves [23]. Three conditions must be satisfied for cracking to occur:

1) hydrogen level is greater than critical concentration within the steel/alloy,
2) microstructure is susceptible to cracking,
3) residual stress level is greater than the threshold value for hydrogen embrittlement (HE).

The HE effect is pronounced at temperatures between ambient to about 149°C and decreases with increasing temperature. HE affects static properties to a much greater extent than impact properties. If the hydrogen is present and sufficient stress is applied, failure can occur quickly. The amount of trapped hydrogen depends on the environment, surface reactions, and the presence of hydrogen traps in the metal such as imperfections, inclusions, and pre-existing flaws or cracks. The amount of hydrogen needed to have a measurable effect on the mechanical properties varies with the strength level, microstructure, and heat treatment. In some cases, thresholds of critical hydrogen concentrations have been established. Residual stresses appear the following cooling during manufacture or welding, and after loads have been applied. Thick wall components are more vulnerable due to increased thermal stress and high restraint and take longer for hydrogen to diffuse out. In general, as strength increases, susceptibility to HE increases. Certain microstructures, such as untempered martensite and pearlite, are more susceptible at the same strength level than tempered martensite. Carbon steel that is severely hydrogen charged will have lower toughness than with no hydrogen. Hydrogen-initiated cracking can be sub-surface as well as surface-breaking where high stresses are present like in weld HAZ. Macro-analysis may show an indication of small surface cracks; while microanalysis will reveal softening of microstructure and may be compared to the fractured surface due to the presence of hydrogen. Higher-strength steels show intergranular cracking because of fabrication or heat-treatment history, steel composition, and hydrogen ingress [24].

Some actions to mitigate HE include [24]:

- Use preheating, dry and low hydrogen electrodes during welding,
- Use lower strength steels and post-weld heat-treatment (PWHT) to minimize residual stresses and hardness through tempering,
- Use de-hydrogenation technique by heating steels to 204°C or higher temperature to diffuse out hydrogen in weld metal after welding,

- Use particular inspection methods like dye penetrant testing (DPT), magnetic particle testing (MT) or fluorescent magnetic particle testing (WFMT), to identify HE surface cracking [24].

1.2 Application of advanced Q&T, Ti-microalloyed steels

This thesis investigates the behaviour of two types of advanced Q&T, Ti-microalloyed steels i.e. Steel L (containing 0.28C-0.4Ti) and Steel H (containing 0.38C-0.6Ti), in particular, their fabrication characteristics. Both types of steel find widespread application for construction, mining, civil engineering, farming equipment, cement works, and quarries. Applications, where very high wear resistance combined with high resistance to cracking is required in service, include [25-26]:

- Bucket liners for the shovel, dozer, excavator, loader, etc.,
- Stiffeners & cutting edges, etc. for different bucket types,
- Chute liners, vibratory feeder liners, truck tray body liners, hopper liners, blade liners for heavy-duty fans, grinder liners (SAG Mill),
- Wear parts for primary and secondary crushers,
- Screens, trommels, pipe elbows, deflectors, demolition tools (recycling), pipes for dredging, etc.

1.3 Requirement of properties (wear resistance with respect to hardness and toughness)

Generally, abrasive wear is a type of wear mechanism that occurs between hard rough surfaces and soft surfaces during sliding over one another. It is a high-cost issue in the agricultural, transportation, mining, and earthmoving industries [27-28]. Wear resistance is not a basic material property, but a complex tribological reaction because of interactive working situations depending upon many parameters. Wear resistance and hardness for a material can be described by a numerical relationship as:

$$\varepsilon = k \cdot \mathrm{H} \text{ or } dV/dl = \mathrm{L} \cdot \tan \theta/\pi \cdot \mathrm{H} \text{ [29-30]}$$

Where k is a constant, ε is the wear resistance, H is the hardness of the material, l is the sliding distance, V is the wear volume, θ is the base angle, and L is the normal load. However, the research conducted in the past showed it is not always true [31-33], and 'V'

and ‘S’-shaped relationships of the hardness and wear rate have been testified [34-36]. Zum Gahr [31, 37-38] proposed other models to consider further mechanical properties, like fracture toughness, and factors of test limitations, abrasive particle size and shape, abrasive type, applied load and incident angle. Since wear resistance is a complex phenomenon as compared with other mechanical properties, so it is difficult to describe wear resistance or abrasion as a function of relevant mechanical properties quantitatively like fracture toughness, hardness, and tensile strength; however microstructural analysis may provide required information to some extent.

Although there is no noteworthy advancement to better understand aspects of wear mechanism, hardness of the material is still believed to be the major indicator of abrasion resistance in the steel industry and hence, classification of steels has been given accordingly. Consequently, high abrasion-resistant steels are developed with a view of their high hardness as the first aim [39].

Many materials handling equipment are exposed to abrasive and impact wear. To enhance this resistance, conventional steels have been developed through mainly higher hardness level. However, increasing hardness level results in a decrease of processing ability of the material and some deterioration to shock resistance, which could be detrimental for equipment manufacturing or use [40].

Ultra-high strength materials, with enhanced properties of hardness, toughness, and abrasion resistance, were produced to cope with the above problems, such as steel grades L and H being used in this project. These steel grades have excellent abrasion resistance, due to the presence of titanium carbides in their microstructure, without increasing hardness and may be a better option in comparison to conventional 360 to 600 Brinell steels [26, 40-41].

1.4 Chemistry and processing of wear-resistant steels

During the last decades, a lot of research has been conducted to evaluate aspects of different microstructural properties on the wear behaviour of steels, to improve the wear resistance through the microstructural change and thus, to enhance the resilience of wear components. Kuzucu [65-66] and Unterwiser [67] reported while working on ferritic steels that, due to specific alloy composition, ferritic steels cannot attain high hardness for their microstructure, so these are relatively softer materials and cannot be used for

applications that require wear resistance. Moore et al. [68] studied and investigated how to increase the abrasion resistance of ferritic steels by introducing a harder phase known as pearlite. Wear resistance was reported to increase with the fraction of pearlite increasing to 100%. Clayton [69-71] and Chattopadhyay [72] reported that low carbon bainitic steels retain equivalent or higher wear resistance as compared to that of high carbon pearlitic steels, due to better ductility and toughness of bainitic steels.

In general, the microstructure with martensite shows a good wear resistance in comparison to ferrite, pearlite, and bainite [73]. As reported by Zum Gahr [31] and Tylczak [27], wear resistance increases gradually with the increase in hardness of the material in the order of ferrite, pearlite, bainite, and martensite respectively. Also, by increasing the carbon content, the abrasion resistance of bainitic and martensitic steels may be further enhanced. Although the hardness increases with increasing carbon contents, yet the abrasion resistance is decreased if the carbon contents exceed a critical value. It is because the toughness and the ductility are decreased adversely, resulting in the crack susceptible and brittle microstructure. Hence, abrasion-resistant microstructure should have an ideal combination of ductility and strength [39].

It is well recognized that V, Ti, and Nb micro-alloying elements exhibit imperative roles in achieving a better combination of high toughness and strength [74-76]; whereas micro-alloying elements precipitate out as nitrides or carbides in austenite and may decrease the rate of grain growth via pinning the grain boundaries [77-78]. This microstructure with fine grains can improve the toughness and strength of steel [79-81]. Since Ni and V are quite costly, so, production of Ti microalloyed steels has appealed more consideration recently [82-84]. For example, there are some research studies dealing with the effects of precipitation on microstructural and mechanical properties in Ti-microalloyed steels [85-89]. According to thermodynamic studies, Ti may precipitate out as TiC, Ti(C, N), TiN, or Ti4C2S2 particles [90-92]. TiN particles play an important role to control austenite grain size due to precipitation at grain boundaries as enlightened through expressions for pinning forces developed by Zener and Gladman [93-94]. The precipitation temperatures for TiC, Ti4C2S2 and TiN particles are above 1000 °C, 1200 °C and 1500 °C, respectively. Higher precipitation temperatures for Ti4C2S2 and TiN may result in bigger particles to grow but detrimental for the mechanical properties. Therefore, TiC particles, due to their smaller size, may have a significant influence on steel properties [42]. These

TiC particles demonstrate 3000 HV Vickers hardness and consequently act as hard spots in the steel microstructure as crushed gravel in concrete [26].

1.5 Thermal cutting of high strength steels

1.5.1 Classification of Cutting Processes: R. S. Parmar states in his book [43], *page 563*, that many thermal cutting processes have been developed for cutting steels including Oxy-fuel and Plasma Arc Cutting. These processes employ material removal viz., fast oxidation reaction, melting or evaporation of base metal. A typical classification is presented in Figure 1.1.

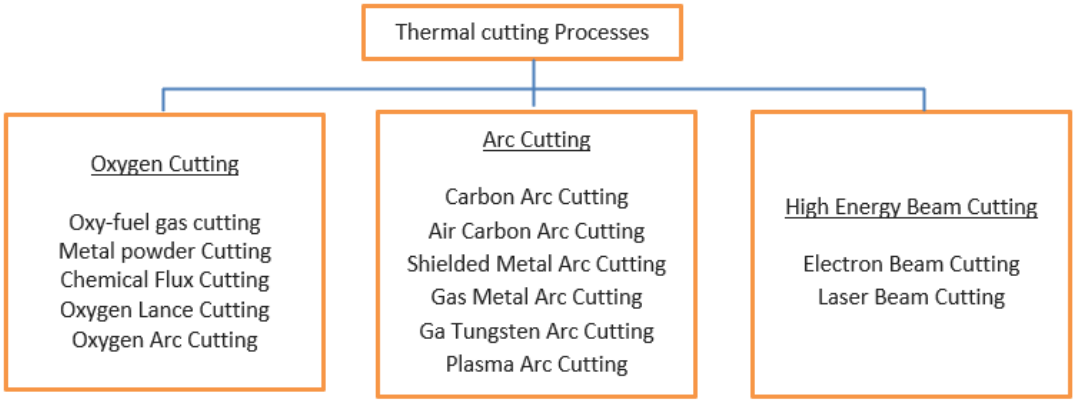

Figure 1.1 Types of thermal cutting processes [43]

1.5.2 Cutting Processes Employed: For this project, plasma arc and oxy-fuel gas thermal cutting methods were used. The effect of the cutting method was also considered and analysed by using water jet cold cutting.

a) *Oxy-fuel gas cutting process:* This is the most frequently used thermal cutting process for steel plates and often known as "flame cutting" or "gas cutting". It can be used to cut up to 2 m thick steel plate. This process involves preheating a small zone, wherefrom the cut is to be started, to the kindling temperature of the material. Compressed oxygen is made to be incident on the hot metal resulting in a very high rate of oxidation, which is often accompanied by an evolution of heat due to the exothermic nature of the reaction. The fuel gas employed is generally acetylene or propane, LPG (liquefied petroleum gas), natural gas or methyl acetylene propadiene stabilised (MAPP or MPS) may be employed depending upon availability and cost considerations. The torch for oxy-acetylene cutting is shown in Figure 1.2.

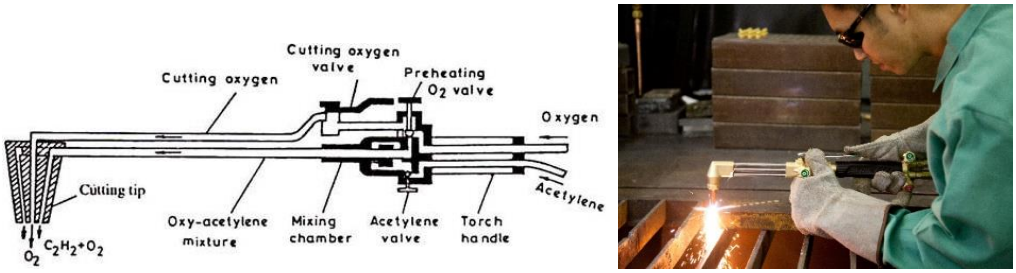

Figure 1.2 Schematic diagram of an oxy-fuel cutting torch [43][148]

When a workpiece is cut by a thermal cutting process, the width of the cut is referred to as kerf, which in the oxy-fuel gas process is a function of oxygen hole size in the nozzle tip, flowrate of oxygen and preheating gases, speed of cutting and the nature of the material being cut. For every metal, there is an optimal cutting speed. The thickness and nature of the material to be cut determine the tip size. The effects of cutting speed on drag, kerf and the nature of cut are shown in Figure 1.3.

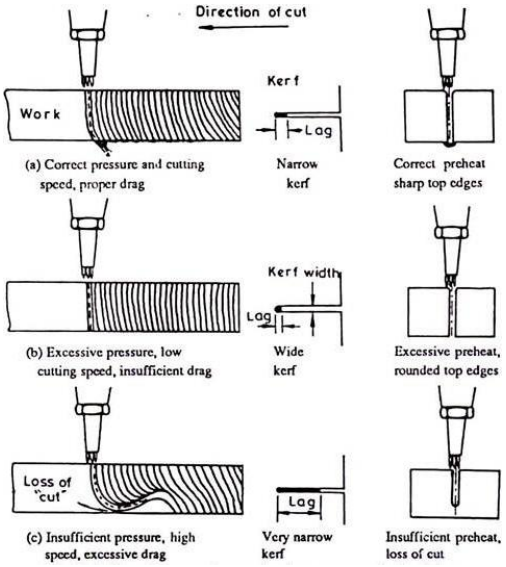

Figure 1.3 Schematic diagram of the effect of cutting speed on drag, kerf, and nature of the cut [43]

Oxy-fuel cutting is used extensively for general purpose cutting of steel. Structural shapes, pipes, rods and similar other materials may be cut to desired lengths for production or cut up for scrap and reclaim processes. The process can be used in the steel mill or foundry for cutting gates, risers, billets and castings. It can be used for heavy cutting up to 2m thick components and stack cutting [43] *page 564-569*. For all applications, the cut-edge microstructural properties vary as a result of this thermal

cutting process, which also develops residual stresses in the HAZ of base metal [101-103]. Such effects of the thermal cutting process are also detailed in the literature [104-105].

b) *Plasma arc cutting process:* This is a high precision and fast cutting method for metal fabrication activities [106-108]. In the plasma arc cutting (PAC) process, the metal is cut due to melting of a localized area with a confined arc and taking out the molten metal with a high-speed hot ionised gas called a plasma jet. PAC is used mainly in transferred arc mode employing a pilot arc for plasma arc initiation. There are three major variants of the PAC process: low current plasma current cutting, high current plasma cutting, and plasma cutting using water injection or water shielding. The design of the plasma torch depends on the method variation. Depending upon the type and thickness of material to be cut, the current of the plasma arc power source may range from 70 and 1000 A. A plasma cutting torch comprises an electrode holder that centres the electrode tip regarding constricting nozzle orifice. Nozzle size depends on the metal being cut and the variation of the process. When using a separate shielding gas, it generally passes through the nozzle orifice and is mixed with plasma jet from constricting nozzle, as shown by the schematic representation of the plasma torch in Figure 1.4.

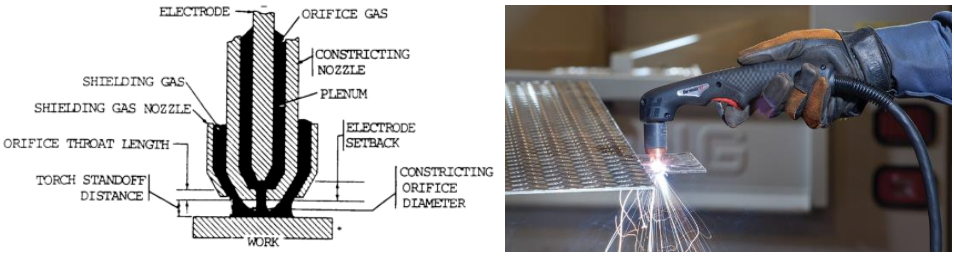

Figure 1.4 Schematic diagram of plasma arc cutting torch [43][149]

Plasma gas selection depends upon the material to be cut and the quality of cut desired. Compressed air (20% oxygen and 80% nitrogen) or nitrogen gas is normally used to cut carbon steels. For cutting of non-ferrous metal, the dual gas system comprising of nitrogen and carbon dioxide are used as plasma gas and shielding gas respectively. To have better quality cuts, nitrogen gas is used as a shielding gas and argon-hydrogen mixture is used as the plasma gas. Most applications are, however, confined to the cutting of plain carbon steels, stainless steels, and aluminium. It can be used for stack cutting, plate bevelling, piercing and shape cutting etc [43] *page 581-590*.

1.5.3 Example of thermal Cutting Effect: During the thermal cutting of specifically thicker steel plates, a localized heat treatment along with microstructural changes occurs at the surface to a few millimetres from the cut edge. These microstructural changes result in the hardening and softening of HAZ near the cut edge. The hardened HAZ is highly prone to cold cracking while the soft zone is developed due to annealing and shows a sharp decrease in hardness (Figure 1.5). The extent of both zones depends upon the cutting parameters and cutting method [44].

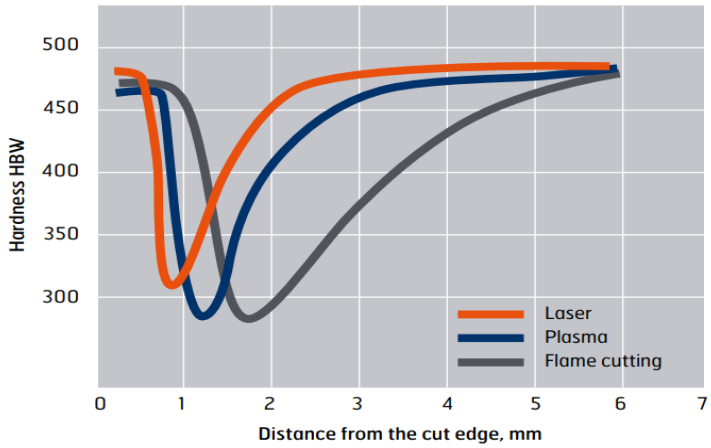

Figure 1.5 Hardness variation from the cut edge towards the base metal for 6 mm steel plates [44]

1.5.4 Effect of oxy-fuel process parameters: For the oxyfuel cutting process, the gas pressure is the same as for plain carbon steels except the travel speed must be reduced to approx. 30% when cutting high strength steels. Correct nozzle size should be selected to cut plate thickness to have minimum HAZ area. Normally, the oxy-fuel cutting may result in 2-3mm HAZ at the cut edge (as shown in Figure 1.6 for a commercial 0.16C-0.2Mo steel grade). Note that the HAZ may comprise of hard and soft areas near the cut edge and the hardness of the plate may return to its original value after that distance from the cut edge. For a commercially used 0.29C-1Cr-0.25Mo steel grade cut by oxyfuel, the HAZ may be up to 4-5mm wide from the cut edge for the plate, as shown in Figure 1.7, [45].

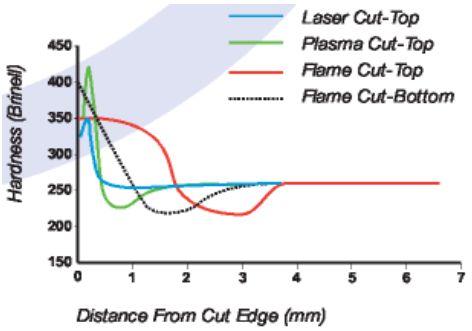

Figure 1.6 Hardness profile of laser, plasma and flame cutting for 6mm commercially used 0.16C-0.2Mo Steel grade, from the cut edge [45].

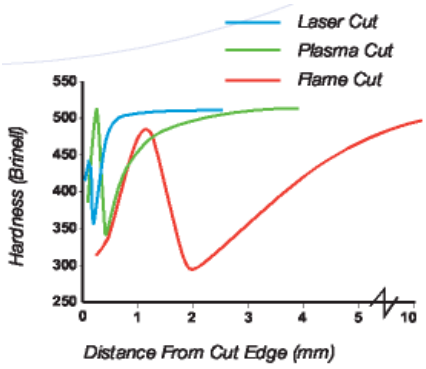

Figure 1.7 Hardness profile of laser, plasma and flame cutting for 6mm commercially used 0.29C-1Cr-0.25Mo Steel grade [45].

Preheating such commercial steel grades before oxy-flame cutting will minimize the hardness of the cut edge and decrease the risk of delayed cold cracking. Preheating is essential for high hardenability grades specifically in cold surroundings with plate temperature less than 19°C. In general, the zone to be preheated should be taken equal to 75 mm on either side of the line of cutting but on the opposite side of heat application for the plate. HAZ must be removed if the flame cut surface will be used for welding. The welding surface must be free from dirt, loose scale, oil and grease etc. Moreover, the use of multiple heads for cutting and selection of proper cutting parameters like gas pressure, nozzles size, and travel speed may help to reduce the distortion during stripping of plates. Flame cutting of small pieces may soften their edges. Softening on edges can also occur when flame cutting small strips, e.g. 50 mm wide x 50 mm thick plate. Cooling in the still air is preferred for flame-cut high strength steels. Plasma cutting is a suitable method to cut all high strength steel grades [45].

1.5.5 Advantage of Plasma cutting process: Plasma cutting process has the main advantage with respect to quality, efficiency and high yield production over flame cutting up to the thickness of 20 mm. HAZ due to a plasma cutting is less than that obtained due to flame cutting but peak hardness is normally higher. All other essentials like preheating, stack cutting of plates, stripping, and removal of HAZ are the same as those for the flame cutting technique [45].

1.5.6 Precautions for structural steels: In most applications, structural steel grades with up to 490 MPa tensile strength are flame cut without specific precautions. The cut

edge of these steels may show high hardness susceptible to cracking, so may not be recommended for critical applications. Preheating or suitable cutting parameters may help to minimize cut edge hardening of the plate, because of slow cooling [46].

1.5.7 Effect of cutting process on fatigue properties: While studying fatigue resistance property, Lawrence, Ho, and Altstette [47] showed that high strength low alloy steel (HSLA) cut with oxy-fuel and plasma had less variation in fatigue resistance compared to Q&T steel. It was assessed that the geometry of the flame-cut surface plays an imperative role rather than the microstructure to identify the initiation point of fatigue cracking. Similarly, Goldberg [96] showed that for HSLA steel plasma cut, fatigue cracking initiated at the upper edge of the flame cut surface. The magnitude of residual stresses was revealed to have a great influence over fatigue crack initiation sites. Compressive residual stresses offer a great advantage to have longer fatigue life by reducing the mean stress level in steels. Tensile residual stresses reduce fatigue life [47]. A similar effect for flame-cut HSLA steel samples was reported in [97].

1.5.8 Effect of cutting process on hardness: Bos, Thomas and Nibbering [95] investigated 25 mm thick plasma cut structural steel Fe510 for its properties and discovered that maximum surface hardness (450 HV) lies at a distance of 0.1 to 0.3mm from the cut edge. The hardness of the oxy flame cut edge was much higher than that of the plasma cut edge, employing the same cutting speed. The plasma cut surface was observed with a 50 µm thick layer of low carbon martensite. Next to this layer was found a transition zone comprising of very fine ferrite-pearlite and bainite, contrary to high carbon martensite as was observed for an oxy-fuel cut surface. Similar results were reported by other researchers for cut edge hardness and microstructural changes of samples cut using oxy-fuel and plasma arc.

1.6 Cold cutting of high strength steels

***1.6.1 Water jet cutting method*:** This method can be performed on all grades of high strength steels. No preheat is required. A basic benefit of employing the water jet cutting method is that it produces negligible HAZ. As cutting is carried out in the water (in the absence of heat), no microstructural changes occur resulting in the cut edge with original plate mechanical properties [45].

1.7 Welding of High Strength Q&T Steels

High strength Q&T steels have a great economical advantage over other types of steels due to their high strength to weight ratio. Ferritic consumables are normally used to weld such steels but may cause HACC in weldments [48, 109-111]. HACC can result from a localized critical diffusion of hydrogen, stress and crack-susceptible microstructure in the HAZ or the weld [131-136]. Hydrogen may come from the moist electrode/filler, atmosphere or impurities on the material surface. Incorrect storage and handling of electrode/ filler materials can have a major undesirable effect on the performance of welds [137]. Generally, pre/post-heating and post-weld heat-treatment (PWHT) are usual ways to avoid HACC, but this increases production cost and PWHT may cause stress relief cracking [49]. Other ways to control hydrogen ingress is through a selection of proper welding process, parameters and electrode/filler material [138-143]. Hydrogen diffusion also depends upon weld joint geometry and the sequence of depositing weld layers [144-147].

1.7.1 Welded joint design: In a welded fabrication, welds are used to join different parts. Such junctions of parts are called weld joints and defined as the locations where two or more members are to be joined. The applied force is transmitted through welded members or joints. Parts like sheets, pipes, rolled plates and many other shapes produced by casting, rolling or forging can be welded together due to the placement of members that help in defining the different types of joins as shown in Figures. 1.8 and 1.9 [50] *p815-818.*

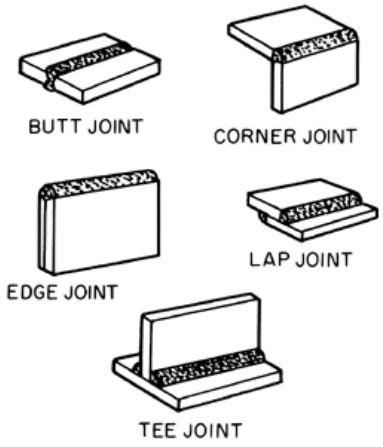

Figure 1.8 Five types of joints [50]

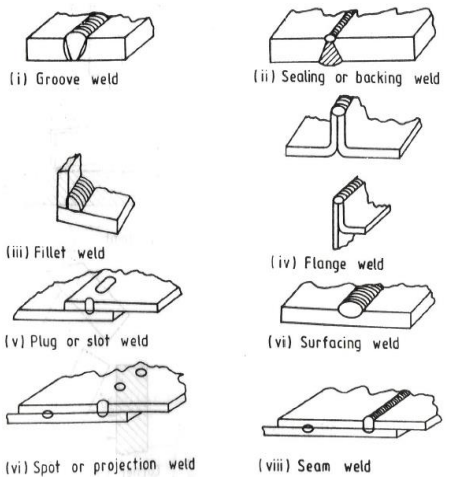

Figure 1.9 Eight types of welds [50]

1.7.2 Welding Techniques/ Technologies/ Methods: Welding is a joining process of two or more parts of similar or dissimilar materials to attain complete coalescence using heat and/or pressure. Most of the materials (metals, plastics, ceramics and composites) can be welded using different processes. To achieve this universality, many welding and allied processes have been developed. Most of the industrially important processes are classified depending upon the nature of the heat source and its movement resulting in spot, seam or zonal welds; or on the extent of heat generation viz., low heat and high heat [50]. American Welding Society (AWS) A3.0M/3.0:2010 [100] classify welding processes, as shown in Figure 1.10.

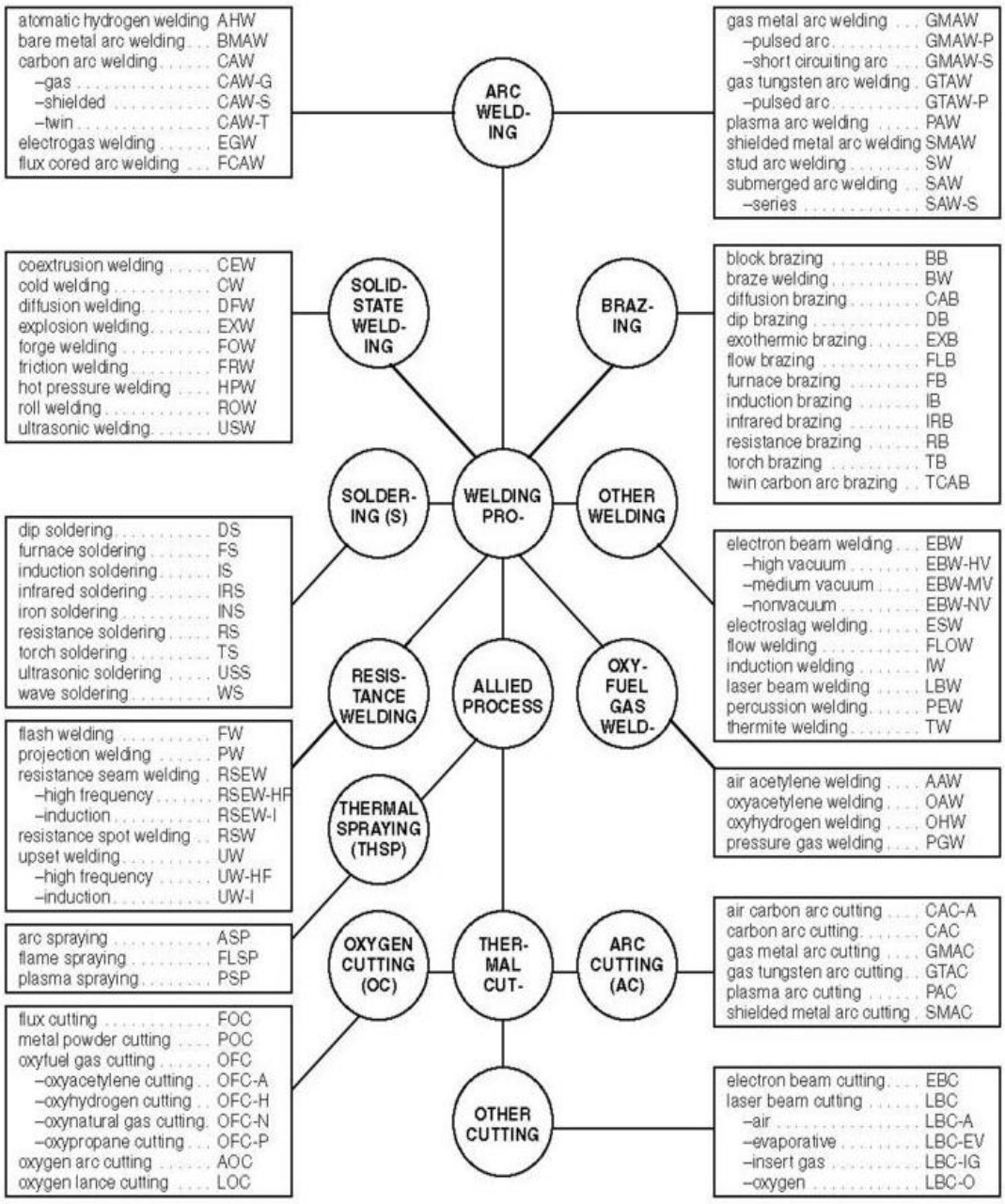

Figure 1.10 Classification of welding and its allied processes [100]

a) *Arc welding equipment and consumables:* For an arc welding process, heat is produced by an arc between the electrode and workpiece to be welded. Mostly these welding processes employ shielding gases, coatings or fluxes to shield the weld pool from oxygen in the surrounding atmosphere [43] *p9*. To have the best quality of welds, it is essential to maintain a stable arc [43] *p79*. Arc welding is normally carried out using power sources with AC or DC function. For AC power source, electrode polarity changes for every half of cycle while for DC power source, either electrode is positive, in case electrode is consumable because more heat is generated on the anode, or negative, in case, the electrode is non-consumable and acts as cathode with minim heat losses [43] *p80*. A conventional power source for arc welding is known as the constant current (CC) machine. It has a drooping volt-ampere characteristic curve and is popular for use in the shielded metal arc welding (SMAW) process. A constant voltage (CV) welding power source has essentially a flat volt-ampere characteristic curve, though usually with a slight droop. The constant voltage welding power sources with volt-ampere characteristics are used only for continuous electrode wire welding for instance gas metal arc welding (GMAW). AC power sources act like single-phase transformers that transform both voltage and current to the required values for arc welding. DC welding power sources are of two kinds: DC welding generators (or converters) and welding rectifiers. The maintenance and stability of a welding arc depend upon the degree of ionisation in the space between the electrode tip and workpiece. To strike the arc, the tip of the electrode is touched against the workpiece, the resulting short circuit causes a heavy current to flow through the spot, which causes a small amount of metal, both from the electrode and the workpiece, to melt and evaporate. The metal vapours produced to provide a conducting path for the current and thus the arc is initiated. However, not all metals produce these conductive vapours with the same ease. The welding of stainless steel is very difficult; aluminium and copper are almost impossible to weld. To overcome these difficulties an additional source of ionisation called the high-frequency ioniser is employed [43] *p85-125*.

All arc welding processes need a consumable to achieve the desired weld joint. These consumables may be of four types:

i) *Coated electrodes:* The coated electrodes consist of the core wire with a covering of coating material to facilitate the initiation and maintenance of welding arc, to protect

the molten metal from the surrounding atmosphere and provide slag blanket on the weld and add alloying elements in the weldment.

ii) *Welding rods and wires:* Bare or flux-cored welding wires and rods are used in short lengths of about 1 m or coiled form in spools as per the type of welding process requirement. These are either used as fillers or electrode wires of different diameters e.g. 0.8 mm, 1.2 mm, etc.

iii) *Welding fluxes:* Normally these are used for the submerged arc welding process and act as flux, insulator, and source of alloying addition.

iv) Shielding gases: Welding processes like tungsten argon welding and gas metal arc welding require shielding gases to achieve specific weld bead shape, weld metal properties and welds without specific defects. These gases may be inert in nature, like argon and helium, or active which dissolve in and react with metal like carbon dioxide, oxygen, hydrogen, and nitrogen. These gases are either used alone or as a mixture [43] *p126-151*.

b) *Gas tungsten arc welding (GTAW):* GTAW is an arc welding process to weld industrial metals with the best possible quality.

i) *Equipment:* The standard but simple manual GTAW equipment comprises a welding torch, power source, connecting cables and gas and water hoses. Depending upon automatic or semi-automatic technique is used, different types of accessories are connected to the machine, such as electrode positioning device, arc voltage control, seam tracking device, oscillator, feed wire mechanism, and feed-back system. Filler wire, shielding gas and tungsten electrode are the main materials used in this process. Both DC and AC types of constant current machines are employed.

ii) *GTAW torch:* GTAW torches are made for automatic or manual operation (Figure 1. 11). There are two types of GTAW torches, water-cooled and air-cooled. A collet is used to hold the electrode in a GTAW torch; the collet size varies according to the electrode size to ensure proper and adequate contact for clamping the tungsten electrode. The gas nozzle of a GTAW torch is its weakest part and is fastened to the torch body by a threaded connection. These nozzles are generally made of ceramic material. For monitoring the shielding gas in GTAW, standard single-stage regulators with flowmeters are used.

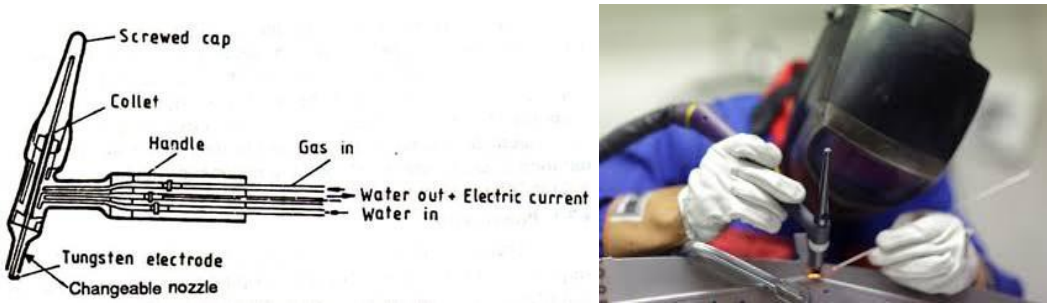

Figure 1.11 Water cooled GTAW torch for manual welding [43][150]

iii) *Wire feed mechanism:* GTAW wire feed mechanism comprises a wire guide attachment, speed controller, and a wire drive mechanism. The wire is pushed through grooved rolls and speed is controlled by a geared motor. The wire runs through a flexible conduit as per the length of the torch.

iv) *Materials:* There are three main materials for the GTAW process, these are shielding gas, filler metal, and tungsten electrode. If the GTAW process is autogenous, the filler metal is not used. The filler wire composition is chosen to match with the base material and diameters are selected with respect to the thickness of the base material. The filler metal may be added manually or through a feed, mechanism depending upon the type of technique used, either manual or automatic. Tungsten (melting point of 3410°C) is used as the electrode material for GTAW and it provides the desired properties of high melting point, low electrical resistance, good heat conductivity and can emit electrons easily. A shielding gas, usually used for GTAW, is argon or helium, while nitrogen or hydrogen gases may also be used depending upon the application. Generally, the selection of a gas or gas mixture depends on the type of metal to be welded. For ferrous materials, including stainless steels, high-temperature alloys, and carbon steels, pure argon or a mixture of argon with helium (or carbon dioxide or hydrogen) is used, while for non-ferrous materials, pure argon is preferred as the shielding gas [43].

c) *Gas metal arc welding (GMAW):* Compared to the GTAW process, which is slow, the demand for high-rate production led to the development of the GMAW process. It is possible to weld all ferrous and non-ferrous metals.

i) *GMAW Equipment and material:* The basic GMAW equipment is normally a semi-automatic system comprising of wire feed unit, power source, shielding gas supply system, welding gun, and water cooling system. For the automatic or mechanised system, an additional item is the travel mechanism for the welding head. GMAW uses DC and almost invariably with electrode positive. Both the transformer rectifier set and a motor-generator power source can be used.

ii) *Wire feed units:* In automatic GMAW, the wire feed unit also includes the welding gun, however, in semi-automatic mode the two are separated to achieve the flexibility of the process. To push the wire through several meters of flexible conduit at a particular speed, it is imperative to have high-powered wire feed motors (DC type electric powered with adjustable speed), driving non-slip knurled or V-groove rollers.

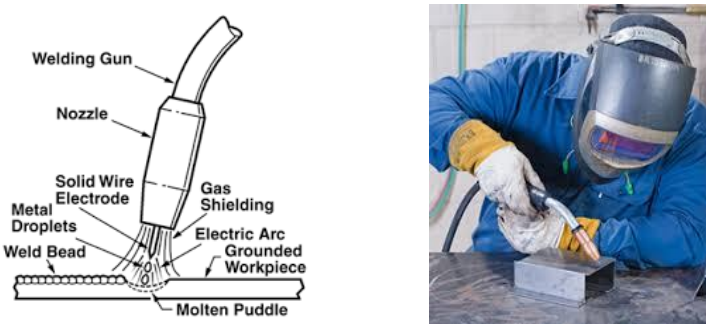

Figure 1.12 GMAW torch for manual welding [43][151]

iii) *GMAW guns and wire feed conduit assembly:* Guns for most of the general-purpose GMAW work have a current carrying capacity of up to about 200A and are air-cooled. There are three types of guns: push-type, pull-type, and push and pull type. GMAW guns for higher currents (200-750A) are of water-cooled type, in which the ducts circulate the water around the contact tube and the gas nozzle. A typical example of a GMAW gun is shown in Figure 1.12.

iv) *Shielding gas and cooling water system:* Gas pressure regulators are connected with gas cylinders to supply continuous flow and pressure of shielding gas. Individual shielding gas is usually viable in the high-pressure cylinder and a gas mixture can normally be obtained. However, gas mixing units are also available which can be connected to two cylinders of different gases to obtain mixtures in desired proportions. Such units are mostly used for mixing CO_2 and argon.

v) *The material used:* The materials used for GMAW are the shielding gas and the filler metal. The feed wire and the shielding gas must be carefully selected to suit the material to be welded, and also regarding the process variation to be employed. GMAW is perhaps the most widely used process in terms of the range of metals and application, if not in the amount of metal deposited. GMAW finds extensive use in the fabrication of structures, shipbuilding, pressure vessels, tanks, pipes, domestic equipment, general and heavy electrical engineering, and the aircraft engine manufacturing industries [43].

vi) *Metal Transfer:* Depending upon the welding conditions, there are different ways in which this transfer of metal can take place. These ways are referred to as modes of metal transfer. There are four modes of metal transfer:

- *Short circuit transfer:* This type is associated with low current and small arc length. The current rises at the time of a short circuit, which results in excessive heating and thus in breaking of the short-circuiting bridge with a metal transfer from the electrode into the weld pool.
- *Dip transfer:* This is a type of short circuit metal transfer mode but in this case, the electrode is fed into the weld pool at a fast pace so that the wire dips into the pool before the droplet is detached.
- *Globular transfer:* In this type, the molten metal droplet is detached from the electrode tip due to gravity and other forces acting on it as in short-circuit transfer.
- *Spray transfer:* It is normally associated with high current densities which leads to a very high temperature of the molten droplet with consequently lowering of the surface tension [43] *p152-170.*

d) *Flux-cored arc welding (FCAW):* Flux-cored arc welding is a GMAW process in which a tubular electrode containing flux is employed. Generally, the equipment used for the conventional GMAW process is found suitable for FCAW as well. The difference between the conventional GMAW and FCAW equipment is that for the latter, a power source and welding gun of higher current capacities are used. The composition of electrode wire depends upon whether it is to be used for the self-shielding process or the CO_2 shielded process.

i) *Process variables: The* FCAW process normally uses DC with electrode positive, however, some electrodes for the self –shielded process operate with electrode negative. Welding current is dependent on the electrode feed rate for a specific composition, diameter, and electrode extension.

ii*)* *Application:* FCAW is used for welding carbon and low alloy steels, HSLA steels, Q&T steels, and some of the cast irons and stainless steels [43] *p265-289.*

1.7.3 Effect of Preheat, Heat Input, and Thickness: Preheat, heat input, and thickness have a great impact on Quenched and tempered steels, so care must be taken into account during the fabrication process. These effects can be summarised as:

a) *The effect of thickness:* In general, slabs are rolled into plates or other shapes in a steel mill, at sufficiently high temperatures. Then rolled parts are allowed to cool down. A thin plate cools faster than a thick plate because a thin plate has more surface area to its mass ratio as compared to that of a thick plate. While in the case of welding, the cooling process is the opposite for thin and thick plates because, the thick plate has a larger mass, so, the weld region in the thick plate cools down quicker than the weld region in a thinner plate. For a thick plate (having a large mass), the heat input is transferred more rapidly out of the weld region due to conduction, in comparison to that of a thin plate (having less mass), where the heat transfer occurs via radiation. A faster cooling rate of the thicker plate results in a higher hardness, tensile strength, and yield stress but lower elongation. Welded steel shapes of plate thickness less than 13 mm are less prone to cracking as compared with thicker plates. Also, for thinner plates, there is a high weld throat to plate thickness ratio and being flexible, so their cooling rate is slow, contrary to thicker plates. Because of this fact, a weld cools faster on a thick member and if it has a higher content of alloying addition, it will have high hardness and strength and low ductility. If these properties are unacceptable, preheating is mandatory to decrease the high cooling rate [51] *p6.1-5*.

b) *The effect of preheating and heat input:* The process of heating a metal to some specific temperature before actual welding is known as preheating [52]. After welding, the microstructure of HAZ is never the same as of the original [53, 54]. Due to the thermal cycle of heating and cooling near the weld region, residual stresses are developed which can lead to cracking in HAZ and weld metal [55-59]. It is because molten metal undergoes contraction during cooling along the weld length but is partially prohibited next to cold base metal; thus, residual tensile stresses generated in this way along the weld may be detrimental to the original base metal properties [55]. This poses a great problem in the production process. Thus, in a particular welding operation, it is mandatory to preheat the assembly before welding. In general, post-heat or heating after welding is required to redistribute the internal stresses. For specific cases, preheat is also required to maintain the inter-pass temperature. Ultimately, preheat will have a positive impact on the quality and integrity of welds, and any work in compliance to a particular code or standard, control of temperature before, during, and after welding may be rigidly specified. The purpose of preheating may also be explained as:

i) Preheating slows down the cooling rate during welding to avoid extreme hardening of HAZ.

ii) Preheating decreases the level of contraction stresses in HAZ and weldments.

iii) Preheating helps to diffuse out trapped hydrogen after welding to prevent cold cracking.

Thus, the amount of preheating applied before welding is imperative. If a plate of higher thickness is subjected to a particular preheat temperature at a localized point or surface for an insufficient period of time, there will no produce a remarkable effect on cooling rate due to fast heat transfer into the cold plate. It may result in excessive hardening of the plate due to the quenching effect. So, it is of significant importance that the plate must be heated, and the temperature maintained to allow uniform heating through-thickness. Preheating of material before welding depends upon its shape, heat transfer properties, and heat contained in it. Without preheating, the microstructure may be highly brittle due to the high hardness in HAZ or weld. In particular, welding of the steel in the winter season definitely requires preheating due to low base metal or surrounding temperature. It is also true in the rainy season to remove moisture by preheating to a specified temperature. The amount and time of preheating at a specified temperature for a particular application are decided based on plate thickness, base metal chemical composition, heat input of the welding process, and rigidity or restraint of the weld joint members. The K-type thermocouple may be attached to the plate to estimate the plate temperature. Other methods may include using crayons. These give estimates of temperature at the spots where they are placed, indicating the heat input, which can then be correlated with thickness and chemistry of metal in tables specifying minimum preheat temperatures. Thus, the temperature is the gauge for preheating inputs, and preheating to specified temperatures is the practical method of obtaining the amount of preheating needed to control the cooling rate after welding. There are several guidelines given in the applicable construction code or from the manufacturers/suppliers to estimate the preheating temperature. Such recommendations may be named as “minimum preheat recommendations”. However, the mechanical properties of Q&T steels might be adversely affected if the preheat is too high because the microstructure is sensitive to heat exposure. While material thickness, type of welding process, and ranges of metal chemistry are considered as the minimum conditions, some adjustments may be needed for specific steel chemistry, welding heat input, joint geometry, and other factors.

Generally, steel with higher carbon contents has a lower critical cooling rate and greater need for the using of low hydrogen electrodes and preheating. Carbon, however, is not the only element that influences the critical cooling rate. In addition to carbon, some more elements are responsible for the hardening of steel during fast cooling. So, other elements must also be considered when deciding a particular preheat temperature for a specific steel grade. The total hardenability can be expressed as 'carbon equivalent" which is indicative of the hardening of steel due to the effects of carbon and other alloying elements. This may be the basis for the estimation of the inter-pass temperature and preheat temperature. Carbon equivalent (C_{eq}) is an empirical relationship calculated as the sum of the hardenability effects of different elements in steel. One of these is [51] *p3.3-3*:

$$C_{eq} = \%C + \%Mn/6 + \%Ni/15 + \%Mo/4 + \%Cr/4 + \%Cu/13$$

This formula is effective for alloying elements up to maximum limits as below:

C = 0.5%, Ni = 3.5%, Cr = 1.0%, Mn = 1.6%, Mo = 0.6%, Cu = 1.0%.

Based upon carbon equivalent values for steels, estimated inter-pass and preheat temperatures are:

Table 1.1 Minimum preheat requirement with respect to carbon equivalent.

Carbon Equivalents (C_{eq})	Preheat Temperatures (˚C)
Up to 0.45	Preheat is elective
0.45 to 0.60	93 to 204
Above 0.60	204 to 371

These values of preheating temperatures are approximate. Whatever technique is used to estimate the preheat temperature, the value obtained should be verified by conducting actual or simulated welding of test coupons before production welding. It will also help to understand the effects of heat input and restraint. It is because heat input has a great impact on the minimum preheat or maximum inter-pass temperature of the material being welded, and it may lower or raise the preheat temperature required to weld the steel using a range of welding currents for automatic or semi-automatic processes [51] *p3.3-3.*

Nobutaka Yurioka, Makoto Okumura, and Tadashi Kasuya, in their research of techniques to predict maximum HAZ hardness and preheat temperature for steel welding, revealed that the HAZ microstructure is accountable for cold cracking susceptibility [55]. In considering the fundamentals of preheating, Funderburk [52] determined that:

a) Preheating may reduce susceptibility to cracking,

b) Preheating must be employed if applicable code identifies,

(c) C-Annex H of AWS D1.1-2015 [99] states recommendations for alternate means of calculating required temperatures of preheating and

(d) The minimum preheat temperature must be maintained by checking inter-pass temperature during welding for each pass.

M. Aksoy, N. Orhan, and M. Eroğlu [60] investigated the influence of coarse grain size with respect to heat inputs for low carbon steel grades and revealed the impact of variation observed on the mechanical and microstructural properties of HAZ and weld metal. They suggested using high heat input values for low carbon steel with coarse grain size microstructure to have good toughness properties.

While welding tool steels, V.C.H. Wiley [61] determined that these steels must never be at room temperature. Hardened tool steels are always preheated for welding below the tempering temperature [61].

For arc welding of high-strength steels, the mechanical and microstructural properties of the welded joint are assessed by the chemistry of parent metal and weld, along with the rate of cooling of the metal in HAZ. These properties have a great dependence on weld joint design, heat input, and thermo-physical properties. The dependence of the welded joint ductility on the heat input becomes stronger with a decrease in strength [62].

Heat input is usually determined by the relationship given as [51] *p3.3-3*:

$$J = (E \times I \times 60)/(V \times 1000),$$

Where V is arc travel speed in mm/min, I is welding current in amperes, E is arc voltage in volts, and J is heat input in kJ/mm. As entire heat input during welding does not go into the plate, the following heat inefficiencies are advised for use with the formula: 75-80% for manual welding and 90-100% for submerged arc welding, [51] *p 3.3-4.*

The method of preheating depends on the plate thickness, the size of weldment, and the apparatus available for heating. In the production welding of small assemblies, preheating in a furnace is the best suitable technique. Another satisfactory method is torch heating,

using natural gas premixed with compressed air. It burns clean in the form of a hot flame. Acetylene, propane, and oil torches can also be an option. For bulky weldments, series of heating torches may be employed to heat the material up to the required temperature quickly and uniformly. Thermal insulation/blanket types of heaters (electrical) are recommended for girth and longitudinal weldments up to 51 mm thick plates. The heaters may be fixed to the plate along the weld joint and about 152 mm from the weld seam. After the plate reaches proper preheat temperature, the heaters may be left in place in case if it is required to provide additional heat to maintain the inter-pass temperature. Further sources of preheating include radiant heating and induction heating (mostly used on piping). Carbon steels may not require high accuracy for preheating at a specific temperature. Though it is essential to preheat the work to a minimum temperature, yet, no demerit has been found, if this temperature is exceeded by 37.8˚C. This is not true, however, for Q&T steels, because welding of the overheated plate may cause harm to microstructure in HAZ. That is why preheat and inter-pass temperatures must be checked as accurately as possible for such types of steel. Crayons for temperature indication and portable pyrometers may be used for checking different temperatures. Usually, steels that need a specified preheating temperature, must also be maintained at the same temperature during welding. Normally, heat input generated during welding is sufficient to maintain the inter-pass temperature but for a heavy weldment, this is not the case. So, additional heating is required during welding using any heating method including torch heating. It always advisable that once welding of an assembly is started after preheating, it should be completed as early as possible to avoid inter-pass heating. Since preheating is required to decrease the quench rate; it eventually causes slow cooling for all weld passes. This is achieved if the inter-pass temperature is maintained at least equal to preheat temperature otherwise each weld pass will result in fast quenching of weld and HAZ. Since Q&T steels are always manufactured in the heat-treated condition, further heating greater than a specified temperature will deteriorate mechanical properties. Certain weldments must be preheated before welding to inhibit cracking due to fast cooling, but the preheat must be controlled so as not to adversely affect the toughness and yield strength which characterise such type of steels for specific uses. Yet, during welding, HAZ will be heated far above the allowable preheat temperatures. This welded region must cool quickly to re-develop the original properties and prevent brittle microstructure. Consequently, preheat temperatures and heat inputs must be closely controlled. Thus, narrow limits are

placed on the procedures. A lot of experimental work was conducted in the past to develop the welding procedures to obtained good ductility, toughness, and high strength in the weldments. These procedures establish guidance and provide correct preheat temperatures and heat inputs to achieve an adequately rapid cooling rate and prevent brittle microstructure. Moreover, welding of Q&T steels requires a low hydrogen welding process, and the preheat temperature is calculated on the basis of the chemical composition of weld metal as well as the thickness of the plate. Once preheat temperature is known for a particular plate thickness, the maximum amount of heat input may be evaluated for each weld pass and thus the welding procedure may be developed to control the critical limit of heat input during a welding process. That is why it is recommended to use stringer beads for weld passes to avoid excessive heat input [51] p3.3-5.

As the presence of hydrogen can have a significant impact on mechanical properties resulting in a reduction in the service life of components [112-116], ISO/TR 17844 [63] summarises the development of different techniques to calculate minimum preheat temperature to get weldments free from HACC. Also, this standard recommends preheating steel at 78˚C for a particular chemistry and heat treatment history as per the CET method (a calculation method based on the carbon equivalent). It shows a dependence of preheating requirements on chemistry steel.

It may also be advisable to use low preheat temperatures if a higher inter-pass temperature is required between intermediate weld passes to diffuse out hydrogen. On the other hand, no specific recommendation is suggested to weld ferritic steel with austenitic consumables. Moreover, maintaining the intermediate weld pass temperature helps to minimize the occurrence of HACC. The range of intermediate weld pass temperature is normally similar to that of preheat temperature. Q&T high strength steels are also susceptible to softening of HAZ in addition to HACC, this may adversely affect mechanical properties. It is advantageous to use the maximum intermediate weld pass temperature without introducing too much softening. It is recommended to ensure maximum inter-pass temperature when designing and qualifying a welding procedure. This may not be mandatory for semi-automatic and manual welding. For high productivity achieved in the automatic robotic welding process with high welding speed, it is imperative to evaluate and estimate the maximum possible intermediate weld pass temperature [48].

While reviewing the “effect of preheating and/or post-weld heat treatment on the mechanical behaviour of ferrous metals”, Bipin Kumar Srivastava explained that actual preheating and post-heating are the main sources to guarantee satisfactory HAZ properties, possibility to have HIC free weldment, and lower levels of residual stresses [64]. Using finite element simulation, Sepe et al. highlighted that residual stresses in longitudinal weldments can be minimized up to 38% via employing preheating and post-weld thermal insulation [117]. Using numerical simulation, Du et al. also demonstrated that pre-weld heating facilitates the re-distribution of residual stresses uniformly in weldments, hence minimizing the adverse effect of post-weld residual stresses on cracking [118].

Sometimes, welding procedures may lead to excessive heating (including preheat, welding heat, and heat input) of weldments greater than that recommended by a steel manufacturer. For these cases, the notch toughness and strength properties should be assessed against requirements; if these properties are essential then preheat temperature is increased and heat input is reduced. Decreasing a preheat temperature may result in cold cracking, along with worsening HAZ toughness properties. In case, good toughness and high yield strength are not the targets, the heat input may be exceeded, although the literature does not provide enough information on the effect of preheating on the impact and fatigue properties *p3.3-6* [51].

1.7.4 Welding Inspection/examination and quality control: Since quality is a relative term, different welds may have different acceptance levels subject to the service requirements [126]. Consistent performance of a part or structural entity is determined by prior service quality of the part and in-service degradation of that part under operating conditions [119]. The welding quality is quite important for the dependability and stability of welds; however, it is not always the case that this quality can be safeguarded in welding. Weld inspection/examination is critical, especially when welding is done by machines. Hence, the main aim of inspection or quality control is to assure the good quality of welded structures through the careful examination of the components and parts for every step-in fabrication practices. It is essential to have a good quality of welded joints by utilising the best available welding equipment, welding procedure, and skilled operator. In general, the inspection and testing of welds may include one or more of the

following procedures (non-destructive or destructive) depending upon the type of structure and importance of its service [50], *p701*:

a) *Visual Inspection and measurement:* Visual examination is an imperative measure of the quality control system [125]. It is probably the most widely used of all the inspection methods. It is easy to apply, simple, non-destructive in nature, swiftly conducted, and generally less costly. Careful visual inspection of the welds at different stages of its fabrication can detect up to 90% of defects and flaws before being revealed by costly examination techniques [50], *p702*. The tools required for visual inspection are quite simple but sufficient lighting is unconditionally necessary. Before the visual inspection, the surface of the weld should be cleaned and made free from spatter, scale and slag. Equipment for visual inspection may include [50], *p702-709*:

- Mirror, boroscope, flashlight, a bundle of fibre optics, or other aids which may be used to inspect normally inaccessible places;
- Indicators, for example, pyrometers and crayons (thermal sticks) may be employed to identify precise preheat and inter-pass temperatures;
- Special templates and welding gauges are also available to assist in the inspection of weldments.

b) Liquid Penetrant Testing (LPT): It is a non-destructive technique to reveal surface defects, for instance, surface porosity, cracks, and inclusions in the weld metals. The basis of this LPT method is the capillary action of a penetrating liquid that penetrates the surface opening or a weld defect. A specified time is allowed after the application of penetrant. After a specified time, the excess penetrant is cleaned by a lint-free cloth soaked with a cleaning agent. Care is taken so that penetrant entrapped in defects must not be over wiped. Finally, the developer of white particles suspension is applied which draws the penetrant towards the surface and reveals that area as an indication of a defect of a particular size and shape. Liquid penetrant testing involves the following basic steps, as shown in Figure. 1.13:

(i) Surface preparation (ii) Penetrant application (iii) Dwell time (iv) Removal of penetrant using a solvent. (v) Application of developer (vi) Surface inspection (vii) Post cleaning	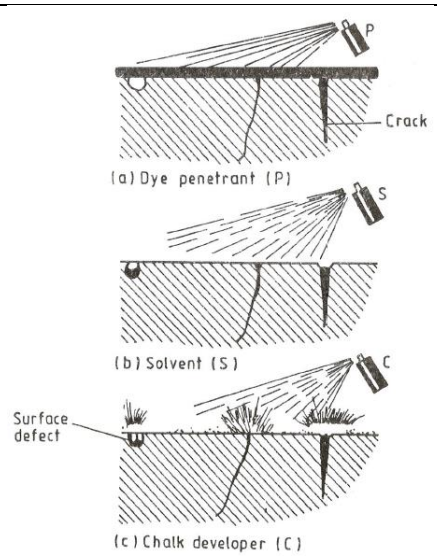

Figure 1.13 Steps of liquid penetrant testing [43]

Liquid penetrant testing techniques may be classified into two main types: dye-penetrant and fluorescent penetrant testing. The main difference between these two kinds of testing methods is that the dye-penetrant test utilises visible penetrants. For fluorescent penetrant testing the medium employed is fluorescent liquid i.e., a liquid that glows when lightened by black or ultraviolet (UV) radiation of a wavelength of approximately 3650Å [50] *p710-716*.

c) *Fabrication Weldability Tests:* These tests are employed to evaluate the fabrication weldability to assess if a specific material along with the process may be utilised to have a defect-free weld joint. These can be grouped as [50] *p436-462*:

i) Hot Cracking Tests: for example, Murex test, Houldcroft test, Varestraint test, ring weldability test, and hot ductility test;

ii) Cold Cracking Tests: for instance, controlled thermal severity (CTS) test, Tekken test, Lehigh restraint test, longitudinal bead-weld test, and Implant test;

iii) Weldability tests related to specific types of cracking: for example, lamellar tearing and reheat cracking. Tests for lamellar tearing may involve through-thickness ductility testing, the Cranfield testing, Lehigh cantilever lamellar tearing testing, the window testing, the H-testing, the Bordeau testing, and the notched tensile strength testing. Reheat cracking test may include Vinckier test, Compact tension test, and Hot tensile test.

d) *Service weldability Tests:* These testing methods are used to assess the welded joint properties whether these are suitable for the intended service or not. These testing methods include [50] *p464:*

(i) Tensile tests
(ii) Nick-break test
(iii) Pillow test
(iv) Bend test
(v) Impact test
(vi) Hardness test
(vii) Fracture test
(viii) Fatigue test
(ix) Corrosion test
(x) Creep test

1.7.5 Weld defects, Causes, and Remedies: The performance of welded structures or components in service depends upon the quality of fabrication, which in turn is based upon defect-free weld joints. The term *weld defect* is related to any stated condition which cannot be fulfilled in a welded joint. It has been suggested by various authorities [50], *p659*, that the term defect should be reserved for faults that are likely to be harmful to service life or functioning of fabricated components, especially in case they are situated in regions of high stress. On the other hand, the same faults could be termed imperfections or flaws or discontinuities if situated in a region of low stress. International Institute of Welding (IIW) defines discontinuity as "an interruption of the typical structure of weldment such as a lack of homogeneity in the mechanical or metallurgical or physical characteristics of the material or weldment" [50], *p. 659*.

Welding defects have adverse effects on the mechanical properties of the welded joints [120-124]. They may fail a whole structure in service. The principal causes of failures are the incorrect application of welding specifications, the use of sub-standard materials, defective welding equipment, or poor welding skill. Weld defects can also originate from a design or drawing error or fault of some manufacturing or shop function, such as material preparation.

a) *General Sources and Causes of Defects:* Following are general sources of defects for most of the conventional arc welding processes [50] *p661*:

(i) Incorrect welding method, for instance, employing a heat source into a narrow gap V groove joint which may cause root rub cracking because of high ratio of depth with respect to width.

(ii) Inaccurate application of the welding procedure variables on a specific material, i.e. wrong selection of electrode, current, wire feed speed, gas shielding gas, etc.

(iii) Defects caused by the weld metal coming in contact with the base metal defects, for example, non-metallic inclusions and laminations, which may serve as crack initiation sites within the welded joints.

(iv) Unwanted microstructures in regard to hardness and grain size.

(v) Unwanted inclusions like metallic oxides and slags.

(vi) Improper size and shape weld beads for example under-fill and overfill.

(vii) Improper preparation of weld joint edge and poor fit-up may lead to lack of root penetration, and lack of side wall or inter-run fusion, etc.

(viii) Poor supervision allowing poor workmanship resulting in arc blow, arc striking, under cuts, slag inclusion, and incorrect weld profile which may reduce the fatigue life of the component.

(ix) Inferior design resulting in inaccessibility for welding and inspection, hard spots and stress raisers leading to cracks, difficult welding positions, and poor weldability of the base material which is not notch-ductile, (a material which continues to deform plastically is said to be notch ductile if it cracks in a rapid brittle manner, it is not a notch tough or notch ductile material).

b) *Classification of weld defects:* International Institute of Welding (IIW) categorizes the weld defects into six groups as [50] *p659*:

- Cracks: include all kinds of cracks, for instance, hot and cold cracks, and crater cracks;
- Cavities: including blowholes, porosity, and shrinkage;
- Solid inclusions: including slag, flux, metal oxides, and tungsten;
- Incomplete penetration or fusion: including lack of penetration, lack of fusion, and suck back;
- Imperfect shape or unacceptable contour: including undercuts, excessive reinforcement, improper weld profile, overlap, under-fill, distortion, and excessive penetration;
- Assorted defects: including uneven weld ripples, rough weld surface, excessive spatter, arc strike, and pock marks;

All of these defects can be categorised into two types:

i) *Visual/Surface Weld Defects:* Defects included in this category are:

- Surface cracks,
- Distortion/warpage,

- Incorrect or bad bead profile,
- Dimensional deviation/ incorrect weld size,
- Overlaps or rolls,
- Undercuts,
- Under-fill/ suck-back,
- Excessive penetration/ excessive reinforcement,
- Start-stop points,
- Interruptions,
- Under-filled craters,
- Burn-through,
- Surface porosity,
- Surface oxidation,
- Uneven & coarse ripples,
- Pock marks/ flat spots,
- Excessive spatter arc strike,
- Bad surface appearance,
- High-low/off-set

Some typical examples are shown in Figure 1.14.

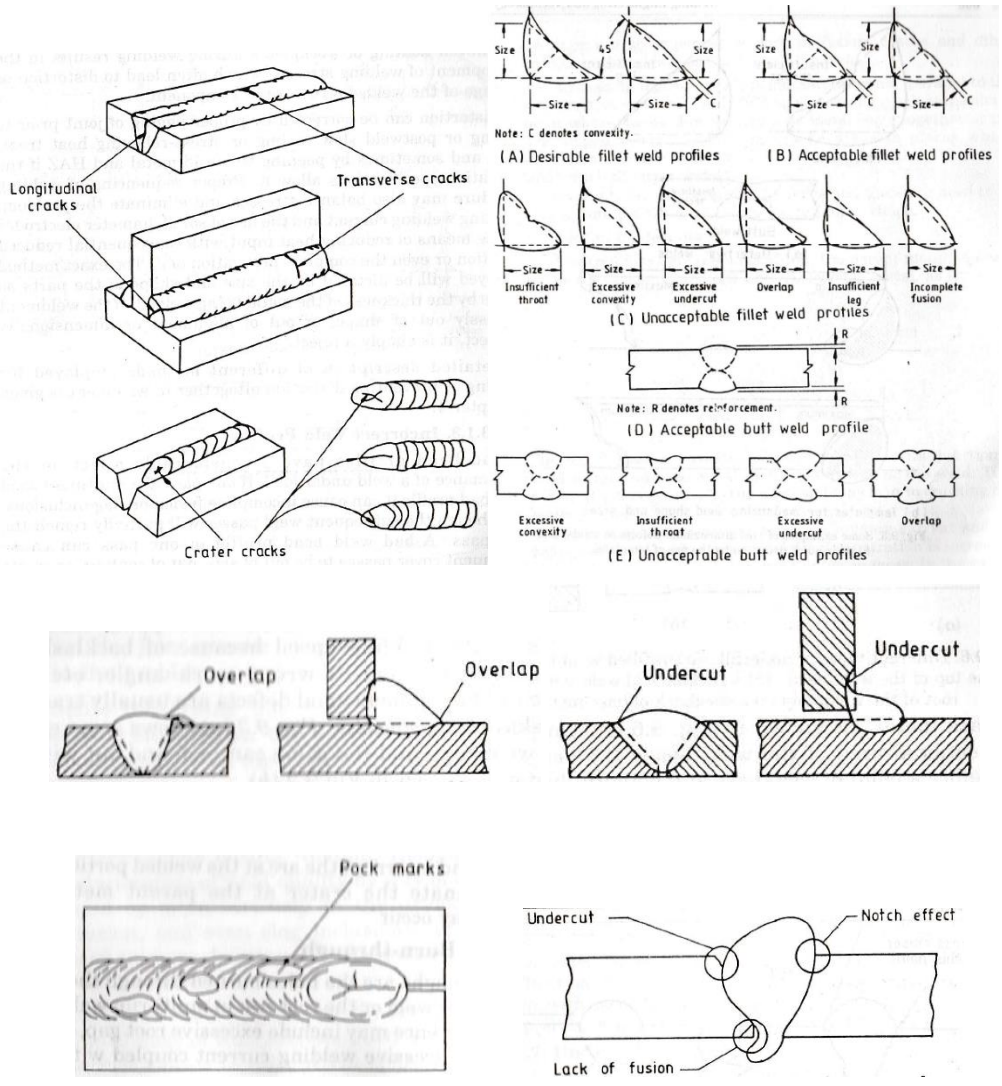

Figure 1.14 Typical examples of surface weld defects [50]

ii) Hidden or sub-surface defects: Defects included in this category are like

- Hidden or subsurface cracks,
- Lack of penetration and lack of fusion,
- Blowholes/ subsurface porosity,
- Shrinkage cavities slag inclusions,
- Tungsten/ copper (metallic) inclusions,
- Finger penetration,
- The coarse microstructure is included in this category.

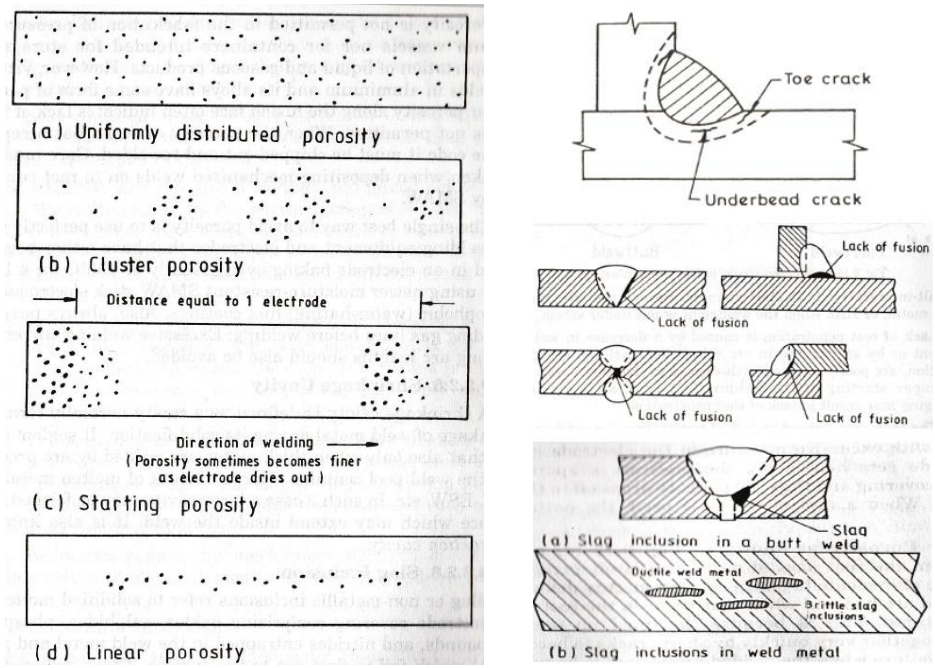

Figure 1.15 Typical examples of sub-surface weld defects [50]

c) *Remedies:* followings are causes and remedies for the above-mentioned defects [50] *p662-682*:

Table 1.2 Remedies of weld defects.

Defect	Remedy
Surface cracks	Cracks are usually the result of high shrinkage stresses (being greater than the hot strength of the weld or parent material); good fit-up, correct welding procedures, and good edge quality must be considered to avoid such defects.

Distortion	During welding, a high level of stresses is induced into the region near the weld line in both longitudinal and transverse direction resulting in dimensional warpage of component known as distortion. Distortion can be corrected by using adequate jigs and fixtures before welding or post-weld slow cooling or stress-relieving heat treatment, and sometimes by peening the weld metal and HAZ if the fabrication specifications allow it. Proper sequencing of welding procedures may also balance stresses and eliminate the problem. Reducing welding current and using electrodes of small diameter are the means of reducing heat input with consequentially reduced distortion or even the complete prevention of it.
Incorrect weld profile	Bad bead profiles have a significant impact on the performance of a weld under load. That is why highly skilled welders are often employed to make the root passes on pipelines and less skilled welders follow them up to complete the remaining weld runs to fill up the joint groove.
Dimensional defects	These include non-uniform width or height of a weld, irregular crests and valleys, and variations in leg length of fillet welds. Such defects may be evaded by choosing correct welding parameters like voltage, current, and welding speed.
Overlaps and rolls	Overlaps or rolls are protrusions of the weld metal away from the bond at the toe, root, or face of the weld. They may be caused by excessive welding current, the wrong tilt of electrode in making fillet welds in the horizontal position, or by an excessive work angle in welding uphill. An overlap tends to produce indentation, along the weld line, where stress will build up and may initiate cracking at the junction of base metal to overlapped region.

Undercuts	Undercuts are the sharp unfilled depression areas of the bevel edge developed at the toe during welding and caused by the melting of base metal due to high current and arc voltage. Proper welding parameters along with good manipulation of the electrode must be taken care of to avoid defects.
Underfill, Suck back	This is a flaw in which the weld bead has a concave type contour or lack of fill on the face of the weld or a suck-back on the root of a groove weld. This may be due to shrinkage of weld bead and can be rectified by depositing one or more weld passes in the joint.
Excessive reinforcement, excessive penetration	It is normally caused by poor fit-up, improper welding technique, lower welding speed excessive welding current, and the type of electrode. It can be avoided if used correct parameters.
Unfilled Craters	Such craters appear after a sudden interruption of the arc. They reduce the cross-section of the weld and may act as a source of crack formation. If no tabs are used, it is necessary to weld up the crater thoroughly and interrupt the arc at the welded portion of the seam.
Burn-through	These are the burned holes through the thickness of base metal either in the root pass of a multi-pass weld or in a single pass weld. The causes for their occurrence may include excessive root gap, an insufficient root face, or excessive welding current coupled with low welding speed. They are rectified by chipping back and welding up.
Surface Porosity	It takes place when the welder uses undried covered electrodes or electrodes with their shelf-life long expired. Dried electrodes and moisture-free weld surfaces are the remedies.
Uneven and coarse ripples	Uneven and coarse ripples indicative of inconsistent solidification pattern. A skilled welder must be employed to avoid such defects.

Flat spots/ Pock marks	These are associated with excessive gas pressure and high welding current and high moisture content in the flux. Proper control of welding current, gas flow rate, and moisture content of flux can eliminate this defect.
Excessive Spatter	Excessive spatter adjacent to the weld is also often a defect and is unacceptable. This may be caused by arc blow, wrong selection of electrode, use of bar electrode or heavy welding current, or the poor technique of welder.
Arc Strikes	This defect is caused when the welder accidentally or inadvertently hits the work piece with an electrode or the electrode holder, commonly next to the weld, resulting in an undesirable arc; it can also happen between a faulty ground clamp and work. Such points are identified as arc strikes which may be a source of initiation of crack failure during cyclic stress. The rectification of such defect may be challenging and costly, which involves chipping, and possibly preheating prior to re-welding specifically for low alloy steels.
High and Low Offset	Offset in a welded joint occurs most often because of poor fit-up and is a problem area in a plate or large diameter pipes and a rolled cylinder joint where the edges simply do not match up. One solution is to use better or more tack welds. Another solution, if the base metal mismatch is caused by heat distortion, is to use welding jigs and clamps or fixtures that will hold the base metal in position until the weld is completed.
Subsurface and Internal Cracks	These are the cracks that develop just below the weld surfaces. Cold cracking or hydrogen embrittlement are examples of such cracking. The proper welding procedure is important to be considered to avoid such cracks in the weld.

Lack of fusion	Lack of fusion (LOF) may occur at the side wall of the weld joint between the weld and base metal, as well as amongst the inter-run multi-pass weld metal. The main causes of LOF are insufficient welding current, an electrode off-set from the weld axis, too high welding speed, and inappropriate wearing procedure so that the edges are not melted thoroughly. Other causes of poor fusion include improper joint preparation and fit-up (inadequate bevelling and narrow spacing) as well as improper edge cleaning from slag (after flame cutting), dirt, rust, scale, etc. It should be rectified by chipping back and rewilding.
Lac of Penetration	Lack of penetration (LOP) occurs most often in the root of the weld joint. LOP is caused by a decrease in welding current or by an increase in arc voltage and welding speed. Also, arc poorly directed with respect to the groove axis and improper starting of the welding operation after electrode changing may result in lack of root penetration. When certain tolerance limits for lack of penetration are exceeded, the defective portion of the weld should be chipped out and re-welded.
Blowholes and Subsurface Porosity	Blowholes and porosity are cavities, openings, or holes formed by gas trapped by solidified weld metal. Gas may be trapped due to grease, paint, dirt, rust, impurities, and moisture in the shielding gas, excessive welding speed because of which the gas envelope around the weld pool becomes ineffective. Porosity in welds may usually be of four types: uniformly scattered porosity, cluster porosity, starting porosity, and linear porosity. It may be controlled by properly cleaning, drying electrodes, and welding equipment that has either been just baked in an electrode baking oven (usually at 150°C for 4 hours) or by using newer moisture-resistant SMAW stick electrodes with hydrophobic (water-hating) flux coatings. Purging the shielding gas lines before welding can also reduce porosity. Excessive welding current and too-long arc lengths should also be avoided.

Shrinkage Cavities	A shrinkage cavity is defined as an opening normally appearing due to the contraction of weld metal as a result of solidification. Proper welding parameters and high skill of welder are required to avoid the defects.
Slag Inclusions	Slag or non-metallic inclusions refer to solidified molten flux or electrode covering comprising oxides, sulphides, phosphorous compounds, and nitrides entrapped in the weld metal and parent metal. These inclusions may be random, intermediate, or continuously distributed. The main reason for slag inclusion is insufficient inter-pass cleaning during welding; as a result, slag gets permanently entrapped in the weld. Slag inclusions reduce the mechanical strength of welds; therefore, welds with slag inclusions should be chipped back and re-welded.
Metallic inclusions	These are mostly tungsten inclusions from the tungsten electrode in GTAW welding or copper from the contact tip in GMAW welding. Tungsten inclusions may be caused by the incorrectly sized or shaped electrode, and oxygen contamination of the shielding gas. Copper inclusion can be caused by inadvertent dipping of the GMAW gun nozzle in the molten weld metal. High frequency or similar arc striking, and correct current and voltage settings are essential to avoid the occurrence of this effect.

d) *Metallurgy of weld cracks:* Crack formation is the most significant issue that occurs in welds. That is why weldability assessment of a material is usually based on its crack susceptibility during and after welding. One method of avoiding or minimizing cracking in and around welds is to heat the parent metal before welding. This reduces the tendency to form martensite in steel during cooling, and in the case of multi-pass welding, it provides more extensive allotropic refinement of beads by the normalising effect of the heat of the succeeding passes. Cracks may occur in weldments or the HAZ. Sometimes

these are originated in one zone and spread into the other. These cracks are grouped into two main classes, i.e., cold cracks and hot cracks [50] *p401*.

i) *Hot Cracking:* Hot cracking is also known as "solidification cracking or liquation cracking" [50] *p401*. Solidification cracks occur when the weld metal temperature is just below solidus. Such cracks are often inter-dendritic following a random path along grain boundaries or areas of alloying elements segregation. A hot crack will show temper colours on its inner surfaces. This is due to the oxide film formed there after the hot crack initiation. Hot cracks may also be transgranular, propagating along the crystal lattice planes. Some of the important factors which promote *solidification cracking* in weldments include [50] *p402:*

- Solidification structure,
- Segregation,
- High stress in the weld metal, material thickness,
- Joint restraint,
- Width / depth ratio,
- Weld bead shape,
- Material composition (high carbon and nickel contents),
- Crack sensitivity of the electrode,
- High current, excessive dilution of filer metal,
- No Preheating (increases liability to cracking),
- Weld procedure (high welding speed and long arc),
- Crater cracking (indicates crack sensitivity) and poor fit-up,
- Lack of ferrite in austenitic stainless steel, and incorrect filler.

ii) *Cold Cracking:* Cold cracking or delayed cracking or *hydrogen-induced cracking* (HIC), is perhaps the most detrimental issue of weld cracking specifically for welding of high strength steels. HIC occurs in weldments due to the following factors:

- Hydrogen present in weldment,
- High level of stresses,
- Joint restraint and high thermal severity,
- Presence of impurities,
- Susceptible microstructure, e.g., martensite,

- low temperature, in a range of -100°C to 200°C,
- Weld of insufficient cross-sectional area,

High stresses are induced during welding because of restraints and heat input. The high carbon, brittle and hard martensite phase of microstructure is highly prone to cold cracking. Since martensite is formed at low temperatures, the cracking associated with it is referred to as cold cracking. Before initiation of crack, there is generally a time delay or incubation time, and propagation of a crack occurs in a slow, irregular mode. The cracking may be either inter- and transgranular or both, and normally occurs at the prior austenite grain boundaries. Cold cracking is predominantly related to defects, for instance, inhomogeneity in microstructure, which acts as a stress concentrator at grain boundaries and causes a hardness gradient. In common, crack propagation due to cold cracking gets enhanced by weld joint geometries and restraints. The main source of hydrogen in welding is the water vapours in the welding arc, but its extent depends upon the type of process employed. Nascent hydrogen diffusion may cause loss of ductility, blistering, and cracking. After diffusion into the steel crystal structure, nascent hydrogen atoms combine to form molecular hydrogen, which then becomes trapped in the lattice imperfections to form blisters. More to that, it may cause cracking in areas having high hardness such as weld metal, HAZ, and localised hard spots. The hardness of steel can lead to cracking; it is recommended that the hardness should be limited to R_C 22 (Rockwell C-Scale) to preclude sulphide stress cracking often encountered in petrochemical plants. Components failed by cold cracking sometimes show a phenomenon called *fisheyes*. These are interpreted as circular areas of quasi-cleavage fracture centred on a large inclusion (e.g., MnS) or clusters of small inclusions, e.g. silicates or Al_2O_3 particles. Apart from water vapours, the hydrogen can come from a variety of sources: corrosion reactions, chemical processing reactions, purposeful addition (to MIG shielding gas or plasma gas), or from the thermal decomposition of SMAW coated electrodes of cellulosic type. The best solution is to bake out the hydrogen before welding commences, as well as, to use preheat and PWHT to reduce hardness and residual stresses of weldments. As a rule, it should be recognised that no steel is resistant to HIC [50] *p410-411*.

iii) *Specific Weld Cracks:* Although all types of weld cracks are covered by hot and cold cracks, some of these are encountered in specific conditions or environments and

associated with certain industries or service conditions. Several examples are listed below [50] *p417:*

Chevron Cracks: These are intergranular and transgranular weld metal hot cracks that are caused when the weldment is subjected to *Ductility Dip Cracking* due to loss of ductility in steel between 1200 °C and 1000 °C which is recovered below 800 °C. Accumulation of sulphur and phosphorous to grain boundaries causes intergranular cracks. The intergranular cracks show plane lines on the surface, representing evidence of exposure to high temperatures. These intergranular cracks are joined by transgranular cracks at low temperature by hydrogen cracking to produce Chevron cracks as shown in Figure 1.16.

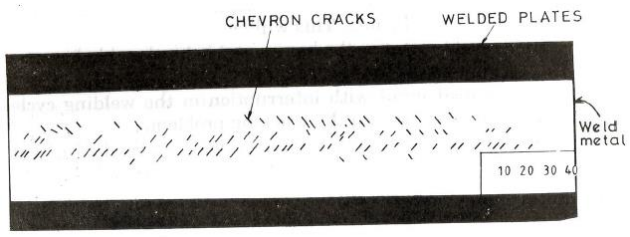

Figure 1.16 Representation of Chevron cracks on a submerged arc welded sample [50]

Another theory says that all cracking is due to hydrogen embrittlement but takes place at two different temperature ranges. Chevron cracking is commonly found in high thickness weldments of C-Mn steel grades. This type of cracking is not only associated with high heat input but also observed in self-shielded cored wire welds. Although such cracks have been observed in two-pass submerged arc high thickness welds, they are more common in multi-pass weldments. Chevron cracks in C-Mn steel weldment may be controlled by employing low hydrogen (≤ 5 ml/100g) welding consumables [50] *p417-418*.

Lamellar Cracks: Lamellar tearing or a lamellar crack, as shown in Figure 1.17, occurs in HAZ due to the combined effect of applied or residual stress and stress concentration near non-metallic inclusions, frequently aligned along the plate rolling direction. Crack initiation occurs at flattened MnS or oxide-silicate stringers by the decohesion.

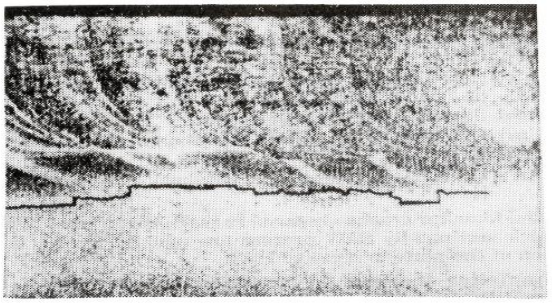

Figure 1.17 Lamellar tearing adjacent to a tee-butt weld in structural steel [50]

In lamellar tearing, the crack appears to be closely associated with the edge of the HAZ. The horizontal and vertical cracking of the base metal is a very typical feature of lamellar tearing. Such issue is usually observed for corner or tee weld joints for which weld is parallel to the plate rolling direction. In general, lamellar tearing susceptibility may occur because of type of joint, inherent restraint, sulphur and oxygen contents in HAZ, type, and morphology of the base metal inclusions, hydrogen contents in the weld, large plate thickness, preheating, and the strength of the material of electrode used. The presence of molecular hydrogen in the crystal lattice is directly related to embrittlement which further leads to cold cracking. The effect of preheating tends to reduce the susceptibility to lamellar tearing, especially when H_2 potentials are present. Low strength electrodes, within design requirements, can compensate for shrinkage stresses during welding and, thus, help to avoid lamellar tearing. Initiation of lamellar tearing may be triggered by the following factors:

- Separation of an opening created at the grain boundaries due to presence of inclusions in the base metal,
- The disintegration of inclusions within the microstructure,
- Sub-microscopic inclusions play a role in the crack generation,
- Silicate and sulphide inclusions accentuate the problem.

The lamellar cracks observed in thick C-Mn steel butt welds produced using the SAW process are usually located in the central section of the plate or close to HAZ. Lamellar tearing may also be due to *banding*, i.e., associated with carbon segregation(Figure 1.18) in the direction of rolling, with cracks appearing in high carbon content zones [50] *p418-420.*

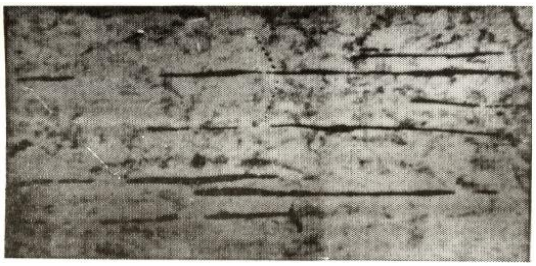

Figure 1.18 Microstructure of steel susceptible to lamellar tearing [50]

The remedies suggested to avoid or at least reduce the occurrences of lamellar tearing include [50] *p420-422:*

- Use steels with low sulphur content i.e., less than 0.007 wt.%,
- Use steels treated with Rare Earth metals (REM) like cerium,
- Use materials and procedures that reduced H_2 content in the weld metal and,
- Improve design as suggested for some joints in Figure 1.19.

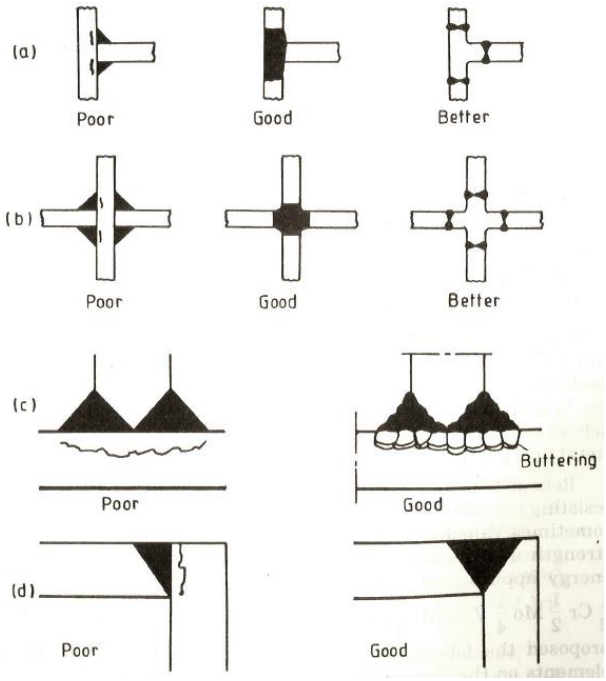

Figure 1.19 Joint design improvements to control lamellar tearing: (a) and (b) replace fillet welds with solid forged sections or weld metal, (c) buttering, (d) modified corner joint [50]

The proper joint design may help to avoid lamellar tearing by permitting shrinkage stresses to work along the rolling direction, rather than the transverse (through-thickness) direction. Figure 2.20 shows the use of such designs.

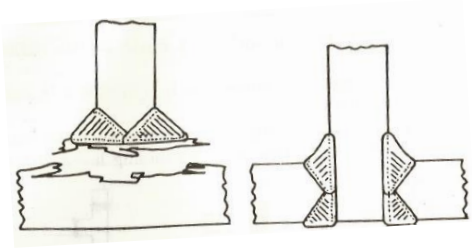

Figure 1.20 Improper and proper designs to avoid lamellar tearing in a T-joint [50]

Industries significantly affected by lamellar tearing include:

- Machine tool industry – corner and tee joints of beds and frames in heavy plates,
- Off-shore platforms,
- Welded appurtenances of boilers and thick-walled pressure vessels.

Reheat Cracks: Reheat or PWHT cracking is a type of cracking that rarely happens during welding [50] *p422-427*. Such type of cracking seems to be limited to steels of high thickness having two or more alloying elements of B, V, Mo, and Cr. Reheat cracking is a typical problem in corrosion and heat-resisting low alloy steels, i.e. ferritic steels containing Cr, Mo, and sometimes V which are used for corrosion resistance and high-temperature strength applications. Typical examples of susceptible alloys are ½Cr ½Mo ½V and ½CrMoV steel. Nakamura and Ito [98] projected relationships that allow predicting the Reheat Cracks Susceptibility (RCS) on alloying element additions.

$$RCS = \%Cr + 3.3(\%Mo) + 8.1(\%V) - 2 \qquad \text{(Nakamura)}$$

$$RCS = \%Cr + \%Cu + 2\%(Mo) + 10(\%V) + 7\%(Nb) + 5(\%Ti) - 2 \qquad \text{(Ito)}$$

Where in case $RCS \geq 0$, the steel can be highly prone to reheat cracking. When post-weld stress relieving is recommended, the welded structure is subjected to heating at high enough temperature, for example, 550°C – 650°C, so that the elastic stresses are relaxed quickly. Since, V, Mo, and Cr, are good carbide formers, carbide precipitation can occur in corrosion and heat-resistant low alloy steels during heating to a stress relief temperature or during stress relief itself. In these materials, carbides are formed in HAZ grains but not

at the grain boundaries, thus making the interior of grains comparatively stronger than the grain boundaries. Consequently, when the residual stresses relax, deformation and rupture occur along the grain boundaries, resulting in intergranular cracking. Cracks occur adjacent to the prior austenite grain boundaries within HAZ of transformable steels, and along any of the grain boundaries in austenite steels. In some welds, reheat cracks can also appear at coarse columnar grain boundaries in the weld deposit. The initiation and growth of reheat cracks take place in the following steps: nucleation of cavities on grain facets and triple junctions, growth of these individual cavities to form cracks of one-grain facet in length and interlinking of these single facet cracks to form cracks of several grain diameters long, which then rapidly lead to fracture. In general, the important factors that contribute to reheat cracking are:

- a microstructure with high hardness or low ductility,
- coarse grains,
- high heat input,
- the thickness of sections greater than 50 mm, where residual stress is high as cracks form above 400 °C,
- a high value of residual stresses and deformations,
- service temperature in the range of creep,
- use of preheating can increase susceptibility to reheat cracking,

Reheat cracking is not confined to the transferable steels; this problem also occurs in the Ni-alloys and austenitic stainless steels. Among the lower alloying steels, the most susceptible are the creep-resistant grades of CrMoV type, for example, 2.5Cr-1Mo, 1Cr-½Mo. As a general rule, however, PWHT of C-Mn steels improves fracture toughness, although low impact toughness has been reported for reheated microalloyed steels, particularly when they were welded by a high heat input process. Low alloy steels, such as 0.7Ni-0.4Cr-0.6Mo steels used in nuclear pressure vessels, or 0.12C-0.62Mn-0.45Cr-0.54Mo-0.06Nb-0.25V used for turbine casings and pipework in high-temperature heavy power equipment are well identified to be susceptible to reheat cracking. Cracks occur in grain growth zones either as longitudinal macro-cracks or more often as a micro-crack network. Design codes typically specify pot weld heat treatments at 550 °C – 650 °C for plate thickness above 38 mm and periods of an hour per 25mm of thickness. Although

these specifications are based on isothermal relaxation tests, they closely correspond to the reheat crack susceptibility temperature range.

Stress Corrosion Cracking: Usually alloying elements penetrate the weld metal through fluxes and coverings of welding consumables, although some time may be needed for these elements to dissolve in the weld metal because of rapid cooling. After cooling, these alloying additions may not be uniformly distributed throughout the weld metal, so martensite may form in regions with enriched chemical composition. This may ultimately result in intergranular or transgranular stress corrosion cracking. Therefore, the hardness of non-annealed welds is limited to 240-260 HV. Such hard spots have been encountered in joints welded by the submerged arc welding process when Mn is added in the form of ferro-manganese in flux and entrapped in weld metal from slag. Occasionally similar problems are encountered with SMAW electrodes and covered wires. To dissolve all the alloying elements and avoid the formation of hard spots in the weld metal preheating can be used. More homogeneous solidification will occur at a slow travel speed or an increased welding current. When carbon steel welded joints are exposed to a severely corrosive environment (for example, warm sea water) there is a tendency for the weldment or HAZ to corrode faster than the base metal, this will limit the structure life. For applications where carbon steels are generally employed, the preferential corrosion of weld metal is not a problem. Stress corrosion cracking of HAZ, however, will occur, if welded joints that have not been stress relieved are exposed to aqueous solutions of hot concentrated caustic soda, and the weldment is subjected to high tensile stresses. Stress corrosion cracks in carbon steel are typically intergranular while they are transgranular in austenitic stainless steel. For carbon steel, the most important stress cracking agents are caustic soda (sodium hydroxide) and aluminium nitrate, but coal gas liquors, cyanides, and possibly sulphates can act in the same way. The limit concentration and temperature of sodium hydroxide which determine the requirement for stress relief of weld joints are indicated in Figure 1.21.

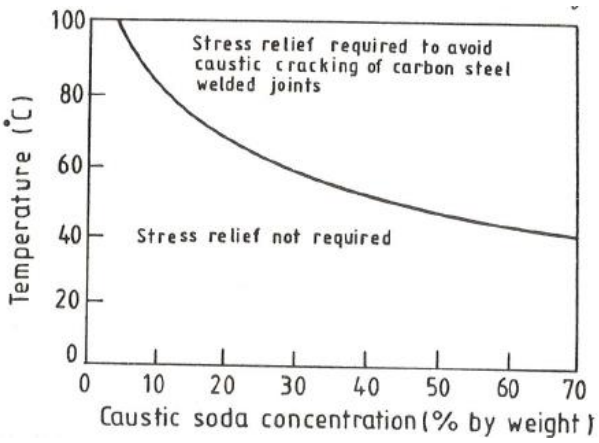

Figure. 1.21 Caustic soda concentration vs temperature relationship to determine the zone in which stress-relieving of weld joints for carbon steel is desirable [50]

When welding austenitic stainless steel, severe residual stresses can be caused by a high thermal expansion coefficient and low thermal conductivity. Upon exposure to the chloride-containing corrosive medium, stress corrosion cracking (SCC) can occur in a heat-affected zone. Such cracking is generally identified by intergranular or transgranular propagation with branches. When stress-relieving heat treatment is conducted, there are chances of chromium carbides precipitation at the grain boundaries. Stress-relieving may, of course, be attained by solution annealing of austenitic stainless steel (ASS), the carbides will be dissolved to the solution at a high temperature of 1000°C. However, new residual stresses may appear due to subsequent quenching. The use of low carbon steels helps to avoid this problem by controlling the cooling rate after solution heat-treatment [50] *p427-428*.

1.8 Hydrogen Embrittlement/ Cold Cracking of Q&T High Strength Steels

The hydrogen embrittlement phenomenon was first described by Johnson in 1875. The following conclusions can justifiably be reached from this 1875 paper [148]:

- it is hydrogen that embrittles steel, not acid;
- that the hydrogen is nascent or diffusible, not molecular;
- it is diffusible hydrogen that embrittles, so the phenomenon is reversible;
- the effusion of diffusible hydrogen from the steel leads to frothing (bubbles);
- that stronger steel is more susceptible to embrittlement than softer versions.

It follows, therefore, that the harmful influence of diffusible hydrogen can be mitigated by preventing its entry into steel or by rendering it immobile once it penetrates the material.

Hydrogen embrittlement (HE) also known as hydrogen assisted cold cracking (HACC) or hydrogen-induced cracking (HIC), describes the embrittlement of a metal by diffusible hydrogen. The essential facts about the nature of the hydrogen embrittlement of steels have now been known for 140 years [148-150]. It is diffusible atomic hydrogen that is harmful to the toughness of iron and steel [151]. It is a low temperature effect: most metals are relatively immune to hydrogen embrittlement above approximately 150°C. In steels, diffusible hydrogen ions come from water that is typically introduced by a wet electrochemical process such as electroplating. It must be distinguished from the entirely different process high temperature hydrogen attack (HTHA) which is where steels operating at high temperatures above 400°C are attacked by hydrogen gas [152].

For hydrogen embrittlement to occur, a combination of three conditions are required:

- the presence and diffusion of hydrogen atoms or ions
- a susceptible material
- stress

Diffusible hydrogen can be introduced during manufacture from operations such as forming, coating, plating or cleaning. The most common causes of failure in practice are poorly-controlled electroplating or bad welding practice with damp welding rods. Both of these introduce hydrogen ions which dissolve in the metal. Hydrogen may also be introduced over time (*external embrittlement*) through environmental exposure (soils and chemicals, including water), corrosion processes (especially galvanic corrosion) including corrosion of a coating and cathodic protection. Hydrogen atoms are very small and diffuse interstitially in steels. Almost uniquely amongst solute atoms they are mobile at room temperature and will diffuse away from the site of their introduction within minutes [148].

Hydrogen embrittlement is a complex process involving a number of distinct contributing micro-mechanisms not all of which need to be present. The mechanisms include the formation of brittle hydrides, the creation of voids that can lead to high-pressure bubbles, enhanced decohesion at internal surfaces and localised plasticity at crack tips that assist

in the propagation of cracks [153]. There is a great variety of mechanisms that have been proposed [153]: and investigated which cause brittleness once diffusible hydrogen has been dissolved into the metal [148]. As the hydrogen is diffusible and mobile, brittleness can only occur when (a) it is captured in microscopic traps, and (b) these traps cause brittleness [154]. In recent years, it has become widely accepted that HE is a complex, material and environmental dependent process so that no mechanism applies exclusively [155].

- Internal pressure: Adsorbed hydrogen species recombine to form hydrogen molecules, creating pressure from within the metal. This pressure can increase to levels where the metal has reduced ductility, toughness, and tensile strength, up to the point where it cracks open (hydrogen-induced cracking, or HIC) [156].

- Hydrogen enhanced localised plasticity (HELP), where the generation and movement of dislocations is enhanced and results in localised deformation such as at the tip of a crack increasing the propagation of the crack with less deformation in surrounding material giving a brittle appearance to the fracture [155][149].

- Hydrogen decreased dislocation emission: molecular dynamics simulations reveal a ductile-to-brittle transition caused by the suppression of dislocation emission at the crack tip by dissolved hydrogen. This prevents the crack tip rounding-off, so the sharp crack then leads to brittle-cleavage failure [157].

- Hydrogen enhanced decohesion (HEDE), where the increased solubility of hydrogen in a tensile strength field, for instance on the tip of a crack or in areas with internal tensile strength or in the tension field of edge dislocations, reduces the yield stress locally [149].

- Metal hydride formation: The formation of brittle hydrides with the parent material allows cracks to propagate in a brittle fashion. This is particularly a problem with Vanadium alloys [158] but most structural alloys do not easily form hydrides.

- Phase transformations: these occur for some materials when hydrogen is present and the new phase may be less ductile.

- Steel with an ultimate tensile strength of less than 1000 MPa (~145,000 psi) or hardness of less than 32 HRC is not generally considered susceptible to hydrogen embrittlement. As an example of severe hydrogen embrittlement, the elongation at failure of 17-4PH precipitation hardened stainless steel was measured to drop from 17% to only 1.7% when smooth specimens were exposed to high-pressure hydrogen.
- As the strength of steels increases, the fracture toughness decreases, so the likelihood that hydrogen embrittlement will lead to fracture increases. In high-strength steels, anything above a hardness of HRC 32 may be susceptible to early hydrogen cracking after plating processes that introduce hydrogen. They may also experience long-term failures anytime from weeks to decades after being placed in service due to accumulation of hydrogen over time from cathodic protection and other sources. Numerous failures have been reported in the hardness range from HRC 32-36 and more above; therefore, parts in this range should be checked during quality control to ensure they are not susceptible.

While most failures in practice have been through fast failure, there is experimental evidence that hydrogen also affects the fatigue properties of steels. This is entirely expected given the nature of the embrittlement mechanisms proposed for fast fracture [154][156]. In general hydrogen embrittlement has a strong effect on high-stress, low-cycle fatigue and very little effect on high-cycle fatigue [159]-160].

Hydrogen embrittlement can be prevented through several methods, all of which are centered on minimizing contact between the metal and hydrogen, particularly during fabrication and the electrolysis of water. Embrittling procedures such as acid pickling should be avoided, as should increased contact with elements such as sulfur and phosphate. The use of proper electroplating solution and procedures can also help to prevent hydrogen embrittlement.

If the metal has not yet started to crack, hydrogen embrittlement can be reversed by removing the hydrogen source and causing the hydrogen within the metal to diffuse out through heat treatment. This de-embrittlement process, known as Low hydrogen annealing or "baking", is used to overcome the weaknesses of methods such as electroplating which introduce hydrogen to the metal, but is not always entirely effective because a sufficient time and temperature must be reached [150]. Tests such as ASTM F1624 can be used to rapidly identify the minimum baking time (by testing using design

of experiments, a relatively low number of samples can be used to pinpoint this value). Then the same test can be used as a quality control check to evaluate if baking was sufficient on a per-batch basis.

In the case of welding, often pre-heating and post-heating the metal is applied to allow the hydrogen to diffuse out before it can cause any damage. This is specifically done with high-strength steels and low alloy steels such as the chrome/molybdenum/vanadium alloys. Due to the time needed to re-combine hydrogen atoms into the hydrogen molecules, hydrogen cracking due to welding can occur over 24 hours after the welding operation is completed.

Another way of preventing this problem is through materials selection. This will build an inherent resistance to this process and reduce the need of post processing or constant monitoring for failure. Certain metals or alloys are highly susceptible to this issue so choosing a material that is minimally affected while retaining the desired properties would also provide an optimal solution. Much research has been done to catalog the compatibility of certain metals with hydrogen [159]. Tests such as ASTM F1624 can also be used to rank alloys and coatings during materials selection to ensure (for instance) that the threshold of cracking is below the threshold for hydrogen-assisted stress corrosion cracking. Similar tests can also be used during quality control to more effectively qualify materials being produced in a rapid and comparable manner.

The three methods of controlling HIC Q&T welds are

- temperature control method,
- isothermal transformation method and
- the use of austenitic stainless steel (ASS) weld metal

The temperature control method depends on holding the weld at an elevated temperature, in particular above that at which hydrogen by diffusion is accelerated. The isothermal transformation method prevents HIC by controlling the cooling rate of the heat affected zone (HAZ) so that it transforms to softer (non-martensite) structure. During welding of Q&T steels, for various reasons it is not possible to use preheat temperature greater than 150 °C, hence the temperature control method is severely restricted and isothermal transformation method cannot be used. The only alternative is to use welding

consumables which virtually prevents the introduction of hydrogen in HAZ and which produces a weld metal insensitive to hydrogen [161].

1.9 Example: Cutting and welding of High Strength Steels

Q&T high-strength steels (with a yield stress of 690 MPa-1300 MPa) find many applications like in the civil construction and machine manufacturing industry [127-130]. The technological difficulties and characteristics during cutting and welding of conventional high strength steels require a suitable selection of consumables, preheating temperature, and heat input, to weld them. This is particularly the case for these steels due to high hardness and abrasion resistance. High hardness poses difficulty for cold forming of steels, that need greater bending forces and so, allowances must be given for spring-back action. Excessive heating above 200 °C must be avoided, otherwise, the mechanical properties may be adversely affected.

The example below characterises fabrication attributes of 0.29C-1Cr-0.25Mo steel with hardness 500 HB. This grade is mainly used for ground engaging tools, cutting edges, earthmoving buckets, wear liners, chutes, and dump truck wear liners. The mechanical properties and chemical composition are presented in Table 1.3 (a, b) [45]:

Table 1.3(a) Properties of 0.29C-1Cr-0.25Mo steel grade.

Properties	**Specification**	**Typical Strength**
0.2% Proof Stress	-	1400 MPa
Tensile Strength	-	1640 MPa
Elongation (50GL)	-	10%
Charpy Impact (Longitudinal) +20°C (10mmx10mm)	-	35J
Hardness	477-534HB	500HB

Table 1.3(b) Chemical composition of 0.29C-1Cr-0.25Mo steel grade.

Thickness (mm)	**C**	**P**	**Mn**	**Si**	**S**	**Cr**	**Mo**	**B**	**CE(IIW)**	**Pcm**
6-100	0.29	0.015	0.30	0.003	0.003	1.00	0.25	0.001	0.61	0.40

1.9.1 Flame cutting of 0.29C-1Cr-0.25Mo grade: Both oxy-fuel cutting processes, i.e. oxy-acetylene and oxy-LPG processes, are adopted to cut most of the thicknesses of 0.29C-1Cr-0.25Mo grade. Using these processes, the following factors need to be considered:

- The surface to be cut must be smooth and cleaned from scale, oil, grease, and moisture.
- Consideration must be given to keep HAZ as minimum as possible, by using the accurate size of nozzle, gas pressure, and travel speed as used for cutting of carbon steels.
- In general, HAZ for the oxy-flame cut edge for carbon steels may extend up to 3 mm. For 0.29C-1Cr-0.25Mo grade, it may be up to 5 mm due to high carbon contents. HAZ usually consists of hard and soft regions.
- Preheating helps to decrease the cooling rate resulting in the reduction of hardness and ultimately lessens the probability of cold cracking.
- It is recommended to utilise more than one cutting-heads and then air cooling after cutting of plates.
- Quench and stack cutting must not be employed.
- Crayons or pyrometers may be used to check the preheating and inter-pass temperature during welding.

1.9.2 Plasma cutting of 0.29C-1Cr-0.25Mo grade: Plasma cutting is an acceptable method of cutting 0.29C-1Cr-0.25Mo steel grade. The after-cut edge quality may be poor because of non-uniform material loss at the top and bottom of the cut surface. The width of heat affected zone is less than that formed by the oxy-flame cutting method, but the maximum hardness peak value is usually greater than that of the oxy-flame cutting technique. The peak hardness value of this grade is 540 HB and a recommended depth of removal of material from the cut edge is 1-1.2mm. Stack cutting of plates, removal of HAZ by grinding or machining, and requirement of preheat temperature may be followed similar to that of the oxy-fuel cutting process.

1.9.3 Waterjet Cutting of 0.29C-1Cr-0.25Mo grade: Water-jet cutting process is a process occasionally used in the manufacturing industry. It may be given a priority by design and fabrication supervisors to avoid issues regarding the cut edge smoothness, the accuracy of size and shape, and non-uniform heat-affected zone, which is normally

observed using conventional thermal cutting processes. The water-jet cutting technique shows minimal effect in material microstructure at the cut edge.

1.9.4 Welding of 0.29C-1Cr-0.25Mo grade: 0.29C-1Cr-0.25Mo steel grade of hardness 500 HB may be easily welded with low hydrogen conventional welding processes. Following techniques are recommended to weld this type of steel grade:

- It is very important to have an understanding and control of heat input, preheating temperature, and hydrogen contents to avoid the possibility of cold cracking due to the hardening of weld and HAZ regions. The hydrogen levels in the weld may be minimized by using low hydrogen welding consumables and employing proper cleaning of weld joint before, during, and after welding. Guidelines and instructions received from supplier or manufacturer must be followed for appropriate handling and storage of welding consumables before, and during welding activity; for instance, it is mandatory to bake low hydrogen welding electrodes in a baking oven at a higher temperature for a specific period of time and then keep them in holding ovens at a lower temperature during welding to protect them from ingress moisture.
- The heat-affected zone (HAZ), a region just near weldment, undergoes a local heat-treatment starting from base metal to adjacent weld pool. The final HAZ properties for 0.29C-1Cr-0.25Mo steel grade depend upon the rate of cooling and chemical composition of the steel.

Chemical composition of 0.29C-1Cr-0.25Mo steel grade may be categorised based on Carbon Equivalent (C.E and CET) and Pcm (a term used for calculations that indicate the weldability of steel) as follows (Table 1.4) [45]:

Table 1.4 Carbon Equivalent of 0.29C-1Cr-0.25Mo steel grade.

Commercial Grade	Plate Thickness (mm)	Carbon Equivalent (IIW)	Pcm% (JWES)	CET
0.29C-1Cr-0.25Mo	5-100	0.62	0.39	0.42

Notes:

C.E. (IIW) = C + (Mn/6) + (Cr + Mo + V)/5 + (Cu + Ni)/15

Pcm% (JWES) = C + (Si/30) + (Mn + Cu + Cr)/20 + (Ni/60) + (Mo/15) + (V/10) + 5B

CET = C + (Mn+Mo)/10 + (Cr +Cu)/20 + (Ni/40)

Preheat and heat input must be defined to confirm that the HAZ cools down at a proper rate and that the accurate hardness and microstructure are attained. A fast-cooling rate produces a harder heat-affected zone which may cause low ductility. A slow cooling rate can cause a softer heat-affected zone which may result in inferior toughness and tensile strength properties. Preheating and correct heat input help to control the cooling rate for a specific thickness of the plate and geometry of a joint. The preheat and heat input endorsements shown in Tables 1.5 and 1.6 will assure the acceptable HAZ cooling rate [45].

Table 1.5 Preheating and inter-pass temperature requirements for specific commercial grades [45].

Commercial grades		Maximum thickness in joint (mm)			
		<13	≥13<25	≥25<50	≥50
Minimum Preheat Temp ˚C	0.16C-0.2Cr-0.2Mo (Hardness: 400HB)	50	75	125	150
	0.16C-0.2Cr-0.2Mo (Hardness: 500HB)	100	150	150	
Maximum Interpass Temp°C	0.16C-0.2Cr-0.2Mo and 0.29C-1Cr-0.25Mo	150	175	200	220

Table 1.6, Permissible heat input for specific commercial grades [45]

Welding Processes		The thickness of joint (mm)			
		3 – 12*	>12 - 25	>25 - 32	>32 - 100
Permissible heat input (kg/mm) for commercial grades (refer to table 1.5)	MMA	1.25 – 2.5	1.25 – 3.5	1.25 – 4.5	1.5 – 5.0
	GMAW	1.0 – 2.5	1.0 – 3.5	1.25 – 4.5	1.5 – 5.0
	FCAW	0.8 – 2.5	0.8 – 3.5	1.5 – 4.5	1.5 – 5.0
	SAW	1.0 – 2.5	1.0 – 3.5	1.5 – 4.5	1.5 – 5.0
Note: MMA: ‘Manual metal Arc Welding’, GMAW: ‘Gas Metal Arc Welding’, FCAW: ‘Flux Cored Arc Welding’, SAW: ‘Submerged Arc Welding’,					

1.10 Summary and Analysis of Literature Review

Q&T martensitic steels are widely used in mining, defence and construction industry due to their excellent mechanical properties (up to 1800 MPa of tensile strength and >10% elongation). These mechanical properties are attained by having chemical composition of up to 0.4 wt.% Carbon (C), <1.5 wt. % Manganese (Mn), alloying with Molybdenum (Mo), Chromium (Cr), Nickle (Ni), Titanium (Ti) and sometimes Boron (B), and a combination of carefully designed thermomechanical processing schedule and post rolling heat treatment. For the past 10 years, addition of <1.5 % Ti was found to have superior mechanical properties at a moderate C content. Improvement in the mechanical properties was achieved through formation of TiC hard particles imbedded in the tempered martensite matrix. Moderation of the C content in Ti-alloyed steels allowed to obtain steels with relatively low hardness, high toughness and enhanced weldability (due to low carbon equivalent of the steel composition). Fabrication of equipment from the Q&T steels is carried out using conventional fusion arc welding and thermal cutting with oxy-fuel or plasma jet. The main problem in this case is the formation of an edge microstructure highly susceptible to hydrogen induced cold cracking (HICC) due to presence of hydrogen and high residual stresses, which results into deterioration of mechanical properties, making steel unsuitable for required application. In case of Ti-alloyed steels, the heat input associated with thermal cutting and welding alters the TiC particle size distribution, in addition to tempering of the martensitic microstructure, occurring in conventional Q&T steels. However, fabrication parameters may be controlled to avoid catastrophic microstructure deterioration and product failure. Although Plasma cutting process has advantage over oxy-fuel cutting process yet water jet cutting process has been proved to be excellent method to cut the metals with least HAZ. To avoid HACC, suitable selection of types of welding equipment, welding consumables, welding parameters (current, voltage, travel speed, electrode/ wire feed mechanism, shielding gases, current polarity, welding metal transfer mode, preheating, post heating, pre-welding, inter-pass welding and post-welding cleaning operations) are made as per requirement of chemistry and thickness of the steel to be welded. Chemistry is directly related to Carbon Equivalent on the basis of which heat input and preheating temperature are selected to have defect free welds. Cutting and welding procedures are developed to cut or weld similar types of steels. After welding, quality of welds is ensured through different inspection tools and methods including visual inspection and liquid

penetrant testing etc. Different fabrication and service weldability tests are employed to have sound and defect free welds, e.g. hot cracking & cold cracking testing, hardness & tensile testing, bend & impact testing etc. Weld defects may be caused due to incorrect welding procedure, unwanted microstructure, poor workmanship and skill etc. These defects may be surface (distortion, surface cracks, burn-though and oxidation etc.) or subsurface (lack of fusion, lack of penetration, porosity and non-metallic inclusions etc.) and remedial actions are mandatory to make welded steels suitable for intended service. Cracking susceptibility increases as the weld metal hydrogen content, material strength and thickness increase. Cold cracking will occur if three conditions are satisfied: susceptible microstructure; type and magnitude of residual stresses; and importantly, the level of diffusible hydrogen that enters the weld pool. Cold cracking can be avoided through selection of controlled heat input (depends upon current, voltage and travel speed of welding) and preheating temperature. However, there is limited research available for such steels to avoid HACC through optimisation of the cutting and welding procedures. Hence, this research work has been aimed to investigate the properties of these steels in relation to chemistry, section thickness, and thermal cycle during fabrication processes. This research has covered most of common fabrication practices for instance, for cutting process Oxy-fuel gas, plasma and water jet cutting methods have been used, while for conventional welding processes Gas tungsten arc welding and flux cored arc welding. The cutting and welding processes were optimised to ensure defect free or crack free microstructures. Following are the research gaps identified and work plan to follow, as a result of a comprehensive literature review.

1.11 Research Gaps Identified:

Based on literature review and critical analysis on existing knowledge, following are the knowledge gaps identified and will be covered by necessary experimental work planning and execution:

- Ti-microallyed Q&T steels are newly developed grades having wide applications in industry and their parent metal properties are worth to be revealed through necessary experimental research work to highlight their behaviour with respect to conventional Q&T steels.
- Though there are recommendations and welding standards to prevent hydrogen assisted cold cracking (HACC) in the heat affected zone (HAZ) of different Q&T high strength steels, a universal and dependable model for HACC prevention in the parent

metal and weld metal for Q&T Ti-microalloyed steels is likely to be more multifarious and difficult. Hence, independent management rules to avoid HACC in these steels, are yet to be established.

- Commonly, the weld metal cold cracking susceptibility appears to increase as the weld metal hydrogen content, strength, and section thickness increases. It is more complex than cracking in HAZ. Hence, behaviour of dependence of thickness need to be explored for a particular commercial grade steel.
- Since Chemical composition and thermal cycle play a vital role towards formation of susceptible microstructure and magnitude of residual stresses which cause HACC, during cutting and welding of Q&T Ti-microalloyed steels, hence their effect must be clarified to avoid cold cracking.
- Since newly developed Q&T Ti-microalloyed steels have good strength as well as toughness, hence it is required to determine the change in their properties due to thermal effect from cutting and welding operation.

1.12 Research Questions:

Following are the research questions developed on the basis of research gaps:

- How Q&T Ti-microalloyed steels are different with respect their mechanical and microstructural parameters from other conventional Q&T steels?
- Whether there is any effect of Ti alloying on martensite morphology and precipitation of fine and coarse Ti-rich particles?
- How conventional cutting processes, namely oxy-fuel, plasma and water-jet cutting, affect mechanical and microstructural properties of these steels?
- Whether Ti-alloying and plate thickness bring additional constraints to thermal cutting process?
- How HAAC can be avoided in these steels through manipulation of preheating temperture?
- What is the effect of variation in welding heat input on hardness of these steels?
- How chemistry and heat input affect fracture toughness of weld and HAZ of these steels during welding?
- What variation in the microstructure parameters (grain structure, precipitation of Ti-rich particles) may be expected during welding and what are the mechanisms of properties development in HAZ of defect free welds?

1.13 Plan to address Research Gaps and Research Questions:

To satisfy the above research questions, investigation will be carried out for advanced Ti-alloyed Q&T steels during arc welding and thermal cutting. Two commercially produced steel grades with varying C and Ti contents will be studied: Steel L (0.28C-0.4Ti, wt.%) and Steel H (0.38C-0.6Ti, wt.%), having thickness of 12 mm and 32 mm for Steel L and 12 mm and 30 mm for Steel H. Following are experimental research methods to address the research questions:

- Assessment of mechanical properties and microstructure of as received plate steels via hardness, tensile testing, Charpy V-notch testing, optical and SEM techniques at room temperature.
- Determination of the hardness profile from the cut edge towards the base plate followed by microstructural characterisation after cutting using oxyfuel, plasma and water-jet cutting methods.
- Investigation of effect of preheat temperature (in the range of 20 - 150 °C) on HACC cracking phenomenon for different chemistries and thicknesses of these steels through CTS (cold cracking severity) test using FCAW process.
- Investigation of effect of heat input (in the range of 1.2kJ/mm – 3.5kJ/mm) for weld and HAZ hardness through BOP (single weld bead on plate) technique, using GTAW process.
- Measurement of toughness followed by the microstructural characterisation of these steels in several HAZ positions after welding using FCAW welding processes.
- Analysis of obtained results and provision of recommendations for defect free cutting and welding of Ti-alloyed martensitic steels.

1.14 Aims & Objectives

The aim of this project is to investigate the effects of thermal cutting and welding parameters on mechanical properties variation in Q&T wear-resistant steels microalloyed with 0.4-0.6 wt. % Titanium. Precipitation of Ti-rich carbonitrides in the novel martensitic steels is going to influence the microstructure-properties relationship; therefore, the fabrication technologies require optimisation.

To achieve this aim, four commercially produced Q&T plate steels with varying chemical composition and thickness were purchased and the following objectives for the research project were set:

- determine the tensile and impact properties in the as-received plates with respect to steel composition, plate thickness, and test direction, discuss the effect of C and Ti contents on the microstructure and properties in as-received hot rolled and heat-treated plate steels.

- conduct thermal cutting experiments and characterise the dependence of microstructural parameters (grain size, size distribution/number density/volume fraction of fine and coarse Ti-rich particles and Fe_3C particles) and hardness near the cut-edge (distribution in the 10 mm wide zone from the cut edge) on the cutting method (oxy-fuel and plasma), plate thickness and steel composition, compare the results to samples cut with water jet, where no thermal effect occurs.

- conduct cold thermal severity (CTS) tests and determine the minimum pre-heat temperature required to produce defect-free welds for various steel compositions and plate thicknesses.

- conduct bead on plate (BOP) tests and determine the effect of heat input on the HAZ hardness for both steel compositions.

- conduct K-type groove welding tests and determine the microstructure, hardness, and toughness (for different test temperatures) variations with the distances from the weld centreline for two steel compositions welded with two heat inputs.

Based on obtained results, propose optimum thermal cutting and welding parameters to obtain defect-free welds in the novel Ti-microalloyed Q&T steels.

References (Chapter 1)

1. K. Maweja, W. Stumpf, *Fracture and ballistic-induced phase transformation in tempered martensitic low-carbon armour steels*, Materials Science and Engineering. A432 (2006) 158–169.
2. K. Maweja, W. Stumpf, *The design of advanced performance high strength low-carbon martensitic armour steels: microstructural considerations*, Mater. Sci. Eng. A480 (2008)160–166.
3. P. K. Jena, K. S. Kumar, V. R. Krishna, A. K. Singh, T. B. Bhat, *Studies on the role of microstructure on performance of a high strength armour steel*, Eng. Fail. Anal. 15 (2008) 1088–1096.
4. P. K. Jena, B. Mishra, M. Ramesh, A. Babu, A. K. Singh, K. SivaKumar, T. B. Bhat, *Effect of heat-treatment on mechanical and ballistic properties of a high strength armour steel*, Int. J. Impact Eng. 37 (2010) 242-249.
5. S. Karagoz, S. H. Atapek, A. Yilmaz, *Microstructural and fractographical studies on quenched and tempered armor steel*, Mater. Test. 52 (2010) 316-322.
6. *Welding Handbook*, 8th Ed., American Welding Society, 2 (1991) 110-155.
7. J. C. Ritter, B. F. Dixon, N. J. Baldwin, *Deformation and weld repair of armour steel*, Mater. Forum 13 (1989) 216–224.
8. N. Yurioka, H. Suzuki, *Hydrogen assisted cracking in C–Mn and low alloy steel weldments*, Int.Mater.Rev.35 (1990) 217–249.
9. G. Magudeeswaran, V. Balasubramanian, G. Madhusudhan Reddy, *Hydrogen induced cold cracking studies on armour grade high strength, quenched and tempered steel weldments,* International Journal of Hydrogen Energy, 33(7) (2008) 1897-1908.
10. L. Kuzmikova, M. Callaghan, N. Larkin, R. Scott, R. De-Jong, H. Li, J. Norrish, *A study of a continuous cooling behaviour and effect of preheat and inter-pass temperature on the HAZ of high strength quenched and tempered steel*, Doc IX-2352-10, IIW Annual Assembly, Istanbul, Turkey, (2010) 11–18
11. I. Barenyi, O. Hires, P. Liptak, *Degradation of mechanical properties of armoured steels after its welding*, Proceedings of International Conference of Scientific Paper, AFA SES 2011, Brasov, Romania (2011) 26–28.

12. T. Shiraiwa, M. Kawate, F. Briffod, T. Kasuya, M. Enoki, *Evaluation of hydrogen-induced cracking in high-strength steel welded joints by acoustic emission technique*, Materials & Design, 190 (2020) paper 108573.
13. L. Kuzmikova, N. Larkin, Z. Pan, M. Callaghan, H. Li, J. Norrish, *Investigation into feasibility of hybrid laser-GMAW process for welding high strength quenched and tempered steel*, Aust. Weld. J. 57 (2012) 43-48.
14. K. Easterling, *Introduction to the physical metallurgy of welding*, Butterworths, 2(1983) 1-2.
15. D. Uwer and H. Hohne: *Characterisation of the cold cracking behaviour of steels during welding*, Welding and Cutting, 43(4) (1991) 195-199.
16. N. Yurioka and H Suzuki: *Hydrogen assisted cracking in C-Mn and low alloy steel weldments*, International Materials Reviews, 35 (1990) 217-249.
17. P. H. M. Hart: *Hydrogen cracking - its cause, costs, and future occurrence*, Proceedings of the 1st International Conference, Wollongong, March 1999.
18. L. Reeve, *A summary of reports of investigations on selected types of high strength steels*, Trans. Inst. Welding, (1940)177-202.
19. M. Pitrun, D. J. Nolan, *Cold Cracking Susceptibility of Weld Metal Deposited by Gas Shielded Rutile Flux-Cored Wire*, Australasian Welding Journal, 50 (2005) 33-46.
20. L. Kuzmikova, M. Callaghan, N. Larkin, R. Scott, R. De Jong, H. Li, J. Norrish, *A study of the continuous cooling behaviour and effect of preheat and interpass temperature on the HAZ of high strength quenched and tempered steel.* IIW 2010 Annual Assembly, (2010) 1-14
21. Alkemade, S.J., *The weld cracking susceptibility of high hardness armour steel*, Defence Science and Technology Organisation, (1996) 24
22. Harrison, P.L. and R.A. Farrar, *Application of continuous cooling transformation diagrams for welding of steels.* International Materials Reviews, 34(1)(1989)35-51.
23. Cottrell, C. L. M.: Journal Iron Steel Institute, 174 (1953) 17
24. API Recommended Practice 571, Second Edition, (2011) 4.215-4.216
25. Technical Information Bulletin (TIB 125, 03/11), Lincoln Electric, Technical Bulletin 5, https://www.totalsteel.com.au/assets/files/technical/lincoln-tib-125.pdf, accessed on 05-04-2018

26. https://industeel.arcelormittal.com/wp-content/uploads/2018/06/CREUSABRO-Dual-GB.pdf accessed on 05-04-2018
27. J. H. Tylczak, A. Oregon, P. J. Blau (Ed.), ASM Handbook: *Friction, Lubrication, and Wear Technology*, ASM International, USA, 18 (1992) 337
28. J. Rendon, M. Olsson, *Abrasive wear resistance of some commercial abrasion-resistant steels evaluated by laboratory test methods*, Wear, 267 (2009) 2055-2061.
29. E. Rabinowitz, *Friction and Wear of Materials*, Wiley-Interscience, New York, (1)(1965)
30. A. D. Sarkar, *Wear of Metals*, Pergamon Press, Oxford (1)(1976)
31. K. H. Z. Gahr, *Microstructure and Wear of Materials*, Elsevier Science Ltd., Amsterdam, (1)(1987)
32. P. J. Mutton, J. D. Watson, *Some effects of microstructure on the abrasion resistance of metals*, Wear, 48 (1978) 385-398.
33. L. Q. Xu, N. F. Kennon, A study of the abrasive wear of carbon-steels, Wear, 148 (1991) 101-112.
34. L. Fang, Q. D. Zhou, Y. J. Li, *An explanation of the relation between wear and material hardness in three-body abrasion*, Wear, 151 (1991) 313-321.
35. K. H. Z. Gahr, D. V. Doane, *Optimizing fracture toughness and abrasion resistance in white cast irons*, Metallurgical Transactions A, 11 (1980) 613-620
36. S. Das, B. K. Prasad, A. K. Jha, O.P. Modi, A. H. Yegneswaran, *Three-body abrasive wear of 0.98% carbon steel*, Wear, 162–164 (1993) 802-810.
37. K. H. Z. Gahr, *Wear by hard particles*, Tribology International, 31 (1998) 587-596
38. K. H. Z. Gahr, *Modelling of two-body abrasive wear*, Wear, 124 (1988) 87-103.
39. X. Xu, W. Xu, F. H. Ederveen, S. V. D. Zwaag, *Design of low hardness abrasion resistant steels.* Wear, 301(1) (2013) 89-93.
40. http://digital.library.aist.org/pages/PR-258-010.htm accessed on 05-04-2018
41. https://www.totalsteel.com.au/assets/files/brochures/jfe-ehsp-catalogue.pdf accessed on 05-04-2018.
42. Y. Han, J. Shi, L. Xu, W. Q. Cao, H. Dong, *Effects of Ti addition and reheating quenching on grain refinement and mechanical properties in low carbon medium manganese martensitic steel.* Materials & Design, 34 (2012) 427-434.

43. R. S. Parmar, "*Welding Processes & Technology*", Khanna Publishers, 2 (1995) 9, 63, 79-80, 85-125, 126-151, 152-170, 227-249, 250-265, 265-289, 563-569, 581-590
44. Technical Brochure by Raex®, Abrasion-resistant Steel for demanding products, *Welding and Thermal Cutting*, pp. 1-16, 2016, https://www.raexsteel.com/raex-downloads accessed on 05-04-2018.
45. https://pdfslide.net/documents/bisalloy-bisplate-technical-manual.html accessed on 05-04-2018.
46. http://www.bluescopesteel.com.au/files/flamecutting.pdf accessed on 05-04-2018.
47. http://files.aws.org/wj/supplement/WJ_1981_11_s231.pdf accessed on 05-04-2018
48. L. Kuzmikova, H. Li, J. Norrish, Z. S. Pan, N. Larkin, *Development of safe optimized welding procedures for high strength Q&T steel welded with austenitic consumables.* Revista Soldagem e Inspecao, 18(2) (2013) 169-175.
49. Welding Technology Institute of Australia, - *Welding & fabrication of quenched and tempered steel*, WTIA Technical Note No. 15 (1996)
50. R. S. Parmar, "*Welding Engineering and Technology*", Khanna Publishers, 1(2) (2002) 1, 401, 402, 410-411, 417-428, 436-462, 464, 659, 661, 662-682, 701, 702-709, 710-716, 815-818.
51. The Lincoln Electric Company, Cleveland Ohio, *"The procedure handbook of Arc Welding"*, 12 (1973) 6.1-5, 3.3-3 to 3.3-7.
52. R. Scott Funderburk, *Key Concepts in Welding Engineering- fundamentals of Preheat*, Welding Innovation Vol. XIV, No. 2, (1997) 1-2
53. Q. Xue, D. Benson M. A. Meyers, V. F. Nesterenko E.A. Olevsky, *Constitutive response of welded HSLA 100 steel*, Materials Science and Engineering A, 354 (2003) 166-179
54. J. E. Ramirez, S. Mishael, and R. Shockley, *Properties and Sulphide Stress Cracking Resistance of Coarse-Grained Heat-affected Zones in V-Micro alloyed X60 Steel Pipe*, Welding Research, welding journal, 84 (2005) 113s-123s
55. T. Kasuya, N. Yurioka, M. Okumura, *Methods for predicting maximum hardness of Heat Affected Zone and selecting necessary Preheat temperature for Steel Welding*, Nippon Steel Technical Report No. 65, (1995) 7-14.
56. T. Teng, P. Chang, *A study of residual stresses in multi-pass girth-butt welded pipes*, International Journal of Pressure Vessels and Piping, 74 (1997) 59–70

57. S. Lee, B. C. Kim, D. Kwon, *Correlation of microstructure and fracture properties in weld heat-affected zones of thermomechanically controlled processed steels*, Metallurgical Transactions A, 23(10) (1992) 2803-2816
58. B. Eigenmann, V. Schulze, O. Vohringer, *Surface residual stress relaxation in steels by thermal or mechanical treatment*, In Proceedings of the Fourth International Conference on Residual Stresses, Society of Experimental Mechanics, Bethel, Connecticut, Baltimore, MD, (1994) 598–607
59. Y. LIN, K. LEE, *Effect of preheating on the residual stress in type 304 stainless steel weldment*, Journal of materials processing technology, 63(1-3) (1997) 797-801
60. M Eroglu, M Aksoy and N Orhan, *Effect of coarse initial grain size on microstructure and mechanical properties of weld metal and HAZ of low carbon steel*, Material Science and Engineering, 259(1-2) (1999) 59-66
61. https://www.azom.com/article.aspx?ArticleID=2451 accessed on 06-07-2018.
62. M. Pirinen, Yu. Martikainen, P. D. Layus, V. A. Karkhin, S. Yu. Ivanov, "*Effect of heat input on the mechanical properties of welded joints in high-strength steels*", Welding International, 30(2) (2016) 129–132.
63. ISO/TR 17844: *Welding - Comparison of standardised methods for the avoidance of cold cracks*, International Organization for Standardization, Geneva, (1) (2004) 1-72
64. http://citeseerx.ist.psu.edu/viewdoc/download?doi=10.1.1.188.8462&rep=rep1&type=pdf accessed on 05-05-2018
65. V. Kuzucu, M. Aksoy, M. H. Korkut, *The effect of strong carbide-forming elements such as Mo, Ti, V and Nb on the microstructure of ferritic stainless steel*, Journal of Materials Processing Technology, 82 (1998) 165-171
66. M. Aksoy, V. Kuzucu, M. H. Korkut, *The influence of strong carbide-forming elements and homogenization on the wear resistance of ferritic stainless steel*, Wear, 211 (1997) 265-270
67. P. M. Unterwiser, H. E. Boyer, J. J. Kubbs (Eds.), Heat Treater's Guide: *Standard Practices and Procedures for Steel*, ASM International, USA, 2 (1993) 418.
68. M. A. Moore, *The relationship between the abrasive wear resistance, hardness, and microstructure of ferritic materials*, Wear, 28 (1974) 59-68

69. P. Clayton, K. J. Sawley, P. J. Bolton, G. M. Pell, *Wear behavior of bainitic steels*, Wear, 120 (1987) 199-220
70. P. Clayton, R. Devanathan, *Rolling sliding wear behavior of a chromium molybdenum rail steel in pearlitic and bainitic conditions*, Wear, 156 (1992) 121-131.
71. R. Devanathan, P. Clayton, *Rolling sliding wear behavior of 3 bainitic steels*, Wear, 151 (1991) 255-267.
72. C. Chattopadhyay, S. Sangal, K. Mondal, A. Garg, *Improved wear resistance of medium carbon microalloyed bainitic steels*, Wear, 289 (2012) 168-179.
73. W. J. Salesky, G. Thomas, *Medium carbon steel alloy design for wear applications*, Wear, 75 (1982) 21-40.
74. P. Ghosh, R. K. Ray, C. Ghosh, D. Bhattacharjee, *Comparative study of precipitation behavior and texture formation in continuously annealed Ti and Ti + Nb added interstitial-free high-strength steels*, Scripta Mater, 58 (2008) 939-942.
75. S. G. Hong, H. J. Jun, K. B. Kang, C. G. Park, *Evolution of precipitates in the Nb–Ti–V microalloyed HSLA steels during reheating*, Scripta Mater, 48 (2003) 1201-1206.
76. P. Ghosh, C. Ghosh, R. K. Ray, *Thermodynamics of precipitation and textural development in batch-annealed interstitial-free high-strength steels*, Acta Mater, 58 (2010) 3842-3850.
77. J. Adamczyk, E. Kalinowska-Ozgowicz, W. Ozgowicz, R. Wusatowski, *Interaction of carbonitrides V(C, N) undissolved in austenite on the structure and mechanical properties of microalloyed V–N steels*, J Mater Proc Technol, 53 (1995) 23-32.
78. S. Matsuo, T. Ando, N. J. *Grant, Grain refinement and stabilization in spray formed AISI 1020 steel*, Mater Sci Eng A, 288 A (2000) 34-41.
79. Y. Tomita, K. Okabayashi, *Effect of microstructure on strength and toughness of heat-treated low alloy structure steels*, Metall Trans A, 17 A (1986) 1203-1209.
80. R. Lazarova, R. H. Petrov, V. Gaydarova, A. Davidkov, A. Alexeev, M. Manchev, V. Manolov, *Microstructure and mechanical properties of P265GH cast steel after modification with TiCN particles*, Mater Des, 32 (2011) 2734-2741.
81. D. Rasouli, Sh. Khameneh Asl, A. Akbarzadeh, G. H. Daneshi, *Optimization of mechanical properties of a microalloyed steel*, Mater Des, 30 (2009) 2167-2172.

82. H. L. Andrade, M. G. Akben, J. J. Jonas, *Effect of molybdenum, niobium, and vanadium on static recovery and recrystallization and solute strengthening in microalloyed steels*, Metall Trans A, 14 (1983) 1967-1977.
83. A. J. Craven, K. He, L. A. Garvie, T. N. Baker, *Complex heterogeneous precipitation in Ti–Nb microalloyed Al-killed HSLA steels*, Acta Mater, 48 (2000) 3857-3868.
84. M. Charleux, W. J. Poole, M. Militzer, A. Deschamps, *Precipitation behavior and its effect on strengthening of an HSLA-Nb/Ti steel*, Metall Mater Trans A, 32 (2001) 1635-1647.
85. G. Xu, X. L. Gan, G. J. Ma, F. Luo, H. Zou, *The development of Ti-alloyed high strength microalloy steel*, Mater Des, 31 (2010) 2891-2896.
86. Z. Jia, R. D. K. Misra, R. O'Malley, S. J. Jansto, *Fine-scale precipitation and mechanical properties of thin slab processed titanium–niobium bearing high strength steels*, Mater Sci Eng A, 528(2011)7077-7083.
87. A. I. Z. Farahat, T. A. El-Bitar, *Effect of Nb, Ti and cold deformation on microstructure and mechanical properties of austenitic stainless steels*, Mater Sci Eng A, 527(2010)3662-3669.
88. B. K. Show, R. Veerababu, R. Balamuralikrishnan, G. Malakondaiah, *Effect of vanadium and titanium modification on the microstructure and mechanical properties of a microalloyed HSLA steel*, Mater Sci Eng A, 527(2010)1595-1604.
89. S. W. Ooi, G. Fourlaris, *A comparative study of precipitation effects in Ti only and Ti-V Ultra Low Carbon (ULC) strip steels*, Mater Charact, 56 (3)(2006)214-226.
90. R. Soto, W. Saikaly, X. Bano, C. Issartel, G. Rigaut, A. Charai, *Statistical and theoretical analysis of precipitates in dual-phase steels microalloyed with titanium and their effect on mechanical properties*, Acta Mater, 47 (12) (1999) 3475-3481.
91. W. Regone, A. M. Jorge Jr., O. Balancin, *Evidence of strain-induced precipitation of Ti4C2S2 during hot deformation of Ti-only stabilized IF steel*, Scripta Mater, 48 (2003) 773-778.
92. P. Ghosh, C. Ghosh, R. K. Ray, D. Bhattacharjee, *Precipitation behavior and texture formation at different stages of processing in an interstitial free high strength steel*, Scripta Mater, 59 (2008) 276-278.
93. C. S. Smith, *Introduction to grains, phases, and interfaces – an interpretation of microstructure*, Trans AIME, 175 (1948) 15-51.

94. T. Gladman, T. N. Baker (Ed.), *The physical metallurgy of microalloyed steels*, The Institute of Materials, London (1997) 176-184.
95. J. J. W. Nibbeing, H. Thomas, and T. J. Bos, "*The Properties of Plasma Cut Edges*," Welding in the World, 18(9&1) (1980) 182-195.
96. F. Goldberg, *Influence of thermal cutting and its quality on the fatigue strength of steel*. Welding Journal 52(9)(1973)392-s to 404-s
97. NIW (Netherlands Institute of Welding), *The properties of flame-cut edges*, Final report of Working Group 1913, SSL 163a (1973) 1-28.
98. Y. Ito, M. Nakanishi, IIW Doc. X-668-72 (1972)
99. AWS (American Welding Society) D1.1/D1.1M, *Guidelines on alternative methods for determining preheat*, Structural Welding Code-Steel, Annex H (23) (2015) 355-364
100. http://materialstandard.com/wp-content/uploads/2019/07/AWS-A3.0-2010.pdf accessed on 16-11-2018
101. D. J. Thomas, *Characterisation of steel cut edges for improved fatigue property data estimations and enhanced CAE durability*, PhD Thesis, UK: Swansea University; 2011
102. D. J. Thomas, *The influence of the laser and plasma traverse cutting speed process parameter on the cut-edge characteristics and durability of Yellow Goods vehicle applications*, J Manuf Proc, 13 (2011) 120-132.
103. S. Cicero, T. Garcia, J.A. Alvarez, A. Bannister, A. Klimpel, A. Martin-Meizosos, J. Aldazabal, *Fatigue behaviour of structural steels with oxy-fuel, plasma and laser cut straight edges, Definition of Eurocode 3 FAT classes*, Eng Struct, 111 (2016)152-161.
104. S. Cicero, T. Garcia, J. A. Alvararez, A. Martin - Meizoso, J. Aldazabal, A. Bannister, A. Klimpel, *Definition and validation of Eurocode 3 FAT classes for structural steels containing oxy-fuel, plasma and laser cut holes*, Int J Fatigue, 87 (2016) 50-58.
105. S. Cicero, T. Garcia, J. A. Alvarez, A. Martín-Meizoso, A. Bannister, A. Klimpel, *Definition of BS7608 fatigue classes for structural steels with thermally cut edges*, J. Constr. Steel Res., 120 (2016) 221-231.

106. S. Ramakrishnan, M. Gershenzon, F. Polivka, T. N. Kearney, M. W. Rogozinski, *Plasma generation for the plasma cutting process*, IEEE Trans. Plasma Sci., 25 (1997) 937-947.
107. S. Ramakrishnan, M. W. Rogozinski, Properties of electric arc plasma for metal cutting, J. Phys. D. Appl. Phys., 30 (1997) 636-644.
108. M. E. Shemshadiana, R. Labbanea, A. E. Schultzae, J. Le, D. F. Laefer, S. Al-Sabah, P. McGetrick, *Experimental study of intermeshed steel connections manufactured using advanced cutting techniques*, Journal of Constructional Steel Research, 172 (2020) 106169.
109. D. Li, Z. Huang, B. Uy, H. Thai, C. Hou, *Slenderness limits for fabricated S960 ultra-high-strength steel and composite columns*, J. Constr. Steel Res., 159 (2019) 109-121.
110. F. Wang, O. Zhao, B. Young, *Flexural behaviour and strengths of press-braked S960 ultra-high strength steel channel section beams*, Eng. Struct., 200 (2019)109735.
111. A. Su, Y. Sun, Y. Liang, O. Zhao, *Material properties and membrane residual stresses of S690 high strength steel welded I-sections after exposure to elevated temperatures.* Thin-Walled Structures, 150 (2020) 106723.
112. H. K. D. H. Bhadeshia, *Prevention of hydrogen embrittlement in steels*, ISIJ Int, 56 (1) (2016) 24-36.
113. X. Z. Liang, M. F. Dodge, S. Kabra, J. F. Kelleher, T. L. Lee, H. B. Dong, *Effect of hydrogen charging on dislocation multiplication in pre-strained super duplex stainless steel*, Scr Mater, 143 (2018) 20-24.
114. H. Uyama, H. Yamada, H. Hidaka, N. Mitamura, *The effects of hydrogen on microstructural change and surface originated flaking in rolling contact fatigue*, Tribology Online, 6 (2) (2011) 123-132.
115. N. Kino, K. Otani, *The influence of hydrogen on rolling contact fatigue life and its improvement*, JSAE Rev, 24 (3) (2003) 289-294.
116. M. A. Stopher, P. E. J. Rivera-Díaz-del-Castillo, *Hydrogen embrittlement in bearing steels*, Mater Sci Technol, 32 (11) (2016) 1184-1193.
117. R. Sepe, E. Armentani, G. Lamanna, F. Caputo, *Evaluation by FEM of the influence of the preheating and post-heating treatments on residual stresses in welding*, Key Eng. Mater., 627 (2015) 93-96.

118. H. Du, D. Wang, C. Liu, H. Zhang, *Finite element analysis of effects of preheating and postweld heat treatment on residual stress in pipe welding*, Adv. Mater. Res., 314-316 (2011) 428-431.
119. B. Raj, T. Jayakumar, B. P. C. Rao, *Non-destructive testing and evaluation for structural integrity.* Sadhana, **20**(1)(1995)5-38.
120. X. Wang, Y. Zhang, J. Yu, J. Zhang, J. Yang, *Characteristics of Welding Crack Defects and Failure Mode in Resistance Spot Welding of DP780 Steel*, Journal of Iron and Steel Research, International, **23**(10)(2016)1104-1110.
121. X. Wan, Y. Wang, C. Fang, *Welding defects occurrence and their effects on weld quality in resistance spot welding of AHSS steel*, ISIJ International, 54(8)(2014)1883-1889.
122. S. C. Sun, L. Z. Chen, *Seed demography of Quercus liaotungensis in Dongling Mountain region,* Acta Phytoecologica Sinica, 24(2)(2000)215-221.
123. D. Q. Sun, B. Lang, D. X. Sun, J. B. Li, *Microstructures and mechanical properties of resistance spot welded magnesium alloy joints.* Materials Science and Engineering A, 460-461(2007) 494-498.
124. M. Marya, X. Q. Gayden, *Development of requirements for resistance spot welding dual-phase (DP600) steels part 2: Statistical analyses and process maps.* Welding Journal, 84(12) (2005) 197S-204S.
125. R. Singh, *Chapter 2 - Visual Inspection*, in *Applied Welding Engineering*, R. Singh, Editor, Butterworth-Heinemann. 2 (2016) 301-304.
126. R. Singh, *Chapter 8 - Weld Defects and Inspection*, in *Applied Welding Engineering*, R. Singh, Editor, Butterworth-Heinemann. 2 (2016) 277-295.
127. B. Ahlblom, P. Hansson, T. Narstrom, *Martensitic structural steels for increased strength and wear resistance*, in Materials Science Forum. 539-543 (2007) 4515-4520.
128. K. Hulka, A. Kern, U. Schriever, *Application of niobium in quenched and tempered high-strength steels*, in Materials Science Forum, 500-501 (2005) 519-526.
129. T. Schaupp, W. Ernst, H. Spindler, T. Kannengiesser, *Hydrogen-assisted cracking of GMA welded 960 MPa grade high-strength steels*, International Journal of Hydrogen Energy, 45(38) (2020) 20080-20093.
130. M.S. Weglowski, M. Zeman, *Prevention of cold cracking in ultra-high strength steel Weldox 1300*, Arch Civ Mech Eng, 14 (2014) 417-424.

131. N. Yurioka, H. Suzuki, *Hydrogen assisted cracking in C—Mn and low alloy steel weldments.* International Materials Reviews, 35(1)(1990)217-249.
132. S. Lynch, *Hydrogen embrittlement phenomena and mechanisms.* Corrosion Reviews, 30(3-4)(2012)105-123.
133. M. B. Djukic, G. M. Bakic, V. S. Zeracic, A. Sedmak, B. Rajicic, *The synergistic action and interplay of hydrogen embrittlement mechanisms in steels and iron: localized plasticity and decohesion,* Eng Fract Mech, 216 (2019) 106528.
134. M. Rhode, J. Steger, T. Boellinghaus, T. Kannengiesser, *Hydrogen degradation effects on mechanical properties in T24 weld microstructures.* Welding in the World, 60(2)(2016) 201-216.
135. P. Zimmer, D. M. Seeger, T. Boellinghaus, *Hydrogen permeation and related material properties of high strength structural steels.* Proc. High Strength Steels for Hydropower Plants, (2005)1-18.
136. J. C. Villalobos, A. Del-Pozo, J. Mayen, S. Serna, B. Campillo, *Hydrogen embrittlement susceptibility on X-120 microalloyed steel as a function of tempering temperature.* International Journal of Hydrogen Energy, 45 (15)(2020) 9137-9148.
137. C. Pandey, M. M. Mahapatra, P. Kumar, N. Saini, *Effect of Weld Consumable Conditioning on the Diffusible Hydrogen and Subsequent Residual Stress and Flexural Strength of Multipass Welded P91 Steels.* Metallurgical and Materials Transactions B: Process Metallurgy and Materials Processing Science, 49(5)(2018)2881-2895.
138. T. Kannengiesser, T. Lausch, *Diffusible hydrogen content depending on welding and cooling parameters.* Welding in the World, 56(11-12)(2012)26-33.
139. T. Schaupp, M. Rhode, T. Kannengiesser, *Influence of welding parameters on diffusible hydrogen content in high-strength steel welds using modified spray arc process.* Welding in the World, 62(1)(2018)9-18.
140. A. Swierczynska, D. Fydrych, G. Rogalski, *Diffusible hydrogen management in underwater wet self-shielded flux-cored arc welding.* International Journal of Hydrogen Energy, 42(38)(2017)24532-24540.
141. D. Fydrych, A. Swierczynska A, J. Tomkow, *Diffusible hydrogen control in the flux-cored arc welding process,* Key Eng Mater 597(2014)171–178.
142. M. Pitrun, D. Nolan, D. Dunne, *Diffusible hydrogen content in rutile flux-cored arc welds as a function of the welding parameters*, Weld World 48(1–2)(2004)2–13.

143. T. Schaupp, M. Rhode, T. Kannengiesser, *Influence of welding parameters on diffusible hydrogen content in high-strength steel welds using modified spray arc process*, Weld World 62(1)(2018)9–18.
144. T. Boellinghaus, H. Hoffmeister, C. Schubert, *Finite element analysis of hydrogen distribution in butt joints*. In: Trends in welding research, proceedings of the 4th International Conference-1995, Gatlinburg, Tennessee, USA, ASM International 28(10) (1996) 836.
145. T. Mente, T. Boellinghaus, M. Schmitz-Niederau, *Heat treatment effects on the reduction of hydrogen in multi-layer high-strength weld joints.* Welding in the World, 56(7-8) (2012) 26-36.
146. E. Steppan, T. Mente, T. Bollinghaus, *Numerical investigations on cold cracking avoidance in fillet welds of high-strength steels*, Welding in the World, 2013. 57(3) (2013) 359-371.
147. P. Wongpanya, *Effects of heat treatment procedures on the cold cracking behaviour of high strength steel welds*, Dissertation, BAM-Dissertationsreihe, Band 36, (2008).
148. *https://www.canadianmetalworking.com/canadianfabricatingandwelding/product/welding/victors-new-oxy-fuel-torch-features-improved-ergonomics* (accessed on 14-02-2018).
149. https://www.thefabricator.com/thefabricator/article/plasmacutting/plasma-cutting-torches-the-long-and-short-of-it (accessed on 14-02-2018).
150. https://awo.aws.org/glossary/gas-tungsten-arc-welding-gtaw/ (accessed on 14-02-2018).
151. https://www.thefabricator.com/thefabricator/article/arcwelding/smooth-moves-with-gmaw (accessed on 14-02-2018).

Chapter 2

2 Materials and Methods

2.1 Introduction

In this chapter, composition, properties, and dimensions of samples being used for this project will be described; types of cutting and welding processes employed along with their conditions will be discussed; mechanical testing and microstructural examination requirement will be presented. All the experimental work has been designed and planned as per the requirement of evaluating the behaviour of advanced quenched and tempered steel grades *Steel L* and *Steel H* for base metal and during cutting and welding.

2.2 Materials

Two types of Ti-microalloyed Q & T wear-resistant steels have been investigated in this project. The nominal chemical composition of these steels reported in the literature [1, 4] is given in Tables 2.1 (a) and 2.1 (b).

Table 2.1(a) Nominal chemical composition of Steel L.

Material Grade	**C**	**Si**	**Mn**	**P**	**S**	**Cr**	**Ti***	**Ceq****
Steel L	≤0.35	≤0.55	≤1.60	≤0.030	≤0.030	0.50-1.50	0.4	0.62
	*Other alloying elements like Mo and V are added for enhancing the abrasion resistant property. **Carbon Equivalent CE = C + Mn/6 + (Cr+Mo+V)/5 + (Ni+Cu)/15							
Thickness: 12mm and 32mm thicknesses of Steel L have been used for this research work.								

Table 2.1(b) Nominal chemical composition of steel H.

Material Grade	**C**	**Mn**	**Ni**	**Cr**	**Mo**	**S**	**Ti***	**Ceq****
Steel H	~0.40	~1.30	~0.45	~0.70	≤0.340	≤0.002	~0.60	0.86

*Other alloying elements like Mo and V are added for enhancing the abrasion resistant property. **Carbon Equivalent CE = C + Mn/6 + (Cr+Mo+V)/5 + (Ni+Cu)/15
Thickness: 12mm and 30mm thicknesses of Steel H have been used for this research work.

Table-2.1(c), Nominal mechanical properties of these steels reported or available in the literature [1, 4]

Material Grade	Yield Strength MPa (ksi)	Tensile Strength MPa (ksi)	Elongation (%)	Charpy Impact Absorbed Energy, J at 0 °C	Hardness
Steel L	1270 (184)	1489 (216)	13.2	24 (1/2t)	461 HB
Steel H	1200 (174)	1630 (236)	10	18 (13)	480 HB

2.3 Cutting Plan and Technological Parameters

As per the requirement for experimental work, the size of steel plates was estimated using AutoCAD software. Following are the details of the cutting plan prepared and executed to cut steel grades.

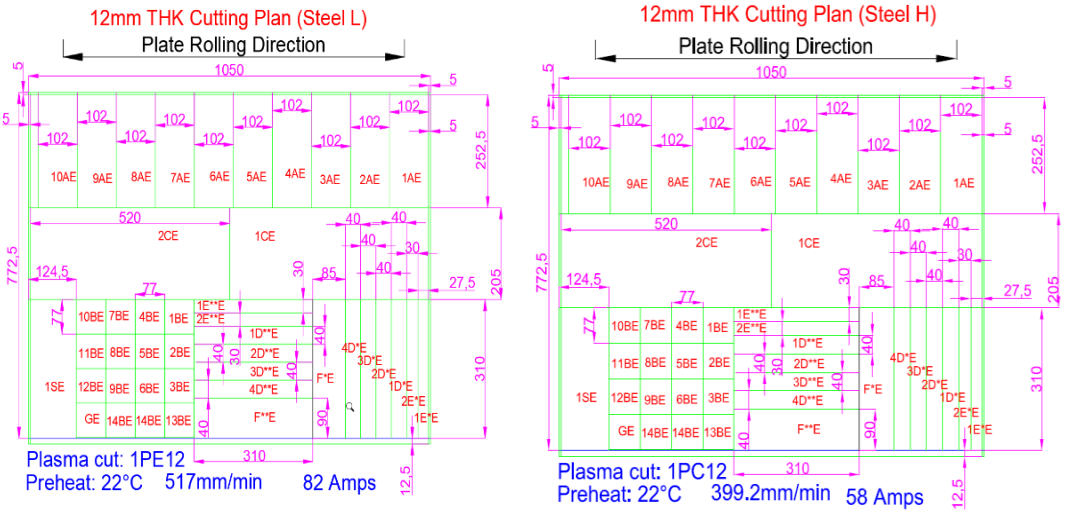

Figure 2.1 Cutting layout of 12mm Plate Steel L and Steel H.

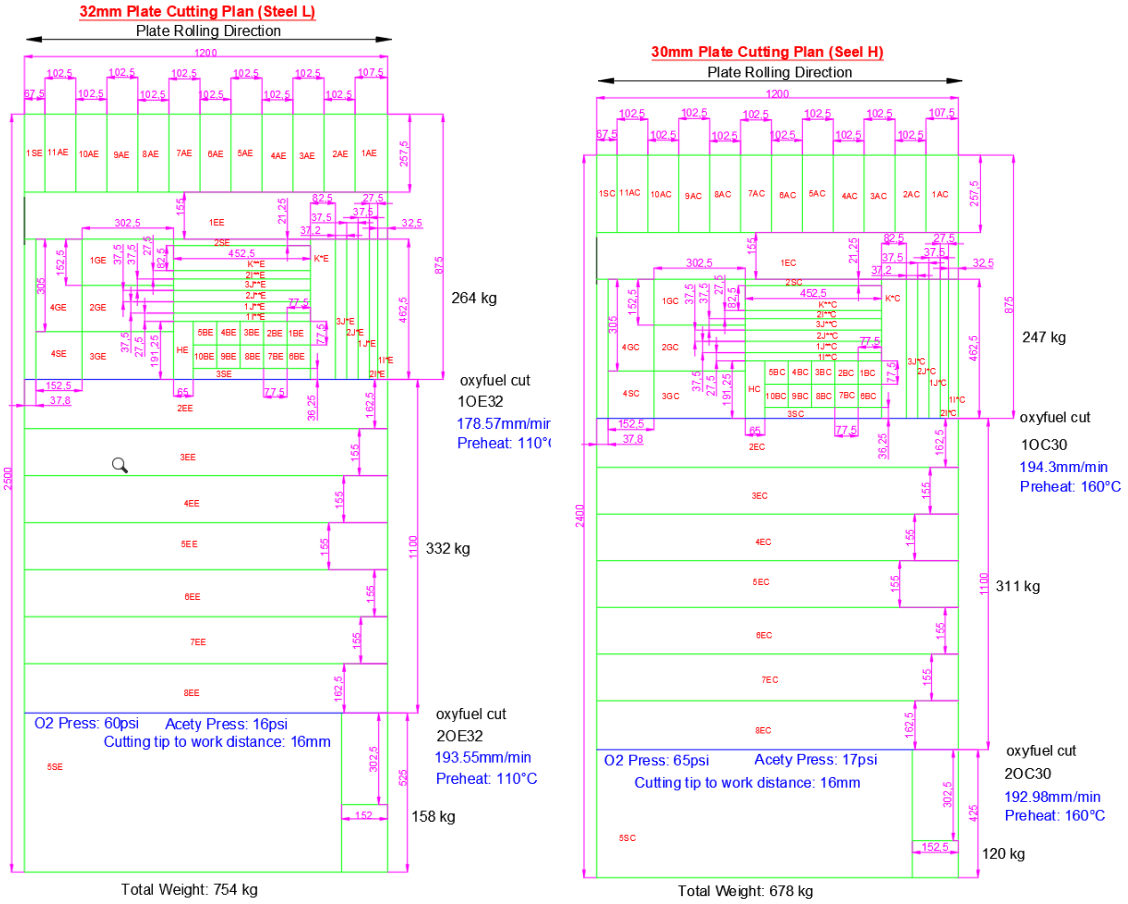

Figure 2.2 Cutting layout 32mm Plate Steel L and 30mm Plate Steel H.

Legend:

Steel L	Steel H	Test Samples	Remarks
AE, BE	AC, BC	CTS test samples	All of these samples were taken along (shown by **) and across (shown by *) the plate rolling direction as per the cutting plan (Figure 2.1)
DE	DC	Bend test samples	
EE	EC	Tensile test samples	
FE	FC	Impact test samples	
GE	GC	Test sample for microstructural studies	
SE	SC	Spare plate piece	

Three types of cutting methods have been used including plasma jet, oxy-fuel cutting process, and water jet cutting process. The plate of each grade and thickness was cut into larger pieces along the rolling direction using oxy-fuel and plasma cutting methods. Smaller pieces were cut using the waterjet cutting process.

2.3.1 Plasma Cutting Process: The plasma cutting process was used to cut 12 mm plates of both grades. The plates were cut into three pieces along the rolling direction of suitable sizes as per the cutting plan. The plasma machine used for this purpose was a Power Max80 Air Plasma machine. The plasma cutting was performed manually at ambient temperature at approx. 24°C RT (Room Temperature).

Table 2.2 (a) Machine parameters of plasma cutting process.

Material Grade	**Thickness**	**Plasma cut ID**	**Preheat**	**Cutting Speed**	**Plasma Machine Current**
Steel L	12mm	1PE12	24°C (RT)	517mm/min	82 amps
Steel H	12mm	1PC12	24°C (RT)	399.2mm/min	58 amps

2.3.2 Oxyfuel Cutting Process: Oxy-acetylene flame was used to cut 32 mm thick Steel L and 30 mm thick Steel H. The plates were cut into three pieces along the rolling direction of suitable sizes as per the cutting plan. The 30 mm plate of Steel H was preheated to 160 °C while the 32 mm plate of grade Steel L was preheated to 110 °C.

Table 2.2 (b) Machine parameters of the oxy-fuel cutting process.

Material Grade	**Thickness**	**Oxy-Acetylene flame cut ID**	**Preheat**	**Cutting Speed**
Steel L	32mm	1OE32	110°C	178mm/min
Steel L	32mm	2PE12	110°C	193mm/min
Steel H	30mm	1OC30	160°C	194mm/min
Steel H	30mm	2OC30	160°C	192mm/min

2.3.3 Water-jet cutting process: This process was used to cut small sample sizes out of previously cut plates of both grades as per experimental work requirements.

Table 2.2 (c) Parameters of water jet cutting process.

Material Grade	Thickness	Water-jet cut Sample ID	Preheat	Cutting Speed
Steel L	12mm	12E-W-1	24°C (RT)	128mm/min
Steel H	12mm	12C-W-1	24°C (RT)	128mm/min

2.4 Welding and Testing Conditions

The following welding and testing conditions were employed for all four plates.

2.4.1 Cold Thermal Severity Testing (CTS testing): Flux-cored arc welding process, utilised using a Lincoln Power Wave S500 Welding Robotic Machine, was employed to conduct CTS welding and the following sample testing according to the standard ISO 17642-2:2005 [5]. It is a type of self-restraint cold cracking test, designed to access the cold cracking sensitivity of the parent material and arc welding consumables. A weld bead was deposited on a test sample consisting of two plates. After processing the welds were cut across to examine the cut surfaces and detect possible cracks either in the weld metal or in the heat-affected zone. A quantitative evaluation approach was exercised aimed at determining the cracking temperature limit; therefore, a series of tests had been performed at various preheating temperatures for all thicknesses of both steel grades. The preheat temperatures for Steel L were chosen to be 100°C, 80°C, 60°C, 40°C, and room temperature, whereas, for Steel H, these were 150°C, 120°C, 90°C, 60°C, and room temperature. The preheat temperature range (0-100˚C) for Steel L was chosen lower than that of Steel H (0-150˚C), because of its lower carbon contents, hardenability, and cracking sensitivity as compared to that of Steel H.

a) *Procedure:* The dimensions of the test piece were in accordance with Figure 2.3.

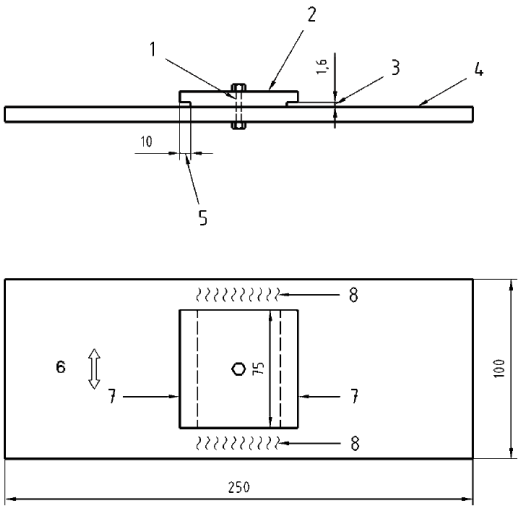

Figure 2.3 Dimension of a test piece [5].

The tests were carried out for both plate thicknesses and steel grades, 12 mm and 30 mm for Steel L, and 12 mm and 32 mm for Steel H.

The machining of test pieces was performed by sawing, milling, and grinding at the UOW workshop. This ensured that the surfaces to be welded were milled or ground finish. Care was taken to minimize the heating and deformation of the material during machining.

The general arrangement of the test piece is shown in Figure. 2.4, and the tolerances and surface finish requirements are given in Table 2.3.

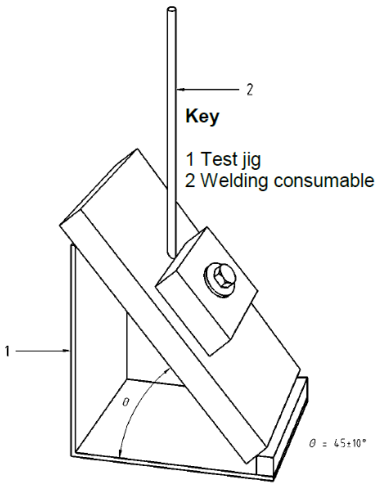

Figure 2.4 General arrangement of a test piece [5].

The top and bottom blocks both had the same thickness. Top and bottom blocks were machined. Both blocks used were of the same material. The principal rolling direction of the top and bottom plates was the same (Figure. 2.3). The surfaces to be welded were

ground smooth and free from scale, rust, oil, grease, and other contaminants. A bolt with a 12 mm diameter was used to keep both the test pieces in contact. The bolts, nuts, and washers were degreased. The bolt was inserted through the top and bottom blocks, and the nut and washers were added and tightened to the required torque (Table 2.3).

Table 2.3 Tolerances and surface finish requirements for the CTS test samples.

Dimension/conditions	Values
Material thickness, *t* Top block	6 mm min. (75 ± 1) mm x (75 ± 1) mm x t
Bottom block	(250 ± 3) mm x (100 ± 3) mm x t
Root notch depth gap	 (10 ± 0,5) mm (1,6 ± 0,10) mm
Torque on bolt	(100 ± 5) N·m
Surface finish on mating faces	3,2 µm R_a max.
Surface finish on area to be welded	6,3 µm R_a max.
Mating face gap	0,05 mm max.

The anchor welds (shown in Figure 2.3) were made with an austenitic stainless steel welding consumables. The anchor fillet welds were started and finished 10 mm (± 3 mm) from the corners of the top plate and the following throat sizes were made:

i) For 12 mm thick plate: 6 ± 1 mm.

ii) For 30mm and 32mm thick plates: 13 ± 1 mm.

The welds were deposited with a procedure to avoid hydrogen cracking, using preheat, and inter-pass temperature control as necessary. The assembly was left for 12 h before test welding.

For test welds, the assembly was heated in a box with electrical resistance thermal pads. Sufficient time was given to equalise the temperature through the assembly. Prior to any welding, the temperature of the test blocks was checked using a calibrated surface pyrometer and thermocouple. Temperature variations between the top and bottom blocks were observed to be less than 5 °C. A jig was used to position the assembly. The position of the electrode with respect to the test block (Figure 2.3) was such that the deposited test welds were symmetrical in the flat positions across the full width of the block in a single direction and a single pass. The test weld didn't extend beyond the ends of the block. The weld length was determined by measuring the distance from the weld start to the centre

of the weld crater, as shown in Figure 2.5, then, the value of heat input (in kJ/mm) was calculated using the expression Equation 2.1:

$$J = (E \times I \times 60)/ (V \times 1000) \ldots\ldots\ldots\ldots \text{Equation 2.1}$$

Where:

V: Arc travel speed in mm/min

I: Welding current in amperes

E: Arc voltage in volts

J: Heat input in kJ/mm

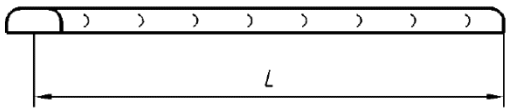

Figure. 2.5 Measurement of the weld length [5].

Following deposition of the first test weld bead, the test assembly was transferred to a cooling bath whereby the end of the assembly opposite to the welded end was immersed in cold flowing water to a depth of (60 ± 5) mm (Figure 2.6). Transfer to the bath was completed within 60 s of the completion of welding. The water temperature at the exit of the cooling bath did not exceed 30 ºC during the test. The assembly was kept in the bath until the temperature decrease to the ambient.

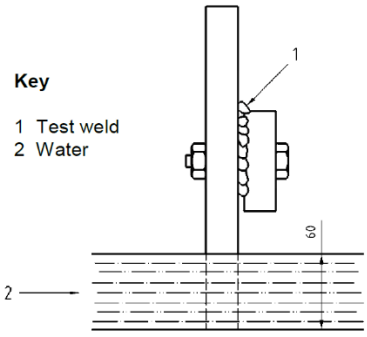

Figure 2.6 Test piece immersed in a bathtub of height 60mm [5].

Minimum 48 hours were allowed from the removal of the test piece from the cooling bath before the second weld was deposited. The cooling of the second test weld was similar to the first. Following cooling of the second test weld to the ambient temperature, the assembly was left for a minimum of 48h before proceeding with further work.

b) *Test Results:* The test pieces were sectioned for equal size samples for metallurgical examination according to EN 1321 (Figure 2.7).

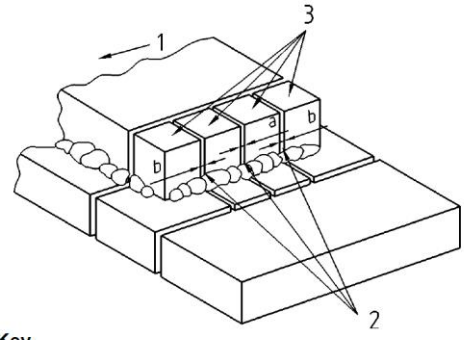

Key

1	Welding direction
2	Indicates faces polished and examined for cracking
3	Test pieces
a,b	Faces polished and examined for cracking

Figure 2.7 Sectioning of CTS test piece [5]

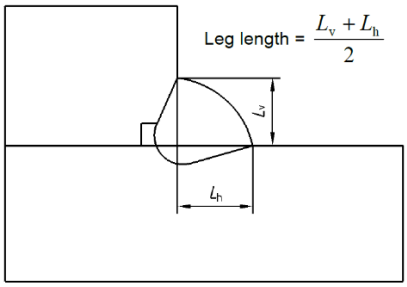

Figure 2.8 Measurement of the leg length [5]

The six cut faces were prepared for the examination. The examination was made for the weld metal and HAZ for cracking at a magnification of x50. The examination was done for either face 2b or 3a first (Figure 2.6) in accordance with EN 1321. Confirmation for the absence or presence of cracking was performed at x200 magnification.

The weld metal, which showed root cracking of a total length greater than 5 % of the throat thickness, was considered invalid. HAZ cracks longer than 5 % of the leg length were reported as "Cracked". The examination was made for all six faces for non-cracked test pieces.

One of the central faces from each test weld (face 3a or 2b in Figure 2.6) was subjected to Vickers hardness testing according to EN 1043-1:1995. A testing load of 5 kg was selected so that the hardness indents were contained within the grain coarsened zone of the HAZ, and 10 indentations could be accommodated along the leg length (Figures 2.8 and 2.9).

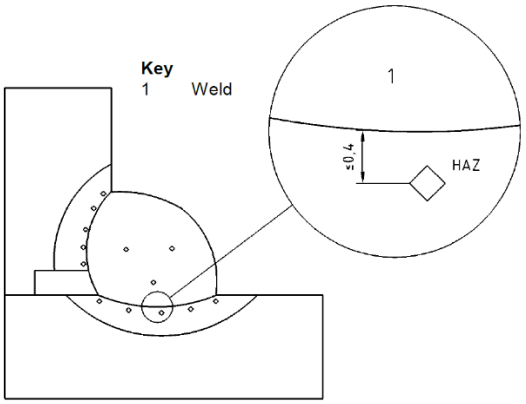

Figure 2.9, Typical positions of hardness test impressions [5]

2.4.2 Bead on Plate Testing (BOP Testing): Automatic GTAW machine was used for Bead on Plate (BOP) Test as per BS 7363:1990 standard requirement [6]. The thicknesses used for this test were 32 mm for Steel L and 30 mm for Steel H. The sole purpose of this test using the GTAW process was to measure HAZ hardness. The dimension of the test piece was 300mm long and 150mm wide. Minimum preheating temperatures of 100˚C and 150˚C were used for Steel L and Steel H, respectively. Different heat inputs of 1.2, 1.5, 2.0, 2.5, and 3.5 kJ/mm were used for the welding, through the variation of voltage, current, and travel speed. Prior to any welding, the temperature of the test piece was checked using a calibrated surface pyrometer. After welding, the test piece was allowed to cool in still air.

As per BS 7363:1990, the type of test performed was for 'Standardized welding conditions for quality control purpose'. A mechanised autogenous GTAW bead-on-plate weld was made in accordance with the conditions given in Table 2.4 (a-c). The weld length was of minimum 290mm, along the longitudinal centreline of the plate (Figure 2.9).

Table 2.4(a) Heat inputs used for BOP testing.

Base Material	**Thickness (mm)**	**Sample IDs**	**Heat Inputs (kJ/mm)**	**Preheat Temp. (˚C)**
Steel L	32	1GE, 2GE, 3GE, 4GE, 5GE	1.2, 1.5, 2.0, 2.5, 3.5	100
Steel H	30	1GC, 2GC, 3GC, 4GC, 5GC	1.2, 1.5, 2.0, 2.5, 3.5	150

Table 2.4 (b). Calculation of Heat Input** = ((60 x A x V)/S) kJ/mm used for BOP testing.

1.2	1.5	2.0	2.5	3.5
(60 x 125 x 24)/ (1000 x 147) = 1.2	(60 x 150 x 25)/ (1000 x 147) = 1.5	(60 x 110 x 22)/ (1000 x 69) = 2.1	(60 x 125 x 23)/ (1000 x 69) = 2.5	(60 x 110 x 22)/ (1000 x 40) = 3.6

** A is current in ampere, V is voltage in volts, S is travel speed in mm/min

Table 2.4(c) Other common welding parameters that were used in BOP testing:

Electrode / wire AWS Specification	AWS A5.12/A5.12M	*Welding Process*	Gas tungsten arc welding (GTAW)
AWS Classification	EWLa-2	*Polarity*	DCSP
Electrode / wire diameter	2.4mm	*Electrode / wire stick out*	5 mm
Filler wire	Not applicable (autogenous weld)	*Inter-pass Temp. (˚C)*	Not applicable
Baking Treatment	Not applicable	*Post heat treatment*	Not applicable
Shielding gas	75-85% Argon / 15-25% CO2	*Temperature measuring method*	K-type thermocouple
Gas flow rate	11 lit/min		

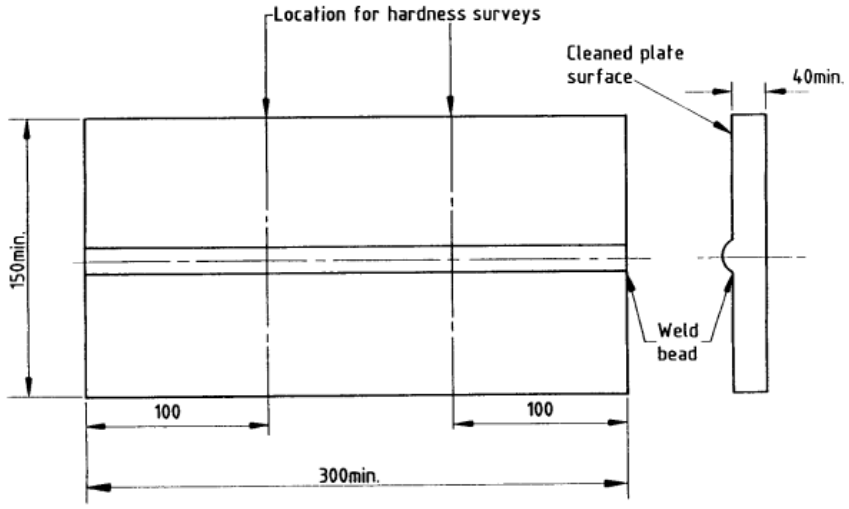

Dimensions are in millimetres.

Weld bead to be full length and within 10 mm of centre of test plate.

Figure 2.10 Test plate details and sectioning for the BOP test [6].

The weld bead was sectioned transversely and polished and etched on the two faces (Figure 2.10) in accordance with *BS EN 1043-1*. 2% Nital was used as the etching agent and it revealed the weld fusion boundary. The prepared faces were subjected to a Vickers

hardness test in accordance with *BS EN ISO 6507* in the positions indicated in Figure 2.11. The testing load of 5 kg was selected so that the hardness indents were located within the grain-coarsened zone of the HAZ, five indentations were made around the bead.

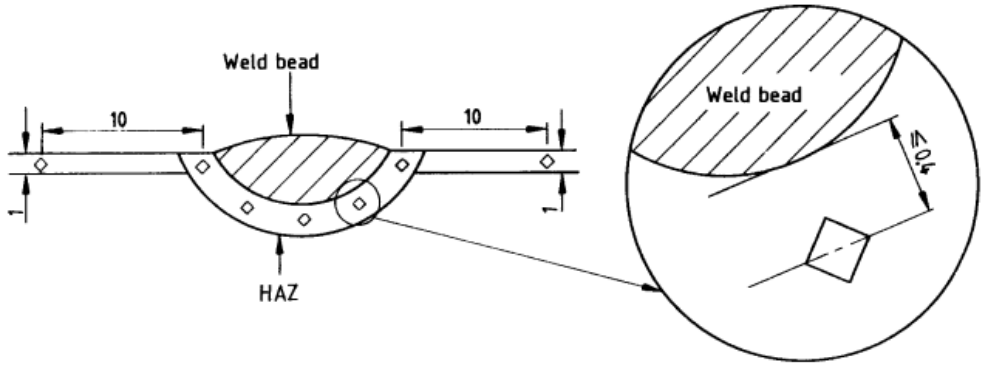

Dimensions are in millimetres.

NOTE The distance of any indentation should be not less than that permitted by BS 427 for the previous indentation

Figure 2.11 Location of hardness indents in the BOP test [6].

2.4.3 K-type grove weld testing (Weld zone toughness assessment): This test is mainly intended for the evaluation of impact properties through weld towards HAZ and base metal. A special double bevel K-type groove joint was prepared for the plates of 32 mm (Steel L) and 30mm (Steel H) thickness according to the design presented in Figure 2.12a,b.

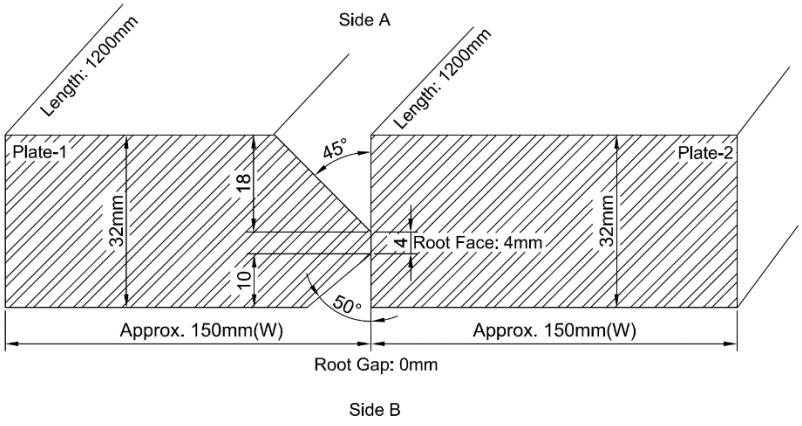

Figure 2.12(a) K-Type Groove weld joint design for Steel L.

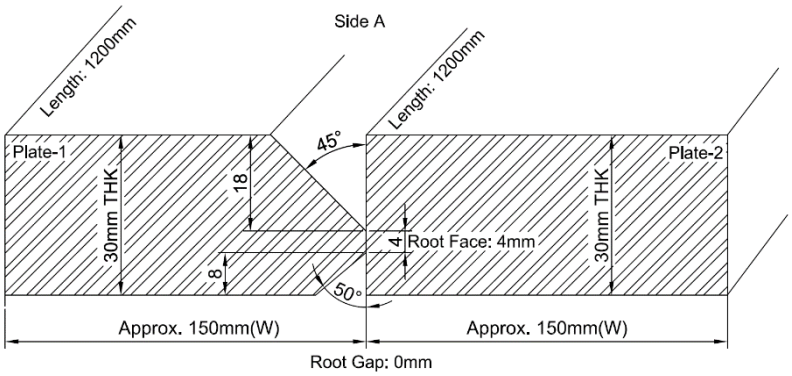

Figure 2.12(b) K-Type Groove weld joint design for Steel H.

Welding parameters were adjusted to maintain the heat input along with the preheat temperature for both types of steel. FCAW with the help of the Automatic Robotic Arm Machine was used for welding various test coupons as per standard testing requirements. Heat inputs used for both steels were 1.2 and 3.5 kJ/mm, while the preheating temperatures were 100 °C for Steel L and 150°C for Steel H. The welds were cut across to prepare Charpy impact samples with the notch position at the weld line, and 2 and 5 mm from the weld line. Optical and scanning electron microscopy (SEM) in the weld cross-section were conducted to characterise the microstructural parameters variation (grain structure and distribution of Ti-rich particles) in the weld cross-section. The following welding parameters were used in this test:

Table 2.5 (a) General welding parameters observed for K-type groove welded joint.

Electrode/ wire AWS Specification	AWS A5.29/A5.29M	*Welding Process*	Flux-cored arc welding (FCAW)
AWS Classification	E91T1-GM (91Ni1-HSR)	*Polarity*	DCRP
Electrode/ wire dia.	1.2mm	*Electrode/wire stick out*	15-25mm
Deposited weld	32mm	*Inter-pass Temp. (˚C)*	Not applicable
Baking Treatment	Not applicable	*Gas flow rate*	18-20 lit/min

Shielding gas	75-85% Argon / 15-25% CO2	*Post heat treatment*	Not applicable
Preheat Temperature	100˚C for Steel L 150˚C for Steel H	*Temperature measuring method*	K-type thermocouple

Table 2.5 (b) Specific welding parameters planned for K-type groove welded joint.

Wire feed speed		amps	volts	Heat Input	Travel Speed		Filler wire diameter
in/min	m/min			kJ/mm	mm/min	mm/sec	mm
200	5	184	18	1.2	165.6	2.76	1.2
400	10	288	29.3	3.5	144.6	2.41	1.2

Table 2.5 (c) Specific welding parameters observed for K-type groove welded joint.

Sample ID	Wire feed speed (m/min)	Travel Speed (mm/s)	Average Current (A)	Average Volts (V)	Average Heat Input (kJ/mm)	No. of Weld layers (top side + bottom side)
For Steel L, 32mm						
1EE+	7.5	4.35	203.4	26.4	1.24	5+7
4EE+2EE	13.9	3.25	315	32	3.1	3+2
For Steel H, 30mm						
3EC+7EC	7.9	4.35	203	26.7	1.25	9+3
2EC+8EC	14	3.25	321	32.1	3.17	4+3

2.5 Hardness Testing

For hardness testing of base metal, weld metal, and HAZ, automatic hardness testing machine Matsuzawa Via-F automatic Vickers hardness tester was used. For base metal testing Australian standard AS 1817-1 [7] was followed, while for welded samples AS 2205.6.1-2003 [56] was used.

2.5.1 Procedure: As per AS 1817-1, a force value of 10 kg was used for experiments. A diamond indenter in the form of a right pyramid with a square base and with a specified angle between opposite faces at the vertex was forced into the surface of a test piece

followed by measurement of the diagonal length of the indentation left in the surface after removal of the test force, F (Figure 2.13).

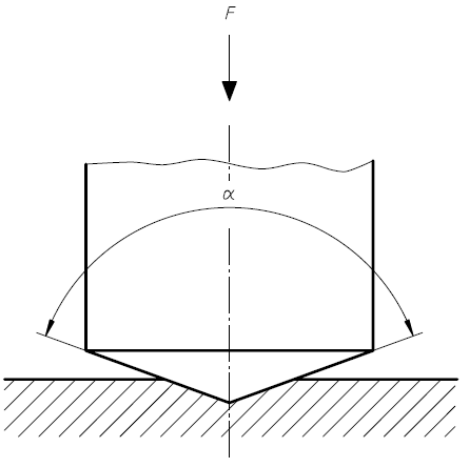

a) Indenter (diamond pyramid)

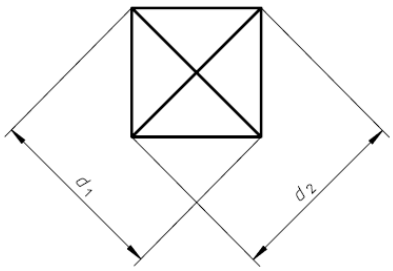

b) Vickers identation

Legend:

Symbol	Designation
α	Angle between the opposite faces at the vertex of the pyramidal indenter (136°)
F	Test force, in newtons
d	Arithmetic mean, in millimeters, of the two diagonals length d_1 and d_2 (see figure 1)
HV	$\text{Vickers hardness} = \text{Constant} \times \frac{\text{Test force}}{\text{Surface area of indentation}}$ $= 0{,}102 \frac{2F \sin\frac{136°}{2}}{d^2} \approx 0{,}189\,1 \frac{F}{d^2}$
NOTE — $\text{Constant} = \frac{1}{g_n} = \frac{1}{9{,}806\,65} \approx 0{,}102$	

Figure 2.13. Principle of hardness test [7].

The test was carried out on a surface that was smooth and even, free from oxide scale, foreign matter, and, in particular, completely free from lubricants. The finish of the surface permitted the accurate determination of the diagonal length of the indentation. Preparation was carried out in such a way that any alteration of the surface hardness, due to heat or cold-working, for example, is minimized. The samples were subjected to grinding and polishing. The test was carried out at an ambient temperature within the limits of 10 °C to 35 °C. The indenter came into contact with the test surface and apply the test force in a direction perpendicular to the surface of the test piece until the applied force attains the specified value of 10Kg. The duration of the test force was 10 s. The distance between the centre of any indentation and the edge of the test piece was at least 2.5 times the mean diagonal length of the indentation.

2.5.2 Sample Preparation and Testing: As per AS 2205.6.1-2003 [8], The test specimens were cut from the weld zone as specified by the relevant application standard using a water jet and abrasive cutting disc. The surface finish of the test specimen was made up to P1200 abrasive quality before hardness testing. Light etching (using 2% Nital) was carried out to reveal the weld zone and to allow hardness indentations to be properly positioned. The hardness was measured by means of the Vickers hardness test (HV5). The locations of hardness test traverses are shown in Figure 2.14.

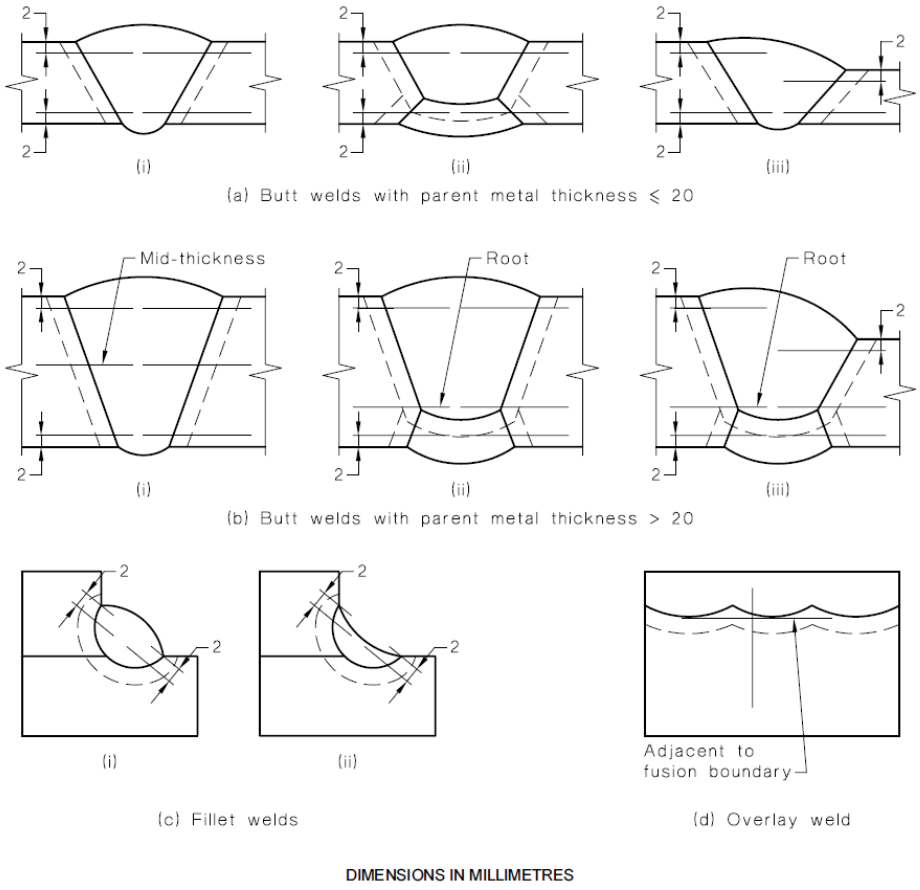

Figure 2.14 Locations of hardness traverses [8].

2.6 Charpy Impact Testing

Charpy Impact testing of the base metal, weld, and HAZ were carried out by using the testing machine.

For the base metal, Australian standard AS 1544.2-2003 [9] was used while for the weld and HAZ of welded samples AS 2205.7.1-2003 [10], was used for evaluation.

2.6.1 Procedure: AS 1544.2-2003 standard specifies the conditions for performing the Charpy V-notch impact test on base metals. The striker was hardened steel with an included angle of 30°, the radius of the curvature of the striking edge was 2 mm to 2.5 mm and the max width of the striker was 18 mm. Standard 10 x 10 x 55 mm Charpy specimens with V-notch angle of 45°, 2 mm depth, and 0.25 mm root radius were used for the impact testing. (Figure 2.15).

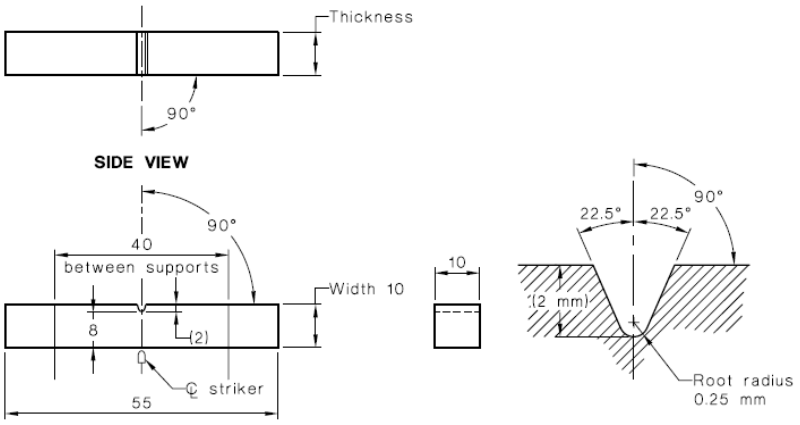

Figure 2.15 Scheme of a standard Charpy impact test sample [9].

Testing was carried out at different temperatures of -70˚C, -40˚C, -10˚C and room temperature (~23˚C). The test pieces were brought to the specified test temperature by immersion in a continuously agitated liquid bath containing a mixture of ethylene glycol and ethanol. The period of immersion of the test piece in the bath was about 30 minutes. At least three samples were tested at each test temperature. Based on obtained results a ductile to brittle transition curve was plotted [9].

2.6.2 Sample Preparation and Testing: As per AS 2205.7.1 – 2003, the shape, dimensions, and method of preparation of the test specimens were in accordance with AS/NZS 1544.2. The test specimens were etched to distinguish between the different zones of the weld metal. The test specimen was located in such a way that the V-notch occurred in the heat-affected zone and weld fusion zone (Figure 2.16). Thus, the notch was at the fusion boundary, at 2 mm from the fusion boundary, and 5 mm from the fusion boundary. Minimum three samples were tested for each of these three locations [10].

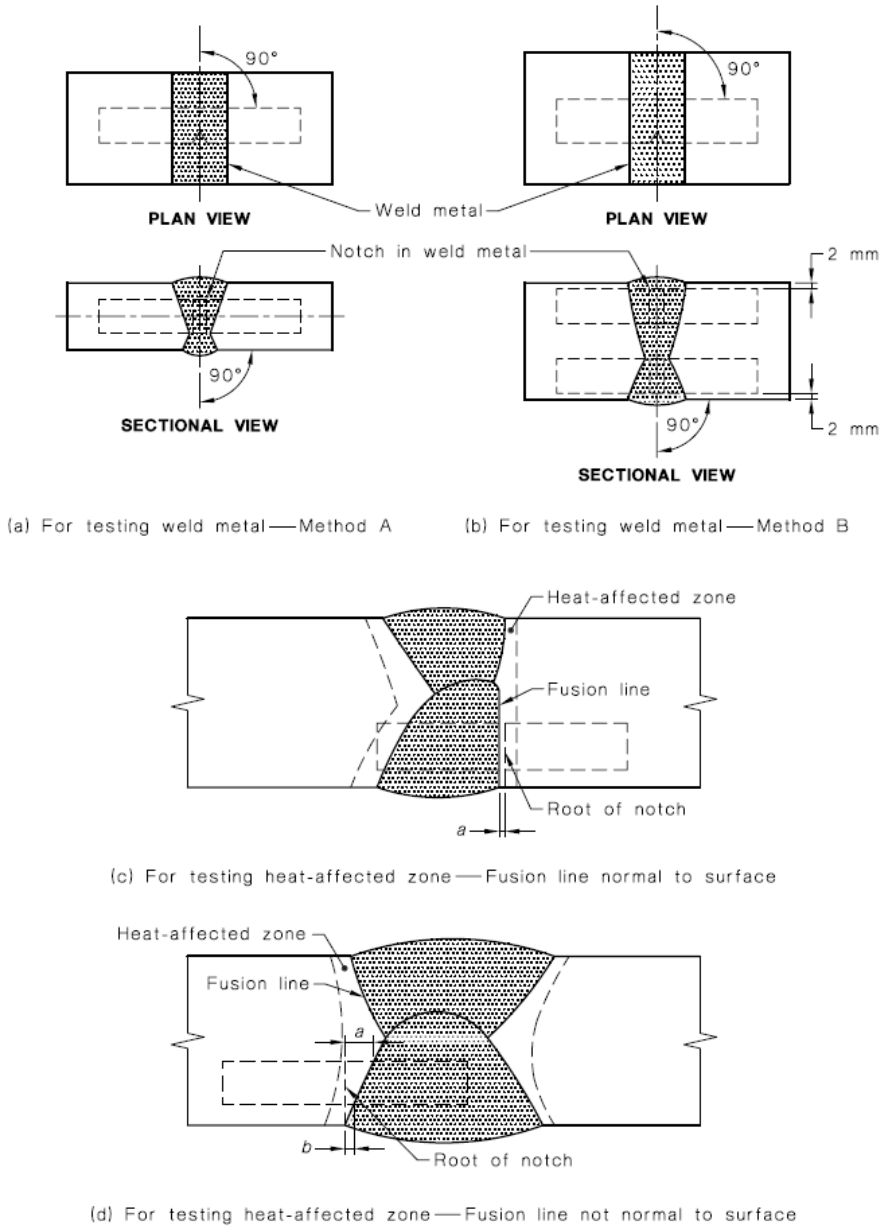

Figure 2.16 Location of Charpy impact test specimens at HAZ and the weld fusion zone [10].

Based on four test temperatures, -70˚C, -40˚C, -10˚C and room temperature (~23˚C), a transition curve was drawn.

2.7 Tensile Testing

Tensile testing was carried out at the UOW laboratories using INSTRON Universal Testing Machine (Model: 8033) with 500 kN maximum load capacity. The tensile specimens were taken from the base material of both thicknesses and both steel grades along the rolling direction and across the rolling direction. The plate thicknesses of 32 mm for Steel L and 30 mm for Steel H were reduced to 20 mm due to the maximum load

limit of the testing machine. The tests were conducted at ambient temperature. For base metal testing, Australian standard AS 1391-2007 [11] was followed.

2.7.1 Testing Procedure: AS 1391 standard specifies methods by which a test piece of metal is strained in uni-axial tension at room temperature to determine one or more of its tensile properties. For all thicknesses of both grades, rectangular samples were machined according to the tolerance requirements (Figure 2.17 and Table 2.6). The gauge length was marked on the specimens' surface, and the elongation was monitored using a video camera [11].

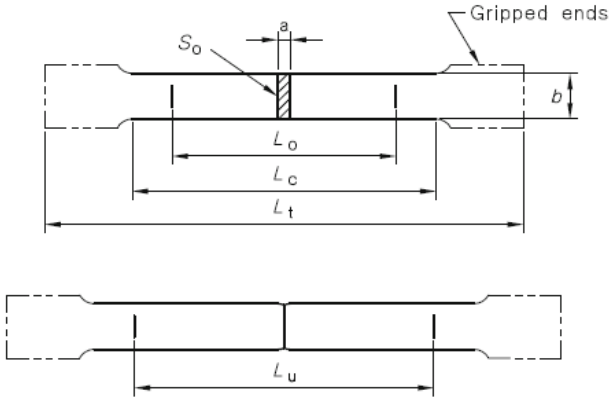

Figure 2.17 AS 1391, Rectangular tensile test sample [11].

Table 2.6 AS 1391, Appendix C (table C2)* [11].

RECTANGULAR TEST PIECE DIMENSIONS

1	2	3	4	5	6
Width b	Maximum variation of width within the parallel length of a test piece	Original gauge length L_o	Minimum parallel length $L_c = L_o + 0.5b$	Minimum free length between grips $L_o + b$	Minimum transition radius r
40 ±2	0.2	200 ±4	220	240	20
20 ±1	0.1	200 ±4	210	220	20
20 ±1	0.1	80 ±1.6	90	100	20
12.5 ±1	0.06	50 ±1	57	62.5	12

* All dimensions are given in mm.

2.8 Bend Testing:

The bend test is a simple and inexpensive qualitative test that can be used to evaluate both the ductility and soundness of a material. Bend testing was performed for all of the available thicknesses of both grades for the base metal. Test samples were taken from base metal plates along and across the rolling direction. Bend testing was performed at the BlueScope facility with the help of a machine capacity of 1000KN with respect to

force application. For base metal testing, Australian standard ASTM E290-2014 was followed.

2.8.1 Testing Procedure: ASTM E290-2014 standard test methods cover bend testing for ductility of materials. Rectangular samples were cut using the water jet cutting method and machined to the final size as required by the standard. The procedure adopted was Guided-Bend Test. It was made by supporting the specimen on pins near each end and applying a force through a pin midway between two supports, as shown schematically in Figure 2.18 until the desired bend was formed. No force was applied directly to the outer face of the bend.

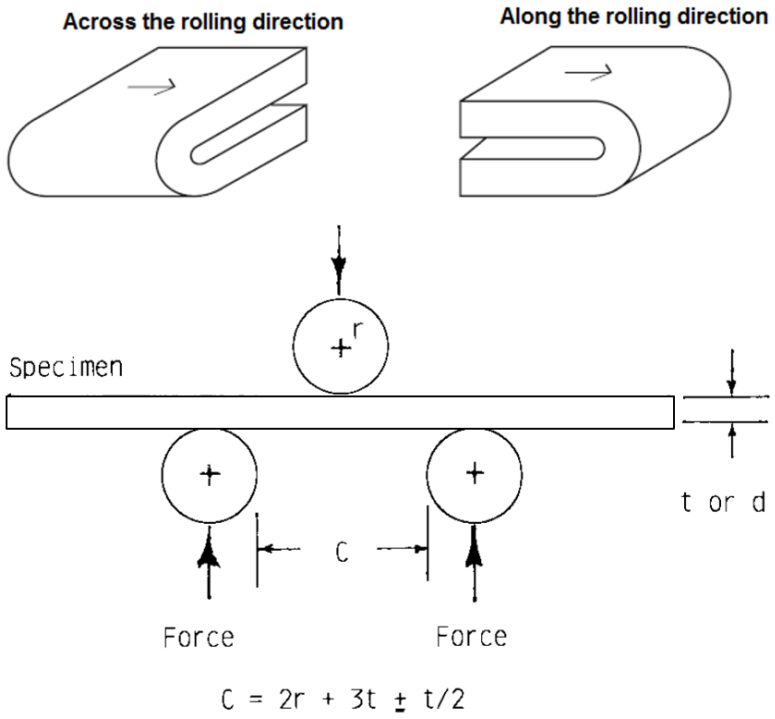

Figure 2.18, Selection of Bend test Samples [12]

Legend:

C: distance between lower supports

r: radius of the pin

t: sheet specimen thickness

d: round specimen diameter

w: Plate specimen width

Note: All the dimensions are in ‘mm’.

The length of the specimen was made such as to perform bend on the machine using different mandrel of the required diameter. For 12mm thickness, it was 350mm while for 32/30mm thickness, the length was 450mm and the final thickness was reduced to 20mm to satisfy the limitation of machine capability. The edges of all samples were rounded up to 3mm maximum to avoid sharp edges as per standard requirements. The width of samples was taken 30mm. The force was removed and examined the external bent portion of the test piece for cracks. The results were recorded accordingly for all thicknesses of both grades.

2.9 Optical Emission Spectroscopy (OES)

An optical emission spectroscope was used to determine the chemical composition of both steel grades. Optical emission spectrometry involves applying electrical energy in the form of spark generated between an electrode and a metal sample, whereby the vaporized atoms are brought to a high energy state within a so-called “discharge plasma”. These excited atoms and ions in the discharge plasma create a unique emission spectrum specific to each element. Thus, a single element generates numerous characteristic spectral lines. This entire plasma light is split by a diffraction grating to extract the emission spectra for the target elements. The intensity of each emission spectrum depends on the concentration of the element in the sample. Detectors (photomultiplier tubes) measure the presence or absence of the spectrum extracted for each element and the intensity of the spectrum to perform qualitative and quantitative analysis of the elements. The terms "optical emission spectrometry" and "photoelectric optical emission spectrometry," however, generally refer to optical emission spectrometry using spark discharge, direct-current arc discharge, or glow discharge for generating the excitation discharge. Shimadzu optical emission spectrometer, used in this work, features Pulse Distribution Analysis (PDA) to enhance the measurement reproducibility (accuracy). This method involves statistical processing of the spark pulse-generated emission spectra obtained from spark discharges in an argon atmosphere. The optical emission spectrometer offers a rapid elemental analysis of solid metal samples, making it indispensable for quality control in steel making and aluminium metallurgy processes [13].

2.10 Characterisation of Microstructure

2.10.1 Sample Preparation: Samples for microstructural characterisation were prepared using standard metallographic techniques: cutting, mounting, grinding, polishing, and etching [14].

The sample cutting was carried out using an abrasive cutting machine of model *"Allied High Tech Powercut 10"*. All the samples were mounted in poly-fast and ground with silicon carbide papers, beginning with 180 grit and finishing with 1200 grit. The samples were then polished with 9 µm, 6 µm, 3 µm, and 1 µm diamond suspensions. The machine used for grinding and polishing was of model *"Allied Tech Metprep4"*. Samples were etched with 2% Nital solution.

2.10.2 Optical Microscopy: Optical microscopy entails the examination of materials using visible light to provide a magnified image of the micro-and macrostructure and is used to characterize structure by revealing grain boundaries, phase boundaries, inclusion distribution, and evidence of mechanical deformation [15].

The polished and etched samples were examined using a *"Nikon Eclipse LV100NDA"* optical microscope equipped with a digital camera. Microstructural studies were conducted at a magnification of x500 for all samples. For the determination of coarse Ti-rich particle size distributions and number density values, 200 - 300 particles were measured for each test condition. The details will be discussed in the next chapters.

2.10.3 Scanning Electron Microscopy: In scanning electron microscopy (SEM), the surface of a specimen is bombarded with a beam of electrons to provide surface topography information. Thus in addition to optical microscopy, SEM can reveal finer microstructural features (such as phase morphology, some grain boundary characteristics, particles of microalloying elements), characteristics of fracture surfaces, and corrosion products. Elemental microanalysis can also be performed [15].

After optical microscopy, the samples were subjected to scanning electron microscopy to investigate the variation in Ti-rich and cementite (Fe_3C) particle size distributions due to thermal cutting and welding. SEM was carried out using a JEOL 7001F Field Emission Gun (FEG) microscope operating at a voltage of 15 keV and a probe current of 8nA. Energy Dispersive X-ray Spectroscopy (EDS) of Ti-rich particles was carried out using Oxford SEM-EDS systems and Aztech software.

References (Chapter 2)

1. https://www.totalsteel.com.au/assets/files/technical/lincoln-tib-125.pdf accessed on 09-03-2018.
2. https://industeel.arcelormittal.com/wp-content/uploads/2018/06/CREUSABRO-Dual-GB.pdf accessed on 15-03-2018
3. https://www.totalsteel.com.au/assets/files/brochures/jfe-ehsp-catalogue.pdf accessed on 15-03-2018.
4. F. Bouchaud, N. Aichoun, J. Mauguin, S. Corre, *New Wear Resistant Steel Creusabro Dual*, Proceedings: International Symposium on the Recent Developments in Plate Steels, Winter Park, Colo., USA, Association for Iron & Steel Technology (AIST), (2011) 93-101
5. ISO 17642-2:2005, *Destructive tests on welds in metallic materials- Cold cracking tests for weldments- Arc welding processes*, part 2: Self-restraint tests, (2005) 3-9.
6. BS 7363-1990, *Method for bead-on-plate (BOP) test for welds*, (1990) 7-11.
7. AS 1817.1-2003, *Metallic materials-Vickers Hardness Test*, Method 1: Test Method (ISO 6507-1:1997, MOD), (2003) 1-6.
8. AS 2205.6.1-2003 *(Method for destructive testing of welds in metal, Method 6.1: Weld joint hardness test)*, (2003) 1-5.
9. AS 1544.2-2003, *(Method for impact tests on metals)*, Part-2 Charpy V-notch, (2003) 5-17.
10. AS 2205.7.1 – 2003 *(Methods for destructive testing of welds in metal, Method 7.1: Charpy V-notch impact fracture toughness test*), (2003) 1-4.
11. AS 1391 *(Metallic materials-Tensile testing at ambient temperature)*, (2007) 1-34.
12. ASTM E290-2014, *Standard test Methods for Bend Testing of Material for Ductility*, 03.01 (2014) 1-10.
13. https://www.shimadzu.com/an/products/elemental-analysis/oes-app/principle-of-optical-emission-spectrometry/index.html accessed on 25-03-2018.
14. https://www.asminternational.org/documents/10192/3447544/06958G_Chapter_4.pdf/a6cda448-291f-491b-bf6f-456322c4e386 accessed on 25-03-2018.

15 ASM Handbook, *Materials Characterization*, Optical Metallography, 10 (2019) 511-527, 543-575.

Chapter 3

3 Effect of C and Ti contents on microstructure and mechanical properties of as-received Ti-microalloyed steels

3.1 Introduction

Required mechanical properties can be achieved by controlling the chemical composition and microstructure of steel, particularly additions of microalloying elements. Improved strength and toughness in microalloyed steels originate from high-temperature precipitation (leading to retardation of austenite grain growth and grain refinement), low-temperature precipitation (leading to strengthening via dislocation immobilisation), dislocation strengthening (particles are known to stimulate dislocation generation), and some phase balance strengthening (minor concentrations of microalloying elements, such as Cr, Mo, Nb, enhance bainite transformation)[1-5]. In addition to composition, process control is also extremely important [8]. Elements such as C, Mn, Si, Ni, B helps in the solid solution strengthening of steels. Mn also increases hardenability, i.e., facilitates bainite/martensite transformation. Similar to Mn, Mo enhances hardenability. Mo and Cr facilitate a solid solution and precipitation hardening and help to increase the solubility of Ti and Nb in austenite, resulting in finer Ti- and Nb-rich particles of a higher number density and stronger precipitation strengthening effect [15-26]. However, those microalloying elements which can combine with C and N and form carbonitride particles are the most important [6]. Q&T steels have higher C contents due to their effect on solid solution strengthening of martensite. Also, coarse carbides would be more stable against dissolution during heat treatment above 900˚C [7]. It was found that the hardness of carbon steels with 0.01-0.02 V increased after tempering at 600°C. The change in strength follows the same pattern as hardness. Microalloying with 0.04 V increases both the YS and TS of Q & T steel by 98 to 147 MPa, respectively. In low C steels, V addition less than 0.1 wt.% increased YS by 35 MPa both in hot rolled and normalized conditions. Although in medium C steels the effect of V addition was stronger, 0.03-0.06 V increased strength by 49-98 MPa. Strengthening is associated with the precipitation of finely dispersed V carbides, additional strengthening is achieved by normalizing [11].

With increasing amounts of Ti, the strengthening of hot rolled products should increase due to precipitation strengthening and grain refinement. For heavy gauge plates, Ti is the most effective in combination with N. A great advantage of Ti is in sulphide shape control. For thermo-mechanically treated steels containing Ti, the yield strength increase due to Ti is complex, because Ti has a high affinity for N to form TiN in liquid steel these particles may facilitate grain refinement; however, TiN may initiate fracture and a reduced N concentration in the matrix decreases the solid solution strengthening effect. Mincher [12] discussed the production of 345(0.09%Ti) and 550(0.22%Ti) YS, Ti treated, low carbon hot rolled steels where Ti was used for both inclusion shape control and precipitation hardening. YS is dependent on Ti content and Ti/C ratio. A peak YS is reached at a Ti/C ratio of about 3.1. Xu et al. [13] found that the yield strength of 0.2C-1.5Mn martensitic steel can be improved by adding Ti, which is associated with precipitation hardening due to the formation of TiC precipitates in the martensite matrix. Yang et al. [14] studied the influence of vanadium precipitation behaviour in a low alloy 0.26C-1.1Mn-0.5Si-0.28V-0.02Ti-0.002 N martensitic steel during the reheating and full austenitisation process. They have found that as the austenitisation temperature increased, the prior nano-sized (Ti, V) C particles coarsened and their volume fraction decreased, which led to increased austenite grain size.

This chapter discusses the effects of steel composition, in particular, C and Ti contents, on microstructure and mechanical properties of as-received hot rolled and heat-treated wear-resistant steel plates. The specimens were taken from all four plates to perform chemical analysis, optical and scanning electron microscopy, and mechanical testing, including tensile, hardness, and Charpy impact testing. The results will be compared with the data available for conventional wear-resistant steel grade containing 0.16C-0.2Cr-0.2Mo wt.%.

3.2 Results

3.2.1 Chemical compositions

Table 3.1 shows the compositions of Steel L and Steel H measured in this work. Table 3.2 shows the composition of Ti-free wear-resistant steel.

Table 3.1 Chemical composition of Steel L and Steel H.

Material Grade	Thickness (mm)	C	Mn	Si	Ni	Cr	Mo	Cu	Al	Ti	V
Steel L	**12**	**0.27**	**0.71**	**0.37**	**0.022**	**0.85**	**0.24**	**0.014**	**0.046**	**0.40**	**0.012**
Steel L	**32**	**0.28**	**0.70**	**0.37**	**0.023**	**0.84**	**0.25**	**0.016**	**0.045**	**0.43**	**0.01**
Steel H	**12**	**0.39**	**1.28**	**0.83**	**0.46**	**0.68**	**0.33**	**0.24**	**0.063**	**0.60**	**0.01**
Steel H	**30**	**0.37**	**1.26**	**0.80**	**0.46**	**0.67**	**0.32**	**0.22**	**0.051**	**0.56**	**<0.003**

Table 3.2 Nominal chemical composition of conventional wear-resistant steel [32].

Material Grade	C	Mn	Si	Cr	Mo	P	S	B	CE (IIW)	Pcm
0.16C-0.2Cr-0.2Mo *Thickness 6-100mm*	**0.29**	**0.30**	**0.30**	**1.00**	**0.25**	**0.015**	**0.003**	**0.001**	**0.61**	**0.40**

3.2.2 Microstructure

Both steels exhibited coarse (<10 μm in Steel L and <20 μm in Steel H) Ti-rich particles (Figure 3.1) and martensitic microstructures (Figure 3.2).

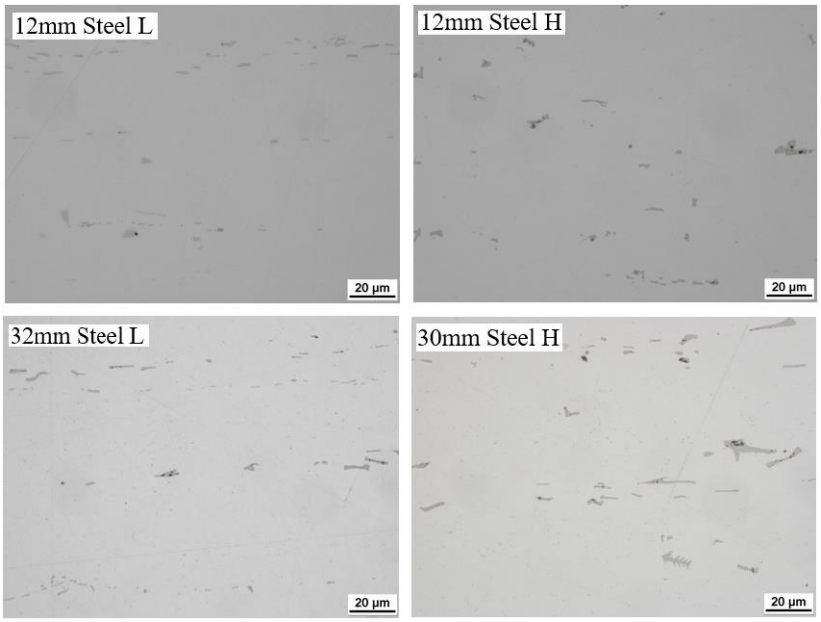

Figure 3.1 Optical images of un-etched microstructures in Steel L and Steel H.

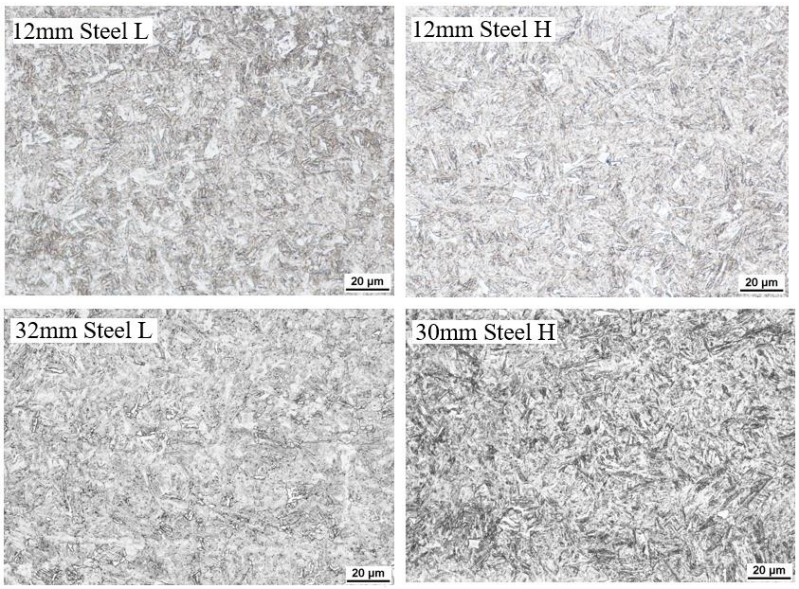

Figure 3.2 Optical images of etched microstructures in Steel L and Steel H.

Many particles were of irregular, triangular or rectangular shape, although some of them were elongated along the rolling direction. These particles precipitated at the grain boundaries as well as in the grain interior. Steel L, having low carbon and titanium contents, showed finer precipitation compared to Steel H with higher contents of carbon and titanium. Obviously, higher C and Ti contents gave rise to the formation of larger volume fraction and number density of carbonitrides (Figure 3.3 and 3.4). No major difference in particle parameters with plate thickness was observed. EDS analysis revealed the coarse particles to be TiMoVCN in both steels of both thicknesses, although N concentration seemed to be higher in larger particles and Mo concentration was higher in smaller particles. This is in line with TiN showing a higher precipitation temperature compared to Mo_2C or VC.

Given higher densities of TiMoVCN particles in Steel H, compared to Steel L, it showed higher hardness (Figure 3.5). The particle size distribution and number density are known to affect the degree of hardening and strengthening [28]. Steel H showed higher hardness and strength values, compared to Steel L, which implies that it had particles that are bigger in size and higher in volume fraction. Chen, Guo, and Shang suggested that the high hardness of these steels is associated with the high dislocation density present after quenching and tempering [27]. These dislocations appear following local straining during austenite-to-martensite phase transformation, originating from the phase volume

variation. Dislocation pile-ups at grain boundaries during deformation may provide further strengthening.

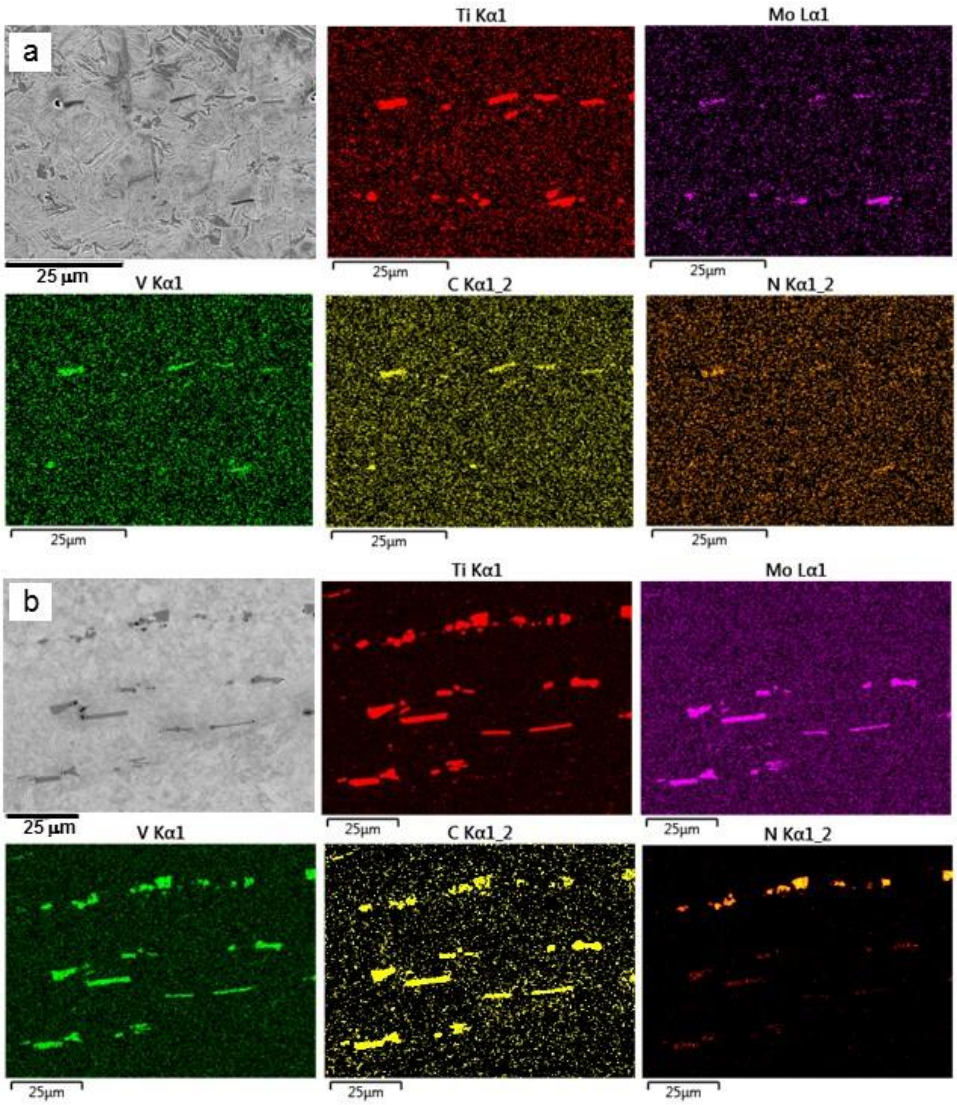

Figure 3.3 SEM images of coarse carbide particles in (a) 12 mm Steel L and (b) 12 mm Steel H.

The key forms of titanium precipitates are TiN, $Ti_4C_2S_2$, and TiC or Ti(C, N) complex particles, among which TiC have the most important effect on steel strength because of their smaller size and higher density. The precipitation temperatures for TiN, $Ti_4C_2S_2$, and TiC particles are above 1500°C, 1200°C, and 1000°C, respectively. Thus, TiN and Ti4C2S2 particles may easily grow to larger sizes. From the SEM analyses, it was found here that TiN and some $Ti_4C_2S_2$ were larger than pure TiC particles, which is consistent with the results given by Zhou et al. [30] and Soto et al [29]. Also, TiN particles are normally cuboidal in shape, while TiC particles are spherical. Thus, TiC is favourable for toughness, as they generate lower stress concentrations [31].

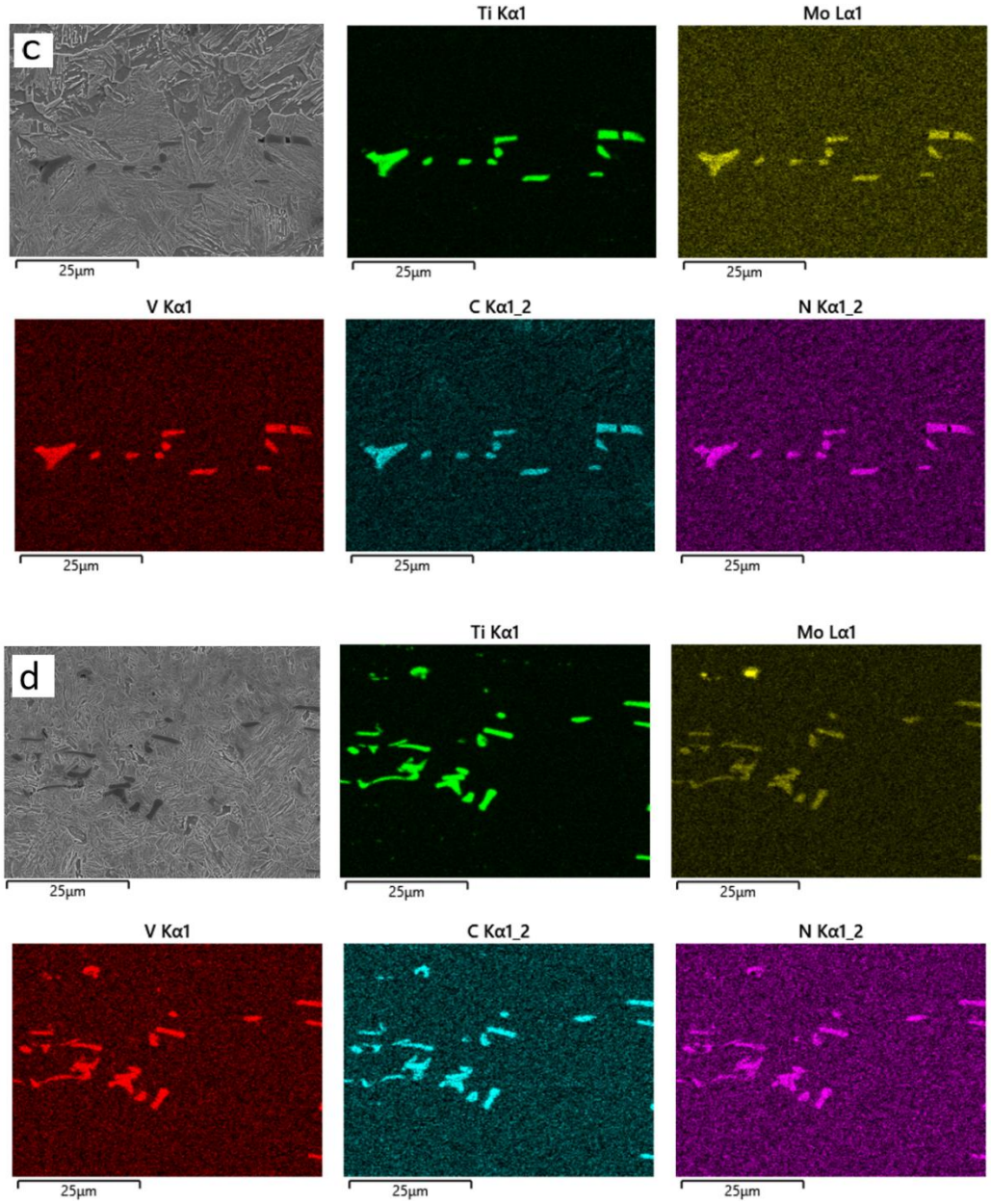

Figure 3.4 SEM images of coarse carbide particles in (c) 32 mm Steel L and (d) 30 mm Steel H.

3.2.3 Mechanical properties

Figure 3.5 shows results of hardness testing for Steel L (*Thickness* 12mm and 32mm) and Steel H (*Thickness* 12mm and 30mm). A variation in hardness through-thickness was observed for 32/30 mm plates.

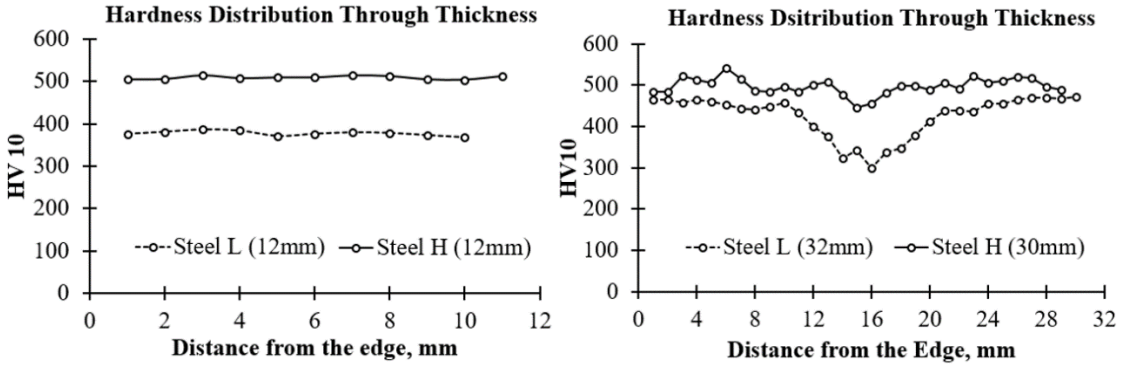

Figure 3.5 Hardness distribution through-thickness for Steel L and Steel H.

For the 12 mm plate thickness of Steel L, the average hardness value was 377.5 HV with a maximum 387 HV and minimum of 368 HV, in comparison to those values for 12 mm thickness of Steel H being 509, 515, and 504 HV, respectively. Although Steel H showed high hardness, compared to Steel L, the values were uniform through the plate thickness for both steel grades. On the other hand, for the 32 mm thickness of Steel L, hardness varied from a minimum of 298 HV at the plate middle thickness, to the maximum of 473 HV at the sub-surface. A difference in hardness of 174 HV (37 %) is evident for Steel L. A similar qualitative but the lower quantitative difference in hardness was observed for Steel H. The minimum hardness at the middle thickness was 445 HV while the maximum was 541 HV at the sub-surfaces, this gave 96 HV (18 %). However, the average hardness value for Steel H (498 HV) was still 72 HV (14 %) higher than this for Steel L (426 HV). The results obviously indicate that high contents of microalloying elements like C and Ti (Table 3.1) in Steel H resulted in higher hardness through the plate thickness. The hardness in studied Ti-microalloyed Q&T steels was lower than 545 HV observed for a 0.16C-0.2Cr-0.2Mo grade [32], despite higher C content in the studied steels. This could be explained if in our Ti-steels the C and N concentrations in the matrix were lower than in the conventional steel, due to the formation of coarse Ti-rich carbonitrides, leading to lower solid solution strengthening.

Tables 3.3 and 3.4 illustrate the tensile properties of Steel L and Steel H.

Table 3.3 Tensile properties of Steel L and Steel H for the 12 mm plate thickness.

Steel Grade / Thickness	Sample ID	Tensile Strength (MPa)	Yield stress (MPa)	Elongation (%)	Orientation of Samples
Steel L / 12mm	1C*E	1538	1244	10%	across the rolling direction
	2C*E	1532	1234	9%	
	1C**E	1545	1194 (lower YS) 1216 (upper YS)	7%	along the rolling direction
	2C**E	1551	1215	7%	
Steel H / 12mm	1C*C	1727	1489	6%	across the rolling direction
	2C*C	1708	1165	6%	
	1C**C	1720	1159	5%	along the rolling direction
	2C**C	1742	1199	5%	

Table 3.4 Tensile properties of Steel L and Steel H for the 32/30mm plate thickness.

Steel Grade / Thickness	Sample ID	Tensile Strength (MPa)	Yield stress YS (MPa)	Elongation, %	Orientation of Samples
Steel L / 32mm	1C*E	1351	952	7.2	across the rolling direction
	2C*E	1313	953	6.9	
	1C**E	1354	952	7.8	along the rolling direction
	2C**E	1365	955	9.4	
Steel H / 30mm	1C*C	1698	1540	8%	across the rolling direction
	2C*C	1688	1547	6.4%	
	1C**C	1682	1542	8.4%	along the rolling direction
	2C**C	1708	1544	8.6%	

The 12 mm Steel H samples showed 11-12 % higher tensile strength but lower elongation, compared to this of 12 mm Steel L samples. Both steels demonstrated a slightly higher tensile strength and lower elongation along the rolling direction.

The 32 mm Steel H samples showed 26-28 % higher tensile strength, 62 % higher yield stress, and similar elongation, compared to 32 mm Steel L samples. Steel L exhibited a slightly higher tensile strength along the rolling direction, although for Steel H no significant difference was observed. The discrepancies in tensile properties with test direction may be associated with the chemical inhomogeneity, leading to the microstructure banding and particle alignment in the rolling direction, which is outside of the current project scope. However, it is worth noting a larger variation in tensile properties with steel composition for 30/32 mm thick plates compared to 12 mm thick ones. This indicates a significant effect of processing history on the properties of thicker plates.

Figures 3.6 and 3.7 show the stress-strain curves for the tested steels as shown below:

Legend:

C**E: Steel L along the rolling direction

C*E: Steel L across the rolling direction

C**C: Steel H along the rolling direction

C*C: Steel H across the rolling direction

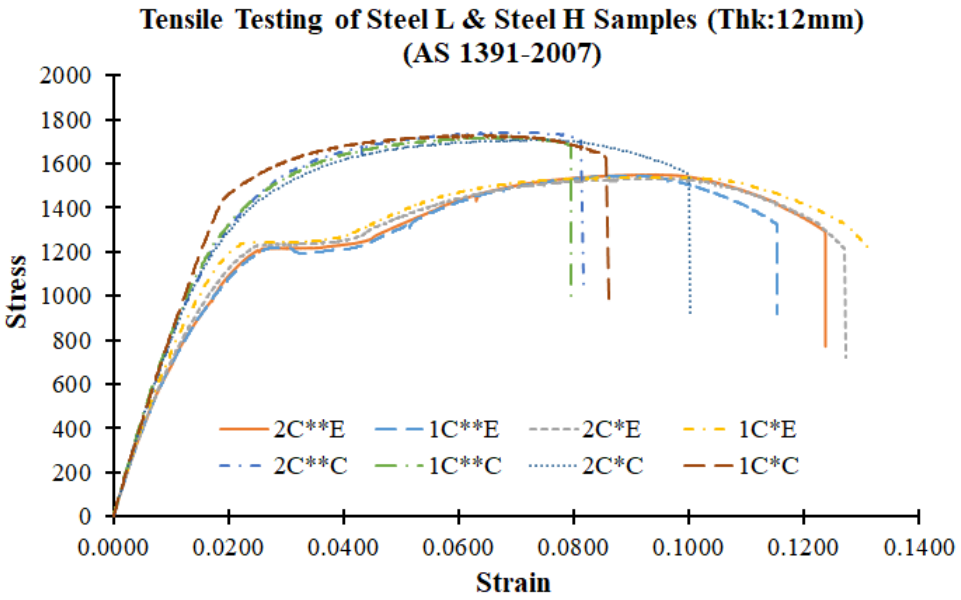

Figure 3.6 Stress-strain curves of Steel L and Steel H (Thickness 12mm).

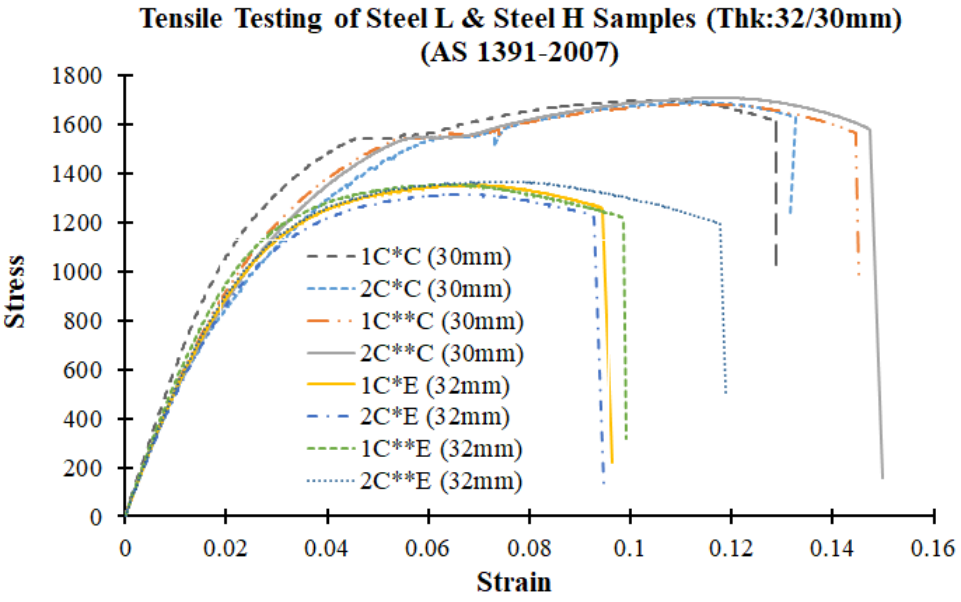

Figure 3.7 Stress-strain curves of Steel L and Steel H (Thickness: 32/30mm).

The 12 mm Steel L samples showed the yielding behaviour, but the 12 mm Steel H samples did not show this, thus0.2% proof stress value was taken as the yield stress. The 32 mm Steel L samples showed no yielding, thus 0.2% proof stress was considered as the yield stress. Whereas the stress-strain curve for the 32 mm Steel H showed a yield point. Samples that showed yielding behaviour (12mm Steel L and 30 mm Steel H) also exhibited a higher elongation to failure.

Tables 3.5 and 3.6 show the results of Charpy impact testing for both steels.

Table 3.5 Charpy impact energy for Steel L and Steel H (Thickness: 12 mm).

Test Temperature, (˚C)	-70	-40	-10	RT*	+50	Steel Grade/ Thickness/ ID**
Absorbed Energy, (J) (average value of 3 samples for each test temperature) ± Standard Deviation	16.9 ±1.8	20.2 ±0.6	21.6 ±2.1	26.3 ±1.1	30.2 ±1.2	Steel L/ 12mm/ F**E, (along the rolling direction)
	12.8 ±3.1	14.8 ±1.8	18.2 ±0.8	20.2 ±0.6	20.1 ±1.2	Steel L/ 12mm/ F*E (across the rolling direction)
	12.1 ±1.0	12.7 ±0.2	13.4 ±0.8	14.3 ±0.4	14.5 ±1.2	Steel H/ 12mm/ F**C (along the rolling direction)
	15 ±0.7	15.5 ±0.2	15.7 ±0.8	17.6 ±1.1	17.9 ±0.9	Steel H/12mm/ F*C, (across the rolling direction)
Note: RT*: Room Temperature (~23˚C), ID**: Identification						

Table 3.6 Charpy impact energy for Steel L and Steel H (Thickness: 32/30mm).

Test Temperature, (˚C)	-70	-40	-10	RT	Steel Grade/ Thickness/ ID
Absorbed Energy, (J) (average value of 3 samples for each test temperature) ± Standard Deviation	11.4 ±0.5	15.84 ±1.1	16.95 ±0.6	28.68 ±1.4	Steel L/ 32mm/ F**E, (along the rolling direction)
	9.82 ±0.9	10.93 ±1.2	12.19 ±1.1	20.29 ±1.5	Steel L/ 32mm/ F*E (across the rolling direction)
	10.89 ±1.6	14.85 ±2.8	16.33 ±1.4	24.65 ±2.2	Steel H/ 30mm/ F**C (along the rolling direction)
	10.66 ±1.1	10.39 ±2.6	11.19 ±1.6	12.38 ±1.4	Steel H/ 30mm/ F*C, (across the rolling direction)

12 mm Steel L samples showed higher absorbed energy compared with 12 mm Steel H samples. 12 mm Steel L samples showed a higher toughness along the rolling direction, although 12 mm Steel H samples showed a higher toughness across the rolling direction.

32 mm Steel L samples showed almost similar toughness properties compared with those of 30 mm Steel H samples. But, 32 mm Steel L samples showed more impact energy absorbed along the rolling direction in comparison to those that were across the rolling direction. A similar case was observed for Steel H samples. The higher toughness of Steel L corresponds to its higher ductility (Tables 3.3 and 3.4) and can be related to smaller sizes and lower number densities of coarse TiMoVCN particles in Steel L (Figures 3.3 and 3.4).

Ductile to brittle transition curves are presented in Figures 3.8 and 3.9 (legend is mentioned in Tables 3.3 and 3.4). The absolute values of absorbed energy, <30 J for Steel L and <20 for Steel H, were slightly lower compared to for conventional Q&T steels of similar plate thickness, ~35J at +20 °C and ~20J at -40 °C. This could be explained if in the studied steels coarse Ti-rich particles acted as fracture nucleation sites and facilitated crack propagation during impact testing. The absorbed energy obviously decreased with a decrease in temperature; however, no sharp ductile to brittle transition was observed.

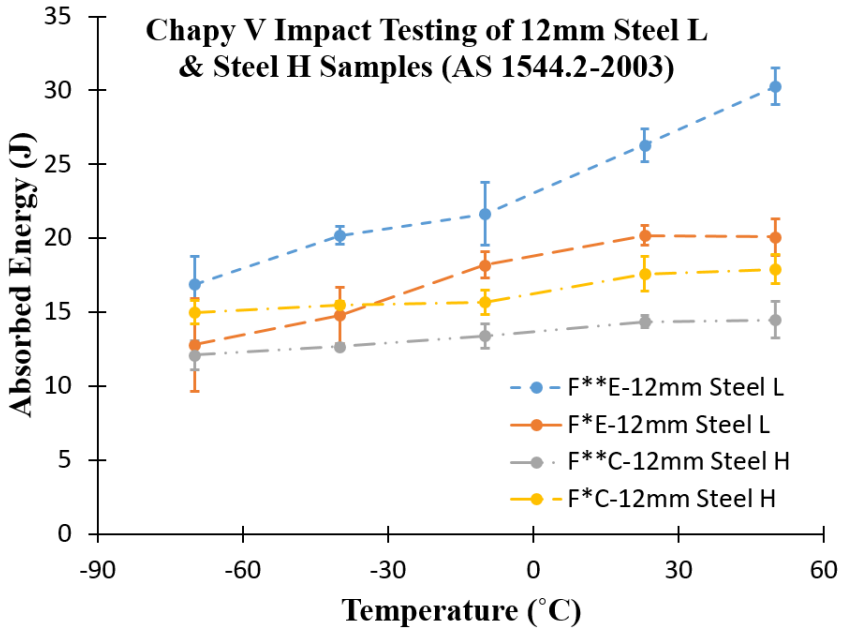

Figure 3.8 Absorbed energy variation with impact testing temperature for Steel L and Steel H (Thickness: 12mm).

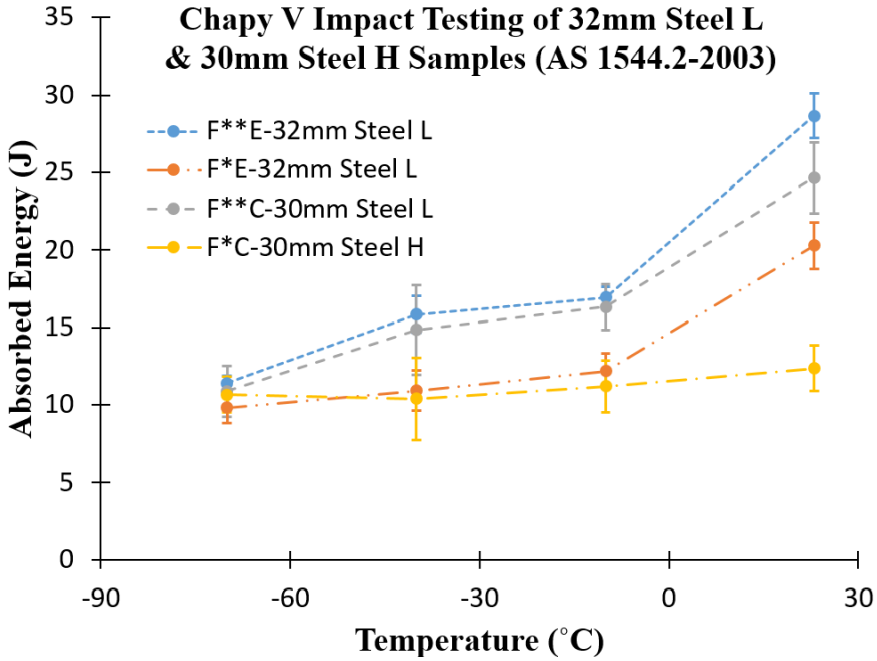

Figure 3.9 Absorbed energy variation with impact testing temperature for Steel L and Steel H (Thickness: 32/30mm).

Table 3.7 shows results of Bend testing of both steels at various radii to reveal the ductility of samples along as well as across the rolling direction.

Fracture surfaces/ morphology were analysed apart from the total energy absorbed, to have additional information. All samples of both steels (Steel L and Steel H) showed typical brittle fracture (Figure 3.10a,b) as per visual inspection carried out. It correlates the finding of absence of sharp ductile to brittle transition curve (Figures 3.8 & 3.9). All the samples failed by cleavage fracture. SEM result showed that cleavage appeared to wind its way through the microstructure and showed broken, cuboidal or angular shaped inclusions at the fracture origins. Typically, fracture faces displayed multiple inclusion-related initiation sites along the crack front. Lower cleavage resistance of these steels may be attributed to microalloy precipitation and martensitic islands. The amount of Ti tied up as TiN inclusions also greatly affect its cleavage resistance and act as initiation sites to cause brittle fracture in microalloyed steels [33].

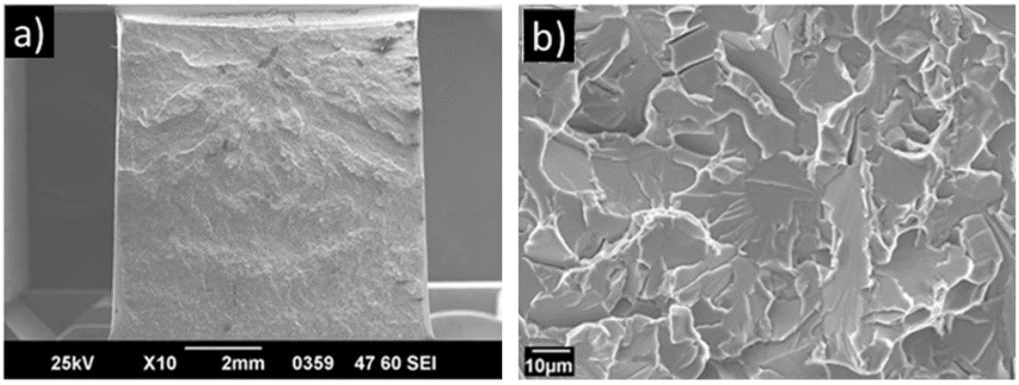

Figure 3.10 Typical SEM fractograph of Steel L and Steel H

Table 3.7 Bend Test for Steel L and Steel H (Thickness: 12mm and 25mm)

Steel Grade/ Thickness, T	Sample ID	Test Direction	Pin Radius	Bend Angle	Test Status
Steel L/ 12mm	1D**E	along the rolling direction	1.5T	90	Fail
	1D*E	across the rolling direction	1.5T	90	Fail
	2D**E	along the rolling direction	2T	90	Pass
	2D*E	across the rolling direction	2T	90	Pass
Steel L/ 25mm	1J**E	along the rolling direction	2T	90	Fail
	1J*E	across the rolling direction	2T	90	Pass
	2J**E	along the rolling direction	3T	90	Pass
	2J*E	across the rolling direction	3T	90	Pass
Steel H/ 12mm	1D**C	along the rolling direction	2T	90	Fail
	1D*C	across the rolling direction	2T	90	Fail
	2D**C	along the rolling direction	3T	90	Fail
	2D*C	across the rolling direction	3T	90	Fail
	3D**C	along the rolling direction	3.5T	90	Fail
	3D*C	across the rolling direction	3.5T	90	Pass
	4D**C	along the rolling direction	4T	90	Pass
	4D*C	across the rolling direction	4T	90	Pass
Steel H/ 25mm	1J**C	along the rolling direction	2T	90	Fail
	1J*C	across the rolling direction	2T	90	Fail
	2J**C	along the rolling direction	3T	90	Pass
	2J*C	across the rolling direction	3T	90	Fail

The thickness of the Steel L and Steel H for their thicknesses of 32mm and 30mm respectively were reduced to 25mm each as per the capacity of the bend testing machine. Steel L 12mm samples passed for 2T bend radius while Steel H 12mm samples passed for 4T. Similarly, for Steel L 25mm, both samples were found passed for 3T bend radius while for Steel H, the sample tested along the rolling direction passed the test for 3T radius but across the rolling direction, failed. These results delineate the behaviour of both steels for their ductility phenomena. Steel L with low hardness (Figure 3.5) showed more ductility than Steel H with high hardness.

Conclusion

- Chemical analysis showed that Steel H exhibited higher contents of C, Ti, Mn, Si, Ni, and Cu compared to Steel L. With respect to this, Steel H exhibited a higher hardness and strength, and lower toughness. Coarse TiMoVCN particles of a higher number density observed in Steel H are believed to contribute to hardness increase and toughness decrease in this steel. The effect of coarse particles on fracture initiation requires further investigation.

- Tensile testing of both types of steels demonstrated typical stress-strain behaviour characteristics for Q&T steels. Steel H showed higher yield stress and tensile strength compared to Steel L, due to higher solid solution and precipitation strengthening associated with higher contents of microalloying elements. Higher Mn, Ni, and Mo concentrations in Steel H had to increase its hardenability, which would decrease the martensite lath width and increase dislocation density, not studied here. Relatively low elongation, measured in the studied Ti-microalloyed Q&T steels to be 5-10 %, is within the low range of values observed in conventional steels with martensitic microstructures. Therefore, the low ductility of these steels should be taken into account in the design of fabrication technologies, particularly cutting and welding.

- Charpy impact testing of both types of steel showed a higher toughness for Steel L compared to Steel H, which is in line with a lower strength of Steel L. No sharp transition from ductile to brittle behaviour was observed for any type of steel either along or across the rolling direction. This is supported with low absorbed energies determined with impact testing. The energies were in the range of 9-30 J in the test temperature range of -70…+50 °C.

- The bend test results of both steels have been found in line with the hardness differentials (Figure 3.5). The lower hardness Steel L samples achieved a tighter bend radius than the harder Steel H samples.

- Optical and SEM/EDS analysis revealed the presence of coarse (<10 μm in Steel L and <20 μm in Steel H) TiMoVCN particles with N concentration seemed to be higher in larger particles and Mo concentration being higher in smaller particles. Many particles were elongated along the rolling direction, this indicates their high precipitation temperature corresponding to increased contents of microalloying elements.

References (Chapter 3)

1. B. Dutta and C. M. Sellars, Mater. Sci. Technol., 3 (1987) 197–206.
2. O. Kwon, A. J. DeArdo, Acta Metall. Mater., 39 (4) (1991) 529–38.
3. T. Gladman, *The Physical Metallurgy of Microalloyed Steels*, The Institute of Materials, Cambridge University Press, Cambridge, (1) (1997).
4. R.W. Cahn: Physical Metallurgy, North-Holland Publishing, Amsterdam, 1970.
5. F.C. Frank and W.T. Read: Phys. Rev. Lett., 79 (1950) 722–23.
6. M. Cohen, W. S. Owen, *Thermo-mechanical processing of microalloyed steels*, Microalloying 75: Proceedings of an International Symposium on High-strength, Low-alloy Steels, Washington, D.C., U.S.A, (1975) 3.
7. F. B. Pickering, High-Strength, *Low-Alloy Steels- A decade of Progress*, Microalloying 75: Proceedings of an International Symposium on High-strength, Low-alloy Steels, Washington, D.C., U.S.A, (1975) 24.
8. T. Gladman, D. Dulieu, I. D. McIvor, *Structure-Property Relationships in High-Strength Microalloyed Steels*, Microalloying 75: Proceedings of an International Symposium on High-strength, Low-alloy Steels, Washington, D.C., U.S.A, (1975) 32-54.
9. M. W. Lui, I. L. May, *Influence of Carbides in Strengthening Microalloyed Steels*, Microalloying 75: Proceedings of an International Symposium on High-strength, Low-alloy Steels, Washington, D.C., U.S.A, (1975) 55.
10. L. Meyer, F. Heisterkamp, W. Mueschenborn, *Columbium, Titanium, and Vanadium in Normalized, Thermo-Mechanically Treated and Cold-Rolled Steels*, Microalloying 75: Proceedings of an International Symposium on High-strength, Low-alloy Steels, Washington, D.C., U.S.A, (1975) 159-163.
11. N. N. Vlasov, *Microalloying of Carbon Steels with Vanadium and Cobalt*, Microalloying 75: Proceedings of an International Symposium on High-strength, Low-alloy Steels, Washington, D.C., U.S.A, (1975) 188-190.
12. A. L. Mincher, R. A. Bosch, R. P. Morgan, *Commercial Production of High-Strength, Titanium-Bearing Hot-Rolled Steel*, Microalloying 75: Proceedings of an International Symposium on High-strength, Low-alloy Steels, Washington, D.C., U.S.A, (1975) 251-260.

13. L. Xu, J. Shi, W. Q. Cao, M. Q. Wang, W. J. Hui, H. Dong, *Improved mechanical properties in Ti-bearing martensitic steel by precipitation and grain refinement*, J. Mater. Sci., 46 (2011) 6384-6389.
14. G. W. Yang, X. J. Sun, Z. D. Li, X. X. Li, Q. L. Yong, *Effects of vanadium on the microstructure and mechanical properties of a high strength low alloy martensite steel*, Mater. Des., 50 (2013) 102-107.
15. R. Uemori, R. Chijiiwa, H. Tamehiro, H. Morikawa, *AP-FIM study on the effect of Mo addition on microstructure in Ti-Nb steel*, Appl. Surf. Sci. 76 (1994) 255–260.
16. R. Wan, F. Sun, L. Zhang, A. Shan, *Effect of Mo addition on strength of fire-resistant steel at elevated temperature*, J. Mater. Eng. Perform. 23 (2014) 2780–2786.
17. R. C. Dimitriu, H. K. D. H. Bhadeshia, *Hot strength of creep-resistant ferritic steels and relationship to creep rupture data*, Mater. Sci. Technol., 23 (2007) 1127–1131.
18. He, R.; Jiang, L.; Dong, W. Development of high corrosion-resistant ferritic stainless steel and its application in the building cladding system. Baosteel Tech. Res., 7 (2013) 54–58.
19. M. G. Akben, B. Bacroix, J. J. Jonas, *Effect of vanadium and molybdenum addition on high-temperature recovery, recrystallization and precipitation behaviour of niobium-based microalloyed steels*, Acta Metall., 31 (1983) 161–174.
20. J. Lu, O. Omotoso, J. B. Wiskel, D. G. Ivey, H. Henein, *Strengthening mechanisms and their relative contributions to the yield strength of microalloyed steels*. Metall. Mater. Trans., A43 (2012) 3043–3061.
21. X. Zhou, C. Liu, L. Yu, Y. Liu, H. Li, *Phase transformation behavior and microstructural control of high-Cr martensitic/ferritic heat-resistant steels for power and nuclear plants: A review*, J. Mater. Sci. Technol., 31 (2015), 235–242.
22. Q. Wang, C. Zhang, R. Li, J. Gao, M. Wang, F. Zhang, *Characterization of the microstructures and mechanical properties of 25CrMo48V martensitic steel tempered at different times*, Mater. Sci. Eng., A559 (2013) 130–134.
23. C. Y. Chen, C. C. Chen, J. R. Yang, *Microstructure characterization of nanometer carbides heterogeneous precipitation in Ti–Nb and Ti–Nb–Mo steel*, Mater. Charact., 88 (2014) 69–79.

24. S. Mukherjee, I. Timokhina, C. Zhu, S. P. Ringer, P. D. Hodgson, *Clustering and precipitation processes in a ferritic titanium-molybdenum microalloyed steel*, J. Alloy. Compd., 690 (2017) 621–632.
25. Z. Wang, H. Zhang, C. Guo, W. Liu, Z. Yang, X. Sun, Z. Zhang, F. Jiang, *Effect of molybdenum addition on the precipitation of carbides in the austenite matrix of titanium micro-alloyed steels*, J. Mater. Sci., 51 (2016) 4996–5007.
26. H. Chen, H. Guo, and C. J. Shang, *Study on wear behaviours of 400 and 450 grade wear resistant steels.* Materials Research Innovations, 18(sup4) (2014) S4.270-S4.275.
27. A. K. Lahiri, *Applied metallurgy and corrosion control*: A Handbook for the Petrochemical Industry (New Delhi: Springer), (2017) 96-98.
28. G. Xu, X. Gan, G. Ma, H. Zou, *The development of Ti-alloyed high strength microalloy steel.* Materials and Design, 31(6) (2010) 2891-2896.
29. R. Soto, W. Saikaly, X. Bano, C. Issartel, G. Rigaut, A. Charai, *Statistical and theoretical analysis of precipitates in dual-phase steels microalloyed with titanium and their effect on mechanical properties.* Acta Materialia, 47(12) (1999) 3475-3481.
30. J. Zhou, Y. Kang, and X. Mao, *Precipitation characteristic of high strength steels microalloyed with titanium produced by compact strip production.* Journal of University of Science and Technology Beijing, Mineral, Metallurgy, Material, 15(4) (2008) 389-395.
31. S. W. Ooi, G. Fourlaris, *A comparative study of precipitation effects in Ti only and Ti–V Ultra Low Carbon (ULC) strip steels*. Materials Characterization, 56(3) (2006) 214-226.
32. https://pdfslide.net/documents/bisalloy-bisplate-technical-manual.html accessed on 05-04-2018.
33. D. P. Fairchild, D. G. Howden, W. A. T. Clark, *The mechanism of brittle fracture in a microalloyed steel: Part 1. Inclusion-induced cleavage*. Metallurgical Materials Transaction A, 31 (2000) 641-652.

Chapter 4

4 Thermal cutting of Ti-microalloyed Q&T steels

4.1 Introduction

Quenched and tempered (Q&T) steels have been in use for many years in the mining, defence, and construction industry due to their excellent mechanical properties [1-5]. Hydrogen is adsorbed by these steels during fabrication activities and may result in the formation of microstructure which is susceptible to hydrogen embrittlement known as delayed cracking or cold cracking [6-13]. It is because the area adjacent to the weld pool or cutting edge, known as heat-affected zone (HAZ), undergoes complex microstructural transformation due to thermal cycles [9]. These steels with martensitic microstructure show better abrasion resistance [14-21] and this can be improved by the addition of more carbon content [22], due to the formation of hard carbide particles in soft microstructure [17, 23, 24]. However, the carbon content should not exceed 0.45 wt.% because it would cause a reduction in toughness and ultimately wear resistance [25]. To achieve a required combination of high strength and high toughness in commercially rolled plate steels, microalloying with carbide forming elements (such as Nb, V, Ti, Cr, Mo, W) can be used. High-temperature precipitation and solute atoms retard the austenite grain growth (by pinning the grain boundaries) and help to refine the room temperature microstructure. Low-temperature precipitation provides particle strengthening and may enhance the dislocation structure development. A combination of strengthening mechanisms operating in steel at room temperature results in simultaneous high strength and toughness. Due to the high prices of microalloying elements, cheaper titanium alloyed steels showed their advantages [26-28].

In this chapter, the experimental evaluation will be conducted for the effect of thermal cutting on microstructure and the hardness of Ti-alloyed wear-resistant steels containing Ti-rich precipitates in a wide range of sizes. As the particle size distributions, grain structure, and dislocation structure are expected to vary with heating, thermal cutting should affect the mechanical properties at the cut edge. A probable strength decrease in HAZ is detrimental for the practical attributes of the studied steels, and, therefore, should be taken into account during edge preparation and welding. Three common cutting

methods were investigated: oxy-fuel (the torch temperature can reach as high as 3480 °C [29, 30]), plasma (the torch temperature may exceed 20000 °C [31,32]), and water-jet (temperature is maintained to 30 °C due to water circulation). The first part of this chapter is dedicated to the investigation of 12 mm thick plates of both grades while in the second part the results for 32 mm thick Steel L and 30 mm thick Steel H have been discussed.

4.2 Cutting of 12 mm thick plates - Results

4.2.1 Hardness Profile

The HAZ width decreased with the cutting method from oxy-fuel to plasma to water-jet (Figure 4.1). Water-jet is believed to produce negligible heat effect. The HAZ width variation observed by optical microscopy was supported by the measurements of hardness profiles from the cut edge towards the base metal (Figure 4.2). The hardness profile shape varied with the cutting method and steel composition. In Steel L both oxy-fuel and plasma cutting methods decreased hardness by a maximum of 100 HV (Figure 4.2a,b); and in Steel H this decrease was slightly higher, by about 130 HV (Figure 4.2d,e). Oxy-fuel resulted in about 5 and 9 mm wide HAZ in Steels L and H, respectively. In contrast, plasma cutting produced only 3 mm wide HAZ in both steels. In Steel, L cut with oxy-fuel the minimum HV point was at about 2 mm from the cut edge (Figure 4.2a), although the plasma cutting resulted in the appearance of a minimum HV point at about 1.5 mm from the cut edge (Figure 4.2b). In Steel, H cut with oxy-fuel the minimum HV point was at about 3 mm from the cut edge (Figure 4.2d), and in the plasma cut sample, the minimum HV point was at about 1 mm from the cut edge (Figure 4.2e). To explain such an intricate shape of the hardness profiles and their variation with steel composition and cutting method, the following microstructural characterization was undertaken.

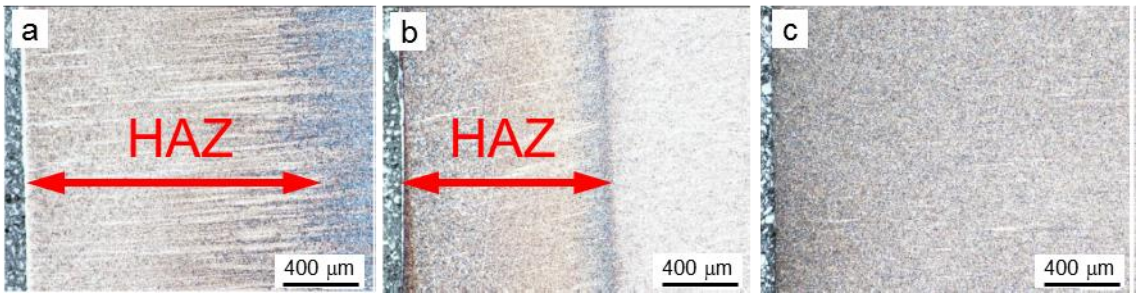

Figure 4.1 Optical microscopy images of heat-affected zone in Steel H cut with (a) oxy-fuel, (b) plasma, and (c) water-jet.

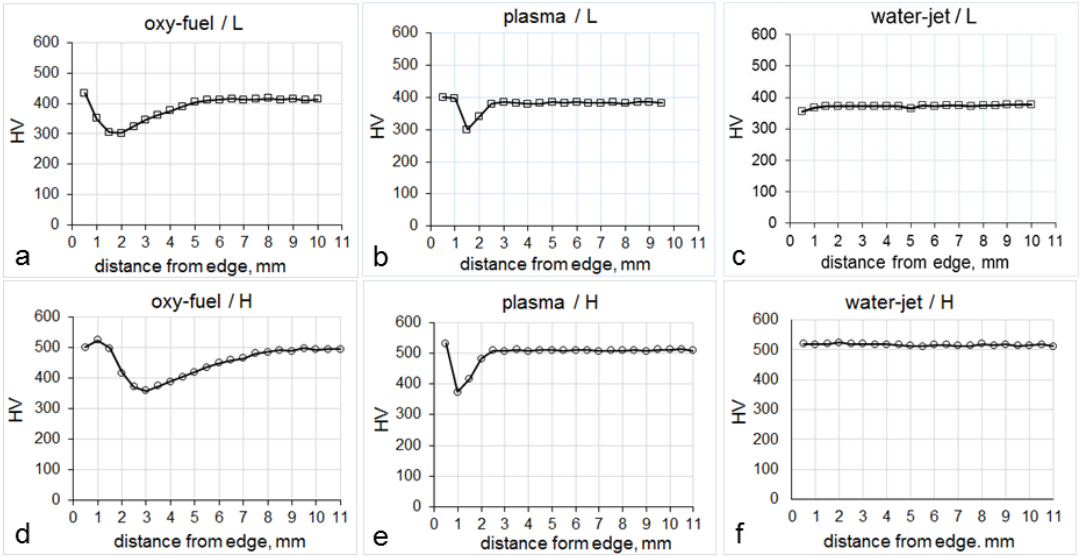

Figure 4.2 Hardness profiles at the plate mid-thickness position for (a-c) Steel L and (d-f) Steel H cut with (a,d) oxy-fuel, (b,e) plasma, and (c,f) water-jet; each point on the hardness profiles is the mean value of 5 indentations made through plate thickness.

4.2.2 Grain Structure

In the as-received condition, both steel grades had a martensitic microstructure. SEM imaging of the cut samples revealed a variation in grain structure with distance from the cut edge.

In the oxy-fuel cut specimens (Figure 4.3), both steels exhibited a martensitic type of microstructure at the cut edge. A bainitic microstructure was observed at the points of minimum hardness (2 and 3 mm away from the cut edge for Steels L and H, respectively), martensitic laths have almost disappeared, and the grains were of irregular shape. Far away from the cut edge (10 mm), the microstructure was also of a martensitic type. In the plasma cut specimens (Figure 4.4), no significant variation in grain structure with the position was observed by SEM in both steels.

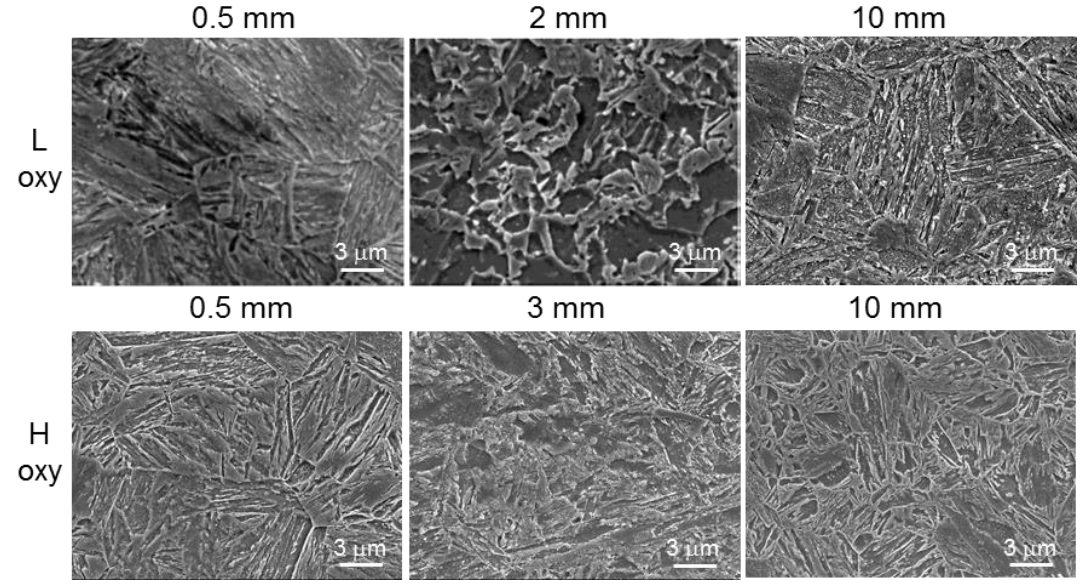

Figure 4.3 SEM images of grain structure in Steels L and H cut using oxy-fuel cutting method at the cut edge, point of minimum HV, and far away from the cut edge (base plate).

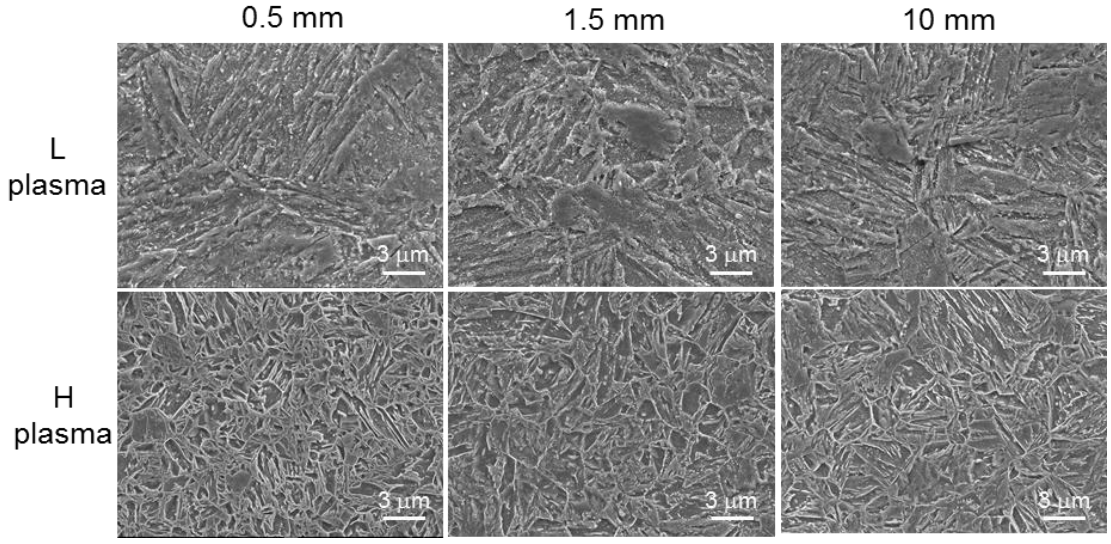

Figure 4.4 SEM images of grain structure in Steels L and H cut using plasma cutting method at the cut edge, point of minimum HV, and far away from the cut edge (base plate).

Measurements of the average grain size (equivalent diameter) are presented in Table 4.1. In both steels cut by oxyfuel, the average grain size minimum was observed at the position of minimum hardness (2 and 3 mm from the cut edge for Steels L and H, respectively). This may indicate the grain structure recrystallization in both steels at this position. In both steels cut by plasma, the grain size variation with the position was within the

experimental error. In the water-jet cut samples also no variation in grain size with the position was observed. Both steels showed similar values of the average grain size in the base plate.

Table 4.1 Average grain size in the studied steels.

Steel grade / cutting method	**Steel L**			**Steel H**		
	Oxy-fuel					
Position from cut edge	0.5 mm	2.0 mm	10 mm	0.5 mm	3.0 mm	10 mm
Average size, µm	2.3±0.2	1.9±0.1	2.3±0.2	3.0±0.2	2.1±0.1	2.5±0.3
	Plasma					
Position from cut edge	0.5 mm	1.5 mm	10 mm	0.5mm	1.5mm	10 mm
Average size, µm	2.4±0.2	2.5±0.2	2.4±0.2	2.3±0.2	2.6±0.1	2.5±0.2
	Water-jet					
Position from the cut edge	0.5 mm and 10 mm			0.5 mm and 10 mm		
Average size, µm	2.6±0.2			2.5±0.2		

4.2.3 Coarse Particles

Optical and SEM imaging revealed three particle types in the studied steels: coarse cuboidal/rectangular/elongated, fine spherical, and fine needle-shaped. Below we present a detailed analysis of these particles in the studied steels and the variation in the particle parameters with cutting method and distance from the cut edge.

SEM-EDS mapping confirmed the coarse particles (< 6 µm) to be TiMoVCN in both steels. The average particle sizes were larger in Steel H (Table 4.2), which is consistent with higher Ti, Mo, and C contents in this steel. Larger particles contained a higher nitrogen content. TiN is known to precipitate at higher temperatures, compared to TiMoV-rich carbides, therefore TiN usually has more time for growth. The particle parameters near the cut edge varied during cutting (Figure 4.5): coarse particles dissolved in Steel L, while in Steel H more particles precipitated. These behaviours seemed to be more pronounced in the samples cut with oxy-fuel compared to the plasma cut.

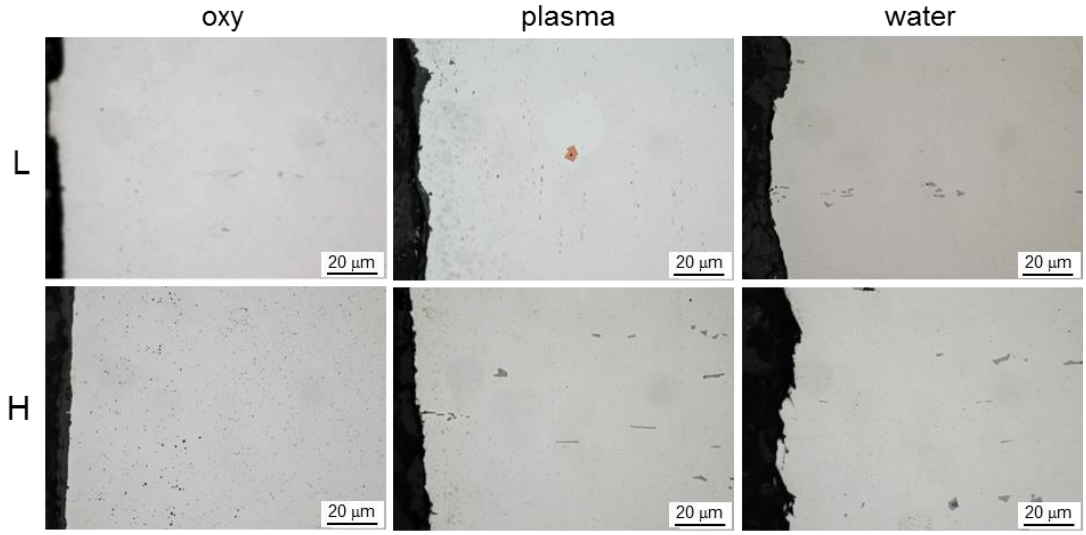

Figure 4.5 Optical images of Steel L and Steel H cut with the three studied methods (un-etched samples).

Analysis of the average TiMoVCN particle parameters (Table 4.2) suggested the following conclusions:

- in Steel L thermal cutting with both methods led to a decrease in the particle number density well below the cut edge surface (2 mm for oxy-fuel and 1.5 mm for plasma, positions corresponding to minimum hardness); this supports particle dissolution. However, the average particle size at these positions increased after cutting with oxy-fuel and decreased after cutting with plasma. This could be explained if during cutting with oxy-fuel the dissolution was more intense (a wider particle size range fully dissolved), and during cutting with plasma larger particles partially dissolved to smaller sizes. Closer to the cut edge (0.5 mm position) the particle number density and average size were similar to that in the base plate. This can be related to shorter times of heat effect associated with faster cooling rates on the surface.
- in contrast, in Steel H cut with both oxy-fuel and plasma the particle number density significantly (near 2 times) increased towards the cut edge; this supports precipitation of new particles and growth of smaller ones to larger sizes.
- cutting with water-jet did not lead to any variation in the particle parameters, due to the absence of heat effect.

Table 4.2. Average parameters of coarse TiMoVCN particles studied with optical microscopy.

Steel grade / cutting method	**Steel L**			**Steel H**		
	Oxy-fuel					
Position from cut edge	0.5 mm	2.0 mm	10 mm	0.5 mm	3.0 mm	10 mm
Average size, μm	1.6±0.7	2.5±0.5	1.8±0.6	2.9±1.2	2.2±0.8	2.9±0.9
Number density, μm^{-2}	0.0020	0.0012	0.0021	0.0039	0.0025	0.0016
	Plasma					
Position from cut edge	0.5 mm	1.5 mm	10 mm	0.5 mm	1.5 mm	10 mm
Average size, μm	1.9±0.4	1.5±0.5	2.1±0.7	2.5±0.5	3.2±1.3	2.8±0.8
Number density, μm^{-2}	0.0021	0.0011	0.0020	0.0033	0.0021	0.0017
	Water-jet					
Position from cut edge	0.5 mm		10 mm	0.5 mm		10 mm
Average size, μm	2.0±0.7		1.8±0.6	2.8±0.8		2.8±1.0
Number density, μm^{-2}	0.0020		0.0019	0.0017		0.0017

To further elaborate on the TiMoVCN particle precipitation kinetics, the number density distributions for various cutting methods and positions have been analyzed (Figure 4.6). With respect to the cutting method, the following was observed closer to the cut edge (0.5 mm position):

- in Steel L cut with oxy-fuel the dissolution of 0.5-1.0 μm particles occurred (note a decrease in the number density of these particles accompanied by an increase in the density of <0.5 μm ones, Figure 4.6a), although cutting with plasma did not affect the distribution at this position;
- in contrast, in Steel H cut with oxy-fuel new particles precipitated and grew in the <1.0 μm size range (note approximately 4 fold increase in these particles' number density,

Figure 4.6b); and cutting with plasma led to partial dissolution of 0.5-1.0 µm particles to <0.5 µm sizes and possible precipitation of new <0.5 µm ones.

With respect to distance from the cut edge during cutting with oxy-fuel:

- in Steel L the particles in whole size range (< 3 µm) dissolved, and this was to a greater extent at the 2 mm position compared to 0.5 mm position (Figure 4.6c);
- in contrast, in Steel H <1.0 µm particles precipitated at both positions, and this was more intense at 0.5 mm distance from the cut edge compared to 3.0 mm (note an increase in the <1.0 µm particle number density by 9 and 5 fold at 0.5 and 3.0 mm positions, respectively, Figure 4.6d).

With respect to distance from the cut edge during cutting with plasma:

- in Steel L >1.5 µm particles dissolved at 0.5 mm position and >0.5 µm particles dissolved at 1.5 mm position (note decreases in their respective number densities, Figure 5.7e); this means that more particles dissolved at 1.5 mm position than at 0.5 mm position, which qualitatively corresponds to the trends observed for cutting with oxy-fuel;
- in contrast, in Steel H <1.0 µm particles precipitated at both positions and more at 0.5 mm than at 1.5 mm distance from the cut edge, which qualitatively corresponds to the behaviour observed during cutting with oxy-fuel.

Comparison of Figure 4.6 (c) against (e) and Figure 4.6 (d) against (f) suggests the following interesting point regarding the effect of the cutting method. In Steel L cutting with oxy-fuel resulted in particle dissolution in the whole size range; however, cutting with plasma led to partial dissolution (only >1.5 µm particles dissolved at 0.5 mm position and >0.5 µm particles dissolved at 1.5 mm position). In Steel, H particles precipitated and grew during cutting with both methods. However, the increase in <1.0 µm particle number density at 1.5 mm position (closer to the edge) during cutting with plasma was less (3.5 times) than this at 3.0 mm position (farther from the edge) during cutting with oxy-fuel (5 times). This indicates a more intense heat input during cutting with oxy-fuel leading to a more pronounced variation in the particle parameters.

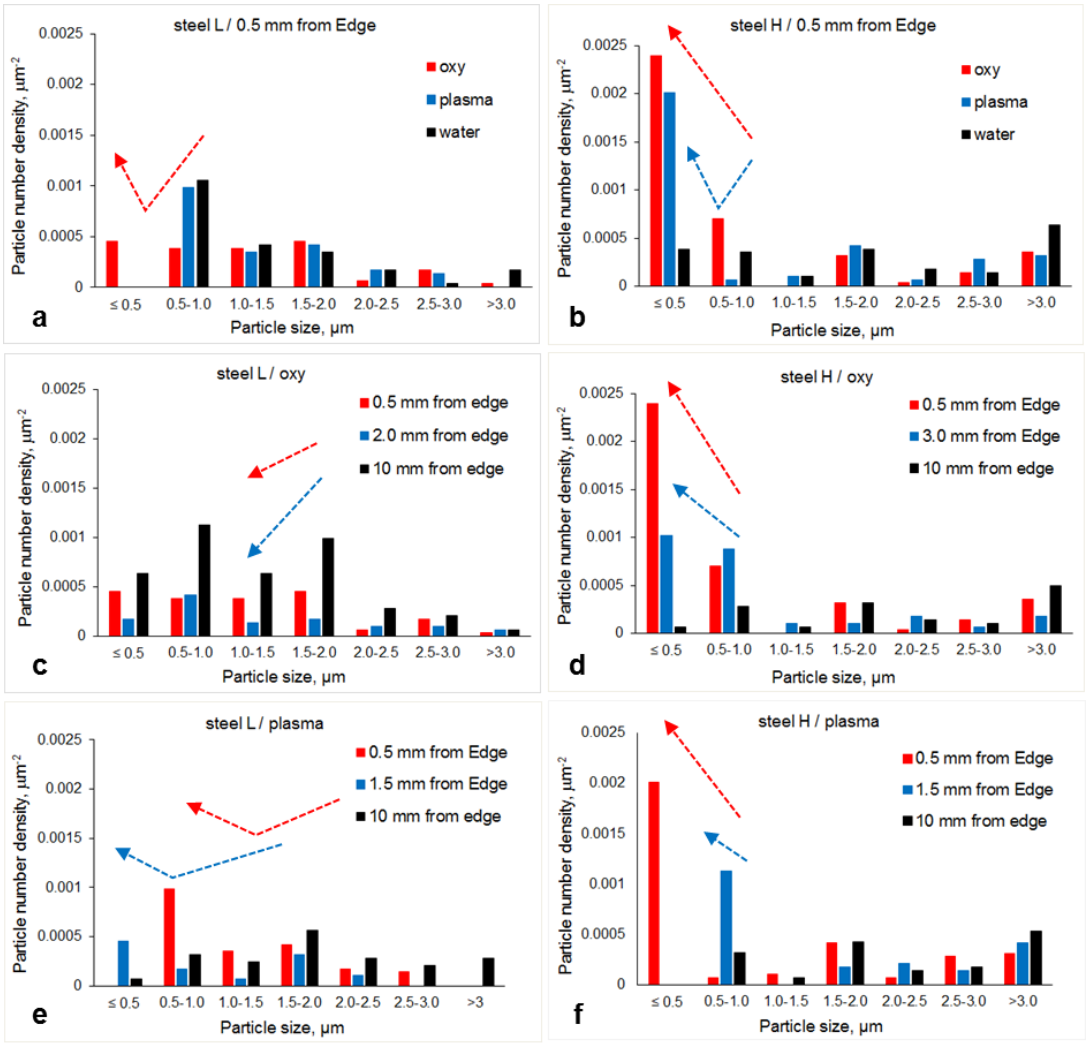

Figure 4.6 Coarse TiMoVCN particle number density distributions at 0.5 mm position from the cut edge in Steels (a) L and (b) H, for the samples cut with oxy-fuel in Steels (c) L and (d) H, and for the samples cut with plasma in Steels (e) L and (f) H.

4.2.4 Fine Ti-rich particles

Fine particles were of two types: spherical Ti-rich carbides or carbonitrides and needle-shaped Fe_3C (Figure 4.7). Their parameters varied with steel composition, cutting method, and distance from the cut edge (Figures. 4.8-4.9). Analysis of Ti-rich particle parameters (Table 4.3) has shown that:

- in Steel, L cut with oxy-fuel (i) the average particle size increased without a significant variation in number density at 0.5 mm position, and (ii) both the average particle size and their number density increased at 2 mm position. These might be explained if the growth of fine Ti-rich particles occurred. However, partially dissolving coarse TiMoVCN particles (discussed above) could also contribute to the increase in size

and number density of fine Ti-rich ones. During cutting with plasma the number density decreased at both positions and the average size increased at 0.5 mm position. These support dissolution.

- in Steel H cutting with both methods resulted in the particle number density and average size increasing. These indicate precipitation and coarsening of Ti-rich particles.

The particle number density distributions (Figure 4.10) supported a general dissolution of fine Ti-rich particles in Steel L and their precipitation and growth in Steel H, although there were certain variations with respect to cutting method and position. Thus, in Steel L the <80 nm particle number density decreased at 0.5 mm position after cutting with both oxy-fuel and plasma, and at 1.5 mm position after cutting with plasma (Figure 4.10a, c, e), although it slightly increased at 2.0 mm position after cutting with oxy-fuel; the number density of >80 nm particles increased at both positions (0.5 and 2.0/1.5 mm) after cutting with both methods (Figure 4.10a, c). This means that in Steel L despite the general dissolution of fine Ti-rich particles some coarsening could take place. In Steel H the <120 nm particle number density increased at both positions (0.5 and 3.0/1.5 mm) after cutting with both methods (Figure 4.10b, d, f), and it was more pronounced during cutting with oxy-fuel. This indicates precipitation and growth of new Ti-rich particles and is in line with the behaviour of coarse TiMoVCN particles presented above (Figure 4.6b,d, f).

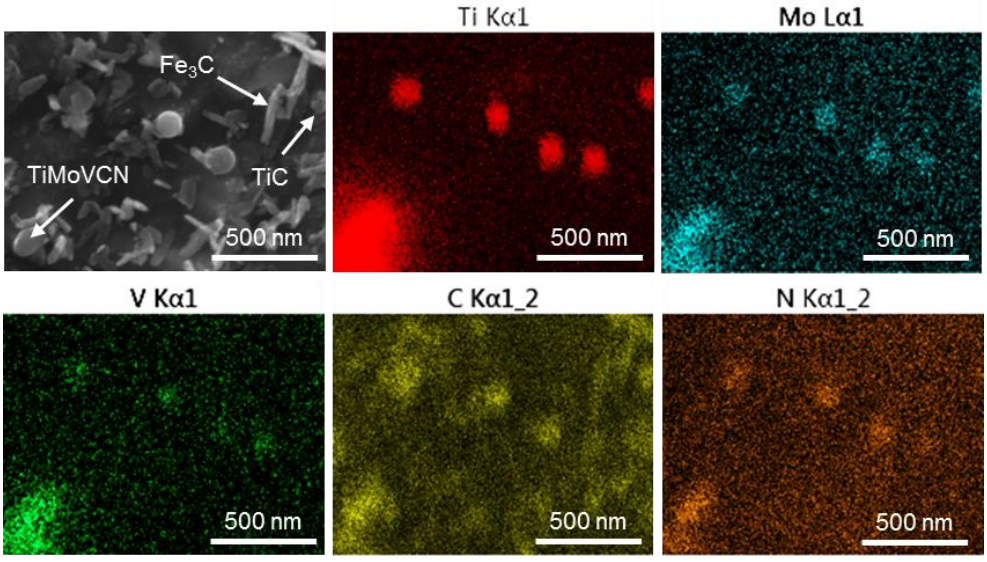

Figure 4.7 SEM-EDS maps of fine particles observed in both steel grades.

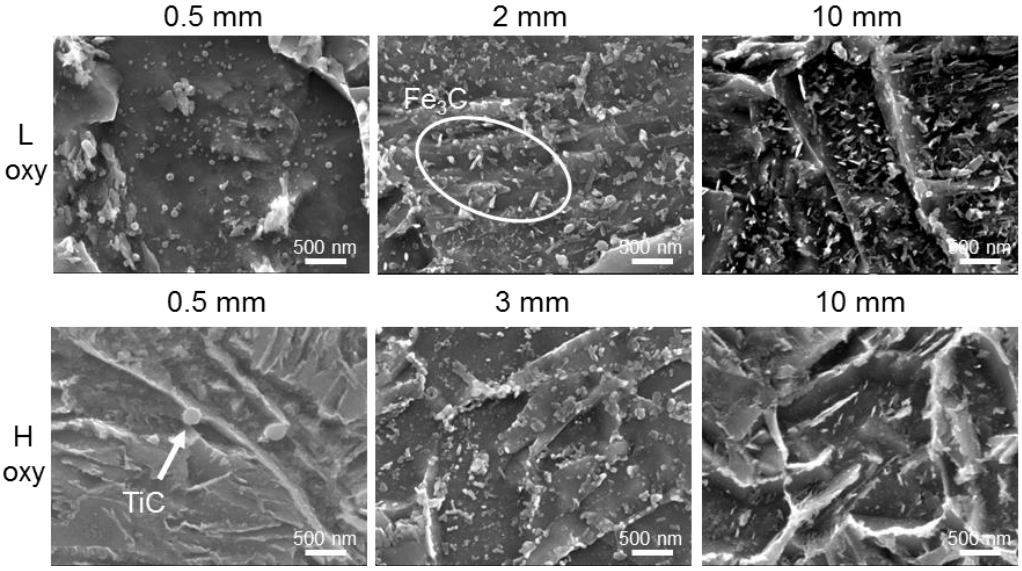

Figure 4.8 SEM images of fine precipitates in Steels L and H cut using oxy-fuel cutting method at the cut edge, point of minimum HV, and far away from the cut edge (base plate).

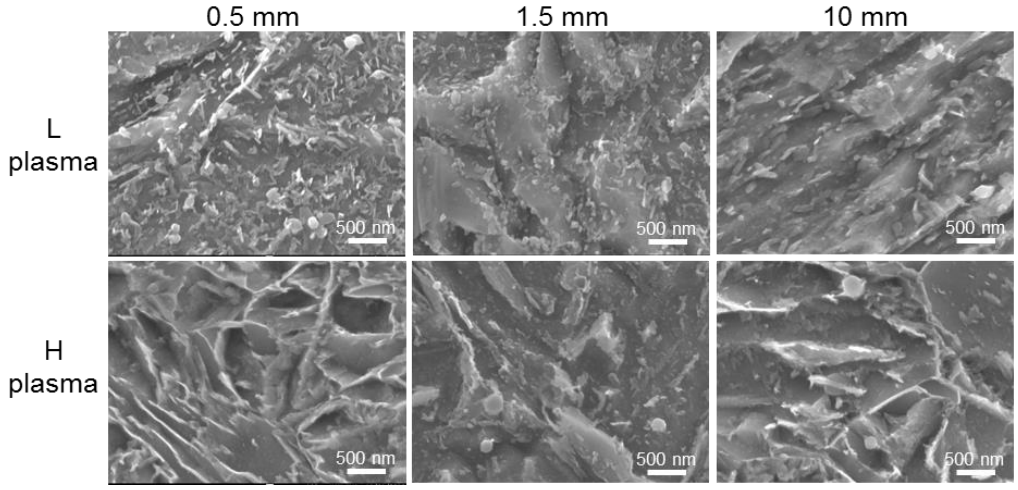

Figure 4.9 SEM images of fine precipitates in Steels L and H cut using plasma cutting method at the cut edge, point of minimum HV, and far away from the cut edge (base plate).

Table 4.3. Average parameters of fine Ti-rich particles studied with SEM.

Steel grade / cutting method	**Steel L**			**Steel H**		
	Oxy-fuel					
Position from cut edge	0.5 mm	2.0 mm	10 mm	0.5 mm	3.0 mm	10 mm
Average size, nm	112±21	93±30	82±26	162±50	104±42	144±48
Number density, μm^{-2}	1.1	2.2	1.3	0.4	0.8	0.3
	Plasma					
Position from cut edge	0.5 mm	1.5 mm	10 mm	0.5 mm	1.5 mm	10 mm
Average size, nm	135±34	85±28	83±23	153±45	210±56	150±43
Number density, μm^{-2}	0.8	0.5	1.4	0.6	0.6	0.3

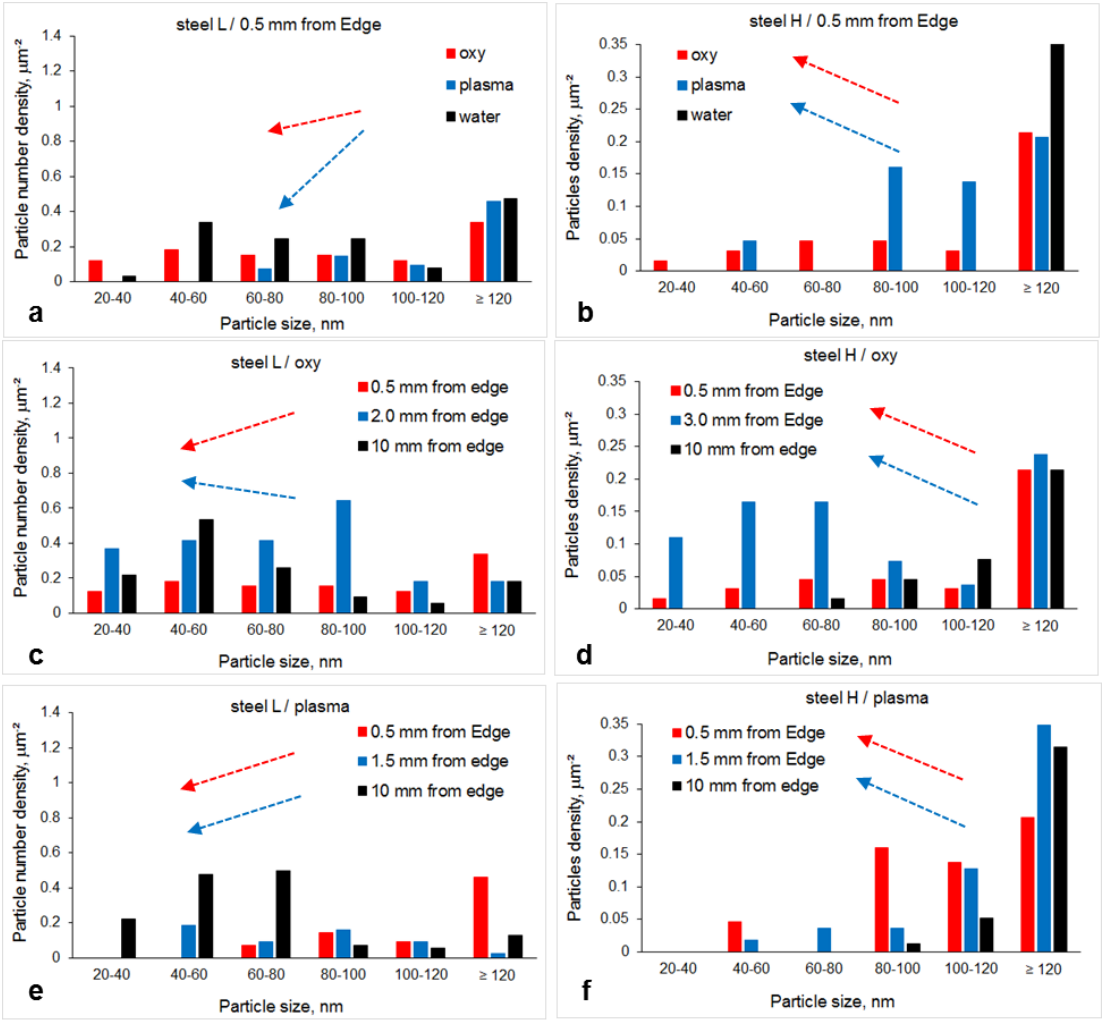

Figure 4.10. Fine Ti-rich particle number density distributions at 0.5 mm position from the cut edge for Steels (a) L and (b) H, for the samples cut with oxy-fuel for Steels (c) L and (d) H, and for the samples cut with plasma in Steels (e) L and (f) H.

4.2.5 Fine Fe_3C Particles

SEM imaging revealed the presence of needle-shaped particles with equivalent diameters being in the range of 30–115 nm for all studied conditions (Figure 4.11a). SEM-EDS mapping showed increased carbon concentrations in these particles and absence of other alloying elements (Figure 4.11b). This allowed to suggest that these particles were Fe3C. In addition to SEM characterization carried out for all studied conditions, a TEM study was performed for the as-received steels (Figure 4.11c,d). Analysis of the diffraction patterns showed the Fe3C particles exhibiting Bagaryatskii orientation relationship to the bcc (termpered martensite) matrix: $[001]_{matrix} \| [321]_{Fe3C}$ (Figure 4.11e,f). This can further support their nature as Fe3C.

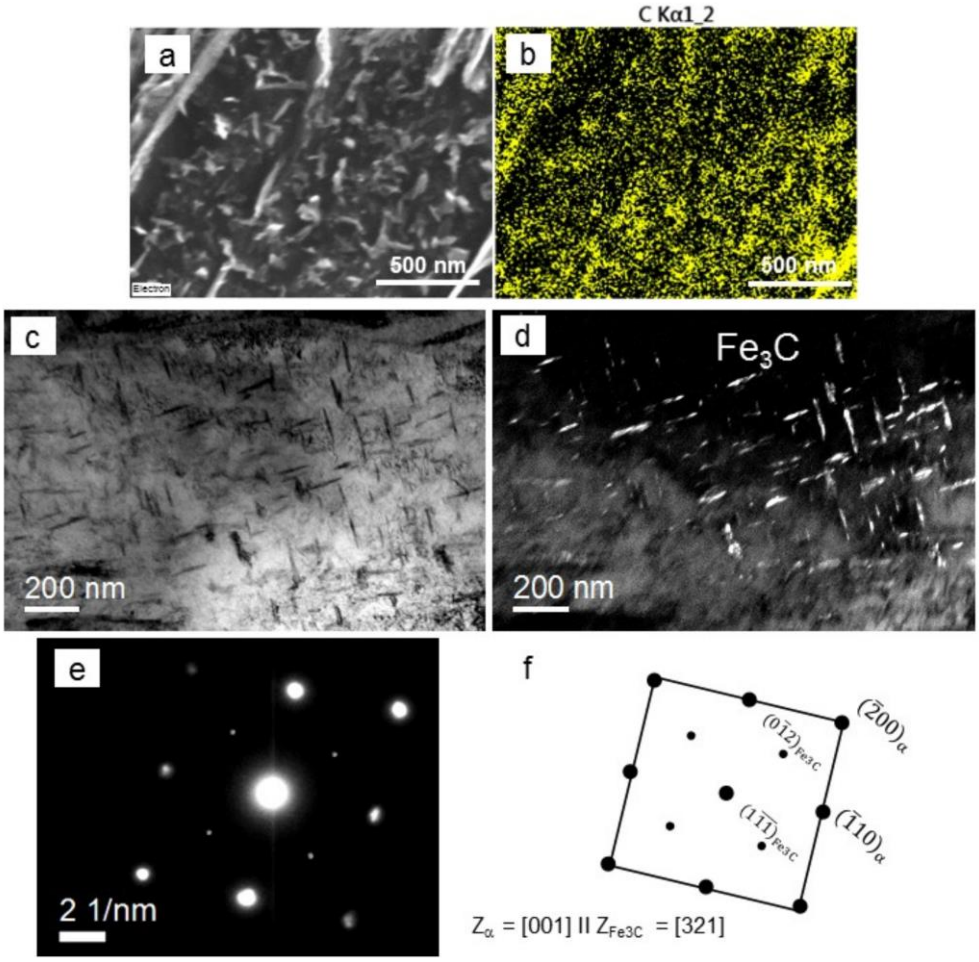

Figure 4.11 Fe_3C particles in the base metal of Steel L: (a,b) SEM image with the corresponding EDS carbon map; (c,d) bright and dark fields TEM images; 9e0 diffraction pattern corresponding to images (c,d); and 9f) indexing of the diffraction pattern shown in (e).

In Steel L the average Fe_3C particle number density decreased for both cutting methods, and their size could slightly increase during plasma cutting (Table 4.4). The decrease in number density was higher away from the cut edge, 2.0 mm position for oxy-fuel cutting and 1.5 mm for plasma cutting, where a longer thermal effect could be expected. The number density distributions supported a decreasing number of, particularly, >40 nm Fe_3C particles, and it was more pronounced during cutting with oxy-fuel (Figure 4.12a, c, e). All these facts indicate the dissolution of Fe_3C particles in Steel L during thermal cutting.

However, in Steel H the average particle size slightly increased during cutting with oxy-fuel despite a decrease in number density (Table 4.4). And during cutting with plasma no significant variation in the average particle parameters was observed. The number density

distributions supported decreasing numbers of the particle in the whole size range during oxy-fuel cutting (Figure 4.12b, d, f), and very minor variations during cutting with plasma. These indicate partial dissolution of Fe_3C particles in Steel H, more pronounced during cutting with oxy-fuel.

Table 4.4, Average parameters of fine Fe_3C particles studied with SEM.

Steel grade / cutting method	**Steel L**			**Steel H**		
	Oxy-fuel					
Position from cut edge	0.5 mm	2.0 mm	10 mm	0.5 mm	3.0 mm	10 mm
Average size, nm	37±9	47±10	49±11	52±9	68±12	45±10
Number density, μm^{-2}	2.0	1.1	2.3	0.5	0.6	1.4
	Plasma					
Position from cut edge	0.5 mm	1.5 mm	10 mm	0.5 mm	1.5 mm	10 mm
Average size, nm	60±11	67±9	58±8	49±10	51±11	53±10
Number density, μm^{-2}	2.2	1.5	2.4	1.0	1.2	1.3

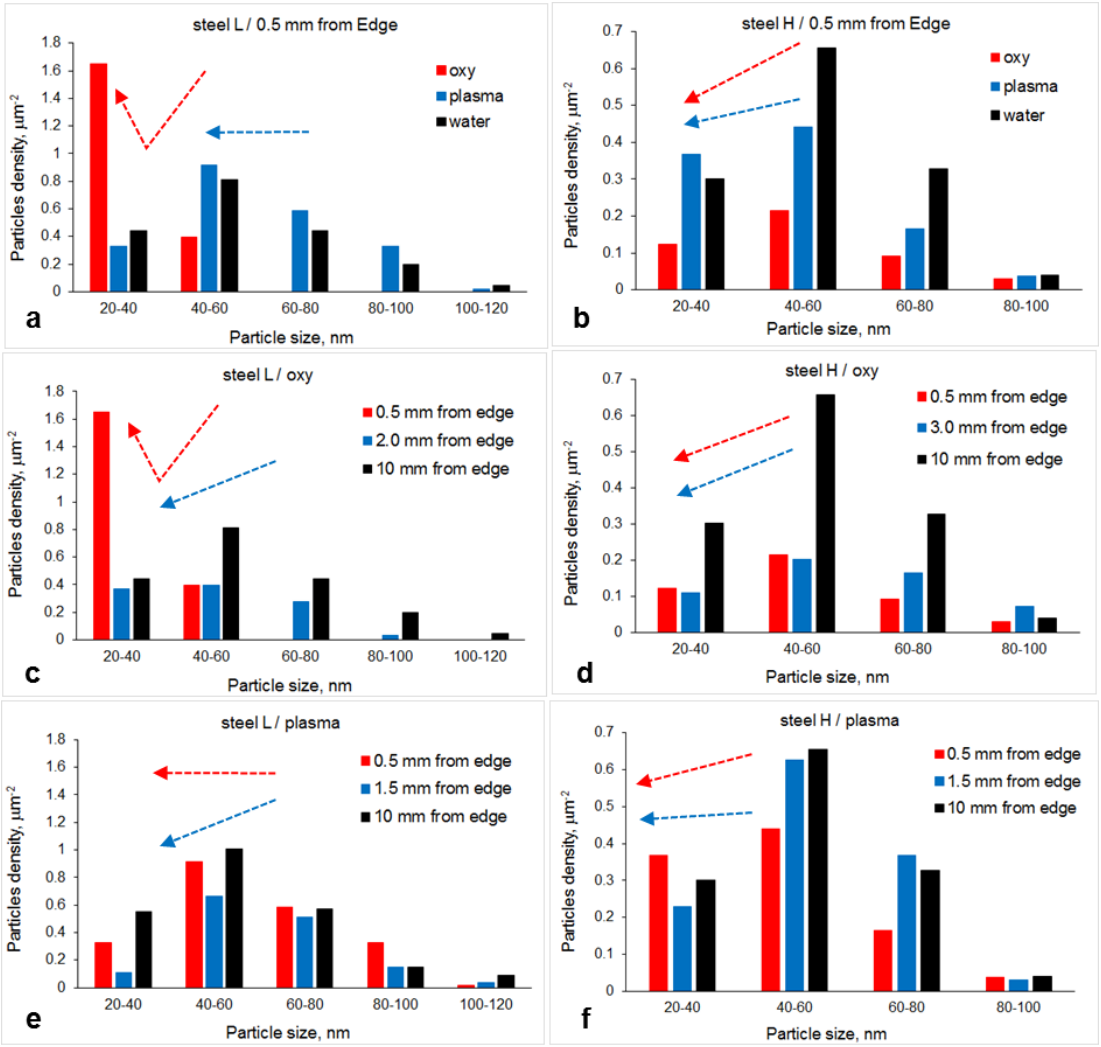

Figure 4.12 Fe_3C particle number density distributions at 0.5 mm position from the cut edge in Steel (a) L and (b) H.

4.3 Cutting of 12 mm thick plates - Discussion

4.3.1 Effect of Steel Composition

The average particle parameters and hardness values with respect to steel composition and cutting method are summarised in Table 4.5. In as-received condition (10 mm away from the cut edge), the grain size was similar in both steels, the number densities of coarse TiMoVCN and fine Ti-rich particles were higher in Steel L (although their sizes were larger in Steel H, Tables 4.3 and 4.4), and the number densities of Fe_3C particles were also higher in Steel L. Larger sizes of coarse TiMoVCN and fine Ti-rich particles correspond to higher contents of Ti, Mo and C in Steel H. However, lower number densities of all particle types in Steel H are an unusual result. Higher concentrations of Ti and C increase the solubility products of TiN and TiC particles [33, 34] and their precipitation start temperatures, traditionally this leads to higher particle number densities

at room temperature [35-37]. Probably, the rolling of Steel H was conducted at high speed, accelerated cooling might also have been used at the end of the hot rolling cycle. These techniques would result in the matrix supersaturation with Ti, Mo, and C and solid solution strengthening. Consequently, the hardness of Steel H was higher than this of Steel L.

During cutting with oxy-fuel the Ti-rich particles exhibited a different type of precipitation kinetics in the two steels. Thus, in Steel L the number density of coarse TiMoVCN particles decreased and this of fine Ti-rich particles increased towards the cut edge. This indicates the dissolution of the coarse particles to smaller sizes in Steel L. In contrast in Steel H, the number densities of both coarse and fine Ti-rich particles increased towards the cut edge. This indicates precipitation and growth of new particles in Steel H. Such a discrepancy in the Ti-rich particle behaviour can be related to two reasons: (i) Ti, Mo, and C concentrations in the matrix were higher in Steel H; during thermal cutting the Ti, Mo and C atoms diffused to the existing particles contributing to their size growth and diffused to each other to form new Ti-rich particles; and (ii) the solubility temperature of Ti-rich particles was lower in Steel L; this would result in fewer undissolved coarse particles in Steel L after heating during cutting. In fact, the solubility equation $\log[Ti]\cdot[C] = 2.75 - 7000/T$ presented in [34] gave 1575K and 1942K for TiC dissolution temperature in Steel L and H, respectively. A decreasing number density of Fe_3C particles in both steels (near 2 times) coincided with an increasing number density of Ti-rich particles. Dissolution of cementite in favour of alloying element carbide precipitation was observed following tempering of martensite [38].

In both steels, the grain size slightly decreased below the cut edge (2.0 and 3.0 mm positions in Steels L and H, respectively) due to recrystallization [39]. However, the microstructure resembled freshly transformed martensite closer to the edge (0.5 mm position, Figure 4.3). This could be explained if, due to heating from oxy-fuel, the original martensite closer to the edge transformed to austenite and back to martensite during cooling. The grain size at the edge (0.5 mm position) was slightly larger in Steel H (3.0 µm) compared to Steel L (2.3 µm). This can be associated with two reasons: (i) fine Ti-rich particles exhibiting a lower number density in Steel H were less effective in retardation of austenite grain growth in Steel H compared to Steel L; and (ii) the ferrite to austenite transformation temperature was lower in Steel H, 770-785 °C, than in Steel L, 835-845 °C (calculated using various formulas presented in [40, 41]), this would give

more time for the matrix to be in austenitic condition and, consequently, more time for austenite grain growth.

Despite decreasing grain size and increasing number density of fine Ti-rich particles, hardness decreased in Steel L at the 2.0 mm position. This corresponds to the decrease in the number density of coarse TiMoVCN and Fe_3C particles. In Steel H a hardness minimum was also observed; although, in contrast to Steel L, the number density of coarse TiMoVCN particles increased in addition to increasing number density of fine Ti-rich particles. This supports the following conclusions: (i) the grain structure recovery (dislocation annihilation) and recrystallization in the HAZ can significantly contribute to a hardness decrease, irrespective of the particle precipitation kinetics, because the number of dislocation-obstacle interaction sites is responsible for strength not the number of particles dispersed in the matrix; (ii) precipitation of coarse TiMoVCN and fine Ti-rich particles cannot fully compensate for the dissolution of Fe_3C; (ii) solution depletion in C (due to precipitation of excessive amount of fine Ti-rich carbides) is detrimental for hardness.

Closer to the cut edge (0.5 mm position) the hardness increased in both steels. Obviously, a reverse martensite-austenite-martensite transformation resulted in a higher dislocation density at the cut edge in both steels. Lower heat effect times, due to faster cooling of the edge compared to 2.0 mm position, resulting in less severe particle dissolution in Steel L. And Steel H significant precipitation of coarse TiMoVCN particle might have contributed to the hardness increase at the edge.

During cutting with plasma, in Steel L the number densities of coarse TiMoVCN, fine Ti-rich and Fe_3C particles decreased at the 1.5 mm position from the cut edge (simultaneously with a size growth of fine Ti-rich and Fe_3C particles, Tables 4.4 and 4.5). This indicates the dissolution of all particles in Steel L. In contrasts, in Steel H the TiMoVCN and fine Ti-rich particles precipitated and grew, although Fe_3C dissolved, and these behaviours were more pronounced closer to the edge (at 0.5 mm position), which is in line with the matrix supersaturation with Ti, Mo, and C in the as-rolled condition.

Despite different kinetics of TiMoVCN and fine Ti-rich particles, the hardness minimum at 1.5 mm position was observed in both steels. This may indicate a variation in strengthening mechanisms utilised to produce the studied steels: in addition to phase balance (namely formation of martensite), strengthening of Steel L relied on particle precipitation, and when their number densities decreased the strength decreased; while in

Steel H the strengthening from solute C, N and Mo atoms [42-44], Ti-Mo-C atom clusters [45-47] and <20 nm TiC particles [48-50] (not studied here) could be significant.

Table 4.5 Correlation of the microstructural parameters and hardness to steel grade and cutting method.

Steel grade/ cutting method		**Steel L**			**Steel H**		
		Oxy-fuel					
Position from cut edge		0.5mm	2.0mm	10mm	0.5mm	3.0mm	10mm
Average grain size, μm		2.3±0.2	1.9±0.1	2.3±2	3.0±0.1	2.1±0.1	2.5±0.3
Number density, μm^{-2}	Coarse Ti-rich	0.0020	0.0012	0.0021	0.0039	0.0025	0.0016
	Fine Ti-rich	1.1	2.2	1.3	0.4	0.8	0.3
	Fe_3C	2.0	1.1	2.3	0.5	0.6	1.4
Hardness HV		430±8	300±5	410±10	520±10	359±7	500±4
		Plasma					
Position from cut edge		0.5mm	2.0mm	10mm	0.5mm	3.0mm	10mm
Average grain size, μm		2.4±0.2	2.5±0.2	2.4±0.2	2.3±0.2	2.6±0.1	2.5±0.2
Number density, μm^{-2}	Coarse Ti-rich	0.0021	0.0011	0.0020	0.0033	0.0021	0.0017
	Fine Ti-rich	0.8	0.5	1.4	0.6	0.6	0.3
	Fe_3C	2.2	1.5	2.4	1.0	1.2	1.3
Hardness HV		400±8	300±5	385±6	530±4	417±4	505±5

4.3.2 Effect of Cutting Method

In Steel L

- the grain size decreased during oxy-fuel cutting below the cut edge (2.0 mm position), but did not show a variation during plasma cutting.
- coarse TiMoVCN particles dissolved during both cutting methods to similar remaining number density values.
- fine Ti-rich particles showed increasing number densities below the cut edge (2.0 mm position) after cutting with oxy-fuel (which could result from the dissolution of Fe_3C in favour of precipitation of fine Ti-rich particles) but dissolved during plasma cutting.
- Fe_3C particles dissolved below the cut edge (2.0 or 1.5 mm position for oxyfuel and plasma) during cutting with both methods, although more during cutting with oxy-fuel; and
- hardness showed a minimum below the cut edge for both methods, although a greater decrease and at a larger distance occurred after cutting with oxy-fuel. Together with a wider HAZ, all these observations indicate a more pronounced heat effect during cutting with oxy-fuel. A high tempering effect during cutting with oxy-fuel was observed recently in low carbon steels [51-53]. Despite higher temperatures applied during cutting with plasma (20000 °C [32]) compared to oxy-fuel (3500 °C [30]), a narrower HAZ and less severe softening observed in Steel L during plasma cutting can be related to two reasons:
- a faster processing speed, giving less time for heat transfer towards the base plate; and
- melting down and removal of the heat-affected material from the edge.
- In Steel H
- the grain size slightly decreased below the cut edge (3.0 mm position) during oxy-fuel cutting, although no significant variation in grain size was observed after plasma cutting.
- coarse and fine Ti-rich particles precipitated for both cutting methods.
- Fe_3C particles dissolved for both cutting methods, although to a greater extent for oxy-fuel; and
- hardness showed a minimum below the cut edge for both methods, although a greater decrease and at a larger distance occurred after cutting with oxy-fuel. Similar to Steel L, in Steel H the oxy-fuel cutting method produced a larger thermal effect on the

cut edge than the plasma cutting method. However, the edge hardness of Steel H remained to be higher than this of Steel L for both cutting methods. This is related to the variation in steel compositions:

- more highly alloyed Steel H exhibited larger sizes of coarse and fine Ti-rich particles, which would be more stable against dissolution [54-56];
- potentially higher solute concentrations of Ti, Mo, and C in the Steel H matrix not only retarded recovery but also facilitated solid solution strengthening and precipitation and growth of new particles during thermal cutting [57-59].

4.4 Conclusion

Thermal cutting of two Ti-alloyed martensitic steels containing 0.27C-0.40Ti and 0.38C-0.60Ti (wt. %) altered the microstructure and hardness near the cut edge in both steels. This must be taken into account during edge preparation for welding and structure fabrication.

1. With respect to practical aspects of this work the following conclusions should be made. In both steels the maximum decrease in hardness due to thermal cutting with oxy-fuel or plasma could reach 25% of the respective original hardness: 100 HV down from the original 400 HV in the lower alloyed Steel L and 130 HV down from the original 500 HV in the more highly alloyed Steel H. Cutting with oxy-fuel produced a wider HAZ (5 and 9 mm for the lower and higher alloyed steels, respectively), compared to plasma cutting (about 3 mm for both steels). No HAZ, microstructure, or hardness variation was observed for the water-jet cutting method. Therefore, in practice cutting of Ti-alloyed martensitic steels should be conducted using water-jet. Plasma cutting is acceptable if certain precautions are put in place, in particular, a maximum cutting speed is guaranteed. This would reduce the time of heat effect and potential implications on microstructure and properties.

2. With respect to microstructure-properties variation with steel composition and cutting method the following fundamental outcomes can be highlighted. Maximum tempering of microstructure (minimum absolute hardness values or maximum relative decrease in hardness associated with the tempering) was observed in the lower alloyed steel (due to weaker solid solution and precipitation strengthening) cut with oxy-fuel (characterised by higher heat input). Minimum tempering occurred in the more highly alloyed steel (due to stronger solid solution and precipitation strengthening) cut with

plasma (characterised by lower heat input). In the lower alloyed steel, coarse TiMoVCN, fine Ti-rich, and Fe_3C dissolved during thermal cutting. In the more highly alloyed steel, both coarse TiMoVCN and fine Ti-rich particles precipitated and grew, while Fe_3C dissolved. These discrepancies in the particle precipitation kinetics can be associated with the variation in steel composition: higher Ti, Mo, and C contents in the more highly alloyed steel (and concentrations of these elements in the matrix) increased the solubility temperatures of existing precipitates and the driving force for precipitation and growth of new particles. Precipitation of Ti-rich particles in the more highly alloyed steel during thermal cutting provided precipitation strengthening, which compensated for the softening associated with dislocation annihilation and dissolution of Fe_3C.

4.5 Cutting of 30/32 mm thick plates - Results

4.5.1 Cut-edge Hardness Variation

Steel samples of thickness 32mm & 30mm for both chemistries were subjected to thermal cutting using oxy-fuel, air plasma, and water-jet processes. Cut-edge of samples for both steels showed variation in through-thickness hardness (Figure 4.13).

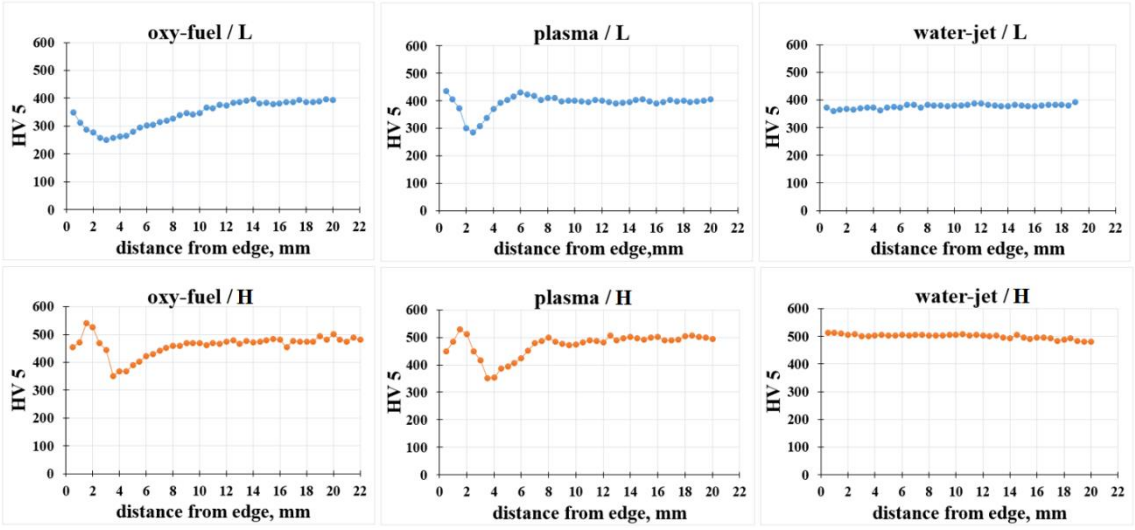

Figure 4.13 Hardness profiles for Steel L and Steel H cut with oxyfuel, plasma, and water-jet; each point on the hardness profiles is the mean value of 5 indentations made through the plate thickness.

For water-jet samples, it was insignificant but oxy-fuel and plasma cut samples showed a decrease in hardness near the cut edge for HAZ regions (2-4mm from the cut edge). The maximum decrease in hardness for Steel L (with oxy-fuel cutting method) was observed to be about 132HV and for Steel H (with oxy-fuel cutting method), it was around 131HV.

Steel L exhibited minimum hardness at 3mm and 2.5mm from the cut edge for oxy-fuel and plasma cutting processes, respectively. On the other hand, Steel H showed minimum hardness at 3.5mm from the cut edge for both oxy-fuel and plasma cutting processes. The variation in hardness was further studied with respect to microstructural changes to evaluate the HAZ properties.

4.5.2 Cut-edge Microstructural Variations

The etched samples showed the largest HAZ region for the oxyfuel cutting process as compared to plasma cut samples while waterjet cut samples showed the least or insignificant HAZ area (Figure 4.14). For both steels, the width of oxyfuel cut edge HAZ was noted to be 5 and 9mm for Steels L and H, respectively, while for the plasma cut edge HAZ was observed to be about 3mm wide. The variation in the HAZ width corresponds to a decrease in heat input from the oxy-fuel to plasma to water jet cutting method.

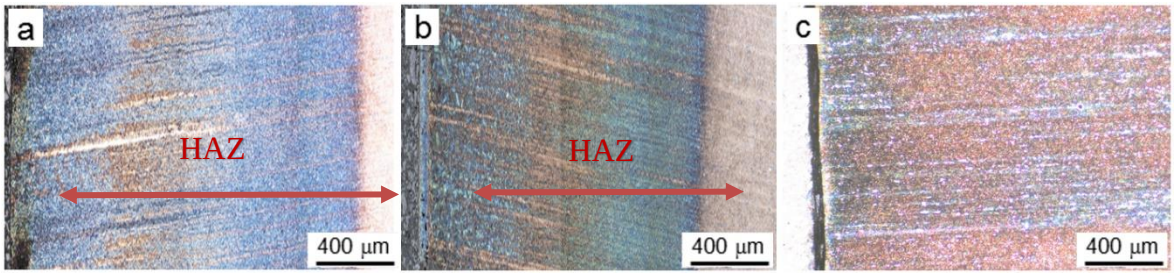

Figure 4.14 Optical microscopy images of heat affected zone in 30mm Steel H cut with (a) oxyfuel, (b) plasma, and (c) waterjet.

Further investigation was made through microstructural characterisation of grain size and carbide particles to analyse their role and impact as per variation observed for HAZ width and hardness profile. Optical microscopy and SEM imaging along with the EDS technique was used for this purpose.

4.5.3 Grain Size Measurements

Grain size in terms of equivalent grain diameter was measured for cut-edges of samples of both steels. SEM images (Figure 4.15 and 4.16) considered for evaluation were near the edge (at a distance of 0.5mm) and at the position of minimum hardness observed for oxyfuel and plasma cut samples. The results were compared with those of an unaffected

base area away from the cut edge. Martensite at the cut edge (at 0.5mm) showed higher hardness compared to tempered martensite and converted to bainite at the points of minimum hardness. Grains of irregular shapes were observed throughout the microstructure. The grain size was measured with respect to different cutting processes.

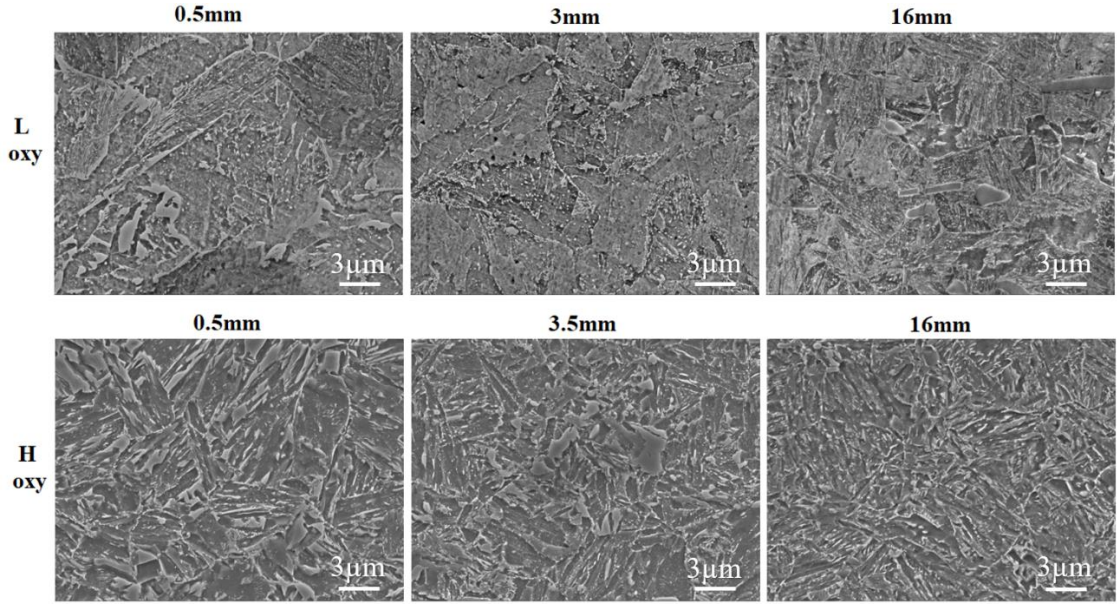

Figure 4.15, SEM images of grain structure in Steels L and H cut using oxy-fuel cutting method at the cut edge, point of minimum HV, and far away from the cut edge (base plate).

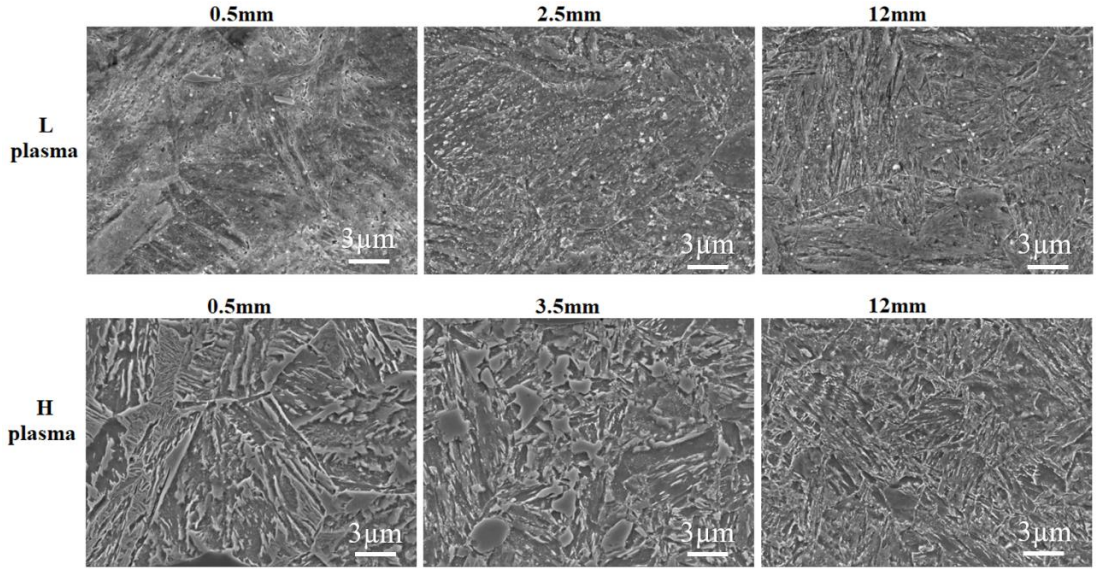

Figure 4.16 SEM images of grain structure in Steels L and H cut using plasma cutting method at the cut edge, point of minimum HV, and far away from the cut edge (base plate).

The base metal has a martensitic microstructure but thermal cycles, due to the cutting process, resulting in the formation of bainite along with martensite. It affected the average grain size (equivalent diameter) for both steels during oxy-fuel and plasma cutting processes as shown in Table- 4.6. At 0.5 mm, a higher value of grain size was noted with respect to that of base metal whereas a slight variation in grain size was noted at the points of lower hardness. Recrystallization may be another important factor that played its role in these regions. On the other hand, a negligible change of grain structure was observed for water jet cut samples.

Table 4.6, Average grain size in the studied steels.

Steel grade / cutting method	**Steel L**			**Steel H**		
	Oxy-fuel					
Position from cut edge	0.5 mm	3.0 mm	16 mm	0.5 mm	3.5 mm	16 mm
Average size, µm	4.1±0.0	2.9±0.1	3.3±0.3	4.3±0.2	4.0±0.2	3.1±0.04
	Plasma					
Position from cut edge	0.5 mm	2.5 mm	12 mm	0.5mm	3.5mm	12 mm
Average size, µm	5.2±0.9	3.7±0.2	3.6±0.4	3.9±0.3	3.8±0.4	3.7±0.2
	Water-jet					
Position from the cut edge	0.5 mm and 10 mm			0.5 mm and 10 mm		
Average size, µm	3.5±0.1			3.8±0.2		

4.5.4 Coarse Particles

Base metal regions of both steels when subjected to optical microscopy at a magnification of X500, revealed coarse carbide particles (Figure 4.17), whose size varied at the cut edge of samples due to different thermal effects of cutting processes. These carbide particles exhibited different shapes: rectangular, cuboidal, or elongated form. The microstructure observation at higher magnifications revealed needle-like as well as fine spherical particles. The size of carbide particles was larger in Steel H compared to Steel L (Table 4.7), which corresponds to higher contents of titanium and carbon in Steel H. SEM/EDS

mapping confirmed the coarse particles to be composed of carbon, titanium, molybdenum, vanadium, and nitrogen. The thermal cycle during cutting changed the coarse carbide particle sizes either due to dissolution or precipitation phenomena for both steels. These particles were found in different combinations like TiN, TiMoVC, and TiC rich particles, depending upon their relative precipitation temperatures.

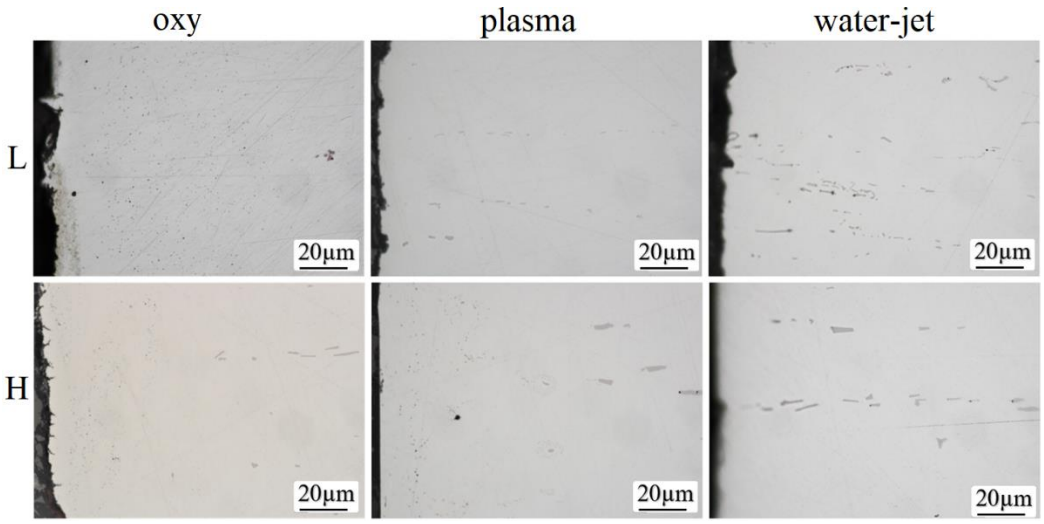

Figure 4.17 Optical images of Steel L and Steel H cut with the three studied methods (un-etched samples).

Steel L: At the points of minimum hardness (3mm for oxy-fuel and 2.5mm for plasma cut samples), Steel L showed a slight increase in average particle size. The number density of particles increased for oxy-fuel cut samples whereas decreased for plasma samples. The area fraction covered by particles for the oxy-fuel sample was calculated to be 0.0086 and for the plasma sample to be 0.0056. Near the cut edge at 0.5mm position, for the oxy-fuel sample, the average size decreased along with an increase in number density, the area fraction was calculated to be 0.0047. On the other hand, at 0.5mm for the plasma cut sample, the average size decreased along with the particle density, with respect to the base, and the area fraction was 0.0038. An increase in particle density indicates dissolution of coarse particles and possible growth of small particles to coarse sizes, associated with the thermal cycle effect. Water jet cut samples showed a minor change in particle parameters due to microstructural inhomogeneity.

Steel H: For the oxy-fuel cut sample, coarse TiMoVCN particles showed a slight decrease of average size at the points of minimum hardness (3.5mm) but increased again near the cut edge at 0.5mm. The reverse phenomenon was noted for particle density, which clearly indicates dissolution of coarse particles at 3.5mm and possible growth of these and smaller particles at 0.5mm, compared to those

at the base point of 16mm. The corresponding area fraction calculated for coarse particles was 0.0023, 0.0079, and 0.0178 at 0.5mm, 3.5mm, and 16mm respectively. For the plasma cut sample, though average particle size was reduced at the point of minimum hardness (3.5mm), yet no major change was observed in particle density. It still represents the dissolution of coarser particles to a smaller size at 3.5mm. At 0.5mm, the average size was increased due to the growth of smaller particles to larger sizes with the same number density of particles in the microstructure. The corresponding area fraction of coarse particles calculated was 0.0092, 0.0065, and 0.0098 at 0.5mm, 3.5mm, and 12mm, respectively. No significant change in the coarse particle parameters was observed for the samples cut with the water jet.

Table 4.7, Average parameters of coarse TiMoVCN particles studied with optical microscopy.

Steel grade / cutting method	**Steel L**			**Steel H**		
	Oxy-fuel					
Position from cut edge	0.5 mm	3.0 mm	16 mm	0.5 mm	3.5 mm	16 mm
Average size, µm	1.74	2.16	2.07	3.97	3.31	3.99
Number density, μm^{-2}	0.0046	0.0041	0.0033	0.0016	0.0028	0.0013
Area fraction of particles	0.0047	0.0086	0.0096	0.0023	0.0079	0.0178
	Plasma					
Position from cut edge	0.5 mm	2.5 mm	12 mm	0.5 mm	3.5 mm	12 mm
Average size, µm	1.66	2.22	1.79	4.16	2.66	2.71
Number density, μm^{-2}	0.0019	0.0018	0.0050	0.0023	0.0024	0.0029
Area fraction of particles	0.0038	0.0056	0.0061	0.0092	0.0065	0.0098
	Water-jet					
Position from cut edge	0.5 mm		15 mm	0.5 mm		15 mm
Average size, µm	2.14		2.04	2.12		3.28
Number density, μm^{-2}	0.0022		0.0037	0.0018		0.0017
Area fraction of particles	0.0078		0.0106	0.0018		0.0115

Distribution of Coarse Carbide Particles: Figure 4.18 shows the representation of the relationship between particle number density of coarse particles and their range of sizes

to study the effect of coarse particles distribution in the microstructure for both steels using oxy-fuel and plasma cutting methods.

At 0.5mm, the Steel L sample cut with oxy-fuel process showed a gradual increase in the particle density in the 1.5µm to ≤0.5µm size range, this corresponds to precipitation of smaller particles near the cut edge. For the Steel H sample cut with oxy-fuel, the maximum number density was observed for ≤ 0.5µm particles but this value is lower than that for the Steel L oxy cut sample. , Steel L cut with plasma showed no major variation in the particle number density distribution compared to this for the water jet cut sample. However, Steel H showed an increase in the particle density for ≤ 0.5µm particle sizes and a decrease in this for >0.5 µm particles.

Relationship for cutting process with respect to cut edge distance. For the oxy-fuel cutting process, Steel L showed an increase in the number density of <1.5µm particles closer to the cut edge, 0.5 mm and 3.0 mm positions (Figure 4.18c). Lower particle densities were observed in the >1.5µm particle size range at 0.5 mm distance. This supports the dissolution of larger particles to smaller sizes and the possible growth of smaller ones (not usually observed by optical microscopy) to larger sizes. In the base metal (16mm), moderate particle size was noticed along with particle density. On the other hand, in Steel L cut with plasma (Figure 4.18e), little precipitation was observed at 0.5mm and 2.5mm positions for particle sizes in the ≤3µm range. Larger particle sizes (1µm-2µm) were observed for the base at 12mm. It indicates the dissolution of larger particles without precipitation of smaller carbide particles. Steel H cut with the oxy-fuel process (Figure 4.18d), showed two types of particle sizes: ≤ 0.5µm ≥3µm. There were smaller particle sizes observed but of very minute number density. Similarly, for Steel H cut with plasma cutting method (Figure 4.18f), the majority of particles were ≤ 0.5µm and ≥ 3µm. In Steel, H cut with oxy-fuel the number of <0.5 µm particles increased towards the cut-edge, which might indicate growth of smaller particles. The dissolution of coarse particles was minor. After cutting with plasma no major variation in the particle distribution was observed, this may be explained by lower heat input compared to oxy-fuel (Figure 4.18f). For similar cutting processes, the following additional facts were noted:

a. A higher number density was observed in oxy cut Steel L sample for particle size in the range of ≤ 0.5µm-2.5µm at 0.5mm, 3mm, and 16mm distance from cut edge in comparison to Steel H sample, however, smaller number density was noted for particle

sizes ≥ 3µm in Steel L with respect to Steel H sample (Figure 4.17c and e). This indicates a higher rate of growth of particles in Steel L compared to Steel H.

b. For plasma cut samples, the Steel L sample showed lower precipitation of particle size ≤ 0.5µm compared to the Steel H sample at 0.5mm, while the particle density increased for larger particle sizes in the range of (0.5µm-2µm) at 0.5mm, 2.5mm and 12mm distance for Steel L with respect to Steel H, although there was a slight increase in the number density of ≥ 3µm particles in Steel H. This supports the dissolution of larger particles in Steel L and precipitation of smaller particles in Steel H.

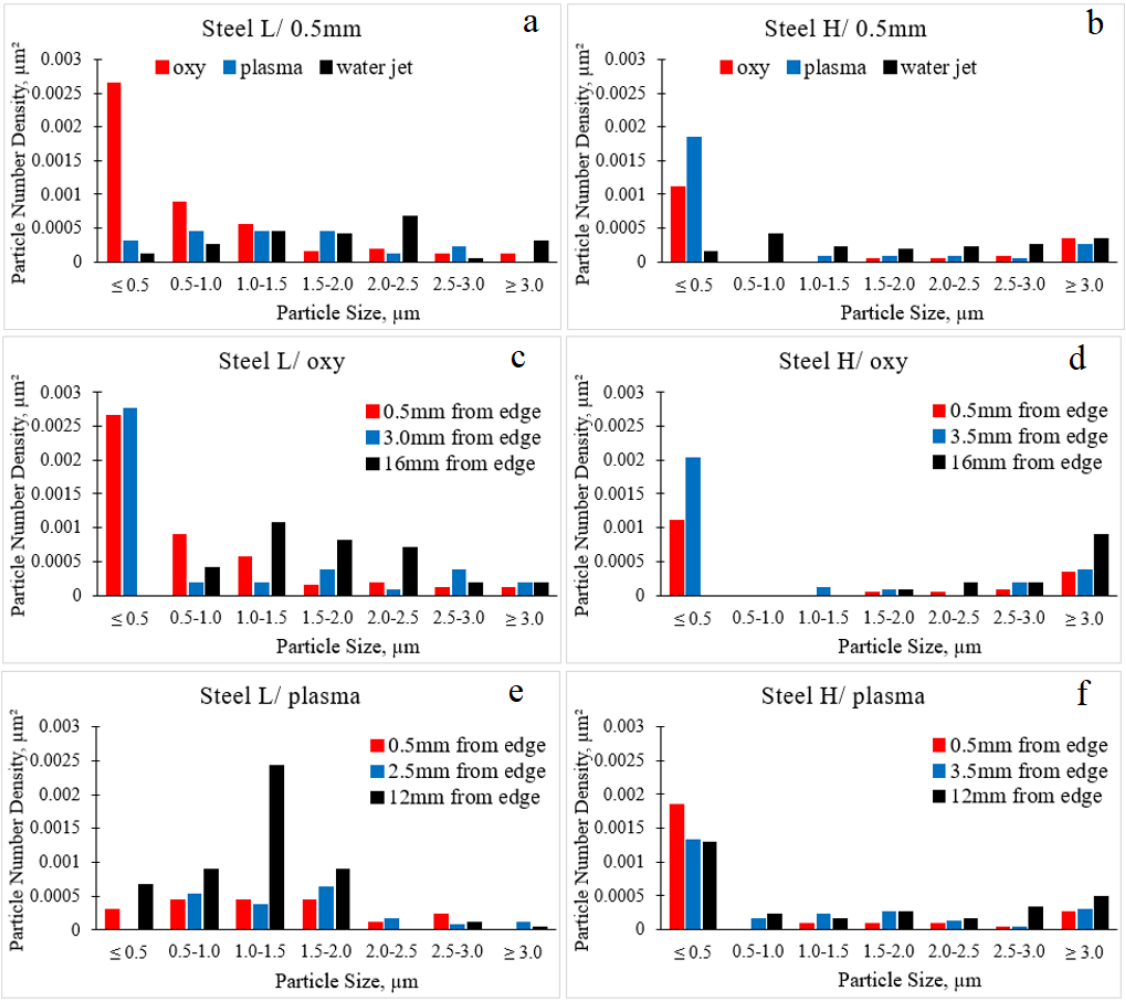

Figure 4.18 Coarse TiMoVCN particle number density distributions at 0.5 mm position from the cut edge in Steels (a) L and (b) H, for the samples cut with oxy-fuel in Steels (c) L and (d) H, and for the samples cut with plasma in Steels (e) L and (f) H

4.5.5 Fine Ti-rich Particles

Both steel samples were analysed for fine Ti-rich carbides at a higher magnification of up to 30000x using a scanning electron microscope (Figures 4.19, 4.20). The particles were observed to be cuboidal, spherical, or needle-shaped. The difference in particle morphology may depend upon the chemical composition and precipitation history. For a similar cutting process, i.e., oxy-fuel (Table 4.8), Steel L showed an increase in the average particle size and number density at 0.5 mm distance. Although, a more pronounced effect of particle growth was noted at 3 mm compared to the 0.5 mm position. This can be related to a slower cooling rate at a 3 mm position, compared to a 0.5 mm position, which would provide more time for the particle growth and precipitation. In contrast, Steel H cut with oxy-fuel showed a decrease in both average particle size and number density at 0.5 mm position, this is associated with the slight dissolution of particles in Steel H. For the plasma cutting method, Steel L showed a similar trend, i.e. both average particle size and number density increased at 0.5 mm and 2.5 mm position with respect to the base metal values, this supports precipitation with further growth of fine TiC particles in Steel L. Whereas, Steel H, at 0.5mm position showed a decrease in the average particle size and number density, this clearly indicates dissolution of fine particles. At 3.5 mm, the average particle size was found decreasing but the number density was increasing, which indicates dissolution of larger size particles to smaller particles along with precipitation of finer particles.

Steel L samples cut with both oxy-fuel and plasma cutting methods showed the average particle size and number density increasing at 0.5mm and 3mm positions with respect to the base metal. However, in Steel H the average particle size decreased closer to the cut edge for both cutting methods, and the number density exhibited a complex behaviour: increased at 3.5mm and decreased at 0.5 mm. These facts are co-related with the above results in terms of dissolution and precipitation phenomena of fine Ti-rich carbide particles: precipitation and growth of particles occurred in Steel L, while in Steel H the dissolution was the predominant effect at the 0.5 mm position and precipitation took place at 3.5 mm from the cut edge. Such a complex particle behaviour is related to two reasons: (i) the concentration of alloying elements in the steel matrix, dependent on the steel grade, and (ii) temperature gradient from the cut edge towards the base metal, which varies with the cutting method.

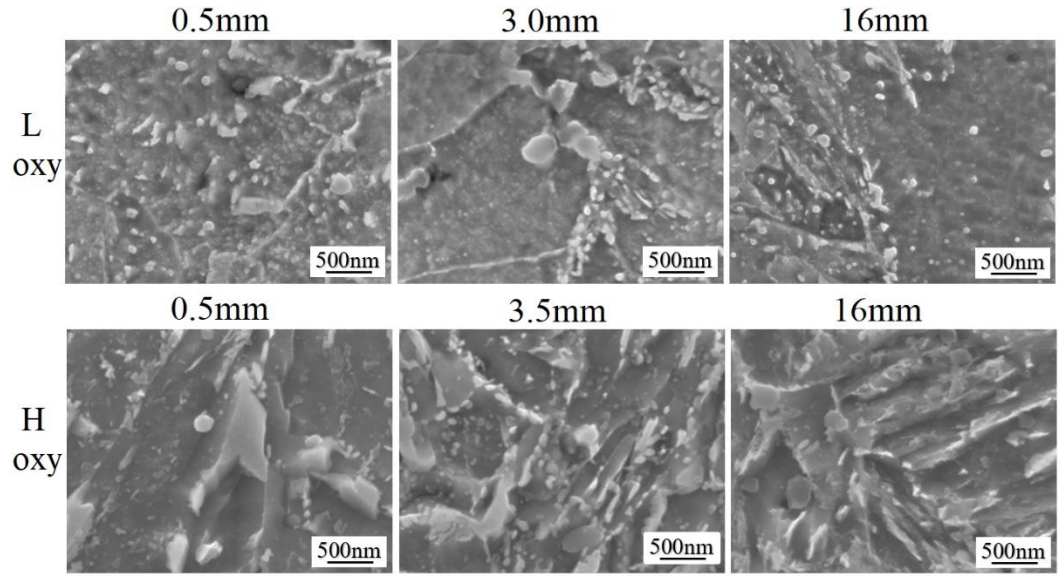

Figure 4.19 SEM images of fine precipitates in Steels L and H cut using oxy-fuel cutting method at the cut edge, point of minimum HV, and far away from the cut edge (base plate).

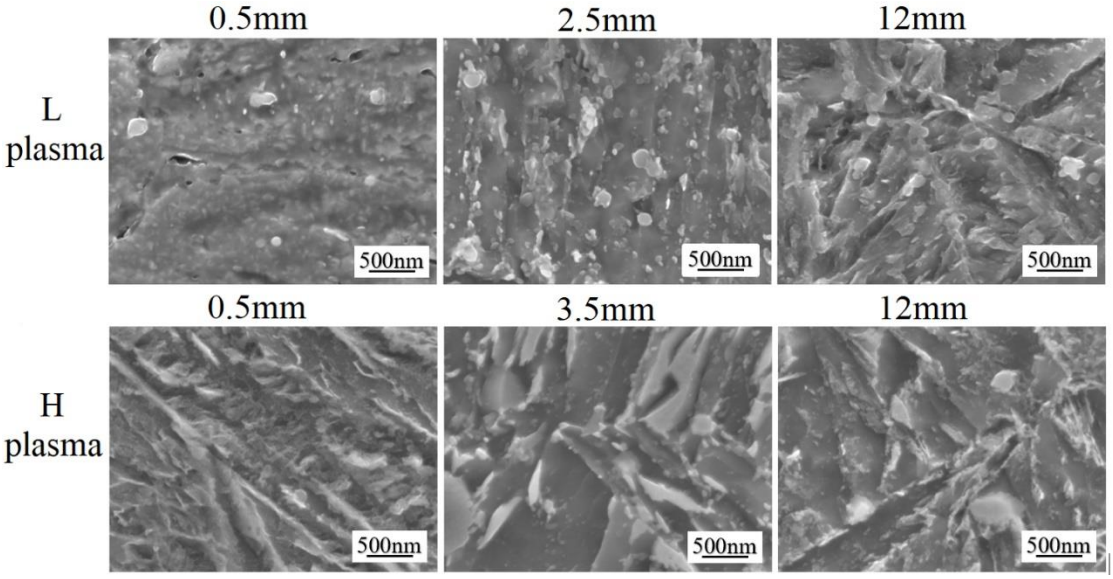

Figure 4.20 SEM images of fine precipitates in Steels L and H cut using plasma cutting method at the cut edge, point of minimum HV, and far away from the cut edge (base plate).

Table 4.8, Average parameters of fine Ti-rich particles studied with SEM.

Steel grade / cutting method	**Steel L**			**Steel H**		
	Oxy-fuel					
Position from cut edge	0.5 mm	3.0 mm	12 mm	0.5 mm	3.5 mm	16 mm
Average size, nm	94±30	117±26	86±5	118±3	124±40	207±2
Number density, μm^{-2}	1.62	1.99	0.92	0.61	1.65	0.79
Area fraction of particles	0.01	0.01	0.005	0.007	0.013	0.028
	Plasma					
Position from cut edge	0.5 mm	2.5 mm	12 mm	0.5 mm	3.5 mm	10 mm
Average size, nm	136±64	100±14	91±10	115±12	91±23	247±11
Number density, μm^{-2}	0.89	1.5	0.58	0.25	1.3	0.55
Area fraction of particles	0.01	0.009	0.006	0.002	0.007	0.027

To further elucidate the Ti-rich particle kinetics, the particle number density distributions were plotted against their sizes (Figure 4.21). Steel L cut with oxy-fuel method (Figure 4.21a) showed the number density of 40-60 µm particles increasing, this supports precipitation of particles compared to the base metal. For the plasma cutting process, Steel L showed a variation for number densities of different particle sizes. This means that the heat input effect on the particle behaviour was weaker during plasma cutting compared to the cutting with oxy-fuel. The Steel H sample cut with oxy-fuel method (Figure 4.21b) showed increased number densities of 20-80µm particles compared to the base metal, this is in line with particle dissolution in Steel H. For the plasma cut sample, lower densities were observed compared to the oxy cut sample. This supports a stronger heat effect during cutting with oxy-fuel. Comparison of both steels at 0.5mm position showed more precipitation in Steel L for both oxy-fuel and plasma cut samples, while less precipitation was noted for the Steel H sample.

The variations in particle number density distributions with distance from the cut edge after cutting with oxy-fuel are presented in Figures 4.21c and d. After cutting, the 20-60 µm particles showed a profound increase in their number density at a 3 mm distance. A qualitatively similar effect was noticed for 20-80µm particles at a 3.5 mm position in Steel H (Figure 4.21d). This means that dissolution at a 3.5mm distance from the cut edge was the major effect in Steel H, while in Steel L precipitation was the dominant effect.

For Steel L cut with plasma (Figure 4.21e), the maximum number density at 0.5 mm position was observed for 20-40µm particles, it decreased for 80-100 µm particles and then increased for 100-120µm particles. At 2.5 mm distance, the particle density was the highest for 20-80µm particles and then it decreased for 80-120µm ones. For the base metal, the maximum density was found for particle size of ≥ 120µm. These distributions indicate that slight precipitation occurred at 0.5mm and 2.5mm positions. For the plasma cut Steel H sample (Figure 4.21f), little precipitation was observed at 0.5mm distance; a minor number density peak was observed for particle sizes in the range of 20-40µm. A much higher number density of particles was observed at 3.5mm for particle sizes in the range of 20-80µm, and the density decreased for 80-120µm particles compared to the base metal. This indicates dissolution followed by substantial precipitation in Steel H at a 3.5 mm position.

With respect to the effect of the cutting method (compare Figure 4.21c and 4.21e), Steel L cut with oxy-fuel process showed more precipitation at 0.5mm and3mm positions, compared to cutting with plasma process. Steel H showed dissolution of larger particles to smaller sizes at 0.5mm and 3.5mm positions, and this seemed to be more pronounced during cutting with plasma, however, precipitation of smaller particles was more intense during cutting with oxy-fuel.

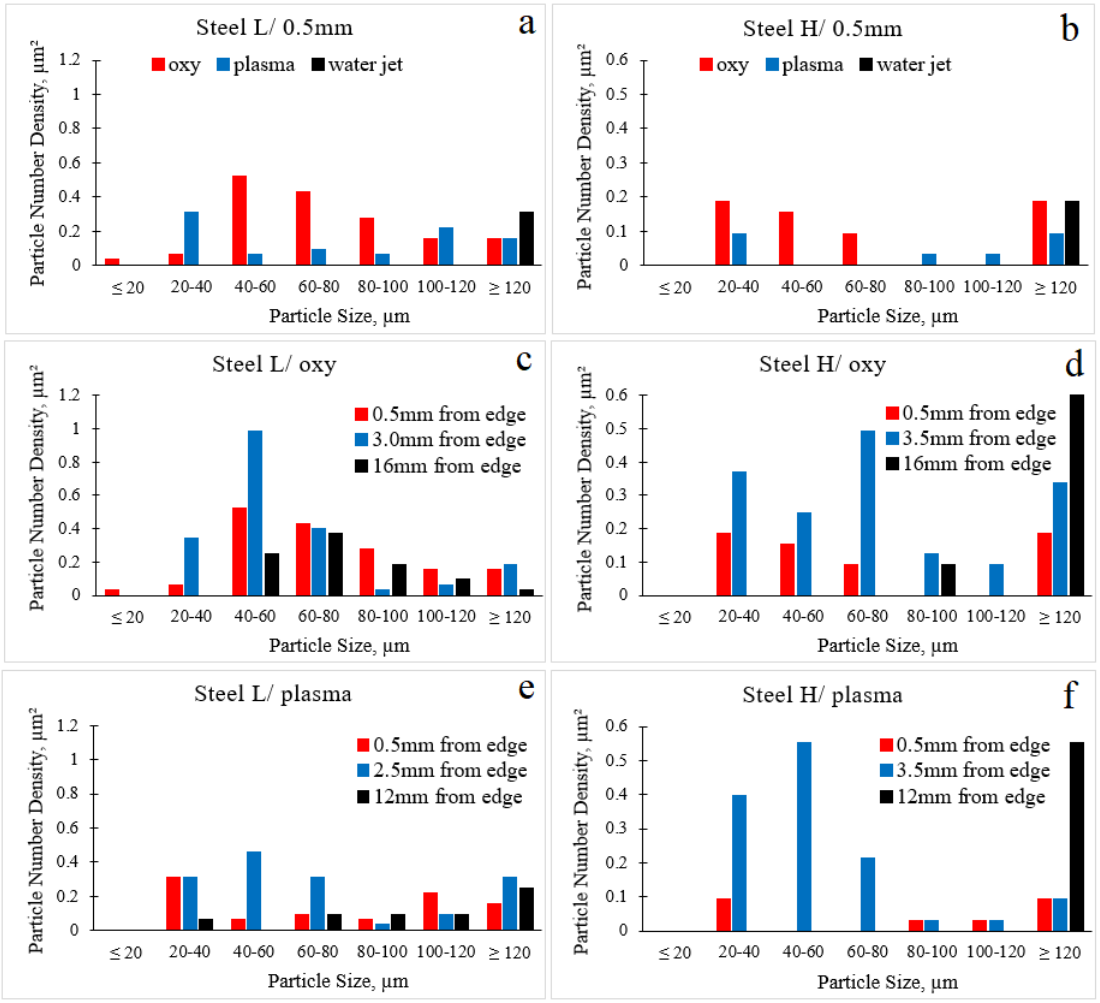

Figure 4.21 Fine Ti-rich particle number density distributions at 0.5 mm position from the cut edge for Steels (a) L and (b) H, for the samples cut with oxy-fuel for Steels (c) L and (d) H, and for the samples cut with plasma in Steels (e) L and (f) H

4.6 Cutting of 30/32 mm thick plates - Discussion

4.6.1 Influence of Steel Chemistry

The studied steel composition has a great impact on the hardness, strength, and toughness of these steels, but these properties may change due to thermal treatment. Steel H has higher Ti and C contents compared to Steel L. Usually, higher concentrations of Ti and C increase the solubility products of TiN and TiC particles [33, 34] and their precipitation start temperatures, this may lead to higher particle number densities at room temperature [35-37] and higher steel strength. However, in this project for oxyfuel and plasma cut samples of Steel L (Table 4.9), the number density of coarse TiMoVCN and fine TiC particles in the base metal were greater than in Steel H, this was accompanied by a larger average size of particles in Steel H. This may originate from a variation in the processing

parameters: the casting of a thinner slab, faster rolling speed and accelerated cooling after hot rolling might have reduced the tendency for particle growth in Steel L leading to their higher number density at room temperature. Higher particle number densities in Steel L, compared to Steel H, remained after thermal cutting for both methods and all positions. Despite higher particle densities, Steel L showed lower hardness for both cutting methods at all studied positions from the cut edge. It is worth remembering, that higher microalloying element concentrations (Ti, Mo, V, and N) in Steel H contribute towards its solid solution strengthening.

In both steels, the grain size (distance between the high angle boundaries across a martensitic or bainitic ferrite lath) slightly increased below the oxy-fuel and plasma cut edge (0.5 mm position) except for 3mm in Steel L oxy-fuel cut sample. The increase in grain size may be associated with a large prior austenite grain size occurring in the thermal cutting processing, compared to the hot rolling process: in fact, the accelerated cooling of austenite leading to the formation of martensite and bainite in the studied steels starts at higher temperatures, compared to hot rolling, thus a larger prior austenite grain size might be expected. Points of lowest hardness in both steels cut with both methods corresponded to the maximum values of fine Ti-rich particle number density. If due to Ti-rich particle precipitation the matrix was depleted in C, N, and Mo it would support the decrease in hardness due to a decrease in solid solution strengthening. The base metal grain size was similar in both steels and probably did not contribute significantly to the observed variation in hardness between the two steel.

Recovery and recrystallization in the HAZ also contribute to a decrease in hardness, irrespective of the particle precipitation kinetics, because the number of dislocation interactions is the main cause of strength and not the number of particles distributed in microstructure s. Recovery might be expected at a farther distance from the cut edge where austenitisation, leading to the martensitic transformation, did not happen due to lower temperatures. This would be another source of hardness decrease at 2.5-3.5 mm positions.

Table 4.9. Correlation of the microstructural parameters and hardness to steel grade and cutting method.

Steel grade/ cutting method		Steel L			Steel H		
		Oxy-fuel					
Position from cut edge		0.5mm	3mm	16mm	0.5mm	3.5mm	16mm
Average grain size, μm		4.1±0.0	2.9±0.1	3.3±0.3	4.3±0.2	4.0±0.2	3.1±0.4
Number density, μm^{-2}	Coarse Ti-rich particles	0.0046	0.0041	0.0033	0.0016	0.0028	0.0013
	Fine Ti-rich particles	1.62	1.99	0.92	0.61	1.65	0.79
Hardness		350	250	381	453	351	483
Plasma							
Position from cut edge		0.5mm	2.5mm	12mm	0.5mm	3.5mm	12mm
Average grain size		5.2±0.9	3.7±0.2	3.6±0.4	3.9±0.3	3.8±0.4	3.7±0.2
Number density, μm^{-2}	Coarse Ti-rich particles	0.0019	0.0018	0.0050	0.0023	0.0024	0.0029
	Fine Ti-rich particles	0.89	1.5	0.58	0.25	1.3	0.55
Hardness		434	284	395	449	352	481

4.6.2 Impact of Cutting Process

Oxy-fuel Cutting Process: Both Steel L and Steel H oxy-fuel cut samples showed the largest grain size at 0.5 mm and demonstrated precipitation of coarse and fine Ti-rich particles. For Steel L, minimum hardness was observed at 3 mm position, while for Steel H it was at 3.5 mm distance from the cut edge. Steel H showed the microstructural variations, due to heat effect, at a longer distance, compared to Steel L. This originated from a high heat input required to cut Steel H, compared to Steel L, due to its higher C and other microalloying elements contents.

Plasma Cutting Process: Steel L and Steel H plasma cut samples showed the largest grain size at 0.5 mm. Both steels demonstrated growth of coarse and precipitation of fine Ti-rich particles. Potentially higher solute concentrations of Ti, Mo, and C in the Steel H matrix not only retarded recovery but also facilitated solid solution strengthening and precipitation and growth of new particles during thermal cutting [57-59]. For Steel L, minimum hardness was observed at 2.5mm, while for Steel H it was at 3.5mm from the cut edge. A larger size of HAZ in Steel H occurred due to the requirement of high heat input to cut Steel H.

Relationship of Cutting Processes with respect to steel composition: Steel H oxy-fuel cut samples showed wider HAZ compared to Steel L, this indicates a higher heat input leading to a wider tempering zone in Steel H. Due to the oxy-fuel cutting being a burning technique, which has a wider heating effect compared to plasma cutting leading to melting of the localized area of material, the HAZ is larger for oxy-fuel, although cutting temperature of plasma arc is around 20000 °C [32] compared to oxy-fuel 3500 °C [30]. Hence, the melting of the material during the plasma cutting process gives less time for heat transfer towards the base plate while the burning phenomenon gives a more pronounced tempering effect.

4.7 Conclusion

In this study, behaviour of two different types of Q&T martensitic wear-resistant Ti-microalloyed steels (of thickness 32mm and 30mm), containing 0.28C-0.4Ti and 0.38C-0.6Ti (wt. %) was investigated with respect to conventional thermal cutting processes. A decrease in HAZ hardness revealed the microstructural changes associated with heat input. The following conclusions can be made out of the study of cutting of 30/32 mm plates:

1. A decrease in hardness for water-jet cut samples was not prominent but oxy-fuel and plasma cut samples showed a decrease in hardness near the cut edge through the HAZ regions. The maximum decrease in hardness for Steel L (with the oxy-fuel cutting method), was observed to be about 131HV and for Steel H (with oxy-fuel cutting method), it was around 132HV. Oxy-fuel cutting produced a wider heat-affected zone (HAZ) (8-12 mm), compared to plasma cutting (about 6-8 mm) for both steels. Hence, the water-jet cutting method is the most preferable to the other two methods, while the plasma method is better than the oxy-fuel cutting method. Such preference is stipulated

not only due to economic reasons but also due to better microstructural parameters and mechanical properties of steel. It will also save fabrication time.

2. Microstructural study of Steel L and Steel H indicated the high impact of the thermal cycle for different chemistries, specifically with respect to C and Ti contents. Low hardness observed for Steel L showed a more tempered microstructure than for Steel H in similar conditions of oxyfuel and plasma cutting methods. Both steels showed grain size growth, however, in oxy-fuel cut samples, it was greater than in plasma cut samples. Oxy-fuel cut samples of both steels exhibited precipitation of coarse and fine particles for low hardness points while plasma cut samples of both steels showed dissolution of coarse particles resulting in precipitation of more fine particles in the microstructure. Although more precipitation occurred for Steel L, yet Steel H showed more solid solution strengthening with high hardness due to higher C, Mo, and Ti contents.

References (Chapter 4)

1. K. Maweja, W. Stumpf, *Fracture and ballistic-induced phase transformation in tempered martensitic low-carbon armour steels*, Materials Science and Engineering A, 432 (1-2) (2006) 158-169.
2. K. Maweja, W. Stumpf, *The design of advanced performance high strength low-carbon martensitic armour steels: Microstructural considerations*, Materials Science and Engineering A, 480(1-2) (2008) 160-166.
3. P. K. Jena, K.Siva Kumar, V.Rama Krishna, A.K. Singh, T. Balakrishna Bhat, *Studies on the role of microstructure on performance of a high strength armour steel*, Engineering Failure Analysis, 15(8) (2008) 1088-1096.
4. P. K. Jena, Bidyapati Mishra, M.Ramesh Babu, Arvindha Babu, A.K. Singh, K. SivaKumar, T. Balakrishna Bhat, *Effect of heat treatment on mechanical and ballistic properties of a high strength armour steel*, International Journal of Impact Engineering, 37(3) (2010) 242-249.
5. S. Karagoz, S. H. Atapek, A. Yilmaz, *Microstructural and fractographical studies on quenched and tempered armor steels*, Materialpruefung 52(5) (2010) 316-322.
6. R. L. O'Brien, Welding Handbook, American Welding Society, Miami, USA, 2 (1991).
7. J. C. Ritter, B. F. Dixon, N. J. Baldwin, *Deformation and weld repair of armour steel*, Material Forum 13 (1989) 216-224.
8. N. Yurioka, H. Suzuki, *Hydrogen assisted cracking in C-Mn and low alloy steel weldments*, International Materials Reviews 35(1) (1990) 217-249.
9. G. Magudeeswaran, V. Balasubramanian, G. Madhusudhan Reddy, *Hydrogen induced cold cracking studies on armour grade high strength, quenched and tempered steel weldments*, International Journal of Hydrogen Energy 33(7) (2008) 1897-1908.
10. L. Kuzmikova, M. Callaghan, N. Larkin, R. Scott, R. De-Jong, H. Li, J. Norrish, *A study of a continuous cooling behaviour and effect of preheating and inter-pass temperature on the HAZ of high strength quenched and tempered steel*, Doc IX-2352-10, IIW Annual Assembly, Istanbul, Turkey (2010) 11–18.

11. I. Barenyi, O. Hires, P. Liptak, *Degradation of mechanical properties of armoured steels after its welding*, Proceedings of International Conference of Scientific Paper, AFASES2011, Brasov, Romania, (2011) 845-848.
12. I. Barenyi, O. Hires, P. Liptak, *Over tempering of armox armoured steels at their secondary processing*, in Proceedings of International Conference of Scientific Paper, AFASES2012, Brasov, Romania, (2012) 641-643.
13. L. Kuzmikova, N. Larkin, Z. Pan, M. Callaghan, H. Li, J. Norrish, *Investigation into the feasibility of hybrid laser-GMAW process for welding high strength quenched and tempered steel*, Australasian Welding Journal 57 (2012) 1-9.
14. X. Xu, W. Xu, F. H. Ederveen, S. van der Zwaag, *Design of low hardness abrasion resistant steels*, Wear 301(1-2) (2013) 89-93.
15. N. Ojala, K. Valtonen, V. Heino, M. Kallio, J. Aaltonen, P. Siitonen, V. T. Kuokkala, *Effects of composition and microstructure on the abrasive wear performance of quenched wear-resistant steels*, Wear 317 (2014) 225–232.
16. X. Deng, Z. Wang, Y. Han, H. Zhao, G. Wang, *Microstructure and Abrasive Wear Behavior of Medium Carbon Low Alloy Martensitic Abrasion Resistant Steel*, Journal of Iron and Steel Research, International, 21(1)(2014) 98-103.
17. M. Lindroos, K. Valtonen, A. Kemppainen, A. Laukkanen, K. Holmberg, V.-T. Kuokkala, *Wear behavior and work hardening of high strength steels in high-stress abrasion*, Wear 322-323 (2015) 32–40.
18. T. S. Wang, B. Lu, M. Zhang, R. J. Hou, F. C. Zhang, *Nano-crystallization and martensite formation in the surface layer of medium-manganese austenitic wear-resistant steel caused by shot peening*, Materials Science and Engineering A 458 (2007) 249–252.
19. G. Bregliozzi, A. Di Schino, J.M. Kenny, H. Haefke, *The influence of atmospheric humidity and grain size on the friction and wear of AISI 304 austenitic stainless steel*, Materials Letters 57 (2003) 4505– 4508.
20. V. Abouei, H. Saghafian, Sh. Kheirandish, Kh. Ranjbar, *An investigation of the wear behaviour of 0.2% C dual-phase steels*, J. Materials Processing Technology 203 (2008) 107–112.
21. K.-H. Zum Gahr, *Microstructure and Wear of Materials*, Elsevier Science Ltd., Amsterdam, (1987) 559.

22. X. Wang, Y. Chen, S. Wei, L. Zuo, F. Mao, *Effect of carbon content on abrasive impact wear behavior of Cr-Si-Mn low alloy wear-resistant cast steels*, Frontiers in Materials, 6 (2019) paper 153.
23. Y. J. Kang, J. C. Oh, H. C. Lee S. Lee, *Effects of carbon and chromium additions on the wear resistance and surface roughness of cast high-speed steel rolls*, Metallurgical and Materials Transactions A 32 (2001) 2515 – 2525.
24. A. K. Bhakat, A. K. Mishra, N. S. Mishra, *Characterization of wear and metallurgical properties for the development of agricultural grade steel suitable in specific soil conditions*, Wear 263 (2007) 228–233.
25. L. Tang, C. Gao, J. Huang, H. Zhang, W. Chang, *Dry sliding friction and wear behaviour of hardened AISI D2 tool steel with different hardness levels*, Tribology International 66 (2013) 165–173.
26. K. I. Parashivamurthy, R. K. Kumar, S. Seetharamu, M. N. Chandrasekharaiah, *Review on TiC reinforced steel composites*, Journal of Materials Science 36 (2001) 4519 – 4530.
27. Y. Han, J. Shi, L. Xu, W.Q. Cao, H. Dong, *Effects of Ti addition and reheating quenching on grain refinement and mechanical properties in low carbon medium manganese martensitic steel*, Materials, and Design, 34 (2012) 427-434.
28. A. G. Kostryzhev, C. R. Killmore, D. Yu, E. V. Pereloma, *Martensitic wear-resistant steels alloyed with titanium*, Wear, 446-447 (2020) article 203203.
29. L. A. Zeatoun, P. W. Morrison Jr, *Optimizing diamond growth for an atmospheric oxyacetylene torch*, Journal of Materials Research, 12(5) (1997) 1237-1252.
30. https://www.twi-global.com/technical-knowledge/job-knowledge/cutting-processes-application-of-oxyfuel-cutting-050 accessed on 20.12.2019.
31. D. J. Eyres, *Welding and cutting processes used in shipbuilding*: in Ship Construction, ed. D.J. Eyres, Butterworth-Heinemann, Oxford, (2007) 75-96.
32. https://www.twi-global.com/technical-knowledge/job-knowledge/cutting-processes-plasma-arc-cutting-process-and-equipment-considerations-051 accessed on 20.12.2019.
33. H. S. El-Faramawy, S. N. Ghali, M. M. Eissa, *Effect of Titanium Addition on Behavior of Medium Carbon Steel*, Journal of Minerals and Materials Characterization and Engineering 11 (2012) 1108-1112.

34. J. Strid, K. E. Easterling, *On the chemistry and stability of complex carbides and nitrides in microalloyed steels*, Acta metal 33(11) (1985) 2057-2074.
35. L.A. Dobrzanski, A. Zarychta, M. Ligarski, *High-speed steels with addition of niobium or titanium*, J. Material Processing Technology, 63 (1997) 531-541.
36. R. Soto, W. Saikaly, X. Bano, C. Issartel, G. Rigaut, and A. Charai, *Statistical and theoretical analysis of precipitates in dual-phase steels microalloyed with titanium and their effect on mechanical properties*, Acta Materialia 47(12) (1999) 3475 – 3481.
37. W.-T. Yu, J. Li, C.-B. Shi, Q.-T. Zhu, *Effect of Titanium on the Microstructure and Mechanical Properties of High-Carbon Martensitic Stainless Steel 8Cr13MoV*, Metals 2016, 6, 193; doi:10.3390/met6080193
38. H. K. D. H. Bhadeshia, S. R. Honeycombe, Steels, *microstructure and properties*, 3rd edition. Butterworth-Heinemann, Oxford, (2006) 183-208.
39. G. Krauss, *Tempering of Lath Martensite in Low and Medium Carbon Steels: Assessment and Challenges*, Steel research int. 88 (10) (2017) paper 1700038.
40. B. Pawłowski, Critical points of hypoeutectoid steel - prediction of the pearlite dissolution finish temperature Ac1f, Journal of Achievements in Materials and Manufacturing Engineering, 49 (2011) 331-337.
41. J. Trzaska, L.A. Dobrzanski, *Modelling of CCT diagrams for engineering and constructional steels*, Journal of Materials Processing Technology 192–193 (2007) 504–510.
42. Q. Lu, W. Xu, S. van der Zwaag, *Designing new corrosion-resistant ferritic heat resistant steel based on optimal solid solution strengthening and minimisation of undesirable microstructural components*, Computational Materials Science 84 (2014) 198–205.
43. J. Kong, C. Xie, *Effect of molybdenum on continuous cooling bainite transformation of low-carbon microalloyed steel*, Materials and Design 27 (2006) 1169–1173.
44. H. Hu, G. Xu, M. Zhou, Q. Yuan, *Effect of Mo Content on Microstructure and Property of Low-Carbon Bainitic Steels*, Metals 6 (2016) paper 173.
45. S. Mukherjee, I. Timokhina, C. Zhu, S. P. Ringer, P. D. Hodgson, *Clustering and precipitation processes in a ferritic titanium-molybdenum microalloyed steel*, Journal of Alloys and Compounds 690 (2017) 621 – 632.

46. S. Dhara, R.K.W. Marceau, K. Wood, T. Dorin, I.B. Timokhina, P.D. Hodgson, *Precipitation and clustering in Ti-Mo steel investigated using atom probe tomography and small-angle neutron scattering*, Materials Science and Engineering A 718 (2018) 74–86.
47. C.-Y. Chen, J.-R. Yang, C.-C. Chen, S.-F. Chen, *Microstructural characterization and strengthening behavior of nanometer sized carbides in Ti-Mo microalloyed steels during continuous cooling process*, Materials Characterization 114 (2016) 18–29.
48. H. S. El-Faramawy, S. N. Ghali, M. M. Eissa, *Effect of Titanium Addition on Behavior of Medium Carbon Steel*, Journal of Minerals and Materials Characterization and Engineering 11 (2012) 1108-1112.
49. K. Zhang, Z.-D. Li, X.-J. Sun, Q.-L. Yong, J.-W. Yang, Y.-M. Li, P.-L. Zhao, *Development of Ti–V–Mo complex microalloyed hot-rolled 900MPa grade high strength steel*, Acta Metall. Sin. (Engl. Lett.), 28(5) (2015) 641–648.
50. Z. Wang, H. Zhang, C. Guo, W. Liu, Z. Yang, X. Sun, Z. Zhang, F. Jiang, *Effect of molybdenum addition on the precipitation of carbides in the austenite matrix of titanium micro-alloyed steels*, J Mater Sci 51 (2016) 4996–5007.
51. A. K. Tingaev, R. G. Gubaydulin, I. A. Ilin, *Study of the effect of thermal cutting on the microstructure and chemical composition of the edges of workpieces made of steel brands S345, S390*, Procedia Engineering 150 (2016) 1783 – 1790.
52. I. A Ilin, A. A. Krasnoperova, E. A. Sirotkin, *Effect study of thermal cutting methods on the edge's microstructure of high-strength steel grade S700MC*, Materials Science Forum, 946 (2019) 928-933.
53. S. S. Pawar, K. H. Inamdar, *Analysis of heat affected zone in plasma arc cutting of SS 316L plates*, International Journal of Innovative Research in Science, Engineering and Technology, 6(5) (2017) 8160-8165.
54. A. Gustafson, *Coarsening of TiC in austenitic stainless steel - experiments and simulations in comparison*, Materials Science and Engineering A287 (2000) 52-58.
55. A. R. Jones, B. Ralph, *Growth and dissolution of NbC particles in an austenitic stainless steel*, Metallography 10 (1977) 469-480.
56. P. Gong, E. J. Palmiere, W. M. Rainforth, *Dissolution and precipitation behaviour in steels microalloyed with niobium during thermomechanical processing*, Acta Materialia 97 (2015) 392-403.

57. J. E. Morral, G. R. Purdy, *Particle coarsening in binary and multicomponent alloys*, Scripta Metallurgica et Materialia, 30(7) (1994) 905-908.
58. S. Papaefthymiou, M. Bouzouni, E. Gavalas, *Theoretical study of particle dissolution during homogenization in Cu-Fe-P alloy*, Metals 2018, 8, 455; doi:10.3390/met8060455.
59. F. Abe, M. Murata, H. Miyazaki, *Effect of TiC and NbC carbides on creep life of stainless steels*, Materials at High Temperatures, 36(1) (2019) 35–47.

Chapter 5

5 Effect of preheating temperature on weld cracking propensity

5.1 Introduction

Currently, the fabrication of steel structures is carried out using conventional fusion arc welding processes. Susceptibility of the microstructure to cold cracking and hydrogen-induced cracking (HIC) is a large problem [4-10]. In general, it increases with an increase in weld metal strength, hydrogen content, and section thickness [11, 12], and this dependence is more complex than heat affect zone (HAZ) cracking [11]. Weldability tests can be used to examine the effects of various factors on cracking susceptibility, such as parent metal composition, welding consumable type, preheat temperature, and other welding conditions [13]. During welding, the area surrounding the weld pool (HAZ) undergoes a complex thermal cycle [14], which causes drastic microstructural changes, particularly the grain size of the base metal. Grain size is one of the key factors in determining the strength and toughness of material as well as the alloy's susceptibility to cold cracking [15] *p135*. Whether HIC will occur relies on three aspects occurring simultaneously: a susceptible microstructure; type and magnitude of residual stresses; and importantly, the level of diffusible hydrogen that enters the weld pool [16]. Cracks typically form in the coarse-grained (CG) sub-zone of the HAZ, which has been exposed to temperatures between 1100-1450°C [17]. It has been shown that the risk of CGHAZ cracking is linearly related to the austenite-to-ferrite transformation temperature, as well as to martensite finish (Mf) temperature during transformation, both of which may be predicted from experimental cooling curves [18]. In this chapter, a series of weldability tests were conducted in accordance with ISO 17642-2-2005 to determine the susceptibility of Ti-microalloyed steels for cold cracking after welding, under conditions of high restraint and controlled heat input. Several test assemblies were subjected to five different preheat temperatures along with optimum welding conditions to produce crack-free welds, using the "Controlled Thermal Severity" (CTS) test arrangement. The tests were conducted for two types of high strength Q&T martensitic steel grades, i.e., Steel L

and Steel H, with thicknesses of 12 mm and 32/30mm (Table 5.1). The flux-cored arc welding (FCAW) process was used along with welding electrodes ER309Si (for anchor welds) and E91T1-GM H4 [20] (for test welds) having 1.2 mm diameter. To investigate the cold cracking susceptibility of welded test coupons with different preheat temperatures, the test welds were subjected to hardness testing and metallurgical examination after 48 hrs of the welding operation. This assisted in understanding the relationship between welding preheat temperatures and cold cracking due to hydrogen adsorption.

5.2 Results

5.2.1 Welding Parameters

The welding parameters used in CTS testing are shown in Table 5.1.

Table 5.1 Welding parameters used in CTS testing series.

Steel Grades, Thickness	Sample IDs	Preheat Temps. (˚C)	Electrode AWS-Class	Current (A)	Voltage (V)	Travel Speed (mm/ min)	Heat Input (kJ/mm)
Steel L 12mm	1E12 2E12 3E12 4E12 5E12	Room Temp., 40, 60, 80, 100	ER309Si for Anchor welds and E91T1-GM H4 for Test welds Trade name: OUTER SHIELD 91Ni1-HSR	191-214	26.3-27.3	4.35	1.16-1.31 (Avg. 1.2)
Steel L 32mm	1E32 2E32 3E32 4E32 5E32			214-241	28.1	3.83	1.57-1.72 (Avg. 1.6)
Steel H 12mm	1C12 1C12 1C12 1C12 1C12	Room Temp., 60, 90, 120, 150		188-213	26.4	4.35	1.14-1.29 (Avg. 1.2)
Steel H 30mm	1C30 2C30 3C30 4C30 5C30			216-237	28.1	3.83	1.58-1.74 (Avg. 1.6)

5.2.2 Metallographic examination and hardness testing

Each welded test coupon was at first cut into two parts and then four equal sections, as shown in Figure 5.1. The test pieces were machined on their faces perpendicular to the weld to perform a metallographic and hardness examination (Figure 5.2). Optical imaging, conducted at a minimum magnification of x50, has revealed cracked and crack-free microstructures in the HAZ (Tables 5.2-5.5).

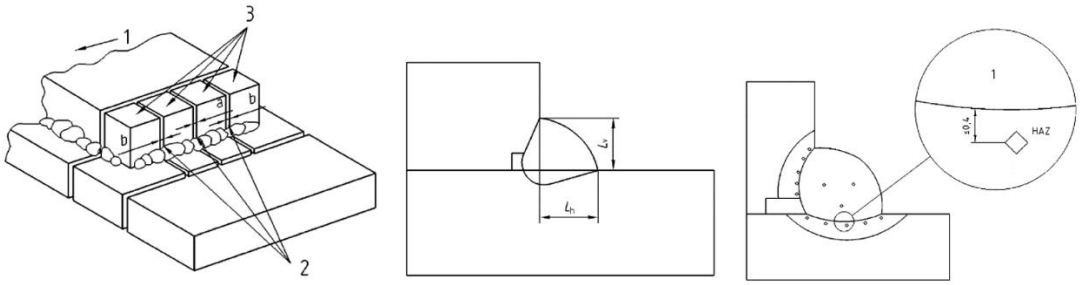

Legend:

a,b faces polished and examined for cracking and hardness measurement

L_h horizontal weld leg length (mm)

Lv vertical weld leg length (mm)

Figure 5.1 Sectioning of welded test coupon for metallographic and hardness examination [19].

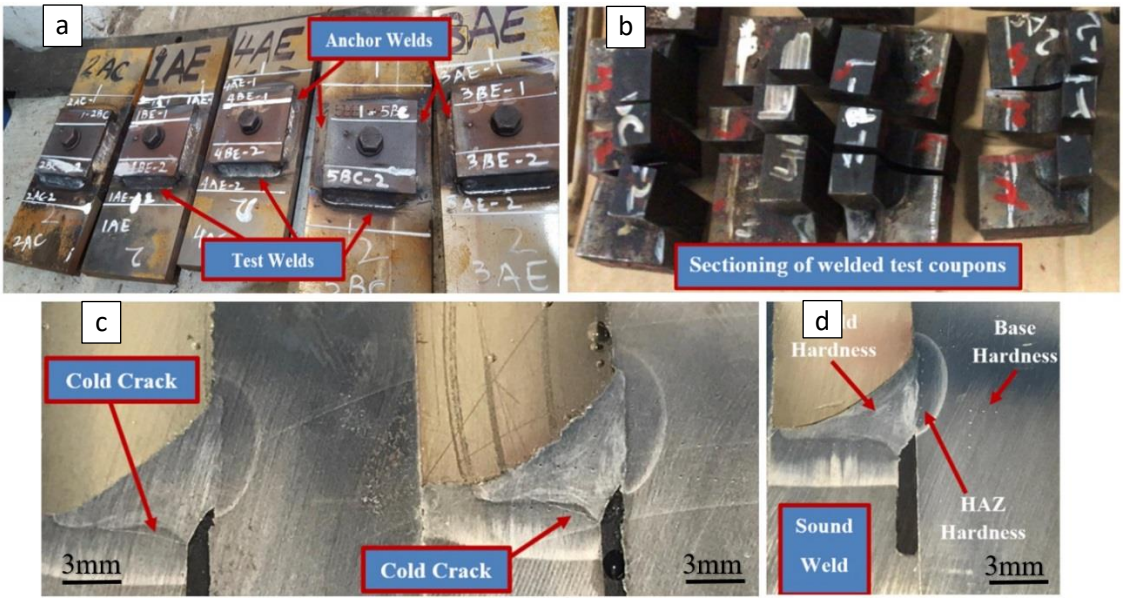

Figure 5.2 (a) Welded test pieces during CTS testing, (b) cut coupons for metallographic examination, (c) optical imaging of cracks, and (d) hardness measurements.

Table 5.2 Metallographic and hardness examination results for *12 mm plates of Steel L*.

Preheat Temp (˚C)	Sample ID	Metallographic Examination		Average Hardness, HV5			
		Mean Leg Length $(L_h + L_v)/2$, (mm)	Result (Cracked)	HAZ		Weld Metal	Parent Metal
				Horizontal	Vertical		
RT	1E12-1	(8.25+6)= 7.12	Yes	522	507	405	437
	1E12-2	(6.5+6.25)= 6.37	Yes	503	507	363	433
40	2E12-1	(6+6.75)/2= 6.37	Yes	482	482	374	414
	2E12-2	(7+7.5)/2= 7.25	Yes	538	490	380	445
60	3E12-1	(6.25+7.5)/2= 6.8	Yes	500	499	402	483
	3E12-2	(6.5+7.2)/2= 6.85	No	487	464	307	414
80	4E12-1	(6.7+7.3)/2= 7.00	No	468	488	325	474
	4E12-2	(5.75+7)/2=6.37	No	517	498	365	464
100	5E12-1	(5.75+6.25)/2= 6	No	531	518	350	436
	5E12-2	(5.5+6.25)/2= 5.87	No	539	502	378	486
Average values		6.6±0.7	-	504±35	491±27	356±31	450±36

Table 5.3 Metallographic and hardness examination results for *32 mm plates of Steel L*.

Preheat Temp (˚C)	Sample ID	Metallographic Examination		Average Hardness, HV5			
		Mean Leg Length $(L_h + L_v)/2$, (mm)	Result (Cracked)	HAZ		Weld Metal	Parent Metal
				Horizontal	Vertical		
RT	1E32-1	(5.75+8)/2= 6.87	No	505	528	426	438
	1E32-2	(7.5+7.5)/2= 7.5	Yes	513	488	396	329
40	2E32-1	(7.2+7.6)= 7.4	Yes	447	412	394	440
	2E32-2	(7.5+7.5)/2= 7.5	No	495	466	397	468
60	3E32-1	(7.5+7.25)/2= 7.37	Yes	479	485	379	426
	3E32-2	(8.75+7.5)= 8.12	No	489	506	380	433
80	4E32-1	(7.75+7.5)/2= 7.62	No	451	496	337	395
	4E32-2	(7.25+6.75)/2= 7.0	No	505	498	368	475
100	5E32-1	(8+6.75)/2= 7.37	No	477	507	375	441
	5E32-2	(7.5+8)/2= 7.75	No	453	519	354	478
Average values		7.5±0.6	-	482±31	470±57	382±44	404±74

Table 5.4 Metallographic and hardness examination results for *12 mm plates of Steel H*.

Preheat Temp (˚C)	Sample ID	Metallographic Examination		Average Hardness, HV5			
		Mean Leg Length ($L_h + L_v$)/2, (mm)	Result (Cracked)	HAZ		Weld Metal	Parent Metal
				Horizontal	Vertical		
RT	1C12-1	(5.5+7)/2= 6.25	Yes	526	511	453	522
	1C12-2	(5.75+7)/2= 6.37	No	549	532	460	533
60	2C12-1	(6+6.5)/2= 6.25	Yes	538	537	454	518
	2C12-2	(6.5+6.75)= 6.62	No	458	466	436	534
90	3C12-1	(6.75+7.5)/2= 7.12	No	560	583	509	556
	3C12-2	(8+6)/2=7.00	No	554	491	488	540
120	4C12-1	(5.75+6.5)/2= 6.12	No	486	581	490	556
	4C12-2	(6.25+7.25)= 6.75	No	568	588	470	522
150	5C12-1	(8.25+7.5)= 7.87	No	530	540	437	481
	5C12-2	(6.5+7.5)= 7.00	No	584	534	446	531
Average values		7.0±0.9	-	527±41	527±60	473±36	519±38

Table 5.5 Metallographic and hardness examination results for *30 mm plates of Steel H*.

Preheat Temp (˚C)	Sample ID	Metallographic Examination		Average Hardness, HV5			
		Mean Leg Length ($L_h + L_v$)/2, (mm)	Result (Cracked)	HAZ		Weld Metal	Parent Metal
				Horizontal	Vertical		
RT	1E30-1	(7+8)/2= 7.5	Yes	464	568	439	554
	1E30-2	(8.5+7.5)/2= 8.0	Yes	498	596	444	569
60	2E30-1	(7.5+ 8.3)/2= 7.9	Yes	594	541	505	558
	2E30-2	(7.2+8)/2= 7.6	Yes	636	620	494	602
90	3E30-1	(8+6.5)/2= 7.25	No	551	504	418	556
	3E30-2	(8+8)/2= 8.0	No	568	573	431	517
120	4E30-1	(7.5+8.5)/2= 8.0	No	552	567	406	531
	4E30-2	(7.75+8.5)= 8.12	No	519	533	415	508
150	5E30-1	(7.5+7.25)/2= 7.37	No	522	549	423	518
	5E30-2	(8+7.5)/2= 7.75	No	517	557	407	542
Average Values		7.7±0.4	-	550±86	562±58	456±49	555±47

Steel L welded test coupons of thickness 12 mm, showed no cracking at a preheat temperature of 80 ˚C and above. The cracked samples showed cracks only in the weld horizontal direction. The average leg length was observed to be 6.6±0.7 mm. A higher hardness was observed in the horizontal HAZ (504±35 HV) compared to the vertical HAZ (491±27 HV). The weld metal showed 21 % lower hardness (356±31HV) compared to the parent metal (450±36 HV). The heat input observed during welding of 12 mm Steel L test coupons, was controlled in the range of 1.16~1.31kJ/mm (Average: 1.2kJ/mm).

Steel L welded test coupons of thickness 32 mm, showed no cracking at a preheat temperature of 80 ˚C and above. The cracked samples showed cracks only in the weld horizontal direction. The average leg length was observed to be 7.5±0.6 mm. A higher hardness was observed in the horizontal HAZ (482±31 HV) compared to the vertical direction (470±57 HV). The weld metal hardness (382±44 HV) was only 5 % lower than this in the parent metal (404±74 HV). The heat input observed during welding of 32 mm Steel L test coupons was controlled in the range of 1.57~1.72kJ/mm (Average: 1.6kJ/mm).

Steel H welded test coupons of thickness 12 mm, showed no cracking at a preheat temperature of 90 ˚C and above. The cracked samples showed cracks only in the weld horizontal direction. The average leg length was observed to be 7.0±0.9 mm. Hardness was similar in both the horizontal and verticals HAZ directions (527±41 HV and 527±60 respectively). The weld metal hardness (473±36 HV) was 9% lower than this in the parent metal (519±38 HV). The heat input observed during welding of 12 mm Steel H test coupons was controlled in the range of 1.57~1.72kJ/mm (Average: 1.2kJ/mm).

Steel H welded test coupons of thickness 30 mm, showed no cracking at a preheat temperature of 90 ˚C and above. The cracked samples showed cracks only in the horizontal direction. The average leg length was observed to be 7.7±0.4mm. A higher hardness was observed in the vertical HAZ (562±58 HV) compared to the horizontal one (550±86 HV). The weld metal hardness (456±49 HV) was 18% lower than this in the parent metal (555±47 HV). The heat input observed during welding of 30 mm Steel H test coupons, was controlled in the range of 1.58~1.74kJ/mm (Average: 1.6kJ/mm).

5.3 Discussion

Cracking mechanisms are usually associated with the welding process, filler material or base metal chemistry, and microstructure. The minimum preheats temperature and heat input is suggested to be 150 ˚C and 1~2 kJ/mm to ensure crack-free welds in Q&T steels [21]. However, from an industrial perspective, a higher preheat temperature increases costs. The Ti-microalloyed medium carbon steels studied in this project are highly susceptible to HIC when subjected to cutting or welding. Therefore, the objective was to find the minimum preheat temperature at which cracking would not occur at heat inputs in the range of 1~1.6 kJ/mm. Steel L (both 12 mm and 32 mm thick) showed HIC in HAZ when welded at room temperature (~23˚C) or preheated at temperatures of 40˚C and 60˚C. Similarly, Steel H (both 12 mm and 30 mm) showed HIC in HAZ when welded at room temperature (~23˚C) or preheated at a temperature of 60 ˚C.

The tendency of HAZ cracking has been studied widely [22-26] and generally attributed to the occurrence of four simultaneous factors [27]:

i) Hydrogen is present to a sufficient degree. It can penetrate the weld from the moisture in electrode coverings or fluxes used in welding and from other sources like oil, dirt, grease, paint, or rust on the surface of welding consumables or base metal. It is absorbed by the weld pool and some amount is transferred to the HAZ by diffusion.

ii) Tensile stresses act on the weld. These inevitably arise from contractions during cooling and may be supplemented by other stresses developed as a result of rigidity in the parts to be joined, because the stress acting upon a weld is a function of weld size, joint geometry, fit-up, and the strengths of the parent steel and weld metal (these are chemistry and phase transformation dependent).

iii) A susceptible HAZ microstructure forms. A reverse martensite-austenite-martensite transformation in the HAZ regions closer to the weld metal, that may take place during fast heating during welding followed by fast cooling, produces hard microstructures susceptible to hydrogen embrittlement. Hydrogen cracks, when present, are invariably found in these transformed regions. As a general rule, the harder the microstructure, the greater is the risk of cracking. The soft microstructure can tolerate more hydrogen than the hard before cracking occurs.

iv) A low temperature is reached. Thus, the greatest risk of cracking may be reached several hours after welding has been completed. Cracking is unlikely to occur in structural steel above ~150 ˚C and in any steel above ~250 ˚C. It is therefore possible to avoid

cracking in a susceptible microstructure by maintaining it at a sufficiently high temperature by post-heating until sufficient hydrogen has diffused out.

Both Steel L and Steel H welded test coupons showed cracks in the HAZ. Cracks in the HAZ are usually sited either at the weld toe, the weld root, or at the under-bead position along the weld length [27]. These can be controlled through cooling rate by choosing proper heat input and preheat temperature depending upon the hardenability of parent metal. Hardenability is governed by the composition of the alloy and can be assessed in terms of an empirical formula that defines a carbon equivalent (Ceq) value and takes account of the important elements which are known to affect hardenability. Carbon equivalent for both steels, Steel L and Steel H, of all thicknesses, was calculated using the following equation [28]:

$$Ceq = C + Mn/6 + (Cr + Mo + V)/5 + (Ni + Cu)/15 \quad \text{Eq. 6.1}$$

Table 5.6 Carbon equivalent calculated for Steel L and Steel H using Eq. 6.1.

Steel Grade	Thickness (mm)	Ceq
Steel L	12	0.61
	32	0.62
Steel H	12	0.85
	30	0.83

The higher is Ceq, the higher is the risk of cold cracking. Table 5.6 shows Ceq calculated based on the bulk chemical composition of the studied steels. Although, some amount of carbon combines with Ti, V, and Mo to form carbide particles. This would reduce the carbon concentration in the martensitic matrix and decrease hardness. A reduction in the solute carbon concentration, associated with additions of microalloying elements and particle precipitation, may improve weldability [29, 30]. Despite lower solid solution strengthening and phase balance strengthening (due to lower hardenability), microalloying facilitates grain refinement and precipitation hardening. Therefore, microalloying may be expected to reduce the hydrogen cracking sensitivity. Hart [29] states that nitrogen may be deleterious for weldability because it increases hardenability. Thus, nitride-forming elements, such as V in the studied steels, have to improve

weldability. Based on these considerations, Steel H, containing more Ti and a larger volume fraction of Ti-rich particles, could be expected to have better weldability. However, higher Mn, Ni, and Mo concentrations increase hardenability (notice that these elements increase Ceq, Eq. 6.1) and, therefore, decrease weldability.

Preheating plays an important role in slowing the cooling rate. It not only softens the microstructure but also helps hydrogen to escape. As a result, higher HAZ hardness levels without cracking can be tolerated after preheating has been used [27]. Therefore, test coupons welded with preheat temperatures ≥ 80˚C for Steel L and ≥ 90˚C for Steel H did not show cracking.

Maximum average leg length was observed for test coupons of Steel H of thickness 30 mm. It might also have contributed towards an increase in stress level, in addition to residual stresses coming from a restraint. Therefore, a weld size must also be considered to limit the stress level in the microstructure.

For both steels, a maximum average hardness (≥500 HV) was observed in the HAZ, which indicates the development of a hard microstructure and the presence of a high amount of hydrogen. Ultimately, under bead cracks developed in the horizontal welds, and not in the vertical welds. The expected hardness can be calculated with an empirical formula as follows [27] p 62-69:

$$HV = 90 + 1050C + [47Si + 75Mn + 30Ni + 31Cr] \quad \text{..... Eq. 6.2}$$

Table 5.7 Hardness for Steel L and Steel H calculated using Eq. 6.2.

Steel Grade	Thickness (mm)	Calculated Hardness (HV)
Steel L	12	471
	32	480
Steel H	12	669
	30	645

The Steel L and Steel H hardness values were calculated to be 471-480 and 645-669 HV, respectively (Table 5.7). However, the measured average hardness was 400-450 HV for Steel L and 500-550 HV for Steel H. Lower measured hardness values can be explained by the microalloying effect [29, 30]: if with microalloying more particles precipitated and

grew to larger sizes, the concentrations of microalloying elements in the matrix could decrease, this would reduce the solid solution strengthening effect; lower hardenability would result in larger martensite laths and lower dislocation density in the matrix, this would also contribute to the hardness decrease. However, for such a high hardness, higher preheat temperatures are still required to obtain crack-free welds. This preheat temperature must be below Ms (martensite formation start temperature) of the steel rather than predicted from the expected HAZ hardness. Otherwise, the risk of austenite retention may increase leading to hydrogen dissolution in HAZ; this would increase the propensity for cracking [27]. K. Easterling explained the hardening effect in microstructures due to hydrogen adsorption leading to cold cracks initiating in the grain coarsening zone of HAZ [31] p216-229. An increase in grain size decreases the transformation temperatures so that in higher Ceq steels, the volume fraction of lower temperature transformation products, such as martensite, bainite or Widmanstatten ferrite, increases. High dislocation densities associated with these phases, together with fine carbide particles, are likely to result in a hard, low ductility matrix. For such hard microstructures, there are three types of welding procedures to control hydrogen-induced cracking [27] p24-29:

a) Temperature Control Method. This is achieved by choosing a proper preheat temperature before welding and maintaining it after welding to slow down the cooling rate and help hydrogen escape.

b) Isothermal transformation. This method relies on knowledge of the isothermal transformation characteristics of the steel. This is attained by controlling the HAZ cooling rate to facilitate an isothermal transformation of austenite and produce softer phases (bainite, acicular ferrite) instead of hard martensite.

c) The use of austenitic and nickel alloy weld metal. This method is used if preheating above 150˚C is impossible, method (a) is severely restricted, and method (b) cannot be used. The only alternative is then to use a combination of welding process parameters and special consumables, which virtually prevent the introduction of hydrogen into the HAZ and produce a weld metal insensitive to hydrogen. This is achieved using austenitic (stainless steel) or nickel alloy electrodes, solid or flux-cored wires.

5.4 Conclusion

Investigation of cracking propensity during welding of two Ti-microalloyed martensitic steels containing 0.28C-0.4Ti (Steel L), of thicknesses 12 mm and 32 mm, and 0.38C-0.6Ti (Steel H), of thicknesses 12 mm and 30 mm, resulted in the following conclusions:

1) Steel L test coupons welded with a heat input of 1.2-1.6 kJ/mm showed no cracking when preheated at 80 ˚C and above. The average hardness measured for test coupons was in the range of 470-504 HV for HAZ, 404-450 HV for the parent metal, and 356-382 HV for the weld metal.

2) Steel H test coupons welded with a heat input of 1.2~1.6 kJ/mm showed no cracking when preheated at 90 ˚C and above temperatures. The average hardness measured for test coupons was in the range of 527-562 HV for HAZ, 519-555 HV for the parent metal, and 456-473 HV for the weld metal.

3) The highest hardness was observed in the HAZ, with the lowest in the weld metal. The change in hardness occurred due to microstructural changes depending upon the nature of the thermal cycle and chemical composition. This corresponds to the formation of more martensite in HAZ due to high carbon contents and less martensite in the weld due to low carbon contents.

4) Hydrogen-induced cracking was observed for Steel L and Steel H samples welded with lower preheat temperatures (below 60˚C) or at room temperature (~23˚C). It was accompanied by simultaneous action of adsorbed hydrogen, high stresses, and susceptible microstructure.

5) Temperature control through preheating along with controlled heat input plays a key role to overcome cracking phenomena in the studied Q&T steel microalloyed with Ti.

References (Chapter 5)

1. J. Fu, Z. Wang, Y. Kang, D. Liu, G. Chen, L. Li, *Research and development of HSLC steels produced by EAF-CSP technology*, 25 (2003) 449-454.
2. D. L. Liu, J. Fu, Y. L. Kang, *Oxide and sulphide dispersive precipitation and effects on microstructure and properties of low carbon steels*, J Mater Sci Technol, l8 (1) (2002) 7-9
3. X. P. Mao, *Microalloying technology on thin slab casting and direct rolling process*, Metallurgical Industry Press, Beijing (2008)
4. *Welding Handbook*, 8th Ed., American Welding Society, vol. 2, 1991, 110-155.
5. J. C. Ritter, B. F. Dixon, N. J. Baldwin, *Deformation and weld repair of armour steel*, Mater. Forum 13 (1989) 216–224.
6. N. Yurioka, H. Suzuki, *Hydrogen assisted cracking in C–Mn and low alloy steel weldments*, Int.Mater.Rev.35 (1990) 217–249.
7. G. Magudeeswaran, V. Balasubramanian, and G. Madhusudhan Reddy; *Hydrogen induced cold cracking studies on armour grade high strength, quenched and tempered steel weldments.* International Journal of Hydrogen Energy, 33(7) (2008) 1897-1908
8. L. Kuzmikova, M. Callaghan, N. Larkin, R. Scott, R. De-Jong, H. Li, J. Norrish, *A study of a continuous cooling behaviour and effect of preheating and inter-pass temperature on the HAZ of high strength quenched and tempered steel*, Doc IX-2352-10, IIW Annual Assembly, Istanbul, Turkey, (2010) .
9. I. Barenyi, O. Hires, P. Liptak, *Degradation of mechanical properties of armoured steels after its welding*, Proceedings of International Conference of Scientific Paper, AFA SES 2011, Brasov, Romania, (2011).
10. I. Barenyi, O. Hiresand P. Liptak, *over-tempering of armox armoured steels at their secondary processing*, Proceedings of International Conference of Scientific Paper AFA SES 2012, Brasov, Romania (2012).
11. N. Yurioka and H Suzuki: *Hydrogen assisted cracking in C-Mn and low alloy steel weldments*, International Materials Reviews, 25 (1990) 217-249.
12. P. H. M. Hart: *Hydrogen cracking - its cause, costs, and future occurrence*, Proceedings of the 1st International Conference, Wollongong, March 1999.

13. M. Pitrun, D. J. Nolan, *Cold Cracking Susceptibility of Weld Metal Deposited by Gas Shielded Rutile Flux-Cored Wire,* Australasian Welding Journal, 50 (2005) 33-46.
14. L. Kuzmikova, M. Callaghan, N. Larkin, R. Scott, R. De Jong, H. Li, J. Norrish, *A study of the continuous cooling behaviour and effect of preheating and interpass temperature on the HAZ of high strength quenched and tempered steel.* IIW 2010 Annual Assembly, (2010) 1-14.
15. K. E. Easterling, Introduction to the Physical Metallurgy of Welding, Butterworth-Heinemann Ltd., Oxford, 2 (1992) 135.
16. S. J. Alkemade, *The weld cracking susceptibility of high hardness armour steel*, Defence Science and Technology Organisation, (1996) 24.
17. P. L. Harrison, R. A. Farrar, *Application of continuous cooling transformation diagrams for welding of steels.* International Materials Reviews, 34(1) (1989) 35-51.
18. C. L. M. Cottrell, J. Iron Steel Institute, 174 (1953) 17.
19. *Destructive test on welds in metallic materials-cols cracking tests for weldments-arc welding processes*, Part-2: Self-restraint tests, ISO 17642-2, (2005).
20. *Welding Consumables*, Product Catalogue, 2nd Edition, The Lincoln Electric Company, 2 (2019) 96.
21. *Specification for Low Alloy Steel Electrodes for Flux Cored Arc Welding*, AWS 5.29 (2010).
22. AWRA Technical Note 15, *Quenched and Tempered Steels*, Welding Technology Institute of Australia, (1985).
23. R. E. Dolby, *The weldability of low carbon structural steels*, The Welding Institute Research Bulletin, (1977) 209 – 216
24. J. A. Davidson, P.J. Konkol, J. F. Sovak, *Assessing fracture toughness and cracking susceptibility of steel weldments - A review*, Welding Research Council Bulletin 345 (1989).
25. *Metals Handbook*, Vol. 6, 9th Ed., American Society for Metals, 6(9) (1983).
26. J. G. Baillie, *Under-bead and toe cracks*, British Welding Journal, (1967) 51 – 61
27. N. Bailey, F. R. Coe, T. G. Gooch, P. H. M. Hart, N. Jenkins, and R. J. Pargeter, *Welding Steels without Hydrogen Cracking*, 2nd Edition, Woodhead Publishing Limited, (2) (2004) 3-14, 62-69, 24-29

28. BS 5135:1984, *Arc Welding of Carbon and Carbon Manganese Steels* (now superseded by EN 1011-1: 2009 and EN 1011- 2, (2001).
29. P. H. M. Hart, R. E. Dolby, N. Bailey, and D. J. Widgery, *The weldability of Microalloyed Steels,* Microalloying 75: Proceedings of an International Symposium on High Strength Low Alloy Steels, Washington, D.C., U.S.A, 1 (1975) 540-551.
30. G. Bernard, *A viewpoint on the weldability of carbon-manganese ad microalloyed structural steels,* Microalloying 75: Proceedings of an International Symposium on High-strength, Low-alloy Steels, Washington, D.C., U.S.A, (1975) 552-569.
31. K. Easterling, *Introduction to Physical Metallurgy of Welding*, 2nd Edition, Butterworth Heinemann Ltd, (2) (1992) 216-229.

Chapter 6

6 Effect of heat input on weld and HAZ hardness

6.1 Introduction

Mechanical properties of the welded steels are affected by microstructural changes in HAZ depending upon the cooling rate of weldment [1-6]. Higher cooling rate results in higher hardness of microstructure depending upon the steel composition and hardenability. This cooling rate is governed by the heat supplied during welding, and the heat sink, which is a function of the initial temperature of steel parts to be welded, their thickness, and geometry. The heat supply is characterised by the heat input which depends on welding parameters, such as voltage, current, travel speed, and efficiency of the welding process being employed [7-10]. Control over the cooling rate in a particular fabrication process (where steel composition and geometry are fixed) is achieved by varying the heat input and preheat temperature [9-11]. A low heat input leads to rapid cooling, as the deposited weld is small in relation to the parent material, and the parent material acts as a heat sink. Toughness can be low in microstructures that have arisen from rapid cooling rates. In general, very low heat inputs are to be avoided as they result in hard, crack susceptible microstructures with poor toughness. A high heat input results in slower cooling rates and grain coarsening in the HAZ if the temperature is high enough to promote grain growth prior to transformation. Very large grain sizes can have poor toughness even when the microstructure is soft [9-10]. In this work, an attempt has been made to disclose the effect of heat input on the weld and HAZ hardness of Ti-microalloyed steels. The gas tungsten arc welding process was used to make autogenous welds in the form of a single bead on the plate as per the requirement of BS 7363:1990 standard. Since microalloying elements are introduced into the weld metal by dilution, the effects of microalloying on HAZ hydrogen-induced cracking also apply to weld metal cracking, although at a reduced level. Higher carbon contents along with higher thickness require higher preheat temperatures to avoid HIC [12]. The objective of this work was to develop a welding procedure to have crack-free weld and HAZ, after assessment of series of tests for both steels, welded with different heat input values. Steel L and Steel H were preheated at 100˚C and 150˚C, respectively. The test coupons were cooled in the air after

welding. Each of the test coupons welded with particular heat input was cut into two sections and the faces were subjected to hardness testing after polishing and etching.

6.2 Results

6.2.1 Welding Parameters

Table 6.1 shows planned welding parameters for the BOP testing. Table 6.2 shows actually observed heat inputs during BOP welding. The efficiency of the Gas Tungsten Arc Welding Process was taken as "1". Table 6.3 shows welding variables used in common for all test coupons.

Table 6.1 Welding parameters for a bead on plate (BOP) testing.

Base Material	Thickness (mm)	Sample IDs	Heat Inputs (kJ/mm)	Preheat Temp. (˚C)
Steel L	32	1GE, 2GE, 3GE, 4GE, 5GE	1.2, 1.5, 2.0, 2.5, 3.5	100
Steel H	30	1GC, 2GC, 3GC, 4GC, 5GC	1.2, 1.5, 2.0, 2.5, 3.5	150

Table 6.2 Actually observed heat inputs during BOP welding.

Welding Process	Current, "A", Amperes	Voltage, "V", Volts	Travel Speed, "S", mm/min	Heat Input = (60xAxV)/S KJ/mm
Gas Tungsten Arc Welding	125	24	147	1.2
	150	25	147	1.5
	110	22	69	2.1
	125	23	69	2.5
	110	22	40	3.6

Table 6.3 Welding variables used in common for BOP weld test coupons.

Welding Process: Gas Tungsten Arc Welding (GTAW)			
Electrode/ wire AWS Specification	AWS A5.12/A5.12M	Gas flow rate	11 lit/min
Electrode AWS Classification	EWLa-2	Polarity	DCSP
Electrode/ wire diameter	2.4mm	Electrode/wire stick out	5mm
Filler wire	Not applicable (autogenous weld)	Inter-pass Temp. (˚C)	Not applicable
Baking Treatment	Not applicable	Post heat treatment	Not applicable
Shielding gas	75-85% Argon / 15-25% CO2	Temperature measuring method	K-type thermocouple

6.2.2 Hardness Testing

Autogenous weld beads of <300 mm length were produced on 150 mm wide plates within 10 mm of the plate centre and cut into two sections as shown in Figure 6.1. The cross-section surfaces of the test pieces were machined, ground, polished, and etched for hardness testing (Figure 6.2). The etched cross-sections showed three microstructural regions (Figure 6.3): weld metal, HAZ, and base metal. For both steels, five heat inputs 1.2, 1.5, 2.1, 2.5, and 3.6 kJ/mm were used to determine the hardness variation with processing. 32 mm Steel L and 30 mm Steel H samples were preheated to 100 ˚C and 150 ˚C, respectively, before making a single weld bead on test coupons. Preheating at a particular temperature helped to obtain crack-free welds. Steel H was preheated at a higher temperature because of its higher hardenability in comparison to that of Steel L. The hardness was measured within 0.4 mm of the fusion line. Tables 6.4 and 6.5 show the hardness testing results for the BOP weld test coupons for weld metal, HAZ, and base metal of both steels.

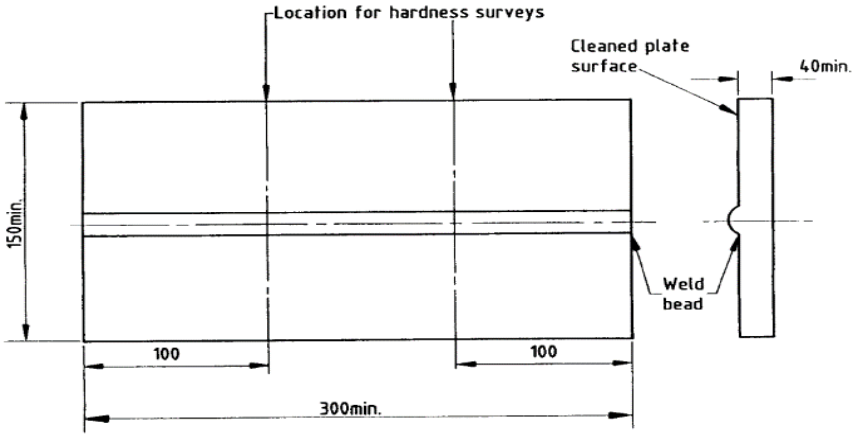

Figure 6.1 Sectioning of BOP test coupons.

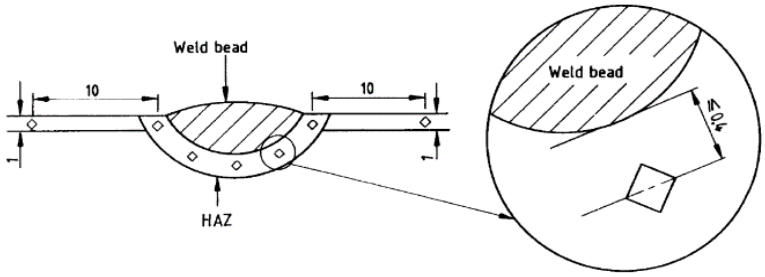

Figure 6.2 Hardness measurement in base, HAZ, and weld metal.

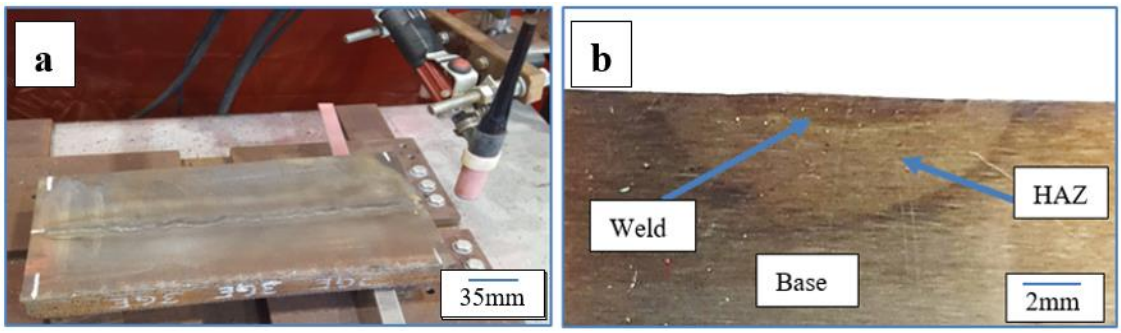

Figure 6.3 (a) BOP test coupon and (b) cross-section of the BOP weld.

Table 6.4 Hardness testing of 32 mm Steel L.

Heat Inputs	Sample ID	Section & Face	Hardness, HV (5kg loading force)		
			Heat Affected Zone (HAZ) (Average of HV)*	Weld Metal (Average HV)*	Parent Metal (Average HV)*
1.2	1GE-1	a & b	493	474	484
	1GE-2	a & b	512	443	417
Average of both test coupons			503	459	450
1.5	2GE-1	a & b	519	384	478
	2GE-2	a & b	493	343	464
Average of both test coupons			506	364	471
2.1	3GE-1	a & b	491	297	481
	3GE-2	a & b	590	296	478
Average of both test coupons			541	297	480
2.5	4GE-1	a & b	478	346	380
	4GE-2	a & b	516	328	466
Average of both test coupons			497	337	423
3.6	5GE-1	a & b	467	510	406
	5GE-2	a & b	311	198	366
Average of both test coupons			389	354	386
Average of all test coupons			465±76	378±81	433±47
Note: * Average of minimum five Vickers hardness values					

Table 6.5 Hardness testing of 32 mm Steel H.

Heat Input	Sample ID	Section & Face	Hardness, HV (5kg loading force)		
			Heat Affected Zone (HAZ) (Average HV)*	Weld Metal (Average HV)*	Parent Metal (Average HV)*
1.2	1GC-1	a & b	547	610	500
	1GC-2	a & b	550	662	544
Average of both test coupons			548	636	522
1.5	2GC-1	a & b	566	638	523
	2GC-2	a & b	571	631	567
Average of both test coupons			568	635	545
2.1	3GC-1	a & b	561	703	528
	3GC-2	a & b	616	675	516
Average of both test coupons			588	689	529
2.5	4GC-1	a & b	556	556	547
	4GC-2	a & b	569	541	523
Average of both test coupons			563	548	535
3.6	5GC-1	a & b	539	394	527
	5GC-2	a & b	563	550	543
Average of both test coupons			551	472	535
Average of all test coupons			570±22	580±108	534±12
Note: * Average of minimum five Vickers hardness values					

The hardness data was plotted against the variation in heat input to investigate the behaviour for both steels (Figure 6.4). *Steel L BOP test coupons of thickness 32 mm* showed a higher average hardness (465±76 HV) for HAZ compared to the base (433±47 HV) and weld metal (378±81 HV) for all heat inputs. In Steel L the base and HAZ hardness decreased with heat input. Although, the weld metal showed a minimum at 2.1 kJ/mm. *Steel H BOP test coupons of thickness 30 mm* showed a higher average hardness (580±108 HV) for the weld metal compared to the base (534±12 HV) and HAZ (570±22 HV) for all heat inputs. In Steel H the base and HAZ hardness did not vary significantly with heat input. However, the weld metal hardness showed a maximum at 2.1 kJ/mm and then decreased with heat input increasing to 3.6 kJ/mm.

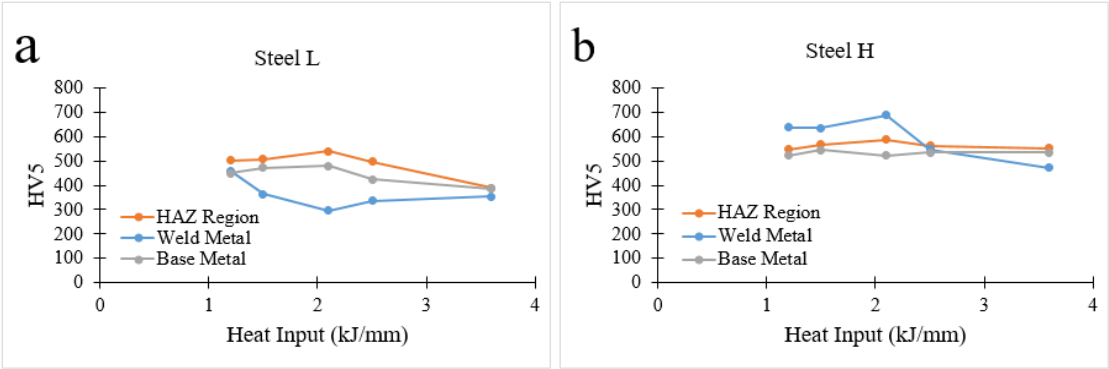

Figure 6.4 Hardness variation with heat input in (a) Steel L and (b) Steel H.

6.3 Discussion

Since, Steel H has higher C and Ti contents, compared to Steel L, it has a higher hardenability. The difference is evident from Tables 6.4 and 6.5: the average hardness of Steel L is higher than this of Steel H for all test conditions. Despite high hardness being observed for both steels, none of the test coupons cracked either at a lower value of heat input (1.2 kJ/mm) or a higher value (3.6 kJ/mm). Sufficient preheat temperature (100 ˚C for Steel L and 150 ˚C for Steel H) was the reason for this. The cooling rate was slow enough to develop a bainitic or tempered martensite microstructure without cracking [13]. The slow cooling rate not only facilitated the development of a less hardenable microstructure but also provided more time for hydrogen diffusion out of the weld. Due to high preheating temperature, heat input had little or no influence on hydrogen-induced cracking in both steels [14].

In Steel L the average hardness increased from the weld metal to HAZ and then decreased in the base metal (Figure 6.4a). Low hardness in the weld metal could result from the substantial dissolution of Ti-rich particles. High hardness in HAZ might be explained if coarse-grained austenite (possessing a larger hardenability than the fine-grained one) transformed to a fine and more dislocated martensite, coupled with not fully dissolved particles of microalloying elements. A hardness dependence with a maximum for HAZ with respect to heat input supports the significance of precipitation strengthening effect in Steel L. Thus, at lower heat inputs (<2.1 kJ/mm) the temperature associated with welding decreased quickly and the heat treatment effect on particle dissolution was minor. At 2.1 kJ/mm, a population of fine particles with a larger number density could be present (due to partial dissolution of coarse particles and potential precipitation of fine ones). An intermediate heat input could accelerate grain structure recrystallization, leading to finer grain sizes of the matrix. At >2.1 kJ/mm the particle dissolution (with a possible coarsening of very large ones), more pronounced recovery (dislocation annihilation), and grain growth decreased the hardness [15,16]. A decrease in hardness of the base plate was probably more related to a larger recovery (dislocation annihilation) at higher heat inputs.

In Steel H, a higher average hardness was observed in the weld metal at low to medium heat inputs. With an increase in heat input the hardness in weld metal even below this in HAZ and parent metal (Figure 6.4b). High hardness in the weld metal at low heat inputs could be explained if after solidification and relatively quick cooling a population of fine particles with high number density formed in the Steel H. With an increase in heat input, and associated with this decrease in cooling rate and increased cooling time, the particle coarsening accompanied with a decrease in number density could occur – this would decrease hardness. The HAZ and base metal hardness did not vary significantly with heat input. This can be explained by the geometrical stability of coarse Ti-rich particles, which are believed to dominate the hardness formation in the Steel H, in the studied heat input range [15-17].

Steel H showed higher average hardness than Steel L for HAZ, weld metal, and base. It may be explained by higher C, Ti. Mn, Ni, and Cu contents in Steel H and associated with these higher solid solution and precipitation strengthening [18], and potentially higher dislocation densities in the finer martensitic matrix. The coarse-grained heat-affected zone (CGHAZ) is recognized to be the smallest section in welds. Coarse-grained ferrite,

Widmanstatten ferrite, and upper bainite can be easily obtained following the decomposition of large prior austenite grains, leading to weak toughness [19-22]. In contrast, intergranular ferrite (IGF), especially intergranular acicular ferrite (IAF) which accounts for the high internal misorientation, can effectively suppress crack propagation [23-25]. Moreover, the formation of IGF is directly related to the prior austenite grain size and the presence of heterogeneous nucleation sites. The prior austenite grain size is primarily determined by the welding heat input, and a relatively larger austenite grain provides more internal area for IGF. Heat input along with preheating temperature lead to a particular precipitation behaviour depending upon the cooling rate of a specific steel composition [26-27].

High heat input samples showed a reduction in hardness. This is related to the high temperature being retained by thick plates resulting in grain coarsening near the fusion line. However, CGHAZ and fine grain heat-affected zone (FGHAZ) located marginally away from the fusion line are closely spaced in real welds [28]. This is prominent in microalloyed steels due to the presence of more grain growth inhibitors like precipitates and solid solute atoms [29-37].

6.4 Conclusion

Following the BS 7363:1990 standard, single autogenous weld beads have been made on plate test coupons of Steel L (0.28C-0.4Ti) of thickness 32 mm and Steel H (0.38C-0.6Ti) of thickness 30 mm. The analysis of heat input effect on hardness has brought the following conclusions.

1) Steel H showed a higher average hardness with respect to Steel L in the whole heat input range due to higher C, Ti, Mn, Ni, and Cu contents in steel composition, leading to a stronger solid solution and precipitation strengthening effects, and potentially higher dislocation density in Steel H because of its higher hardenability.

2) Both steels showed a decrease in hardness for the maximum heat input of 3.6 kJ/mm used for BOP testing.

3) Steel H showed unexpectedly high weld metal hardness, compared to this for HAZ and base metal. Probably, dissolution of many coarse Ti-rich particles enriched the solid solution with microalloying elements and facilitated the formation of a population of fine Ti-rich particles with a significant number density.

4) No cracking was observed in any of the studied samples. The can be explained by the application of the proper preheat temperature that resulted in inhomogeneous internal stress redistribution.

References (Chapter-6)

1. M. Zhu, G. Xu, M. Zhou, H. Hu, *The Effects of Cooling Mode on the Properties of Ti-Nb Microalloyed High-strength Hot-rolled Steels.* The Journal Wuhan University of Technology, Materials Science Edition, 34(3) (2019) 692-697.
2. C. Y. Zhou, G.L. Wu, and X.B. Liu, *Static recrystallization behaviour of Ti-Nb microalloyed high-strength steel.* Journal of the Southern African Institute of Mining and Metallurgy, 117(5) (2017) 451-456.
3. M. John, P.A. Kumar, K. Udaya Bhat, *Effect of wire feed rate on microstructure development during bead on plate welding of microalloyed steel using P-GMAW,* Materials Today: Proceedings, (2020).
4. H. Wu, C. Liu, Z. Zhao, S. Zhu, Y. Liu, S. Bhole, *Design of air-cooled bainitic microalloyed steel for a heavy truck front axle beam.* Materials and Design, 27(8) (2006) 651-656.
5. R. D. K. Misra, *Microstructural evolution in a new 770 MPa hot rolled Nb-Ti microalloyed steel,* Materials Science and Engineering A, 2005. 394(1-2) (2005) 339-352.
6. J. F. Lancaster, *The Metallurgy of Welding, Brazing and Soldering*, George Allan and Unwin, London, (1970).
7. G. Bernard, *A viewpoint on the weldability of carbon-manganese ad microalloyed structural steels*, Microalloying 75: Proceedings of an International Symposium on High-strength, Low-alloy Steels, Washington, D.C., U.S.A, (1975) 552-569.
8. S. J. Alkemade, *The weld cracking susceptibility of high hardness armour steel.* 1996, Defence Science and Technology Organisation, (1996) 24.
9. N. Bailey, F. R. Coe, T. G. Gooch, P. H. M. Hart, N. Jenkins, and R. J. Pargeter, *Welding Steels without Hydrogen Cracking*, 2nd Edition, Woodhead Publishing Limited, (2) (2004) 3-14.
10. BS EN 1011-2:2001 Welding - *Recommendations for welding of metallic materials*, Arc welding of ferritic steels, BSI, (2001) 1-62.
11. R. Jessman, *Columbium Pickup in High-Dilution, Submerged-Arc Weld Deposuts,* Microalloying 75: Proceedings of an International Symposium on High-strength, Low-alloy Steels, Washington, D.C., U.S.A, (1975) 578-592.

12. P. H. M. Hart, R. E. Dolby, N. Bailey, D. J. Widgery, *The weldability of microalloyed steels*, Microalloying 75: Proceedings of an International Symposium on High-strength, Low-alloy Steels, Washington, D.C., U.S.A, (1975) 540-550.
13. N. Bailey, F. R. Coe, T. G. Gooch, P. H. M. Hart, N. Jenkins, and R. J. Pargeter, *Welding Steels without Hydrogen Cracking*, 2nd Edition, Woodhead Publishing Limited, (2) (2004) 3-14.
14. P. H. M. Hart, R. E. Dolby, N. Bailey, D. J. Widgery, *The weldability of microalloyed steels*, Microalloying 75: Proceedings of an International Symposium on High-strength, Low-alloy Steels, Washington, D.C., U.S.A, (1975) 540-550.
15. L. Sharma, R. Chhibber, *EStudy of weld bead chemical. Microstructural analysis using submerged arc welding fluxes for line pipe steel applications*, Ceramics International:2020. 46(15) (2020) 24615-24623
16. Q. Sun, H. Di, J. Li, B. Wu, R. D. K. Misra, *A comparative study of the microstructure and properties of 800 MPa microalloyed C-Mn steel welded joints by laser and gas metal arc welding.* Materials Science and Engineering A, 669 (2016) 150-158.
17. M John, P. A. Kumar, K. U. Bhat, *Effect of wire feed rate on microstructure development during bead on plate welding of microalloyed steel using P-GMAW*, Materials Today: Proceedings - Elsevier, (2020).
18. G. Krauss, Steels - Processing, Structure, and Performance (second ed.), ASM International, Materials Park, OH (2015) 294-296, 380-383.
19. Z. Shi, C. Yang, R. Wang, H. Su, F. Chai, J. Chu, Q. Wang, *Effect of nitrogen on the microstructures and mechanical properties in simulated CGHAZ of vanadium microalloyed steel varied with different heat inputs*, Materials Science and Engineering A, 649 (2016) 270-281.
20. S. Kumar, S. K. Nath, V. Kumar, *Continuous cooling transformation behavior in the weld coarse-grained heat affected zone and mechanical properties of Nb-microalloyed and HY85 steels.* Materials and Design, 90 (2016) 177-184.
21. X. Yang, Z. Liu, F. Hu, Y. Lin, J. Zhang, C. Lu, C. Shen, *Soil Rare Earth Element and Nitride Pollution on Plant Growth and Physiology.* Zhongguo Xitu Xuebao/Journal of the Chinese Rare Earth Society, 37(1) (2019) 1-11.

22. Barrick, E. J. and J. N. DuPont, *Mechanical properties and microstructural characterization of simulated heat-affected zones in 10 wt pct Ni steel.* Materials Science and Engineering A, 748 (2019) 189-204.
23. Z. Shi, X. Chai, F. Chai, S. Hang, T. Pan, Q. Wang, R. Wang, C. Yang, *The mechanism of intragranular ferrite formed on Ti-rich (Ti, V)(C, N) precipitates in the coarse heat-affected zone of a V-N-Ti microalloyed steel*. Materials Letters, 175 (2016) 266-270.
24. J. Hu, L. X. Du, M. Zang, S. J. Yin, Y. G. Wang, X. Y. Qi, X. H. Gao, R. D. K. Misra, *On the determining role of acicular ferrite in V-N microalloyed steel in increasing strength-toughness combination*. Materials Characterization, 118 (2016) 446-453
25. X. Luo, Y. Niu, X. Chen, H. Tang, Z. Wang, *High performance in base metal and CGHAZ for ferrite-pearlite steels.* Journal of Materials Processing Technology, 242 (2017) 101-109.
26. F. Ishikawa, T. Takahashi, *The Formation of Intragranular Ferrite Plates in Medium-carbon Steels for Hot-forging and Its Effect on the Toughness.* ISIJ International, 35(9) (1995) 1128-1133.
27. J. Hu, L. X. Du, and J. J. Wang, *Effect of v on intragranular ferrite nucleation of high Ti bearing steel.* Scripta Materialia, 68(12) (2013) 953-956.
28. K. Easterling, *Introduction to the Physical Metallurgy of Welding*, Butterworth-Heinemann, Oxford (1992) 138–172
29. P. L. Harrison, R. A. Farrar, *Application of continuous cooling transformation diagrams for welding of steels.* International Materials Reviews, 34(1) (1989) 35-51.
30. G. Spanos, R. W. Fonda, R. A. Vandermeer, A. Matuszeski, *Microstructural changes in HSLA-100 steel thermally cycled to simulate the heat-affected zone during welding.* Metallurgical and Materials Transactions A, 1995. 26(12) (1995) 3277-3293.
31. G. Spanos, R. W. Fonda, R. A. Vandermeer, NRL Rev., NRL/PU/5230/95/274, (1995) 59–70.
32. G. R. Speich, T. M. Scoonover, *Continuous cooling transformation behaviour and strength of HSLA-80 (A710) steel plates.* Processing, Microstructure and Properties of HSLA Steels, (1988) 263-286.

33. Y. Arata, *Weldability concept on hardness prediction*, JWRI (Japanese Welding Research Institute) Journal, 8(1) (1979) 43-52.
34. M. Takahashi, H. K. D. H. Bhadeshia, *The interpretation of dilatometric data for transformations in steels.* Journal of Materials Science Letters, 8(4) (1989) 477-478.
35. Y. E. Smith, C. A. Siebert, *Application of Modern Metallographic Techniques*, ASTM STP 480, ASTM, (1970) 131-150.
36. S. Suzuki, H. K. D. H. Bhadeshia, *Reversibility of the allotriomorphic ferrite and austenite transformations.* Materials Science and Engineering A, 186 (1-2) (1994) 157-162.
37. P. J. Alberry, W. K. C. Jones, *Diagram for the prediction of weld heat-affected zone microstructure.* Metals Technology, 4(1) (1977) 360-364.

Chapter 7

7 Toughness and microstructure of weld and HAZ

7.1 Introduction:

In the past, structural and machine designers were using mainly strength as a design criterion. Although, due to loss of ductility in some high-strength materials developed, later on, catastrophic failures occurred without any indication of plasticity issues. This led to the development of new design criteria to select materials based on strength and toughness [1]. Q&T steels were developed for this purpose. However, conventional Q&T steels were replaced by thermo-mechanically processed microalloyed steels, due to their low production cost and better strength and toughness properties [2-7]. Fabrication of these steels using welding may cause deterioration of the base metal properties due to thermal cycles [8]. Also, hydrogen may be entrapped in the weld microstructure and base metal HAZ, causing hydrogen-induced cracking [9-16]. A tough weld metal microstructure can better resist hydrogen-induced cracking than one which is less tough [17]. Weldability of steel is a complex property because of problems associated with it, such as hydrogen cracking, solidification cracking, HAZ toughness, and weld toughness [18]. Hence, to avoid brittle fracture at low temperatures, the weld joints, in particular their HAZ, should have adequate toughness. Obviously, the weld thermal cycle that results in a peak temperature of about 1300 °C in the area adjacent to the molten metal can lead to pronounced precipitates dissolution. The consequences are austenite grain growth and the formation of hard transformation products during cooling, which result in rather low toughness zones susceptible to brittle fracture initiation. To prevent embrittlement, which results from excessive grain coarsening and formation of complex bainitic microstructure containing coarse martensitic/austenitic constituents, steel manufacturers have attempted to restrict the austenite grain growth via introducing finely dispersed thermally stable particles, such as Ti nitrides or Ti oxides. Research [19-22] indicates that fine-grained HAZs can be achieved in high heat input welds by using Ti-microalloyed steels for over a decade. In contrast, it was reported [23-25] that conventional Ti addition techniques for improving HAZ toughness cannot be applied for welding with high heat input, due to the dissolution of Ti carbides/nitrides and subsequent

fast austenite grain growth. The highest weld metal toughness is achieved when the intra-granular microstructure consists of acicular ferrite and when a low amount of pro-eutectoid inter-granular ferrite is also present [19]. However, this study was limited to steel grades containing low Ti contents (~0.015 wt.%).

In this chapter, the weld and HAZ toughness were assessed using Charpy-V notch impact testing according to AS 2205.7.1-2003 standard for two Ti-microalloyed steels, Steel L of 32 mm thickness and Steel H of 30 mm thickness, containing higher Ti contents than previously studied. The samples were taken from K-type groove welded plates. Welding was carried out with flux-cored arc welding (FCAW) process. Two heat input values (1.2kJ/mm and 3.5kJ/mm) were used to weld each steel. The samples were subjected to hardness testing, optical and SEM microstructural analysis, and Charpy impact testing.

7.2 Results

7.2.1 Hardness Profile

Samples taken from the K-type groove welded plates were subjected to Vickers hardness testing using 5 kg force. Both types of steel demonstrated similar patterns in hardness variation with distance from the weld fusion line: the hardness was minimal in the weld, increase in the HAZ, and decrease towards the base metal (Figure 7.1). For Steel L and Steel H, welded with a heat input of 1.2 kJ/mm, the average hardness in the weld region was 234 HV and 230 HV, respectively; and welded with heat inputs of 3.5 kJ/mm, the average hardness in the weld was 220 HV and 228 HV, respectively. As can be seen, the hardness of Steel H did not vary significantly with heat input, although it decreased by about 6 % in Steel L with an increase in heat input. For both steels welded with both heat inputs, an increase in HAZ hardness was noted at a distance of ~2mm from the fusion line, and the HAZ hardness decreased at a distance of approximately 5 mm from the fusion line. For both steels, the variation in hardness corresponded to a change in microstructure presented below. Ultimately, thermal cycling may induce a detrimental impact on toughness. Therefore, the microstructural investigation and toughness assessment were conducted at the points of hardness extremes: fusion line, and 2 mm and 5 mm away from the fusion line.

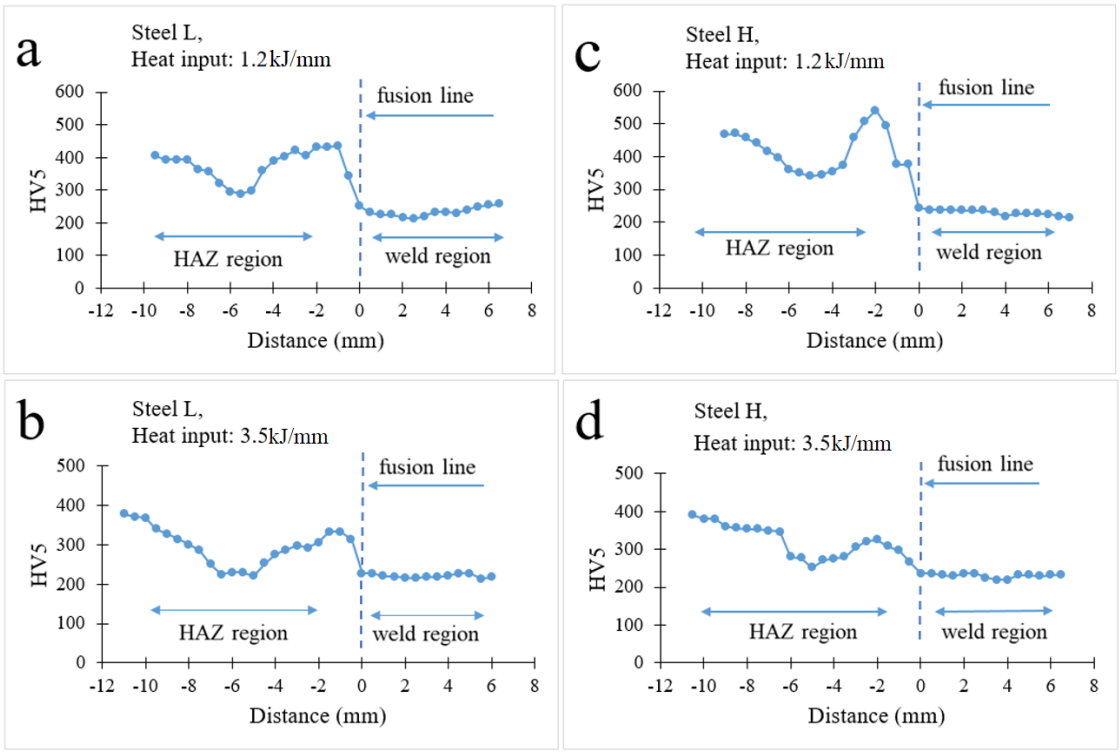

Figure 7.1 Hardness profiles for (a, b) Steel L and (c, d) Steel H welded with heat inputs of (a, c) 1.2 kJ/mm, and (b, d) 3.5 kJ/mm using flux-cored arc welding (FCAW) process.

7.2.2 Toughness Assessment

Based on hardness testing results, impact test samples were taken at 0, 2, and 5 mm from the fusion line. Three samples for each position were tested at four test temperatures of -70˚C, -40˚C, -10˚C, and room temperature (RT). Table 7.1 and 7.2 show the results of impact testing of both steels welded with heat inputs of 1.2 kJ/mm and 3.5 kJ/mm, respectively.

Table 7.1 Absorbed energy during Charpy impact testing of Steel L and Steel H samples welded with 1.2kJ/mm.

Test Temperature, (˚C)	-70	-40	-10	RT*	Steel Grade/ Thickness	Location of Samples
Absorbed Energy, (J) (average value of 3 samples for each test temperature) ± Standard Deviation	6.4 ±1.1	10.2 ±1.5	13.5 ±1.2	15.9 ±1.3	Steel L / 32mm	fusion line
	11.3 ±1.5	17.3 ±1.3	21.1 ±1.1	29.2 ±1.2	Steel H / 30mm	
	8.9 ±1.3	12.2 ±1.5	16.8 ±1.1	27.5 ±1.2	Steel L / 32mm	2 mm from the fusion line
	3.6 ±1.6	5.1 ±1.2	11.2 ±1.1	18.1 ±1.3	Steel H / 30mm	
	8.0 ±1.4	10.5 ±1.1	17.6 ±1.5	18.9 ±1.1	Steel L / 32mm	5 mm from the fusion line
	4.6 ±1.2	6.1 ±1.1	6.4 ±1.6	7.8 ±1.1	Steel H / 30mm	
RT*: Room Temperature						

For 1.2 kJ/mm heat input, Steel H showed higher absorbed energy at the fusion line position than Steel L; this coincides with a slightly higher hardness of Steel H (250 HV) than Steel L (240 HV) in the weld. Contrarily, Steel H showed less absorbed energy than Steel L at 2 mm from the fusion line, with hardness values of 541 HV for Steel H and 435 HV for Steel L, and 5 mm from the fusion line, with 340HV for Steel H and 289HV for Steel L. As can be seen, the trend for toughness does not follow this for hardness: in the below ~300 HV hardness range higher hardness results in higher toughness, although in the higher hardness range an opposite trend is observed – a higher hardness value leads to lower toughness. It is worth noting a decrease in absorbed energy in Steel H with an increase in distance from the weld metal. However, in Steel L an opposite trend was observed – energy increased with distance from the fusion line. This is obviously related to a variation in the microstructure and strength response to heat input for steels with different compositions.

Table 7.2 Absorbed energy during Charpy impact testing of Steel L and Steel H samples welded with 3.5kJ/mm.

Test Temperature, (˚C)	-70	-40	-10	RT*	Steel Grade/ Thickness	Location of Samples
Absorbed Energy, (J) (average value of 03 samples for each test temperature)	6.2 ±1.7	9.5 ±1.1	15.9 ±0.8	28.3 ±1.2	Steel L/ 32mm	fusion line
	6.1 ±0.8	7.3 ±1.3	10.3 ±1.7	16.4 ±0.9	Steel H/ 30mm	
	12.6 ±1.2	16.5 ±1.6	16.5 ±0.8	18.9 ±1.1	Steel L/ 32mm	2 mm from the fusion line
	6.0 ±0.9	6.0 ±1.5	8.2 ±1.1	10.7 ±0.9	Steel H/ 30mm	
	10.3 ±1.2	14.7 ±0.8	13.8 ±1.3	22.5 ±1.5	Steel L/ 32mm	5 mm from the fusion line
	7.3 ±1.6	7.3 ±0.8	8.3 ±2.1	10.2 ±0.9	Steel H/ 30mm	

For 3.5 kJ/mm heat input, Steel H showed less absorbed energy than Steel L for all test positions. This corresponded to higher hardness values for Steel H compared to Steel L (237 HV against 226 HV at the fusion line, 325 HV against 305HV at a distance of 2 mm, and 340 HV against 297 HV at the 5 mm position). The results show a characteristic relationship for high energy absorbed with respect to low hardness. In contrast to 1.2 kJ/mm heat input, Steel H showed the hardness dependence with a minimum (except for room temperature) at a 2 mm distance from the fusion line (which corresponded to the peak hardness). However, Steel L showed a dependence with a maximum (except for room temperature) at a 2 mm distance from the fusion line (which also corresponded to peak hardness in Steel L). As can be seen, hardness-toughness dependence shows different trends in steel with various compositions.

The absorbed energy dependences on testing temperature are plotted in Figures 7.2 and 7.3. For all the test positions in both steels, no sharp transition of behaviour was observed. Obviously, the absolute values of impact energy are already quite low to expect any further transition. This is characteristic of the studied Q&T steels with martensitic microstructure.

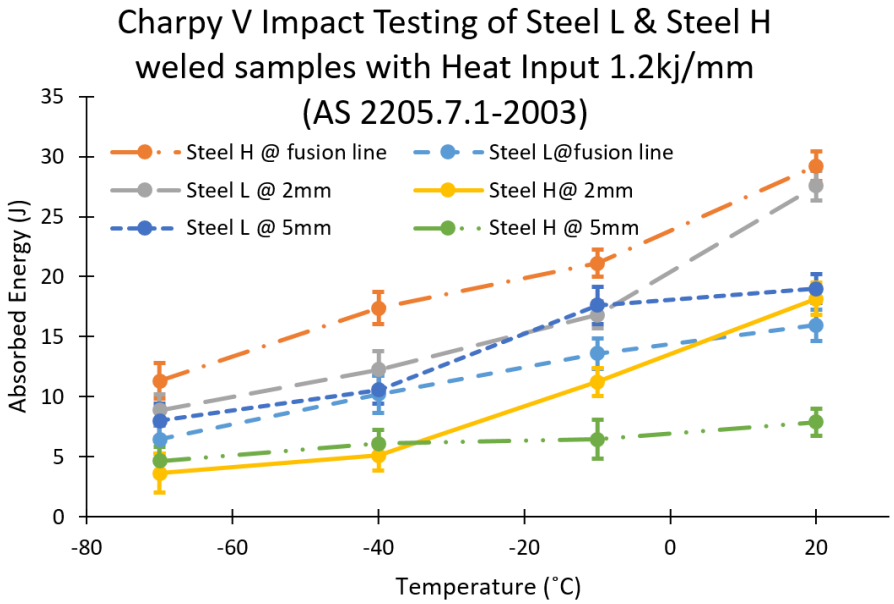

Figure 7.2 Toughness variation with testing temperature for Steel L and Steel H welded with a heat input of 1.2 kJ/mm.

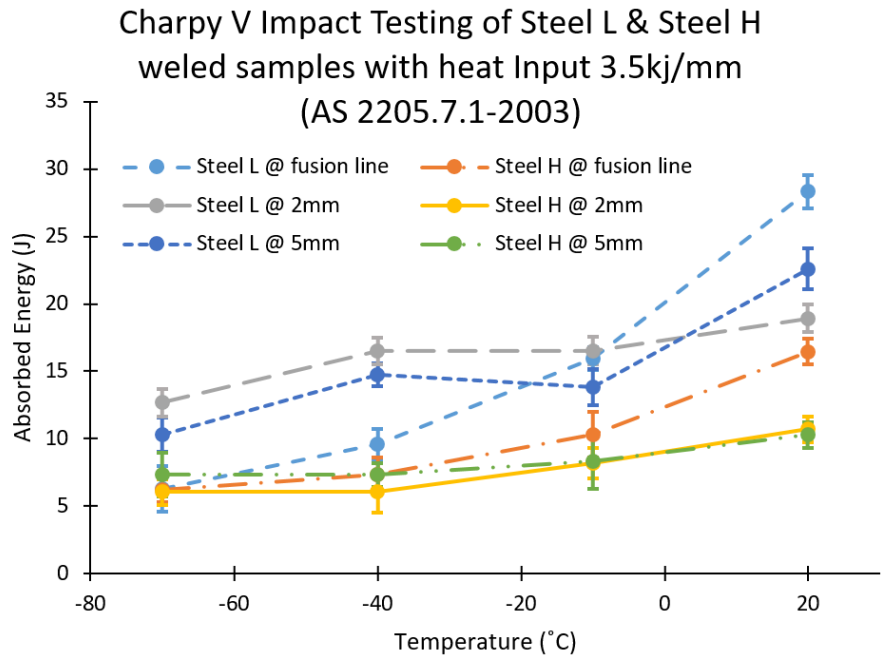

Figure 7.3 Toughness variation with testing temperature for Steel L and Steel H welded with a heat input of 3.5 kJ/mm.

7.2.2 Grain Structure

In the as-received condition, both steels had a martensitic microstructure (Figure 7.4). SEM imaging of the welded samples revealed a variation in grain structure with distance from the fusion line for different heat inputs (Figure 7.5 and 7.6).

Both steels welded with 1.2 kJ/mm heat input exhibited similar microstructures at the same position from the weld: granular bainite at the fusion boundary, martensite at the 2 mm from the fusion boundary, and tempered martensite at 5 mm from the fusion boundary. These can be explained by a relatively slow cooling rate of the weld metal, high cooling rate (originating from the heat transfer to the base metal) at the 2 mm position during reverse martensite-austenite-martensite transformation, and substantial heating (although below the temperature A1 of martensite transformation to austenite) at the 5 mm position. This corresponds to the measured hardness at these positions: the lowest for bainite at the fusion line, the maximum for martensite at the 2 mm position, and the medium value for tempered martensite at the 5 mm position.

Welding with 3.5 kJ/mm heat input resulted in slower cooling rates. Therefore, the microstructure at the fusion line and 2 mm position was similar, i.e. granular bainite. Remarkably, the microstructure at 5 mm position significantly varied with steel composition: it was a dual-phase ferrite + tempered martensite microstructure in Steel L and martensite in Steel H. This could be explained if the ferrite to austenite transformation temperatures (A1 and A3) were higher in Steel H due to grain boundary pinning effect of solute atoms and particles. In this case, the partial martensite-austenite transformation could occur in Steel L but Steel H at the 5 mm position.

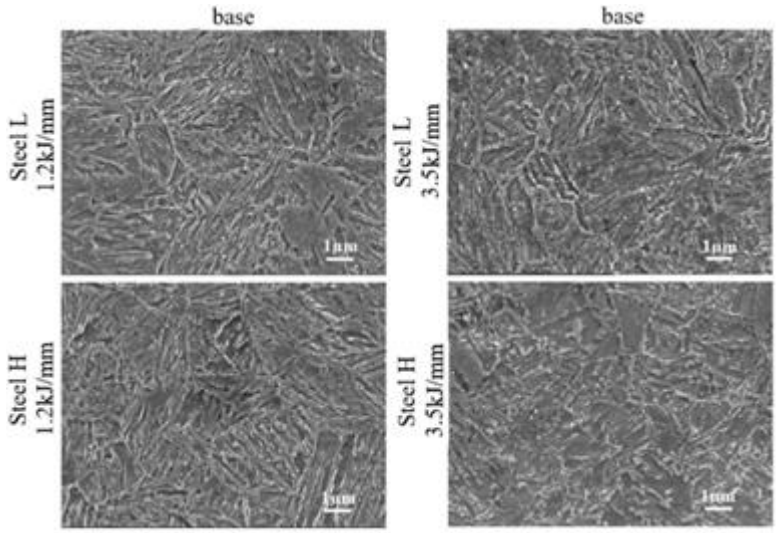

Figure 7.4 SEM images of grain structure in Steels L and Steel H at the base plate position.

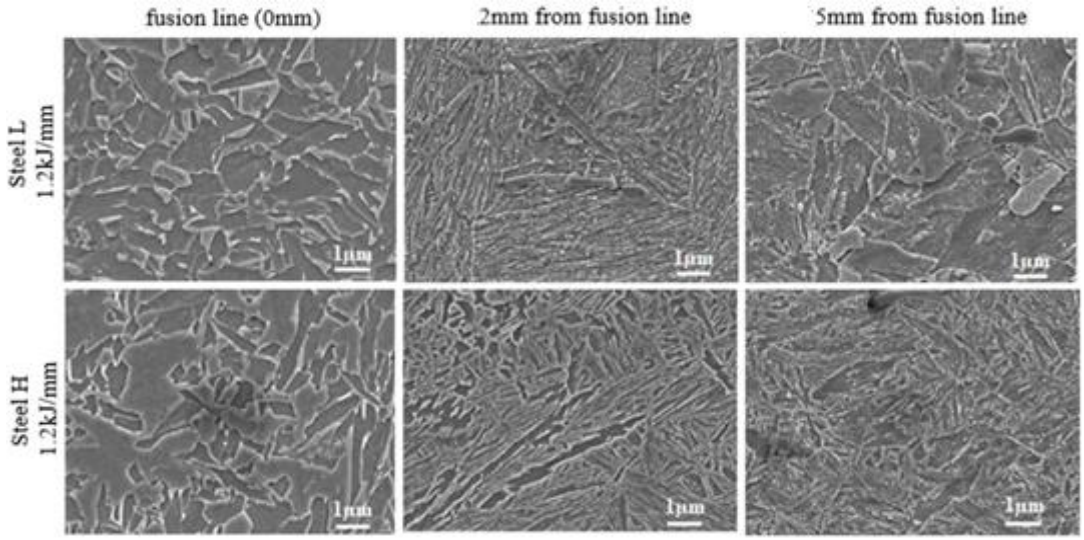

Figure 7.5 SEM images of grain structure in Steel L and Steel H after welding with 1.2 kJ/mm heat input.

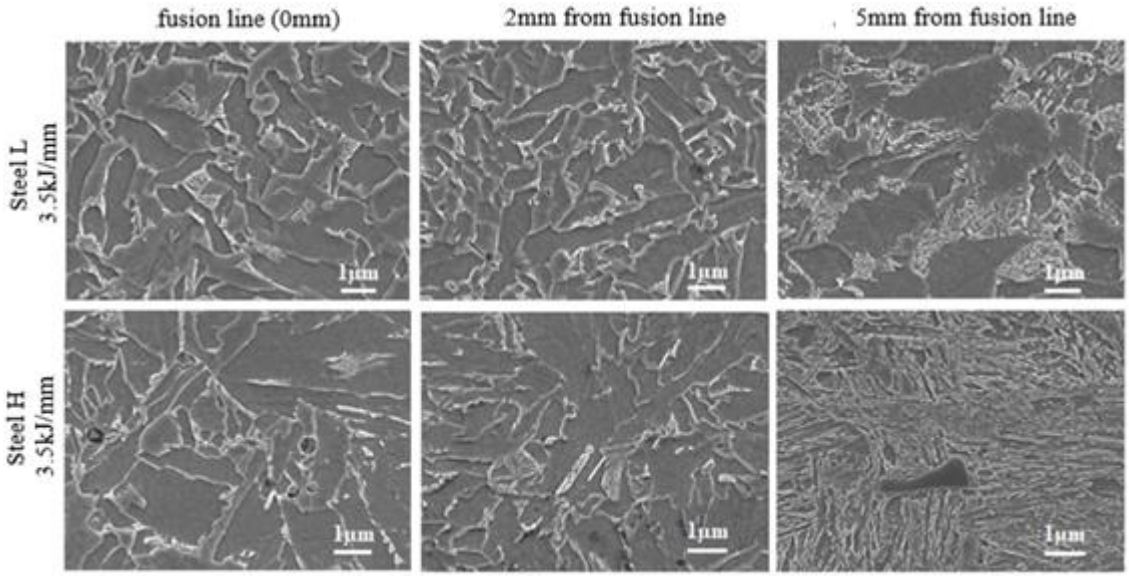

Figure 7.6 SEM images of grain structure in Steel L and Steel H after welding with 3.5 kJ/mm heat input.

Measurements of the average grain size (equivalent diameter) are presented in Table 7.3. In both steels welded with 1.2 kJ/mm, the minimum average grain size was observed at the position of the fusion line, where a bainitic microstructure was observed. Despite the narrow width of martensitic laths, they exhibited large lengths; therefore, martensitic microstructures away from the fusion line showed a larger equivalent diameter. In Steel H the equivalent diameter was smaller, probably due to narrower lath width, associated with a higher hardenability of Steel H.

Similar trends were observed after welding with 3.5 kJ/mm heat input. Although, the average grain size in the HAZ (namely, at 2 and 5 mm positions) was slightly higher for Steel L. This might be related to a larger prior austenite grain size in Steel L, originating from weaker grain boundary pinning due to lower concentrations of microalloying elements.

Table 7.3 Average grain size (equivalent diameter) in the studied steels.

Steel grade / Heat Input	**Steel L**				**Steel H**			
	1.2kJ/mm							
Position from fusion line	0 mm	2.0mm	5mm	base	0 mm	2.0mm	5mm	base
Average size, µm	1.7	2.8	2.6	2.4	2.0	2.1	2.1	2.5
	3.5kJ/mm							
Position from fusion line	0 mm	2.0mm	5mm	base	0mm	2.0mm	5mm	base
Average size, µm	2.1	2.7	2.6	2.4	2.2	2.5	2.6	2.5

7.2.3 Ti-rich particles

Optical and SEM imaging revealed three particle types in Steels L and H: coarse cuboidal/rectangular/elongated, fine spherical, and fine needle-shaped. Below is a detailed analysis of these particles in the studied steels after welding with two heat inputs (1.2 kJ/mm and 3.5 kJ/mm) for the three studied positions from the fusion line. SEM-EDS mapping confirmed the coarse particles (< 6 µm) to be TiMoVCN in both steels (Figure 4.3). Fine particles were of two types: spherical Ti-rich carbides or carbo-nitrides, and needle-shaped Fe_3C. Parameters of these particles varied with steel composition and distances from the fusion line (Figure 7.7, 7.8, and 7.9). Analysis of Ti-rich particle parameters (Table 7.4) has shown that:

- In Steel L, welded with 1.2 kJ/mm heat input the average particle size near the weld pool (118±82 nm at the fusion line and 164±97 nm at 2 mm position) was larger than in the base metal (114±22nm), while at the 5 mm potion (82±12nm) it was smaller than in the base. This was accompanied by a decrease in the particle number density, from 2.57 μm^{-2} in the base metal to 1.8, 0.73, and 0.50 μm^{-2} at 5 mm, 2 mm, and 0 mm from the fusion line, respectively, and a decrease in the particle area fraction, from 0.029 in the

base metal to 0.009, 0.014 and 0.008 at 5 mm, 2 mm and 0 mm from the fusion line, respectively. These can be explained by particle dissolution in the weld pool and coarsening in the HAZ. Partially dissolving coarse TiMoVCN particles and newly precipitating fine TiC closer to the base metal (areas of relatively lower temperature) may have contributed to a decrease in the size of fine TiC ones at 5 mm position.

- In Steel L welded with 3.5 kJ/mm heat input, the average particle size significantly (by 2-2.6 times) increased from the base metal (97±5nm) to the weld pool and HAZ (256±165 nm at the fusion line and 209±54 nm at the 2 mm position). At the same time, the number density of TiC particles was found to decrease by more than 10 times, from 2.9 μm^{-2} in the base metal to 0.25 and 0.24 μm^{-2} at 2 mm and 0 mm from the fusion line, respectively. Although the area fraction increased by about 1.7 times, from 0.015 in the base metal to 0.025 at the fusion line. This indicates particle dissolution in the weld and coarsening in the HAZ, and it was more pronounced after welding with 3.5 kJ/mm heat input compared to 1.2 kJ/mm. A larger particle coarsening after welding with a higher heat input can be related to longer cooling times (giving more time for particle growth) after welding with higher heat input. Partially dissolving coarse TiMoVCN and newly precipitating fine TiC particles may have contributed to a decrease in the size of fine Ti-rich particles at a 5 mm position. A variation in particle parameters for this position with heat input is probably within the experimental error.
- In Steel H, welded with a heat input of 1.2 kJ/mm the average particle size increased by 2.2 times from 106±20 nm in the base metal to 233±84 nm at the fusion line. This was accompanied by a decrease in the number density by 6 times from 2.05 μm^{-2} in the base to 0.34 μm^{-2} at the fusion line. After welding with a heat input of 3.5 kJ/mm the average particle size increased by 3.4 times from 99±37 nm in the base metal to 337±76 nm at the fusion line. At the same time, the number density decreased by 5.5 times from 2.5 μm^{-2} in the base to 0.45 μm^{-2} at the fusion line. These indicate the particle dissolution in the weld, and this was more pronounced during welding with higher heat input. A decrease in the particle size at 2 mm position during welding with 1.2 kJ/mm (98±7 nm) may be related to the particle precipitation, occurring closer to the weld compared to this for Steel L (remember the particle size in Steel L decreased at 5 mm position). This could originate from the higher microalloying element concentrations in the steel matrix of Steel H shifting the temperature field of particle precipitation to higher values.

- In Steel H, welded with 3.5 kJ/mm heat input the average particle size steadily increased from the base metal (99±37 nm) through the HAZ (123±59 nm at 5 mm and 142±52nm at 2 mm) to the weld pool (337±76 nm at the fusion line). This was accompanied by a steady decrease in the number density from the base metal (2.5μm^{-2}) through the HAZ (0.67μm^{-2} at 5 mm and 0.55μm^{-2} at 2 mm) to the weld pool (0.45μm^{-2} at the fusion line). These indicate the particle coarsening in the HAZ. Despite similar particle sizes in the base metal, the particle coarsening resulted in generally larger particle sizes and volume fraction in the HAZ for Steel H compared to Steel L. This is related to higher concentrations of microalloying elements in the matrix of Steel H. During thermal cycling these atoms may contribute to particle growth and precipitation in the HAZ.

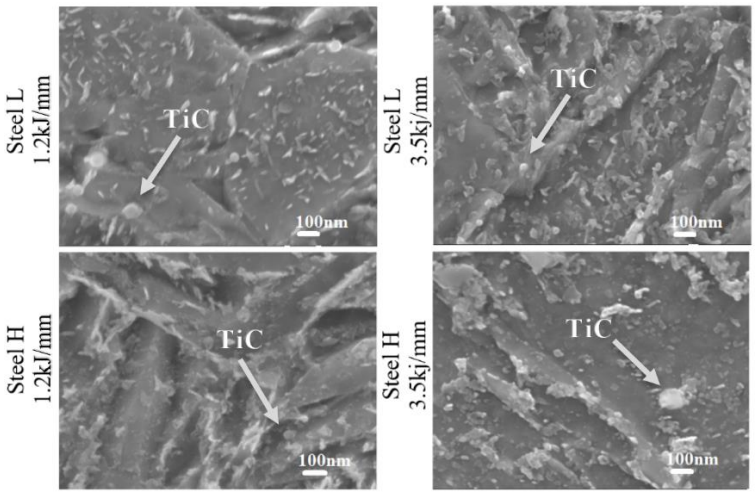

Figure 7.7 SEM images of fine TiC precipitates in the base metal of Steel L and Steel H welded with FCAW process using 1.2 kJ/mm and 3.5 kJ/mm heat inputs.

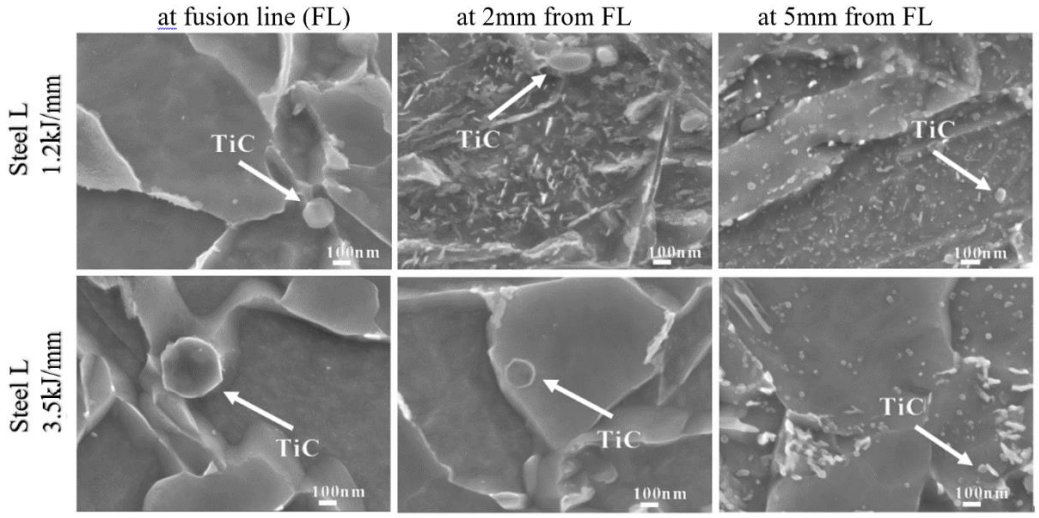

Figure 7.8 SEM images of fine precipitates in Steel L at the fusion line, 2 mm from the fusion line, and 5 mm from the fusion line.

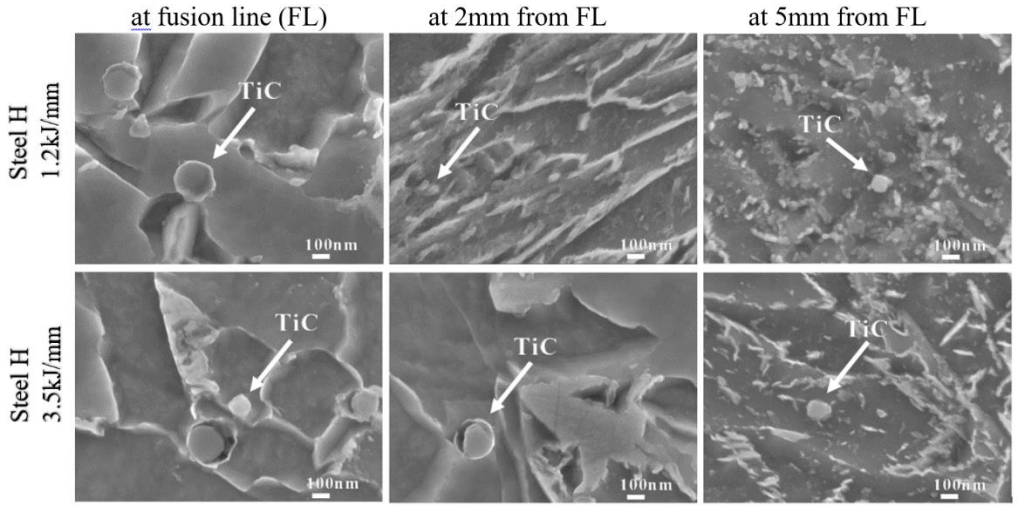

Figure 7.9 SEM images of fine precipitates in Steel H at the fusion line, 2 mm from the fusion line, and 5 mm from the fusion line.

Table 7.4 Average parameters of fine Ti-rich particles studied with SEM.

Steel grade/ Heat Input	**Steel L**				**Steel H**			
	1.2kJ/mm							
Position from fusion line	0 mm	2 mm	5 mm	base	0 mm	2 mm	5 mm	base
Average particle size, nm	118±82	164±97	82±12	114±22	233±84	98±7	129±53	106±20
Number density, μm^{-2}	0.50	0.73	1.80	2.57	0.34	0.46	1.07	2.05
Area fraction of particles	0.008	0.014	0.009	0.029	0.020	0.004	0.016	0.017
	3.5kJ/mm							
Position from fusion line	0 mm	2 mm	5 mm	base	0 mm	2 mm	5 mm	base
Average particle size, nm	256±165	209±54	78±20	97±5	337±76	142±52	123±59	99±37
Number density, μm^{-2}	0.24	0.25	1.49	2.90	0.45	0.55	0.67	2.5
Area fraction of particles	0.025	0.012	0.007	0.015	0.05	0.01	0.005	0.013

The particle number density distributions (Figures 7.10) support a general trend for dissolution of fine Ti-rich particles in Steel L and Steel H discussed above. In Steel L welded with a heat input of 1.2 kJ/mm, the particle density peaks, noted in the particles size range of 40-60 nm and ≥120 nm, decreased from near 1.0μm^{-2} in the base metal to ~0.4 μm^2 at 5 mm and to <0.1 μm^2 at 2 mm away from the fusion line and the fusion line (Figure 8.10a). At the same time, the particle size fraction distribution showed a larger fraction of <20 nm particles at the fusion line compared to other areas (Figure 7.10b). This indicates a not complete dissolution of TiC particles in the weld pool at the lower heat input of 1.2 kJ/mm.

At the higher heat input of 3.5 kJ/mm, a similar qualitative trend was observed in Steel L (Figure 7.10c): dissolution of TiC particles. However, it occurred more intensively. Thus, at 5 mm position no particles were observed in the 100-120 nm size range, although they were present after welding with 1.2 kJ/mm; at 2 mm position the particles completely dissolved in the 40-120 size range, and at the fusion line even very small <20 nm particles were not observed after welding with 3.5 kJ/mm.

In the base of Steel H, the particle density and size fraction distributions showed the presence of relatively large particles compared to Steel L (note a flat-shaped part of the distribution in the 60-120 nm particle size range Figure 8.10e, compared to a high peak in the 40-60 nm size range in Figure 7.10a). This is in line with all the particle characterisation results discussed previously. During welding with 1.2 kJ/mm heat input many particles in the 20-60 size range at the 5 mm position and 60-80 nm size range at the 2 mm position survived. This could be related to a more complex composition of Ti-rich particles in Steel H, associated with higher contents of microalloying elements in it. More complex particles are known to exhibit higher solubility temperatures. Compared to Steel L welded with 1.2 kJ/mm heat input, no particles in the ≤ 20 nm size range were observed in Steel H at the fusion line (Figure 7.10e) and very few of 20-40 nm particles were present at 2 mm position. This is in line with generally larger particles in Steel H than in Steel L in view of their variations in composition.

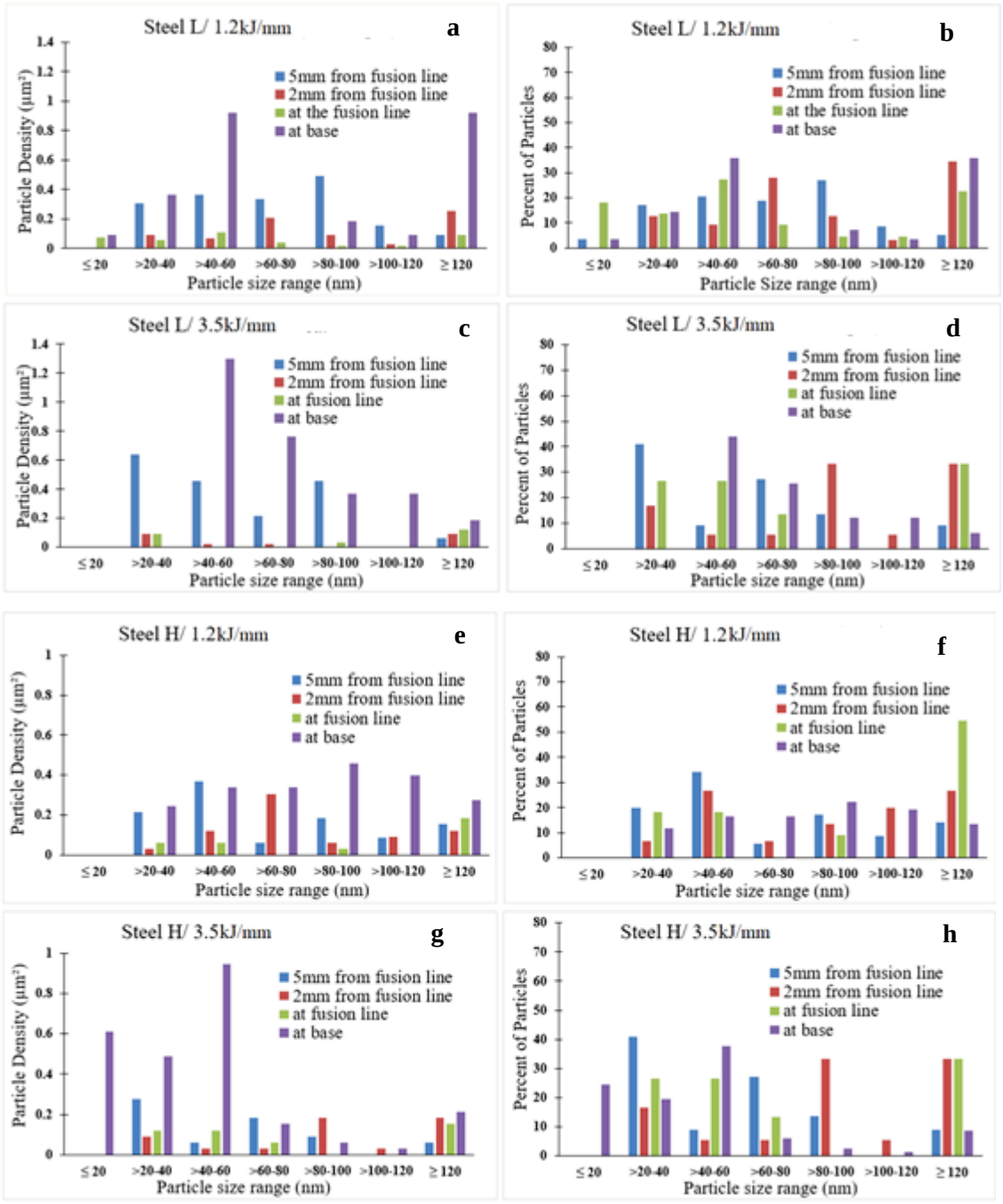

Figure 7.10 Fine Ti-rich particle number density distributions and size fraction distributions in Steel L and Steel H welded with heat inputs of 1.2 kJ/mm and 3.5 kJ/mm, observed at the base, fusion line, and distances of 5 mm and 2 mm from the fusion line.

Welding of Steel H with a higher heat input of 3.5 kJ/mm resulted in a decrease in the number density of 40-120 nm particles at both 2 mm and 5 mm positions (Figure 7.10g), compared to welding with 1.2 kJ/mm (Figure 7.10e). The fraction of >120 nm particles in the fusion line also decreased compared to the welding with 1.2 kJ/mm. These support

a more pronounced dissolution of particles at a higher heat input. Precipitation of <60 nm particles in the base requires further investigation (Figure 7.10g). Although, at the higher heat input of 3.5 kJ/mm a larger HAZ size might be expected, this would affect the conditions of the samples selected for investigation. Supersaturation of the matrix in Steel H with microalloying elements makes it susceptible to low-temperature precipitation, which could be observed at a higher distance from the fusion line.

7.3 Discussion

7.3.1 Effect of heat input on microstructure

Titanium (Ti) is mainly added because of its ability to form nitrides and carbides stable even at higher temperatures (~1350˚C). The expected role of Ti in steels, however, can be complex if the steel composition contains more than one microalloying element, e.g., Ti, Nb, and V, because of mutual solid solubility. These complex Ti carbonitrides precipitate in steel, influence grain growth, and precipitation hardening during welding [20]. In high Mn, Mo, and Cr steels the particle solubility temperature may decrease, this would weaken the austenite grain boundary pinning effect and allow grain growth. With the temperature gradient from the weld pool to the base metal, several zones with different thermal cycles and phase transformation history appear. This results in the hardness variation with distance from the fusion zone.

The Steel L and Steel H samples welded with 1.2 kJ/mm showed the grain size increasing towards the fusion line, which experienced very fast heating and cooling from an average peak temperature of 1300 to 1350˚C [54]. The grain size observed for both steels at the base was found to be similar but changed at the fusion line, and away from the fusion line towards the base, due to the effect of heat input. The microstructure of Steel L and Steel H showed substantial dissolution of microalloying element particles and growth of a limited number of TiC (Figure 7.8 and 7.9). A granular bainite microstructure formed at the fusion line. At 2 mm and 5 mm from the fusion line, martensite and tempered martensite microstructures were observed. Granular bainite microstructure at the fusion line indicates relatively slow cooling rates in the weld pool compared to the 2 mm and 5 mm positions away from the fusion line. High cooling rates at the 2 mm position (which are required to obtain martensite) originated from the heat transfer towards the base metal. Martensitic type of microstructure obviously resulted in the highest hardness at the 2 mm

position. The chemical composition of the welding electrode (low carbon steel) also influenced the phase transformation kinetics in the weld pool. Lower carbon content in the weld pool would increase the austenite to ferrite transformation start temperature and decrease hardenability, i.e., facilitate the transformation to ferrite instead of martensite. In combination with the cooling rate effect, the decreased carbon content favoured the formation of a bainitic microstructure. Away from the fusion line (5 mm position), the effect of electrode composition did not show itself, and, thus, a heat transfer has led to recovery (dislocation annihilation) and associated with it, the hardness minimum.

Steel L and Steel H welded with a higher heat input of 3.5 kJ/mm revealed larger microstructural changes. A more pronounced dissolution of microalloying element particle might have caused grain growth and recrystallization, and the presence of undissolved microalloying constituents could serve as nucleation sites for small ferritic grains of smaller diameters at the fusion line, compared to those observed at a distance of 2 mm from the fusion line. Because the higher heat input generated a wider heat effected zone with a slower cooling rate, bainitic microstructure formed at a wider distance (up to 2 mm away from the fusion line) compared to welding with the lower heat input (just at the fusion line); and this was observed in both steels. The effect of composition was observed at the 5 mm position: Steel L transformed to exhibit a ferrite-tempered martensite microstructure and Steel H – a martensitic microstructure. Probably, in Steel L the temperature A1 (ferrite to austenite transformation start temperature) was crossed at the 5 mm position and this resulted in the formation of ferrite (from austenite) during cooling and tempered martensite (in those areas where the reverse martensite-austenite transformation was not completed). In Steel H only tempering of the martensitic microstructure occurred at 5 mm position.

Investigation of the behaviour of the Ti-rich particles showed that their average sizes were larger at the fusion line compared with that at 2 mm, 5 mm, and base metal. At the same time, the particle density was decreasing in order from the base towards the fusion line. These phenomena were revealed for both grades of steel welded with both heat inputs of 1.2 kJ/mm and 3.5 kJ/mm. It is evident that the number of Ti-rich particles in the base was maximum, but decreased towards the weld pool due to dissolution associated with heat input. Some particles adjacent to the fusion line showed growth to larger diameters. Given the low carbon steel electrode, the base metal had higher contents of Ti, C, Mo, and V, so their concentrations decreased the solubility of TiMoVCN and TiC particles

[26, 27] and increased their precipitation start temperatures. Traditionally, this leads to higher particle number densities at room temperature [28-30]. Due to the chemical composition effects, Steel H showed a higher dissolution temperature of Ti-rich particles than Steel L, but the qualitative hardness trend was similar for both steels. Steel H showed higher hardness values due to a higher solid solution, precipitation strengthening, and phase balance strengthening (remember a higher hardenability of Steel H) effects. The solid solution strengthening could be based on super-saturation of the matrix with Mn, Si, Mo, Ni, Cu and C. High density of precipitation in the base metal showed higher hardness for both steels while it decreased at the fusion line and in the weld metal, irrespective of the heat input values. Hardness showed a maximum at 2 mm from the fusion line, due to martensite formation following fast cooling from austenite during welding. Steel L welded with 1.2 kJ/mm and 3.5 kJ/mm showed different behaviour in comparison to Steel H, in terms of grain sizes adjacent to the fusion line. Steel L showed a higher average grain size, which supports grain growth just after recrystallization at the fusion line. The higher particle density was likely less effective in retarding austenite grain growth in Steel L compared to Steel H, which showed lower particle density along with lower grain size. It may be explained if fine TiC particles were less effective in Steel L than coarse TiMoVCN particles in Steel H[20]. Also, the matrix of Steel H might be enriched in Mn, Mo, Ni, C, and N, this would also contribute to the solute drag effect and retardation of the grain boundary migration.

Hardness decreased at 5 mm position for both steel grades. There was no appreciable grain size variation with respect to that, but there was a variation in TiC particle average size and number density. For Steel, L welded with 1.2 kJ/mm and 3.5 kJ/mm, average particle size and particle number density decreased, which confirms dissolution of TiC particles at 5 mm. In addition to recovery (dislocation annihilation), this contributed to the hardness decreasing. This supports the concept that the grain structure recovery (dislocation annihilation) and recrystallization in HAZ can significantly contribute to a hardness decrease, irrespective of the particle precipitation kinetics because the number of dislocation-obstacle interaction sites is responsible for strength, not the number of particles dispersed in the matrix.

Steel H welded with both heat inputs showed an increase in the average particle size and a decrease in the number density. This supports coarsening of the particle (dissolution of small and growth of large) more pronounced at the higher heat input. For both heat inputs,

Steel H appeared super-saturated with solute atoms. However, this caused less effect on hardness increasing than tempering of the microstructure on the hardness decreasing. Eventually, the hardness decreased to 5 mm from the fusion line.

Despite different precipitation kinetics of fine Ti-rich particles, hardness reduction at the fusion line and 5 mm position was observed in both steels. This indicates a strong effect of phase balance strengthening (namely formation of martensite) on mechanical properties, compared to the precipitation strengthening: martensitic microstructure will show a higher hardness than a bainitic or tempered martensite microstructure strengthened with solute atoms and particles. However, for similar matrix condition (namely the major phase being martensite) strengthening of Steel L with fine TiC particles was significant, and when their number densities decreased, the strength decreased; while in Steel H, the strengthening from solute C, N, and Mo atoms [31-33], Ti-Mo-C atom clusters [34-36] and <50 nm TiC particles [26][37-38] (not studied here) could be significant.

7.3.2 Effect of heat input on weld and HAZ toughness

The weldability of steel is a complex property since it depends on both the sensitivity to weld cracking and the requirement to produce high toughness. Microalloying elements appear in the weld metal via deliberate additions coming from the consumable electrode and as a result of dilution from the parent material. These elements have two major effects on the weldment and heat-affected zone properties. They modify the microstructure phase balance and promote precipitation hardening, which may be detrimental to toughness [39]. Tables 7.1 and 7.2 showed the toughness results obtained for the studied steels. Locations of samples were chosen according to the hardness minimum and maximum points (namely at the fusion line, 2 mm and 5mm from the fusion line). Previous studies indicate that small additions of titanium are beneficial to the Charpy toughness of multipass welds [44-49]. Titanium does not appear to have a direct effect on the hardenability of HAZ but the effect of titanium on hardenability is highly dependent on the prior thermal history of the material [40]. In wrought steel, the impact of microalloying elements on austenite transformation is often obscured because of carbide formation, which restricts austenite grain growth and removes carbon from the solution. This leads to a loss of hardenability which offsets the positive effects of microalloying

elements [40-41]. Steel L samples welded with 1.2 kJ/mm and 3.5 kJ/mm heat inputs, indicated more energy was absorbed for 2 mm samples for all test temperatures with respect to results at the fusion line and at 5 mm. This is because the weld metal and HAZ are rapidly cooled through the delta ferrite and high-temperature austenite temperature ranges, this gives less time for the growth of carbo-nitrides which could act as stress concentrations and deteriorate toughness. Thus, the activity of carbon in austenite is not significantly reduced, while in weld metals, austenite grain size is largely determined by columnar delta-ferrite grain size. Titanium more actively suppresses pro-eutectoid ferrite formation in weld metals and HAZs than in wrought materials [42].
In contrast, Steel H samples welded with 1.2 kJ/mm and 3.5 kJ/mm heat inputs, showed more energy absorbed at the fusion line compared to results for 2 mm and 5 mm distance. It may be due to solid solution strengthening and precipitation strengthening with very fine <20 nm TiC particles not studied here. The potential advantages of producing a tougher microstructure must be weighed against the possibility of precipitation hardening. While strengthening by grain refinement improves cleavage resistance, precipitation of coarse particles may result in some toughness loss. The magnitude of this effect, and how much it offsets a reduction in pro-eutectoid ferrite content, depends upon the thermal cycle of the weld and the amount of alloying elements present [39].

No sharp ductile to brittle transition temperature was observed, though the samples taken at different locations of weld joints showed different behaviour for the energy absorbed at different test temperatures. In multi-pass welds, toughness depends upon the structure of regions reheated by subsequent runs and on the as-deposited structure. Here the grain-refining action of the microalloying elements comes into play. Useful improvements in Charpy toughness have been achieved from titanium additions in the weld metal [43-44]. Some authors [44-48] have quoted 0.04% titanium as the optimum addition to carbon-manganese weld metals, though smaller additions are required for more highly alloyed deposits [49]. This optimum level reflects the balance between the grain-refining and precipitation-hardening effects of titanium. In single pass 1.6 kJ/mm CO_2 welds, cleavage resistance was continuously reduced by titanium additions [50]. Fehervari and Rittinger [51] showed that excess titanium is more harmful in two- than in multi-pass welds. Borisenko and Novozhilov [52] questioned whether optimum titanium levels could be achieved in practice with adequate reliability, given the low and variable transfer

efficiency of titanium and variations in dilution encountered in practice. Although deliberate titanium additions to the weld may be of uncertain value, no serious adverse effects of small amounts of pick up from titanium-bearing steel have been observed. Since the toughness of the HAZ depends on microstructure, the effect of microalloying elements will depend upon transformation characteristics and precipitation behaviour. Some degree of brittleness can be expected if precipitation behaviour occurs upon cooling, i.e. when the austenite decomposition products are predominantly ferrite. Such structures appear at comparatively slow cooling rates [53]. In a typical two-pass weld, the second pass remains in the as-cast condition and often has comparatively poor impact characteristics due in part to the weld metal microstructure [54-57].

Although Steel L welded with 3.5 kJ/mm showed slightly higher hardness at 2 mm from the fusion line, good toughness was observed, which may be associated with fine-grained bainitic microstructure, in comparison to other test positions. Steel H toughness after welding with 3.5 kJ/mm was slightly higher compared to welding with 1.2 kJ/mm, due to (i) dissolution of a larger number of coarse particles, (ii) precipitation of finer TiC particle with a higher number density, and (iii) potentially higher strengthening with <20 nm TiC not studied, here and solid solution strengthening – all these would have facilitated the formation of a more homogeneous stress field during impact testing of the Steel H and increased the absorbed energy.

7.4 Conclusion

Welding of two Ti-microalloyed martensitic steels containing 0.28C-0.4Ti (Steel L of 32 mm thickness) and 0.38C-0.6Ti (Steel H of 30 mm thickness) altered the microstructure, hardness, and toughness of the steels, and these changes varied with distance from the fusion line. The following conclusions can be drawn from the investigation conducted using samples welded with two heat inputs of 1.2 kJ/mm and 3.5 kJ/mm.

1. The microstructural study carried out for welded test coupons following the hardness variation profile revealed a larger grain size at the 2 mm position from the fusion line irrespective of steel grade and heat input. Dissolution of TiC particles was observed at the fusion line for both steel grades irrespective of the heat input. Generally, the particle number density decreased from the base metal towards the fusion line, and a minimum value was observed at the fusion line. This supports the dissolution of TiC particles

towards the fusion line, i.e., with an increase in temperature. Although this phenomenon was observed for both steel grades irrespective of the heat input value, the decrease in particle density was more prominent during welded with a higher heat input of 3.5 kJ/mm. A similar observation was made for the average size of TiC particles i.e. it was higher for steel grades welded with 3.5 kJ/mm.

2. Impact testing carried out for both steels at the fusion line, 2 mm and 5 mm positions from the fusion line showed a decrease in absorbed energy with a decrease in test temperature. Higher toughness was observed at 2 mm from the fusion line for Steel L and at the fusion line for Steel H. This was associated with a combination of grain refinement and precipitation strengthening at respective positions. No sharp transition from ductile to brittle fracture behaviour was observed in any steels at any position.

3. In view of the obtained results, it is advisable to weld Q&T steels microalloyed with Ti using lower heat inputs, since steels welded with 1.2 kJ/mm heat input showed a higher toughness. This is associated with the formation of fine-grained microstructure coupled with higher densities of small Ti-rich particles.

References (Chapter-7)

1. M. E. Haque, K.V. Sudhakar, *ANN back-propagation prediction model for fracture toughness in microalloy steel.* International Journal of Fatigue, 24(9) (2002) 1003-1010.
2. L. Ceschini, A. Marconi, C. Martini, A. Di Scino, *Tensile and impact behaviour of a microalloyed medium carbon steel: Effect of the cooling condition and corresponding microstructure.* Materials and Design, 45 (2013) 171-178.
3. S. Shanmugam, N. K. Ramisetti, R. D. K. Misra, T. Mannering, D. Panda, S. Jansto, *Effect of cooling rate on the microstructure and mechanical properties of Nb-microalloyed steels*, Materials Science and Engineering: A, 460–461 (2007) 335-343.
4. X. Fang, Z. Fan, B. Ralph, P. Evans, R. Underhill, *Influence of accelerated cooling on microstructure and mechanical properties of C -Mn steels, Materials Science and Technology*, 18(1) (2002) 47-53.
5. M. Thompson, M. Ferry, P. A. Manohar, *Simulation of hot band microstructure of C-Mn steels during high-speed cooling*, ISIJ International, 41(8) (2001) 891-899
6. J. H. Ai, T. C. Zhao, H. J. Gao, Y. H. Hu, X. S. Xie, *Effect of controlled rolling and cooling on the microstructure and mechanical properties of 60Si2MnA spring steel rod*, Journal of Materials Processing Technology, 160(3) (2005) 390-395.
7. E. V. Pereloma, C. Bayley, J. D. Boyd, *Microstructural evolution during simulated OLAC processing of a low carbon microalloyed steel*, (1996) Materials Science and Engineering: A, 210 (1-2) (1996) 16-24.
8. J. Rittinger, A. Fehervari, *The influence of Microalloying Elements on the Toughness of steel in Welded Structures*, Microalloying 75: Proceedings of an International Symposium on High-strength, Low-alloy Steels, Washington, D.C., U.S.A (1975) 593-598.
9. R. L. O'Brien, *Welding Handbook*, Volume 2, American Welding Society, Miami, USA, 2 (1991).
10. J. C. Ritter, B.F. Dixon, N.J. Baldwin, *Deformation and weld repair of armour steel*, Material Forum 13 (1989) 216-224.
11. N. Yurioka, H. Suzuki, *Hydrogen assisted cracking in C-Mn and low alloy steel weldments*, International Materials Reviews 35(1) (1990) 217-249.

12. G. Magudeeswaran, V. Balasubramanian, G. Madhusudhan Reddy, *Hydrogen induced cold cracking studies on armour grade high strength, quenched and tempered steel weldments*. International Journal of Hydrogen Energy 33(7) (2008) 1897-1908.
13. L. Kuzmikova, M. Callaghan, N. Larkin, R. Scott, R. DeJong, H. Li, J. Norrish, *A study of a continuous cooling behaviour and effect of preheat and interpass temperature on the HAZ of high strength quenched and tempered steel*, Proceedings of the International Institute of Welding Annual Assembly, Istanbul, Turkey, 63 (2010) paper IX-2352-10.
14. I. Barenyi, O. Hires, P. Liptak, *Degradation of mechanical properties of armoured steels after its welding*, Proceedings of International Conference of Scientific Paper, AFASES2011, Brasov, Romania, (2011) 845-848.
15. I. Barenyi, O. Hires, P. Liptak, *Over tempering of armox armoured steels at their secondary processing*. in Proceedings of International Conference of Scientific Paper, AFASES2012, Brasov, Romania, (2012) 641-643.
16. L. Kuzmikova, N. Larkin, Z. Pan, M. Callaghan, H. Li, J. Norrish, *Investigation into feasibility of hybrid laser-GMAW process for welding high strength quenched and tempered steel*, Australasian Welding Journal 57 (2012) 1-9
17. N. Bailey, F. R. Coe, T. G. Gooch, P. H. M. Hart, N. Jenkins, R. J. Pargeter, *Chapter 1 - Defining the problem, Welding Steels Without Hydrogen Cracking* (Second Edition), Woodhead Publishing, (2) (2004) 12.
18. P. H. M. Hart, R. E. Dolby, N. Bailey, and D. J. Widgery, *The weldability of microalloyed steels*, Microalloying 75: Proceedings of an International Symposium on High-strength, Low-alloy Steels, Washington, D.C., U.S.A. 1 (1975) 540-550
19. I. Rak, V. Gliha, M. Kocak, *Weldability and toughness assessment of Ti-microalloyed offshore steel*, Metallurgical Materials Transactions, 28A (1997) 199-206.
20. S. Suzuki, Weatherly GC, Houghton DC, *The response of carbo-nitride particles in HSLA steels to weld thermal cycles*, Acta Metallurgica, 35(2) (1987) 341-352.
21. S. Kanazawa, A. Nahashima, K. Okamoto, K. Knaya, *Improvement of weld fusion zone toughness by TiN*, (1976) Trans Iron Steel Institute Japan, 16 (1976) 486.

22. B. Loberg, A. Nordgren, J. Strid, K. Easterling, *Role of alloy composition on the stability of nitrides in ti-microalloyed steels during weld thermal cycles*. (1984) Metallurgical Materials Transactions A, 15(1) (1984) 33-41.
23. M. Shome, O. P. Gupta, O. N. Mohanty, *A modified analytical approach for modeling grain growth in the coarse grain HAZ of HSLA steels*, Scripta Materials 50(7) (2004) 1007-1010.
24. E. J. Palmiere, C.I Garcia, A. J. DeArdo, *Compositional and microstructural changes which attend reheating and grain coarsening in steels containing niobium*, Metallurgical Materials Transactions A, 25 (19994) 277-286.
25. A. Ghosh, S. Das, S. Chatterjee, P. R. Rao, *Effect of cooling rate on structure and properties of an ultra-low carbon HSLA-100 grade steel*. Materials Characterization, 56(1) (2006) 59-65.
26. H. S. El-Faramawy, S. N. Ghali, M. M. Eissa, *Effect of Titanium Addition on Behavior of Medium Carbon Steel*, Journal of Minerals and Materials Characterization and Engineering 11 (2012) 1108-1112
27. J. Strid, K. E. Easterling, *On the chemistry and stability of complex carbides and nitrides in microalloyed steels*, Acta metal 33 (1985) 2057-2074
28. L. A. Dobrzanski, A. Zarychta, M. Ligarski, *High-speed steels with addition of niobium or titanium*, J. Material Processing Technology, 63 (1997) 531-541.
29. R. Soto, W. Saikaly, X. Bano, C. Issartel, G. Rigaut, and A. Charai, *Statistical and theoretical analysis of precipitates in dual-phase steels microalloyed with titanium and their effect on mechanical properties*, Acta Materialia 47(12) (1999) 3475 – 3481
30. W. Yu, J. Li, C. Shi, Q. Zhu, *Effect of Titanium on the Microstructure and Mechanical Properties of High-Carbon Martensitic Stainless Steel 8Cr13MoV*. Metals, 6(8) (2016) 193.
31. Q. Lu, W. Xu, S. van der Zwaag, *Designing new corrosion-resistant ferritic heat resistant steel based on optimal solid solution strengthening and minimisation of undesirable microstructural components*, Computational Materials Science 84 (2014) 198–205.
32. J. Kong, C. Xie, *Effect of molybdenum on continuous cooling bainite transformation of low-carbon microalloyed steel*, Materials and Design 27 (2006) 1169–1173.

33. H. Hu, G. Xu, M. Zhou, Q. Yuan, *Effect of Mo Content on Microstructure and Property of Low-Carbon Bainitic Steels*, Metals 6 (2016) paper 173.
34. S. Mukherjee, I. Timokhina, C. Zhu, S. P. Ringer, P. D. Hodgson, *Clustering and precipitation processes in a ferritic titanium-molybdenum microalloyed steel*, Journal of Alloys and Compounds 690 (2017) 621 – 632.
35. S. Dhara, R. K. W. Marceau, K. Wood, T. Dorin, I. B. Timokhina, P. D. Hodgson, *Precipitation and clustering in Ti-Mo steel investigated using atom probe tomography and small-angle neutron scattering*, Materials Science and Engineering A 718 (2018) 74-86.
36. C.-Y. Chen, J.-R. Yang, C.-C. Chen, S.-F. Chen, *Microstructural characterization and strengthening behavior of nanometer-sized carbides in Ti-Mo microalloyed steels during the continuous cooling process*, Materials Characterization 114 (2016) 18–29.
37. K. Zhang, Z.-D. Li, X.-J. Sun, Q.-L. Yong, J.-W. Yang, Y.-M. Li, P.-L. Zhao, *Development of Ti-V-Mo complex microalloyed hot-rolled 900MPa grade high strength steel*, Acta Metall. Sin. (Engl. Lett.), 28(5) (2015) 641–648.
38. Z. Wang, H. Zhang, C. Guo, W. Liu, Z. Yang, X. Sun, Z. Zhang, F. Jiang, *Effect of molybdenum addition on the precipitation of carbides in the austenite matrix of titanium micro-alloyed steels*, J Mater Sci 51 (2016) 4996–5007.
39. P. H. M. Hart, R. E. Dolby, N. Bailey, and D. J. Widgery, *The weldability of Microalloyed Steels*, Microalloying 75: Proceedings of an International Symposium on High Strength Low Alloy Steels, Washington, D.C., U.S.A, 1 (1975) 540-551.
40. G. F. Comstock: *Titanium in Iron and Steel*, John Wiley & Sons, New York, (1955) 56-60.
41. W. O. Binder: *Boron, Calcium, Columbium, and Zirconium in Iron and Steel*, John Wiley & Sons, New York, (1957) 155-158.
42. D. J. Widgery: *Deoxidation Practice and the Toughness of Mild Steel Weld Metal*, PhD Thesis, University of Cambridge, (1974).
43. T. Boniszewski: *Titanium Steel Wires for CO_2 Welding*, Metal Construction, 1(5) (1969) 225-229.
44. F. Bonomo: *A Metallographic Investigation of Titanium-Bearing Weld Metal Deposited by the GMA Process*, British Welding Research Association Members' Report, M/28/68, April (1968).

45. J. Vrtel: Zvaranie, *The toughness of welded joints on steels with increased yield point*, (6) (1968) 161-166.
46. M. W. F. Cane and R. E. Dolby: *Metallurgical Factors Controlling the HAZ (Heat Affected Zone) Fracture Toughness of Submerged Arc Welded Carbon-Manganese Steels,* Welding Research International, 4(3) (1974) 51-72.
47. J. L. Kaae and N. Baoley, Metal construction, 1(8) (1969) 371-377.
48. N. E. Hannerz and B. M. Jonsson-Holmquist, Metal Source Journal, 8(7) (1974) 228.
49. R. C. Cochrane: *The effect of second phase particles on mechanical properties of steel*, British Steel Corporation, and Iron and Steel Institute Conference, March (1971).
50. B. M. Patchett, F. W. Collins and R. L. Apps: *Welding low-temperature containment plant,* Paper for Welding Institute Conference, London, November 20-22, (1973).
51. A. Fehervari and J. Rittinger, *Effect of Titanium on Transition Temperature of CO2 Weld*, IIW Document XII-B-98-71, (1971)
52. M. M. Borisenko and N. M. Novozhilov, *Effect of titanium on the impact toughness of the weld metal of CO2 joints*, Welding Production, 21(1) (1974) 36-39.
53. G. Bernard, *A viewpoint on the weldability of carbon-manganese ad microalloyed structural steels*, Microalloying 75: Proceedings of an International Symposium on High-strength, Low-alloy Steels, Washington, D.C., U.S.A, (1975) 552-569.
54. J. Heuschkel, *Welding Journal*, 52 (1973) 1s-25s.
55. S. S. Tulianni, N. F. Eaton, and T. Boniszewski, *Welding and Metal Fabrication*, 37 (1969) 325-339.
56. W. Cole and P. Colvin, *Metal Construction and British Welding Journal*, 3 (1971) 131-135.
57. D. J. Widgery: *Welding Research International*, 2 (1973) 1-20

Chapter 8

8. General Conclusions, Recommendations, and Future Work

8.1 General Conclusions

Investigation of the behaviour of advanced Q&T Ti-microalloyed wear-resistant steels during thermal cutting and arc welding led to the following general conclusions:

Research techniques and methods

1. Conventional cutting methods, such as oxy-fuel, plasma, and water-jet, may be successfully used to cut Q&T wear-resistant steels without cold cracking, provided minimum preheat temperature is maintained. PWHT may not be required in this case.
2. Conventional welding methods, such as FCAW and GTAW may also be used to weld Q&T wear-resistant steels without cold cracking, provided minimum preheat temperature and heat input is controlled. PWHT may not be required in this regard. Although the carbon equivalent is quite high for both steels (Ceq = 0.6-0.8).
3. AutoCAD software was successfully used to estimate the size of plate material to be procured. It involved considering the sizes and number of test coupons taken for each part of the experimental work.
4. Ceramic thermal pads along with insulation blankets were successfully used to maintain preheat temperature for welding CTS test coupons.
5. A propane gas heating torch was successfully used to preheat the high thickness K-type groove weld joint, while a ceramic blanket was used under the plate during welding to maintain the preheat temperature.

As-received plate steels

Mechanical properties of as-received Q&T steels were evaluated through tensile and impact testing. The following general conclusions may be drawn:

1. The correlation was found for the chemical analysis of steels with their mechanical properties. Steel H having higher contents of C and Ti showed higher strength. This

originated from a higher solid solution strengthening from C atoms and precipitation strengthening from coarse TiMoVCN, fine TiC, and Fe_3C particles.

2. A mixed brittle-ductile fracture mode was observed for both steel compositions. This means that for the studied microalloying element ranges the effect of steel composition on impact properties was insignificant, and the similarity in thermo-mechanical processing parameters played an important role in defining the impact properties.
3. Both steels did not show a sharp ductile to brittle transition within the studied temperature range of -70…+50 °C.
4. Microstructural analysis through SEM and EDS techniques showed uniformly distributed streaks of carbide particles of microalloying elements.

Effect of thermal cutting

1. A 25-34 % decrease in hardness was observed for all cut edges depending upon the cutting methods and distances from the cut edge. So, the preparation of edges must be considered before fabrication and welding.
2. The water-jet cutting method has been shown to generate no HAZ and no microstructure or properties variation in the vicinity of the cut edge. Therefore, this method is preferable for cutting Ti-alloyed Q&T steels. The plasma cutting is better than the oxy-fuel cutting method because the oxy-fuel cutting produced a very large (up to 9 mm) HAZ and excessive softening.
3. Microstructural evaluation of cut edges of both steels of thickness 12 mm, showed tempering of martensite. It was more in the case of the oxy-fuel cutting method as compared to the plasma cutting method. In the lower alloyed steel L, coarse TiMoVCN, fine Ti-rich, and Fe_3C dissolved during thermal cutting. In the more highly alloyed steel H, both coarse TiMoVCN and fine Ti-rich particles precipitated and grew, while Fe_3C dissolved. These discrepancies in the particle precipitation kinetics can be associated with the variation in steel composition, in particular, with concentrations of C and Ti in the martensitic matrix.
4. The tempering effect of cutting methods also had an influence on cut edge martensitic microstructures of both steel with a thickness of 32 mm for Steel L and 30 mm for Steel H. In the lower alloyed steel, coarse TiMoVCN particles dissolved and fine Ti-rich particles precipitated and grew during thermal cutting. In the more

highly alloyed steel, both coarse TiMoVCN and fine Ti-rich particles precipitated and grew.

Effect of preheating temperature on weld cracking propensity

1. CTS test coupons of both steels welded with heat input 1.2-1.6 kJ/mm showed no cracking when preheated at 80˚C and above. Maximum hardness was observed for HAZ and least for weld regions. The preheat temperature is much less than that required for conventional Q&T steels with the same carbon equivalent. This can be associated with lower C concentrations in the matrix, as the microalloying elements combined with carbon to form carbides of high-volume fraction. During cooling after welding lower C concentrations in the matrix resulted in lower hardenability and residual stresses in the Ti-microalloyed steels compared to the conventional ones.
2. Similar results were observed for each grade/ chemistry irrespective of the thickness of the steel. Both steels found cracked for preheat temperature of 60˚C and lower temperature.

Effect of heat input on weld and HAZ hardness

1. Both steels showed a drop in hardness for maximum heat inputs used for BOP test coupons. No cracking was observed as the test coupons were preheated at about 100-150˚C as per the supplier's recommendation which helped to redistribute stresses within the microstructure and minimise the cooling rate after welding.
2. Steel H with higher C and Ti contents showed higher hardness than Steel L, for all heat inputs. It may be due to the availability of more carbon in microstructure and the dissociation of TiC particles, to make hard martensitic microstructure.

Toughness assessment of K-type groove welded joint

1. A change in hardness was observed for weld and HAZ of K-type groove welded samples using the FCAW process with heat inputs of 1.2kJ/mm and 3.5kJ/mm. Impact test samples were taken at fusion boundary, 2 mm, 5 mm away from the weld centreline and the base metal did not show any sharp ductile to brittle transition, however, absorbed energy during impact testing decreased with a decrease in test temperature from 23˚C to -70˚C.

2. Both steels welded with 1.2kJ/mm and 3.5kJ/mm heat inputs, exhibited irregular grains of ferritic bainite at the fusion boundary. While at a distance of 2mm and 5mm from the fusion line, Steel L & Steel H welded with heat inputs of 1.2kJ/mm showed bainitic and martensitic microstructure. For heat inputs of 3.5kJ/mm for both steels at a distance of 2mm, the microstructure was found ferritic bainite but it transformed to bainitic and martensitic at a distance of 5mm.
3. The grain size observed for both steels at the base was found to be similar but changed at the fusion line, and away from the fusion line towards the base, due to the effect of heat input.
4. Steel L and Steel H welded with a low heat input of 1.2kJ/mm, revealed less change in microstructure as compared to the significant effect in steel samples welded with high input of 3.5kJ/mm. The dissolution of microalloying elements caused recrystallization of microstructure and the presence of undissolved microalloying constituent served as nucleation sites to form grains of smaller diameters at the fusion line as compared to those observed at a distance of 2mm from the fusion line
5. Growth of a limited number of TiC particles was observed at the fusion line for both steel grades, irrespective of the heat input level. Also, a general decreasing trend in particle density was noted from the base metal towards the fusion line. This indicates the dissolution of fine TiC particles towards the fusion line.

8.2 Scientific Novelty and Practical Recommendations

Literature survey indicates that steels with < 1.5 wt.% Ti content has been studied to improve the wear resistance. However, it is the first time when the steels with 0.4-0.6 wt.% Ti and 0.28-0.38 wt.% C contents were investigated for their behaviour during thermal cutting and arc welding. Ti forms hard carbides in tempered martensitic microstructure, which not only results in relatively low hardness but also improves the wear resistance, strength, and toughness of these steels. The effort was successfully exercised to cut and weld the steel without hydrogen-induced cracking or cold cracking. Also, variations in parameters of TiMoVCN, TiC, and Fe_3C particles were studied during thermal cutting and arc welding. The process parameters were optimized to study the mechanical and microstructural properties through a series of cutting and welding tests. All research work was planned for two different chemistries (Steel L & Steel H) and lower

and higher thicknesses (12mm & 32/30mm) as per availability on the market. Scientific novelty and practical recommendations consist of the following:

1. Co-relation was established between the chemical compositions, microstructure, and mechanical properties of hot rolled and heat-treated Q&T steel microalloyed with Ti.

2. Steels were successfully cut using conventional cutting methods (oxy-fuel and plasma techniques). Dye penetrant testing confirmed the cut edge surfaces being free from cracks. The operational parameters are helpful to control the heat input with the provision of preheating requirements.

3. The water-jet cutting method is recommended to cut such types of steel because it leaves no HAZ. Plasma is the second most favourable method with less HAZ in comparison to the oxy-fuel cutting method.

4. This study helped to understand the behaviour of TiC particles with respect to precipitation and dissolution during thermal cutting. These microstructural changes have a great impact on mechanical properties. More precautions should be taken during cutting of higher plate thicknesses due to the pronounced effect of high heat input used for cutting.

5. Welding of steel was performed using different sets of preheat and heat input values. The microstructural evaluation was carried out for the fusion zone and HAZ to compare properties with those of the base metal. The obtained results helped to optimise the welding process parameters, which can be used in the industry successfully.

6. A great success was observed to weld steels without cracking, using minimum preheating requirement. It will save a lot of time and cost from an industrial application point of view.

7. For higher thickness steels, welding heat input plays an important role. High heat input resulted in a higher weld hardness, which may facilitate cracking.

8. Toughness properties were also found more affected in the case of welding of higher thickness steel with high heat input. Microstructural analysis revealed the growth of TiC particles with less density, which adversely affected the steel toughness.

9. Welding of high thickness steel plates using preheating with propane gas torch and provision of ceramic insulation wool under the plates to maintain the preheating and allow slow cooling after welding allowed to avoid hydrogen-induced cracking of cold cracking in the steels studied in this project.

10. For CTS testing, a manifold was designed to preheat the steels with the help of electrical-resistant ceramic thermal jackets. It was a novel way of preheating and maintaining the test coupons at different temperatures.

11. Studying different welding test conditions helped to understand how operational parameters may be optimized to produce crack-free microstructure in the as-welded condition through employing conventional ways of fabrication techniques. The obtained results allow producing sound weldments without post-weld heating or post-weld heat treatment, which will provide a significant economic benefit in the industry.

8.3 Future Work

In this research work, advanced Q&T Ti-microalloyed wear-resistant steels were used to investigate their behaviour during thermal cutting and arc welding. Microalloying additions of Ti, V, and Mo provided excellent mechanical properties but the fabrication attributes deteriorated due to the thermal cycle effect on microstructure, which is susceptible to cold cracking. Based on the results obtained in this project, the following suggestions can be made for future research work:

1. In this work, cutting of steels with oxy-fuel and plasma methods was carried out using particular preheat temperatures as per the manufacturer's recommendation. In future work, a dependence of microstructure and properties on the preheat temperature before cutting can be studied. If a possibility to cut after a lower

temperature preheating is discovered, it would allow saving energy and time during cutting.

2. This project investigated cutting and welding of 12mm and 32/30mm thickness plates. Further investigation may be carried out for thicknesses higher than 32 mm. As the thickness increases, the operation parameters during cutting and welding become more critical to produce crack-free components.

3. Cutting of steels was performed via conventional ‘Manual’ cutting methods. In the future, the effect of automatic cutting technology may be investigated.

4. For CTS testing, a different set of preheating temperatures were used to obtain a crack-free microstructure. In future work, the effect of heat input can be investigated. Also, the effect of residual stresses and dissolved hydrogen may be investigated by using measurement techniques.

5. For the BOP testing conditions, a relationship between welding heat inputs and hardness was established. In future work, microstructural evaluation and toughness testing can be conducted to investigate the effect of BOP welding parameters on weld quality.

6. For the K-type groove testing in this research work, two heat inputs were analysed with respect to microstructural change at the fusion boundary, 2mm and 5mm distance. In future work, a larger range of heat inputs may be considered. Tensile testing would provide valuable additional knowledge of the effects of welding parameters on microstructure and properties of Ti-microalloyed Q&T steels.

List of Future Publications

On the basis of obtained results the following publications are currently under preparation:

1. Andrew G. Kostryzhev, M. Rizwan, Chris C. Killmore, Dake Yu, Chris A. Jones, Huijun Li, Paul Zulli, *Edge microstructure and strength gradient in thermally cut Ti-microalloyed martensitic steels.*

2. M. Rizwan, Andrew G. Kostryzhev, Chris C. Killmore, Dake Yu, Chris A. Jones, Huijun Li, Paul Zulli, *Evaluation of chemical composition, microstructure, and mechanical properties via base metal testing of Ti-microalloyed martensitic steels.*

3. M. Rizwan, Andrew G. Kostryzhev, Chris C. Killmore, Dake Yu, Chris A. Jones, Huijun Li, Paul Zulli, *Thermal cutting effect on hardness and microstructure of Ti-microalloyed martensitic steels.*

4. M. Rizwan, Andrew G. Kostryzhev, Chris C. Killmore, Dake Yu, Chris A. Jones, Huijun Li, Paul Zulli, *Effect of preheat temperature on weld cracking propensity of Ti-microalloyed martensitic steels.*

5. M. Rizwan, Andrew G. Kostryzhev, Chris C. Killmore, Dake Yu, Chris A. Jones, Huijun Li, Paul Zulli, *Effect of heat input on weld and HAZ hardness of Ti-microalloyed martensitic steels.*

6. M. Rizwan, Andrew G. Kostryzhev, Chris C. Killmore, Dake Yu, Chris A. Jones, Huijun Li, Paul Zulli, *Toughness and microstructural assessment of weld and HAZ of Ti-microalloyed martensitic steels.*